Transactions of the ASME, Journal of Heat Transfer (ISSN 0022-1481) is published monthly by The American Society of Mechanical Engineers, Three Park Avenue, New York, NY 10016. Periodicals postage paid at New York, NY and additional mailing offices. POSTMASTER: Send address changes to Transactions of the ASME, Journal of Heat Transfer, c/o THE AMERICAN SOCIETY OF MECHANICAL ENGINEERS, 22 Law Drive, Box 2300, Fairfield, NJ 07007-2300. **CHANGES OF ADDRESS** must be received at Society headquarters seven weeks before they are to be effective. Please send old label and new address. **STATEMENT from By-Laws.** The Society shall not be responsible for statements or opinions advanced in papers or ... printed in its publications (B7.1, Para. 3).

Journal of Heat Transfer

Published Monthly by ASME

VOLUME 130 • NUMBER 5 • MAY 2008

RESEARCH PAPERS

TECHNICAL BRIEFS

(Contents continued on inside back cover)

This journal is printed on acid-free paper, which exceeds the ANSI Z39.48-1992 specification for permanence of paper and library materials. ♾™
♻ 85% recycled content, including 10% post-consumer fibers.

Journal of Heat Transfer **Volume 130, Number 5** **MAY 2008**

The ASME Journal of Heat Transfer is abstracted and indexed in the following:

Applied Science and Technology Index, Chemical Abstracts, Chemical Engineering and Biotechnology Abstracts (Electronic equivalent of Process and Chemical Engineering), Civil Engineering Abstracts, Compendex (The electronic equivalent of Engineering Index), Corrosion Abstracts, Current Contents, E & P Health, Safety, and Environment, Ei EncompassLit, Engineered Materials Abstracts, Engineering Index, Enviroline (The electronic equivalent of Environment Abstracts), Environment Abstracts, Environmental Engineering Abstracts, Environmental Science and Pollution Management, Fluidex, Fuel and Energy Abstracts, Index to Scientific Reviews, INSPEC, International Building Services Abstracts, Mechanical & Transportation Engineering Abstracts, Mechanical Engineering Abstracts, METADEX (The electronic equivalent of Metals Abstracts and Alloys Index), Petroleum Abstracts, Process and Chemical Engineering, Referativnyi Zhurnal, Science Citation Index, SciSearch (The electronic equivalent of Science Citation Index), Theoretical Chemical Engineering

Heat Transport Characteristics in a Miniature Flat Heat Pipe With Wire Core Wicks

A. J. Jiao

H. B. Ma[1]
e-mail: mah@missouri.edu

J. K. Critser

Department of Mechanical and Aerospace Engineering,
University of Missouri-Columbia,
Columbia, MO 65211

A mathematical model predicting the heat transport capability in a miniature flat heat pipe (FHP) with a wired wick structure was developed to analytically determine its maximum heat transport rate including the capillary limit. The effects of gravity on the profile of the thin-film-evaporation region and the distribution of the heat flux along a curved surface were investigated. The heat transfer characteristics of the thin-film evaporation on the curved surface were also analyzed and compared with that on a flat surface. Combining the analysis on the thin-film-condensation heat transfer in the condenser, the model can be used to predict the total temperature drop between the evaporator and condenser in the FHP. In order to verify the model, an experimental investigation was conducted. The theoretical results predicted by the model agree well with the experimental data for the heat transfer process occurring in the FHP with the wired wick structure. Results of the investigation will assist in the optimum design of the curved-surface wicks to enlarge the thin-film-evaporation region and a better understanding of heat transfer mechanisms in heat pipes. [DOI: 10.1115/1.2887858]

Keywords: flat heat pipe, thin film evaporation, heat transfer

Introduction

Heat generation rates increase rapidly with the fast development of very large scale integrated (VLSI) circuits. Effectively dissipating the heat generated by VLSI is very important to maintain and keep their peak performance [1]. Conventional cooling methods, such as conventional heat sinks without phase-change heat transfer, are of impractical function at such high heat fluxes due to the constraints in the low thermal conductivity, volume, and weight associated with metal fin-array heat sinks. While an impingement cooling jet can be operated at a relatively high heat flux condition [2], however, it needs an additional pump with a power supply. Therefore, the removal of the huge amount of heat became the motivating research on a broad variety of advanced thermal management solutions. Heat pipes as the peerless choice in the electronics cooling field have been widely used recently. Heat pipe technology presents a promising approach to a higher level of heat transfer capability, heat flux, and importantly, requires no pump power input. However, the heat transport capacity of a heat pipe is often restricted by its capillary, sonic, boiling, entrainment, and viscous limit. The most critical limitation for a typical heat pipe in the electronics cooling is the capillary limit. Theoretical analyses and experimental investigations on the capillary limits for different wicks have been conducted [3–11]. Recently, Hanlon and Ma [8] developed a two dimensional model to investigate the evaporation heat transfer in sintered porous media to predict the effects of particle size, wick thickness, and porosity on the dryout heat flux. All those investigations, however, were limited to the evaporation and fluid flow in thin-film regions occurring or assuming on a flat surface.

The motivations behind the current work are to establish the correlation between the heat load and fluid flow, investigate the effects of the superheat and gravity on the liquid film profile and heat transfer through the evaporating thin-film region on a curved surface, calculate the total thermal resistance of the heat pipe, and predict the maximum heat transport capacity. In order to verify the theoretical analysis, a novel flat heat pipe with wired wicks was fabricated and an experimental investigation conducted.

Theoretical Analysis

Figures 1 and 2 illustrate the physical model of the flat heat pipe in the current investigation. The heat pipe consists of several subparallel heat pipes and each pipe includes three parts: a condenser, adiabatic section, and evaporator. As the heat transfer rate increases, the total pressure drop occurring in the heat pipe will increase, which directly results in the decrease of the meniscus radius in the evaporator to increase the capillary pressure and overcome the pressure drop. When the meniscus radius of liquid-vapor interface in the evaporator decreases, the liquid level in the evaporator (shown in Figs. 1 and 2) will change with the heat transfer rate added on the evaporator. The liquid film thickness characterized by δ_f, shown in Fig. 1, will decrease as the heat transfer rate increases until it reaches the nonevaporation film thickness, shown in Fig. 2, where it creates the longest thin-film-evaporation region (Case II). If the heat transfer rate continuously increases, the thin-film region will break into two regions (Case III), shown in Fig. 3, and the total length of the thin-film region will become shorter. As a result, the temperature difference across the evaporating film region will increase at the same heat transfer rate. Although the heat pipe has not reached the capillary limit, the temperature drop occurring in the evaporator will increase, which directly reduces the effective thermal conductivity of the whole heat pipe. Because the highest effective thermal conductivity is of the greatest concern for a highly efficient heat pipe cooling device, the current investigation will focus on the temperature drop from the evaporator to the condenser, i.e., the effectively thermal conductivity of the whole heat pipe. Because the liquid distribution in the heat pipe including the liquid level in the evaporator is governed by the capillary limitation, the following analysis will start with the capillary flow. Once the meniscus radius distribution in the heat pipe is determined for a given heat transfer rate, the detailed liquid distributions in the evaporator and condenser can be calculated, and the temperature drop found.

[1]Corresponding author.

Contributed by the Heat Transfer Division of ASME for publication in the JOURNAL OF HEAT TRANSFER. Manuscript received December 17, 2006; final manuscript received July 23, 2007; published online April 10, 2008. Review conducted by Raj M. Manglik.

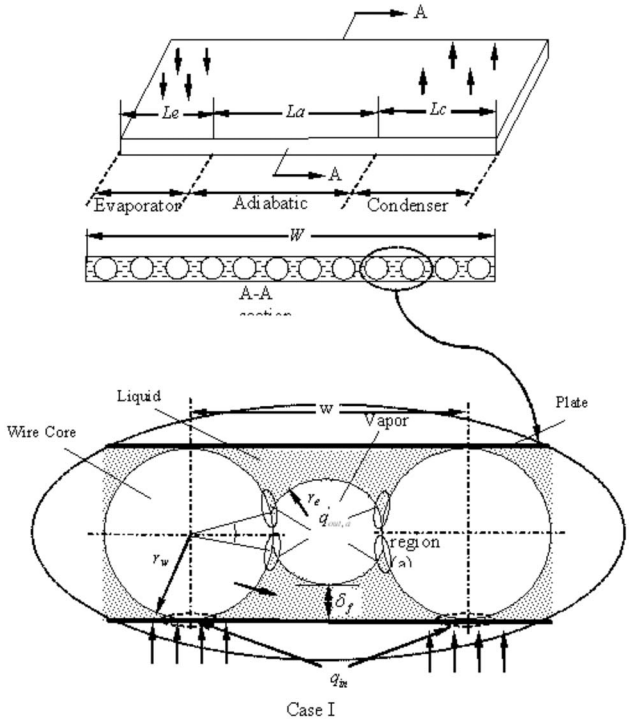

Fig. 1 Schematic of the FHP

Capillary Flow. The capillary limitation depicts that the sum of pressure drop occurring in the flow path shall not surpass the maximum capillary pressure head so that the fluid flow can be pumped back from the condenser to evaporator. The basic relationship can be expressed as

$$p_c \geq \Delta p_l + \Delta p_v + p_g \tag{1}$$

To simplify the calculation, the average radii at the evaporator and condenser are used, and thus, the capillary pumping pressure can be predicted by the Laplace–Young equation. The pressure drop of the liquid fluid and vapor fluid can be calculated by momentum equations at a steady state. As shown in Figs. 1 and 2, for the flat heat pipe with wired wick structure, Eq. (1) can be rewritten as

$$\sigma\left(\frac{1}{\bar{r}_e}-\frac{1}{\bar{r}_c}\right)=\left[\frac{4f_l\,\mathrm{Re}_l\,\mu_l}{2D_{h,l}^2}\cdot\frac{1}{N}\frac{Q_{\mathrm{tot}}}{\rho_l A A_{ac} h_{fg}}+\left(\frac{f_v\,\mathrm{Re}_{h,v}\,\mu_v}{2r_{h,v}^2}\right)\cdot\frac{1}{N}\frac{Q_{\mathrm{tot}}}{A A_v \rho_v h_{fg}}-\rho_l g\,\sin\phi\right]L_{\mathrm{eff}} \tag{2}$$

where,

$$2\beta=\frac{\pi}{2}-\lambda_{ai},\quad 0<\lambda_{ai}\leq\frac{\pi}{2},\quad i=B\text{ or }T$$

$$N=\frac{W}{w}$$

$$\bar{r}_e=\frac{\sin^2\beta}{\cos\beta\cos(0.5\beta+\alpha)}r_w$$

$$\delta_f=\begin{cases}r_w-[(r_w+\bar{r}_e)\sin\lambda_{ai}+\bar{r}_e] & \text{for CaseI}\\ \delta_0 & \text{for Case II}\end{cases}$$

$$L_{\mathrm{eff}}=\frac{L_e}{2}+L_a+\frac{L_c}{2}$$

$$A_{ac}=2\left[\frac{wr_w}{2}(1-\sin\lambda_{ai})-r_w^2\left(\beta-\frac{1}{2}\sin\lambda_{ai}\sin 2\beta\right)-r_e^2\left(\frac{\pi}{2}-\beta+\frac{1}{2}\sin\lambda_{ai}\cos\lambda_{ai}\right)\right]$$

$$D_{h,l}=\frac{4A_{ac}}{[2r_w tg\beta+2r_w\beta+r_e(2\alpha+\beta)]}$$

$$r_{h,v}=\frac{2A_v}{P_e}$$

$$A_v=2r_w w-\pi r_w^2-A_{ac}$$

$$P_e=2w+2\pi r_w+4r_e(2\alpha+\beta)-8r_w tg\beta-8r_w\sin\beta \tag{3}$$

Considering Eqs. (2) and (3) and Figs. 1 and 2, it can be found that β depends on λ_{ai}, and λ_{ai} is determined by the heat input. For the liquid flow, the Poiseuille number in an open groove $f_l\mathrm{Re}_l$ can be calculated by [5]

$$f_l\,\mathrm{Re}_l=14.11\alpha^{0.06009}\exp\left\{-0.5\times\left[\frac{\left(\log\frac{C_c}{22.22\alpha^{-0.3366}}\right)}{(2.083\alpha^{0.0372})}\right]^2\right\} \tag{4}$$

where $C_c=r_w\cos(\lambda_{ai}/4r_c)\cos\alpha$. Vapor can be considered as ideal gas. As shown in Fig. 1, the vapor flow channel in the condenser and adiabatic section can be approximated as a round tube, and its Poiseuille number is equal to 16 for a laminar flow. For the evaporator section, the vapor flow path can be approximated as rectangular channel, which $b/a=\pi r/w=0.785$ and its Poiseuille number is equal to 14.5. Once Eqs. (2) and (3) are solved for a given heat transfer rate, the liquid distribution along the heat pipe can be calculated and the meniscus radius and liquid level in the evaporator and condenser can be determined.

Heat Transfer in the Evaporator. In order to find the temperature drop occurring in the evaporator, the heat transfer process must be determined. When heat is added on the evaporator, some of the heat will transfer through the solid wire to the working fluid, and the rest of the heat directly through the heat pipe shell to the working fluid. While the temperature of the heat pipe shell can be assumed to be constant, the temperature distribution on the solid wire must be determined.

Temperature Distribution in the Wire Core. Thin-film-evaporation heat transfer plays an important role in the phase-change heat transfer on a flat surface [1,10,11]. Stephan and Busse [12] found that the effects of interface temperature variation on the heat transfer in the thin-film-evaporation region cannot be neglected. As shown in Fig. 1, in order to investigate the heat transfer characteristics including the interface temperature effect of thin-film evaporation, the temperature distribution in the wire core should be determined first. The equation governing the temperature distribution in the wire can be found as

$$\frac{\partial^2 T}{\partial r^2}+\frac{1}{r}\frac{\partial T}{\partial r}+\frac{1}{r^2}\frac{\partial^2 T}{\partial\theta^2}=0 \tag{5}$$

The required boundary conditions can be expressed as

$$-k_w\left.\frac{dT}{dr}\right|_{r=r_w}=q'_{in}\quad\text{at}\quad\frac{3\pi}{2}-\gamma_{in}\leq\theta\leq\frac{3\pi}{2}+\gamma_{in} \tag{6}$$

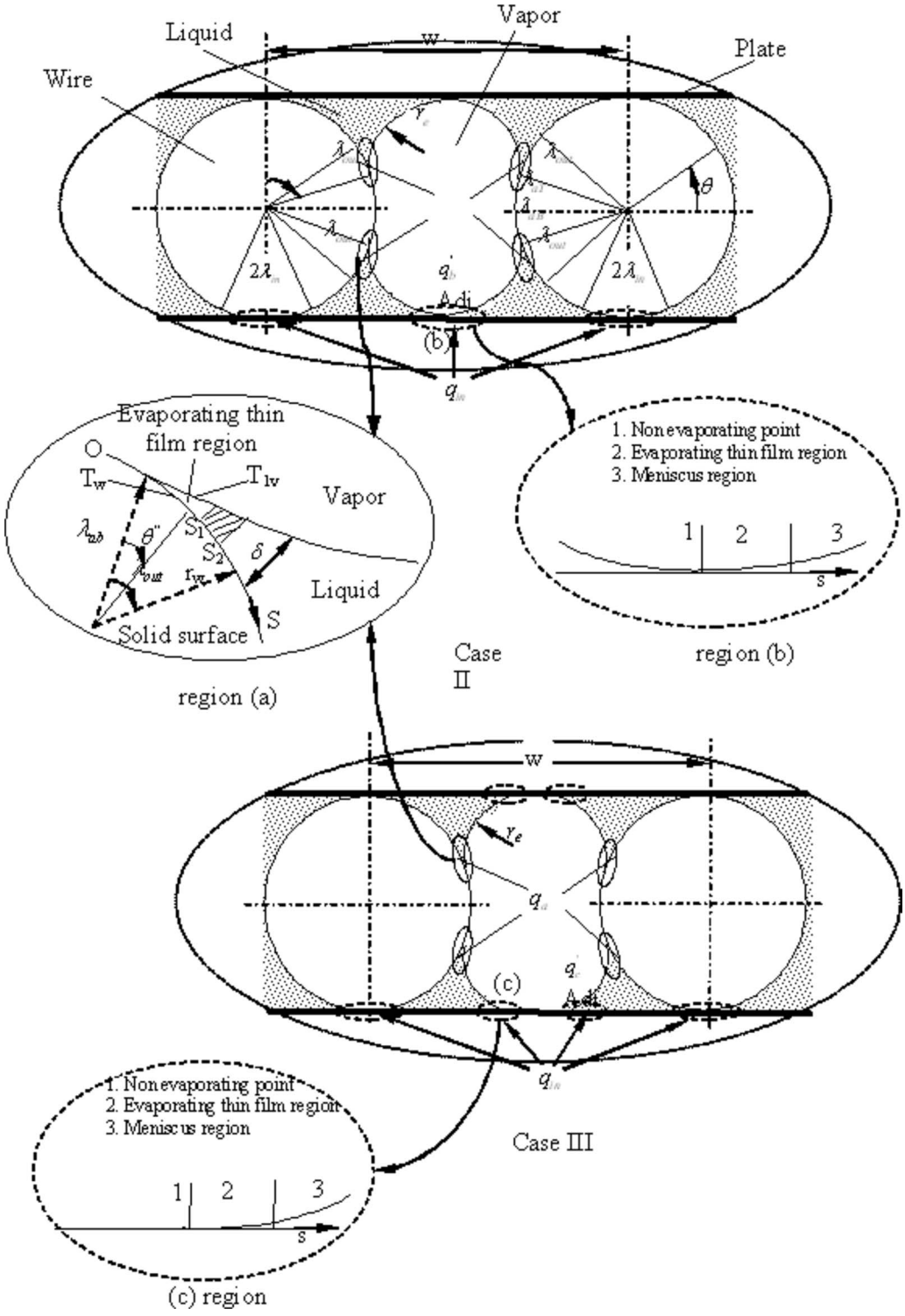

Fig. 2 Thin-film regions in the evaporator of FHP with wire core wicks

$$-k_w \left.\frac{dT}{dr}\right|_{r=r_w} = \begin{cases} 0 & \text{at } -\lambda_{ab} \le \theta \le \lambda_{at} \\ q'_{\text{out}} & \text{at } \lambda_{aT} \le \theta \le \lambda_{aT} + \lambda_{\text{out}}, \quad -(\lambda_{aB} + \lambda_{\text{out}}) \le \theta \le -\lambda_{aB} \\ q'_{\text{out},b} & \text{at } \lambda_{aT} + \lambda_{\text{out}} \le \theta \le \pi/2, \quad \dfrac{3\pi}{2} + \lambda_{in} \le \theta \le 2\pi - (\lambda_{aB} + \lambda_{\text{out}}) \end{cases} \tag{7}$$

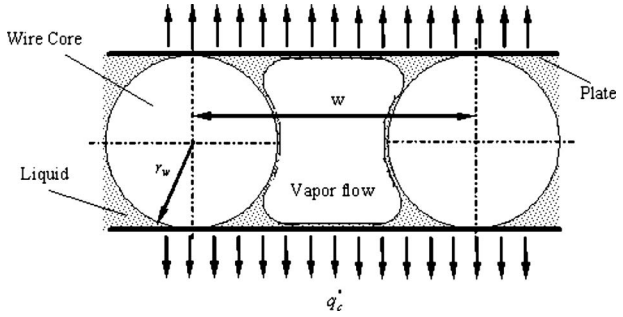

Fig. 3 Condensation heat transfer in the condenser

Equation (5) can be solved using the separation of variables. The temperature distribution of the wire core can be expressed by

$$T_w(r,\theta) = a_0 + \sum_{n=1}^{\infty}\left\{\left(\frac{r}{r_w}\right)^n [a_n \cos(n\theta) + b_n \sin(n\theta)]\right\} \tag{8}$$

where

$$a_n = \frac{2r_w}{n\pi}\left(\int_{\lambda_{aT}}^{\lambda_{aT}+\lambda_{\text{out}}} q'_{\text{out},a}\cos(n\theta)d\theta + \int_{\lambda_{aT}+\lambda_{\text{out}}}^{\pi/2} q'_{\text{out},b}\cos(n\theta)d\theta + \int_{3\pi/2+\lambda_{in}}^{2\pi-\lambda_{aB}-\lambda_{\text{out}}} q'_{\text{out},b}\cos(n\theta)d\theta + \int_{2\pi-\lambda_{aB}-\lambda_{\text{out}}}^{2\pi-\lambda_{aB}} q'_{\text{out},a}\cos(n\theta)d\theta + \int_{3\pi/2}^{3\pi/2+\lambda_{in}} q'_{in}\cos(n\theta)d\theta\right) \tag{9}$$

$$b_n = \frac{2r_w}{n\pi}\left(\int_{\lambda_{aT}}^{\lambda_{aT}+\lambda_{\text{out}}} q'_{\text{out},a}\sin(n\theta)d\theta + \int_{\lambda_{aT}+\lambda_{\text{out}}}^{\pi/2} q'_{\text{out},b}\sin(n\theta)d\theta + \int_{3\pi/2}^{3\pi/2+\lambda_{in}} q'_{in}\sin(n\theta)d\theta + \int_{3\pi/2+\lambda_{in}}^{2\pi-\lambda_{aB}-\lambda_{\text{out}}} q'_{\text{out},b}\sin(n\theta)d\theta + \int_{2\pi-\lambda_{aB}-\lambda_{\text{out}}}^{2\pi-\lambda_{aB}} q'_{\text{out},a}\sin(n\theta)d\theta\right) \tag{10}$$

and a_0 can be calculated by $a_0 = T_{\text{sat}} + \text{superheat}$.

Heat Transfer Through the Evaporating Thin-Film Region on the Curved Surface. When the heat transfer rate in the heat pipe changes, the liquid distribution in the liquid channel will be different. The meniscus radius in the evaporator will be different depending on the heat transfer rate. Based on the configuration of thin-film region, there exist three cases, as shown in Figs. 1 and 2. For the Case I ($\delta_f > \delta_0$), the liquid thickness δ_f decreases when the heat load increases and the thin-film region evaporation only occurs in Region (a). The fluid flow in Region (a) is driven by the curvature variation and disjoining pressure to overcome the viscous pressure loss and gravity effect, the governing equation can be written as

$$\sigma\frac{dK}{dS} + K\frac{d\sigma}{dS} - \frac{dp_d}{dS} = \frac{dp_l}{dS} + \frac{dp_{hg}}{dS} \tag{11}$$

For Region (a), using the coordinate transformations,

$$S = r_w\theta', \quad \theta' = 2\pi - \lambda_a - \theta \quad \text{at } 2\pi - \lambda_a - \lambda_{\text{out}} \le \theta \le 2\pi - \lambda_a \tag{12}$$

Eq. (11) can be rewritten as

$$\sigma\frac{dK_a}{d\theta'} + K_a\frac{d\sigma}{d\theta'} - \frac{dp_d}{d\theta'} = \frac{dp_l}{d\theta'} + \frac{dp_{hg}}{d\theta'} \tag{13}$$

where

$$p_{hg} = -\rho g r_w(1-\sin\lambda_{at}) \quad \text{or } p_{hg} = \rho g r_w(1-\sin\lambda_{ab}) \quad \text{at } 0 \le \theta' \le \lambda_{\text{out}} \tag{14}$$

$$K_a = \frac{-\frac{d^2\delta}{d\theta'^2}(\delta+r_w) + 2\left(\frac{d\delta}{d\theta'}\right)^2 + (\delta+r_w)^2}{\left[\left(\frac{d\delta}{d\theta'}\right)^2 + (\delta+r_w)^2\right]^{3/2}} \tag{15}$$

and

$$\frac{dp_l}{d\theta'} = -\frac{\mu_l\cdot\dot{m}_\delta}{\rho_l\left[\frac{3}{2}\delta^2 + r_w\delta + (r_w+\delta)^2\ln\left(\frac{r_w}{r_w+\delta}\right)\right]} \tag{16}$$

The boundary conditions can be summarized as

$$\delta|_{\theta'=0} = \delta_0, \quad K|_{\theta'=0} = K_0 = \frac{1}{r_w+\delta_0}, \quad \left.\frac{d\delta}{d\theta'}\right|_{\theta'=0} = 0 \tag{17}$$

where

$$p_d = -\frac{A}{\delta^3}, \quad A = 10^{-19}\ \text{J and } \delta_0 = \left[\frac{AT_v}{(T_w-T_v)\rho_v h_{fg}}\right]^{1/3}$$

Then, the film thickness distribution can be calculated by Eqs. (13)–(16) with the boundary condition of Eq. (17).

As the heat load increases, δ_f decreases. When δ_f decreases and becomes equal to δ_0, a new thin-film-evaporation region forms along the flat surface. This case is called Case II and there exists hybrid thin-film-evaporation regions, which consist of Regions (a) and (b). The governing equation of the thin-film thickness distribution in Region (b) can be expressed as Eq. (11) without the dp_{hg}/dS term, and the terms of curvature and dp_l/dS can be rewritten as

$$\frac{dp_l}{dS} = -\frac{f_l\,\text{Re}_{l,\delta}\,\mu_l\int_0^s\frac{q(s)}{h_{fg}}ds}{2\delta^3(s)\rho_l} \tag{18}$$

$$K_b = \frac{\frac{d^2\delta}{ds^2}}{\left[1+\left(\frac{d\delta}{ds}\right)^2\right]^{3/2}} \tag{19}$$

and

$$K = 0, \quad \delta = \delta_0, \quad \frac{d\delta}{dS} = 0 \quad \text{at } S = 0 \tag{20}$$

As shown in Fig. 2, the contact angle can be considered as zero in the thin-film Region (b) in Case II. With the further increase of the heat load, the thin-film-evaporation Region (b) breaks into two zones where the contact angle is not equal to zero, which is called Case III. Once the liquid film distribution reaches Case III, the effective thermal conductivity of the heat pipe decreases although the heat pipe has not reached the capillary limit. Therefore, the heat transfer rate corresponding to Case II is considered as the design-point "maximum" heat transport of flat heat pipe (FHP). Because this maximum heat transport occurring in Case II can result in the highest effective thermal conductivity of the heat pipe, which is of the most concern, the heat transfer characteristics in Case III will not be discussed here.

Maximum Heat Transport Capability in the Evaporator. Thin-film-evaporation heat transfer can be considered as one dimensional heat conduction since the thickness of this region is very thin. Therefore, the local heat flux can be calculated by $q' = k_l(\Delta T/\delta)$, which depends on the thin-film distribution and temperature difference between the wall temperature and interface temperature. For Case I, heat transfer through the evaporating thin film only exists in Region (a), and the local heat flux can be expressed as [13]

$$q_a' = k_l \frac{T_w(r_w,\theta) - T_{\delta a,v}(\theta)}{\delta(\theta)} \tag{21}$$

where $T_w(r_w,\theta)$ can be predicted by Eq. (8) and $\delta(\theta)$ can be found by Eqs. (11) and (13).

For Case II, the thin-film-evaporation heat transfer occurs in both Regions (a) and (b); the heat flux in Region (a) can be calculated by Eq. (21) and the heat flux in Region (b) can be expressed as

$$q_b' = k_l \frac{T_w - T_{\delta b,v}}{\delta(s)} \tag{22}$$

where T_w is the local wall temperature, and $\delta(s)$ can be calculated by Eq. (11) without dp_g/dS term and with boundary conditions shown in Eqs. (18) and (19).

Local liquid-vapor interface temperatures in thin-film regions, $T_{\delta a,v}(\theta)$ and $T_{\delta b,v}$, can be depicted by the Clausius–Clapeyron equation:

$$\left(\frac{dp}{dT}\right)_{\text{sat}} = \frac{h_{fg}}{T_{\text{sat}}\left[\left(\frac{1}{\rho_v}\right) - \left(\frac{1}{\rho_l}\right)\right]} \tag{23}$$

Integrating Eq. (23) from T_{sat} to the interface temperature $T_{\delta,v}$ yields [14]

$$T_{\delta,v} = T_v\left[1 + \left(\frac{\Delta p}{\rho_v h_{fg}}\right)\right] \tag{24}$$

where $\Delta p = K_i\sigma + p_d$, and $p_d = -A/\delta^3$.

Although the heat transport capability for Case II has not reached the capillary limit, the thermal resistance from the evaporator to the condenser for Case II is the lowest. Therefore, it is defined that the heat transfer rate in Case II is the maximum heat transport capacity. For Case II as shown in Fig. 2, the maximum heat transport capacity consists of heat transfer through bulk liquid (macroliquid region) and evaporating heat transfer through thin-film Regions (a) and (b). In this case, the heat transfer rate that passes through bulk liquid can be neglected [8,14]. For thin-film Region (a), heat transfer through this region can be calculated by

$$q = \int_0^{\lambda_{\text{out}}} q_a' dA'' = L_e r_w \int_0^{\lambda_{\text{out}}} k_l \frac{T_w(r_w,\theta') - T_{\delta,v}(\theta')}{\delta(\theta')} d\theta' \tag{25}$$

where $\theta_1'' = \theta - \lambda_a$ at $\lambda_a \leqslant \theta \leqslant \lambda_a + \lambda_{\text{out}}$ and $\theta_2'' = 2\pi - \lambda_a - \theta$ at $2\pi - \lambda_a - \lambda_{\text{out}} \leqslant \theta \leqslant 2\pi - \lambda_a$, respectively. The total heat transport through thin-film Region (a) on a given wire core can be calculated by

$$q_a = 2L_e r_w \left(\int_{\lambda_a}^{\lambda_a+\lambda_{\text{out}}} k_l \frac{T_w(r_w,\theta) - T_{\delta a,v}(\theta)}{\delta(\theta)} d\theta + \int_{2\pi-\lambda_a}^{2\pi-\lambda_a-\lambda_{\text{out}}} k_l \frac{T_w(r_w,\theta) - T_{\delta a,v}(\theta)}{\delta(\theta)} d\theta \right) \tag{26}$$

In the same way, the heat transfer rate through thin-film Region (b) can be found by

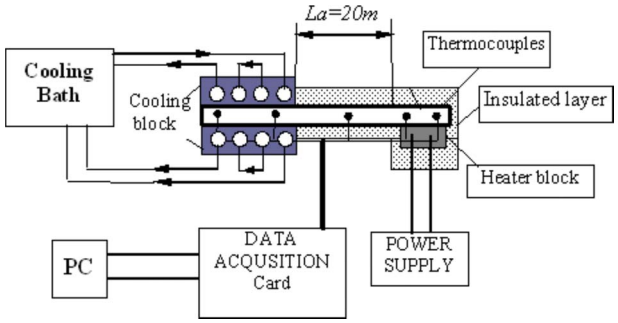

Fig. 4 Schematic of the experimental system

$$q_b = 2L_e \int_0^s k_l \frac{T_w - T_{\delta b,e}}{\delta(s)} ds \tag{27}$$

Combining Eqs. (26) and (27), and considering the evaporator structure shown in Fig. 1, the maximum heat transport capacity for the FHP can be expressed as

$$Q_{\text{tot}} = \frac{W}{w}(q_a + q_b) \tag{28}$$

Thin-Film-Condensation Heat Transfer in the Condenser. When the condensation heat transfer occurs in the condenser, the latent heat of vapor is released. As shown in Fig. 3, the condensation process can be simply modeled as the film condensation on a surface. The velocity of vapor flow decreases along the condenser direction to zero at the cap end. Its inlet Reynolds number can be calculated by

$$\text{Re}_{v,i} = \frac{\rho_v u_{v,i} D_h}{\mu_v} \tag{29}$$

where $D_h = 4A_e/P_e$, $A_e = 2r_w w - \pi r_w^2 - A_{ac}$, and $u_{v,i}$ is the inlet velocity of vapor flow in the condenser and can be expressed by

$$u_{v,i} = \frac{Q_{\text{tot}}}{NA_e \rho h_{fg}} \tag{30}$$

Thus, the average heat transfer coefficient in the condenser can be calculated by

$$\overline{h_D} = C\left[\frac{g\rho_l(\rho_l - \rho_v)k_l^3 h_{fg}'}{\mu_l(T_{\text{sat}} - T_{wc})D_h}\right]^{1/4} \tag{31}$$

where $h_{fg}' = h_{fg} + \frac{3}{8}c_{p,l}(T_{\text{sat}} - T_{cw})$. Since the inlet velocity of vapor flow is not very high ($\text{Re}_{v,i} < 3500$), Chato [15] recommended that the constant C is equal to 0.555. Based on the condenser geometry, as shown in Fig. 1, and considering Eq. (31), the correlation between the heat load and condensation temperature difference can be expressed by

$$Q_{\text{tot}} = 0.9334\frac{W}{w}\left[\frac{g\rho_l(\rho_l - \rho_v)k_l^3 h_{fg}'}{\mu_l(2w - \pi r_w)r_w}\right]^{1/4}(w + \pi r_w)^{5/4} L_c \Delta T^{3/4} \tag{32}$$

Experimental System and Investigations. Figure 4 illustrates the experimental system, which consists of the test section (FHD), data acquisition system, heater power supply system, and cooling system. The data acquisition system includes a PC, thermocouples, and a data acquisition card to measure the temperature responses of evaporator and condenser, and power inputs. The cooling system contains two flat aluminum cooling blocks and one cooling bath where the temperature was maintained at $60 \pm 0.1\,^\circ\text{C}$. The maximum heat load of the heater power supply is 250 W. In order to supply a uniform heat flux, the top surface size

of the heater was fabricated as the same as the evaporator bottom surface, which was 15 mm width and 30 mm length. The largest measurement uncertainties of the current investigations were less than 1%. The test section is a FHP, which consists of 15 subparallel heat pipes and each of these heat pipes consists of the condenser (L_e=15 mm), adiabatic section (L_a=20 mm), and evaporator (L_c=40 mm). As shown in Fig. 1, the wire diameter is equal to 1 mm (r_w=0.5 mm) and the distance between two wires is 2.0 mm (w=2.0 mm). The width and length of the FHP are 30 mm and 75 mm, respectively. The total amount of water charged to the FHP is 0.6 g. In order to reduce the contact thermal resistance, the Omega "201" thermal paste was used between the aluminum cooling block and the condensing surface in the condenser, and between the heater and the evaporating surface in the evaporator.

Results and Discussion

From the above analysis, heat transfer through thin films formed on the curved surface can be predicted by the third-order differential equations, which can be solved by the fourth-order Runge–Kutta method to obtain the interface temperature and film thickness distribution. It should be noted that the following assumptions are made in the calculation. (1) Previous results [8,12] indicate that most of the heat added on the solid wire will transfer through the thin-film region. So it is assumed that the heat added on the particle is equal to the total evaporating heat transfer through the thin-film region. (2) The vapor flow is saturated and considered as ideal gas. (3) The meniscus radius of liquid-vapor interface in the wicks is constant at a given heat load. (4) When the film thickness increases, the disjoining pressure effect decreases until it is so small that it can be neglected. The length of the thin-film region is determined by the cutoff value of 0.015 Pa of disjoining pressure. (5) Water is used as the working fluid and its thermophysical properties at 60°C are used for the numerical calculations. (6) As shown in Fig. 1, the contribution of the heat transfer through Region (b) in Case I is negligible since the thermal resistance is very large due to the thick liquid film. However, as the heat load increases, the liquid thickness becomes thinner and thinner, and the contribution of the heat transfer through Region (b) should be considered. In the evaporation heat transfer calculation, the heat pass through Region (b) has been added when the film thickness δ_f=0.05 mm until δ_f reaches δ_0. If the heat load continues to increase after δ_f reaches δ_0, Case III situation is used to predict the temperature response in the evaporator. (7) Only film condensation heat transfer occurs in the condenser. Heat flux through the thin-film region depends on the input heat load and the temperature distribution on the solid wire, which in turn determines the evaporating heat transfer and the viscous fluid flow in the thin-film region. Therefore, an iterative technique has been utilized to solve for the temperature distribution on the solid wire, liquid film profile, interface temperature, and heat flux in the thin-film region. The calculation procedure for the evaporation heat transfer at a given heat load can be summarized as follows:

(1) Select a contact angle of α.
(2) Solve Eqs. (2) and (3) for $\bar{r}_e$, λ, and δ_f.
(3) Select a superheat.
(4) Calculate the temperature distribution of the solid wire by Eq. (8).
(5) Calculate the thin-film profile by Eqs. (13)–(20).
(6) Calculate the vapor-liquid interfacial temperature and heat flux distribution by Eqs. (21)–(24).
(7) Calculate the total heat load and compare the prediction with the given heat load. If the error is greater than 0.5 W, then go to Step 3.
(8) When the error between the prediction and the given heat load is less than 0.5 W, output the superheat, thin-film profiles, and heat flux distributions.

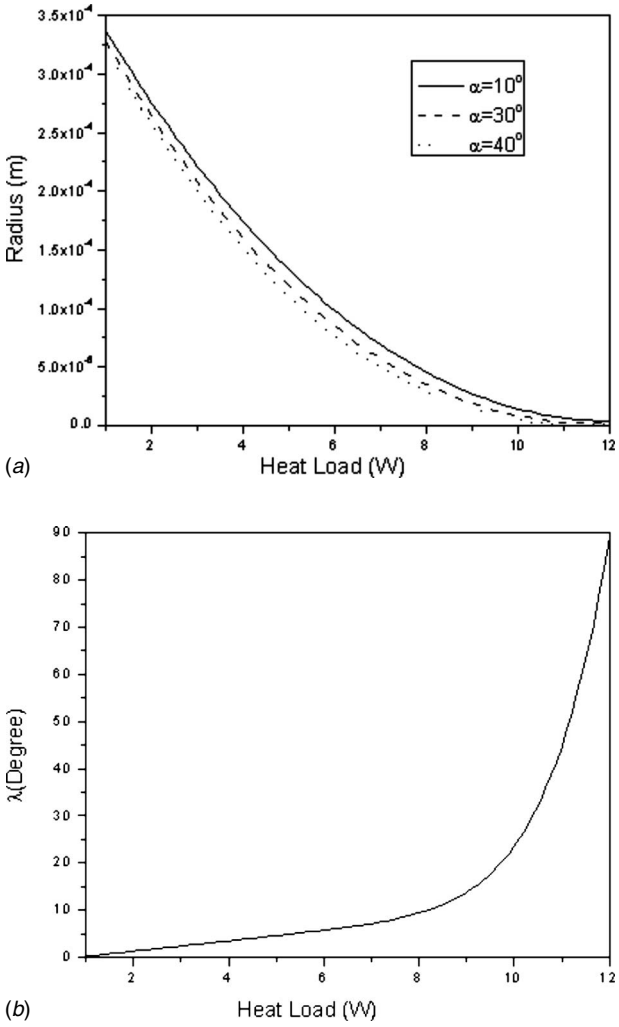

Fig. 5 Heat load effects on (*a*) average radius of evaporator at different contact angles; (*b*) λ at α=30 deg

Figure 5(*a*) illustrates the heat load effect on the average radius in the evaporator at different contact angles in one subparallel heat pipe. The net capillary pressure difference pumping the condensate back to evaporator can be calculated by the Laplace–Young equation: $\Delta P_c=\sigma((1/\bar{r}_e)-(1/\bar{r}_c))$. Solving Eqs. (2) and (3) for a given heat load, the average curvature radius of evaporator $\bar{r}_e$ can be determined and it is found that it depends on the contact angle, heat load, and dimensions of wick structures. As the heat load increases, the flow rates in both the liquid and vapor phases result in the increase of the total pressure drop. In order to maintain a steady-state operation of the heat pipe, higher capillary pressure difference between the evaporator and condenser results in. Therefore, the average meniscus radius in the evaporator decreases as the heat load increases, as shown in Fig. 5(*a*), and it depends on the contact angle. Figure 5(*b*) illustrates the heat transfer rate effect on the angle λ, which stands for the liquid thickness in the evaporator in one subparallel heat pipe. The angle λ changes slowly when the heat load is low. As the heat load becomes higher than 9 W, however, the angle varies dramatically with the heat load.

Figures 6(*a*)–6(*c*) illustrate the thin-film thickness profiles of Case I (α=30 deg, only for the curved surface), Case II (α=30 deg, for the curved surface and α=0 deg, for the flat surface), and Case III (α=30 deg, for both the curved and the flat surface) at a superheat of 1.0 K, respectively. As shown in Fig. 6, the

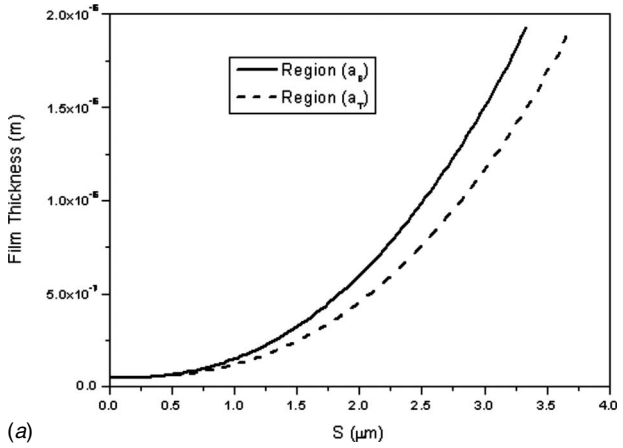

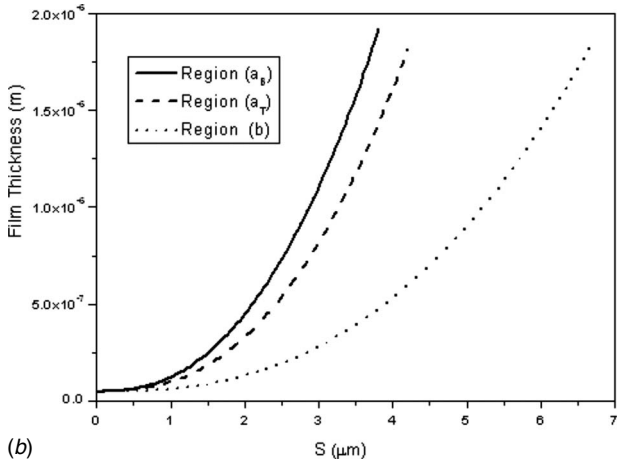

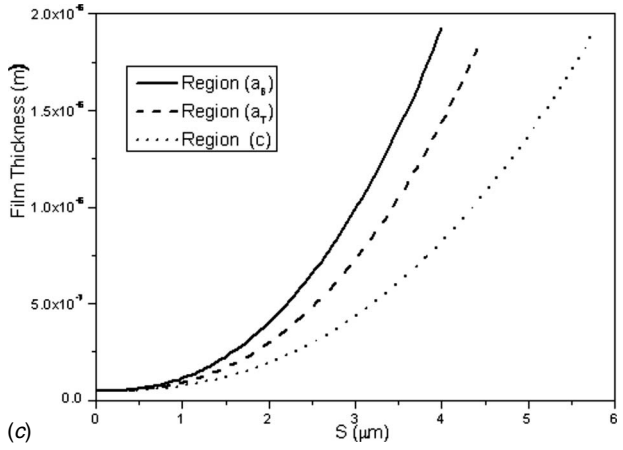

Fig. 6 Thin-film profiles for (*a*) Case I, (*b*) Case II, and (*c*) Case III ($T_w - T_v$=1.0 K)

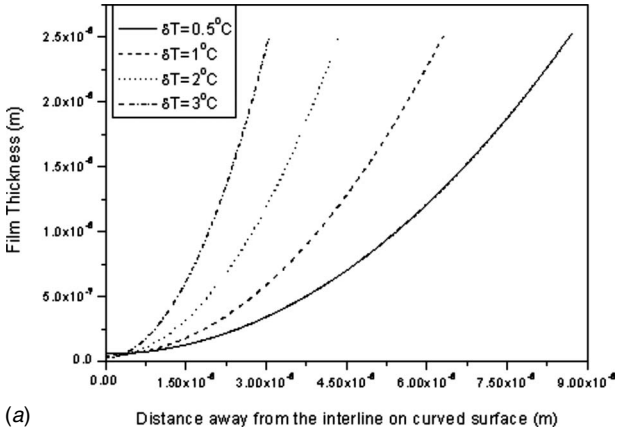

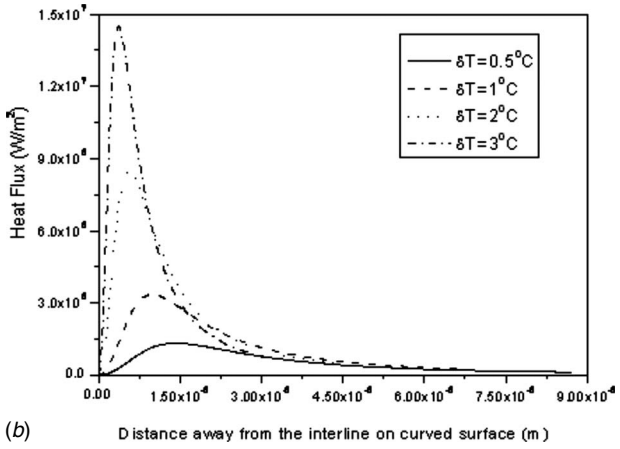

Fig. 7 Superheat effect on the thin-film profile and heat flux distribution on the upper curved surface (Case I, α=30 deg)

thin-film region in Case I yields the lowest heat transport capability because it has the thin-film-evaporation region only on the curved surface. Case II yields the highest because of the curved surface and flat surface with a contact angle equal to zero. As shown in Fig. 6(*c*), the film thickness distributions of Region (a_B) and Region (a_T) illustrate the gravity effect on the thin-film distribution on the curved surface. Results shown in Figs. 6(*b*) and 6(*c*) indicate that the gravity directly affects the length of the thin-film region. In addition, the length of the thin-film regions on the flat surface is much longer than that of thin-film region on the curved surface.

When the interface temperature of vapor-liquid is equal to the wall temperature, no evaporation heat transfer occurs in this region. The nonevaporation thin-film thickness can be determined by Eq. (24). If $T_{\delta,v}=T_w$ and $d\delta/d\theta''|_{\theta''=0}=0\Rightarrow k\rightarrow 0$, the nonevaporating film thickness can be found by $\delta_0=[AT_v/(T_w-T_v)\rho_v h_{fg}]^{1/3}$. The heat flux through the thin-film region calculated by a 1D heat conduction heat transfer model. When a superheat (T_w-T_{lv}) between the solid surface and the interface temperature exists, the high heat flux takes place in the thin-film-evaporation region. As shown in Fig. 7, this superheat drastically affects the evaporation thin-film profiles both in length and shape. A larger superheat results in a higher heat flux and higher mass flow rate in the thin-film region, which directly increases the viscous pressure drop over a given length. In order to maintain the steady-state evaporating heat transfer in the thin-film region and pump enough liquid to the thin-film region, the disjoining pressure must increase and overcome the viscous pressure drop and the pressure difference due to the curvature variation. As shown in Fig. 7(*a*), when the superheat increases, the thin-film region decreases significantly. In other words, the curvature of thin-film region is sensitive to superheat and the thickness of evaporating thin film increases dramatically with the superheat at a given location. With a higher superheat, the nonevaporating film thickness becomes thinner, and that produces an even higher heat flux in the evaporating thin-film region than the case with a smaller superheat.

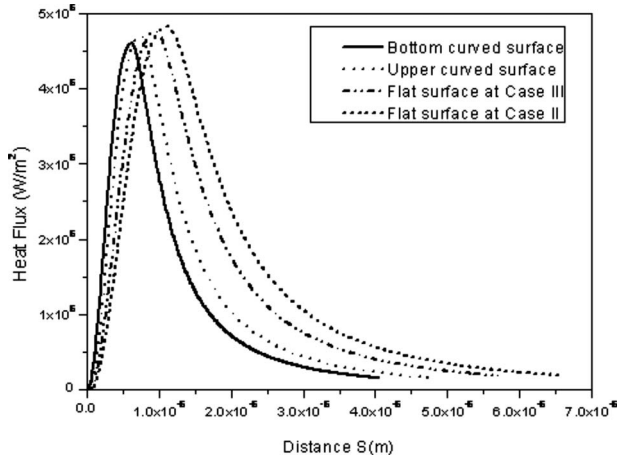

Fig. 8 Curved-surface effect on the heat flux distribution ($T_w - T_v$=1.5 K)

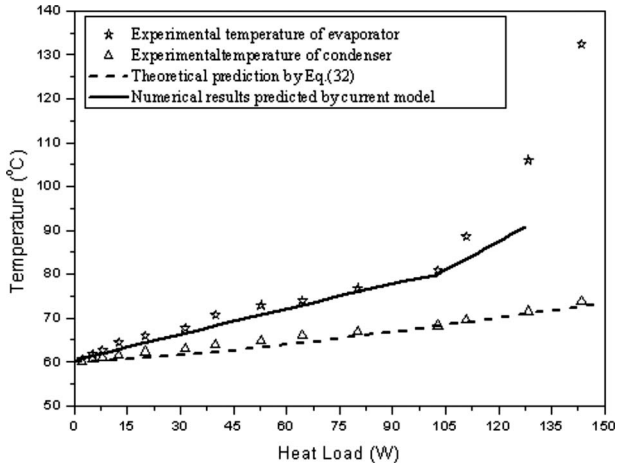

Fig. 9 Comparison between the theoretical prediction and experimental data of the evaporator and condenser temperature response versus heat load input (working fluid, water; charged amount=0.6 g)

At the same conditions, the effects of the gravity and contact angle on heat flux distributions along different surfaces were conducted with a superheat of 1.5 K. As shown in Fig. 8, the heat flux profiles through the liquid films of the bottom and upper surfaces on a curved wire core in the FHP are different due to the effects of gravity on the fluid flow in the thin-film region with the contact angle α=30 deg. Obviously, the gravity force produces a longer length of thin-film region and results in a better heat transfer performance on the upper surface than that on the bottom surface. Integrating the heat flux profiles, the amount of heat through the upper surface is 8.4% higher than that through the bottom surface. Clearly, the gravity directly affects the heat transfer rate through the evaporating thin-film region. As shown in Fig. 2, thin-film evaporation on the flat surface will play an important role when the heat pipe operates in Case II. When the heat load further increases after the heat pipe reaches Case II, the thin-film-evaporating region on the flat surface would break into two thin-film zones and the heat pipe would operate in Case III. The heat flux distributions on the flat surface in Cases II (α=0 deg) and III (α=30 deg) have been conducted also, herein, by integrating the heat flux, and the results show that the heat transport capacity of Case II is 1.11 times of that in Case III. Comparing these heat flux distributions, it can be concluded that the contact angle significantly affects the thin-film profiles and heat transfer rate through the thin-film regions.

Based on the model presented above, the temperature response to the heat load in the evaporator and condenser has been predicted. In order to verify the theoretical prediction, the experimental data of the temperature response with the heat load in the evaporator and condenser have been compared with the theoretical prediction. As shown in Fig. 9, the theoretical results agree very well with experimental data for the condenser. The current model can be used to predict the temperature response in the evaporator with heat load if the heat load was less than 105 W, which corresponds to the situation of Case II. When the heat loads continue to increase, the thin-film-evaporating region on the flat surface would break into two thin-film zones and the heat pipe would operate in Case III, where a contact angle of 30 deg was selected. The increase of the contact angle would directly increase the temperature drop across the liquid film. Although the model considered this effect, the experimental results are still much higher than the theoretical prediction. The heat pipe also worked when the heat load was higher than 105 W but its performance became worse as heat load increased, and it completely lost function when the heat load reached 138 W.

Conclusions

A detailed mathematical model for the heat transfer process in a miniature FHP with wire core wicks was developed. The effects of gravitational force and contact angle on the thin-film profiles and heat flux distribution on the curved surface are investigated. The theoretical results show that the gravity effect on thin-film distributions and heat flux profiles on curved surfaces cannot be neglected. Based on the capillary limit and thermal resistance, the maximum heat transport capacity of the heat pipes is predicted. When the heat pipes were operated in Case II, the heat load reached its maximum transport capacity since the further increase of heat load would result in the sharp increase of the temperature drop due to the heat transfer degradation in thin-film evaporation although the heat pipe has not reached the capillary limit. The comparison with the experimental data shows that the theoretical model can be used to precisely predict the temperature response of the evaporator and condenser in Cases I and II. The current investigation will assist in the optimum design of curved-surface wick to enlarge the thin-film-evaporation region and enhance the evaporation heat transfer of the heat pipe, and a better understanding of the heat transfer mechanisms in FHP.

Acknowledgment

This work was supported by the Office of Naval Research under Grant No. N00014-06-1-1119 and Intel Corporation, Luvata Copper Franklin, and Foxconn.

Nomenclature

A = modified Hamaker constant 10^{-19} J; cross-sectional area, m^2
a = defined by Eq. (9)
b = defined by Eq. (10)
C = constant defined by Eq. (31)
C_c = defined by Eq. (4)
D = diameter, m
f = friction factor
g = gravity acceleration, m/s^2
h = height, m
h_{fg} = latent heat of vaporization, kJ/kg
K = curvature, 1/m
k = conductivity, W/m K
L = length, m
N = number of grooves

P = wetting perimeter, m
p = pressure, N/m^2
p_d = disjoining pressure, N/m^2
Q = heat load, W
q' = heat flux, W/m^2
R = gas constant, J/kg K
Re = Reynolds number
r = radius, m
S = coordinate, m
T = temperature, K
u = velocity, m/s
W = width of heat pipe, m
w = with of groove, m

Greek

α = contact angle, rad
β = angle defined by Fig. 2, rad
δ = film thickness, m
δ_0 = nonevaporating film thickness, m
ϕ = slant angle of heat pipe, rad
λ = angle defined in Fig. 2, rad
μ = viscosity, $N\,s/m^2$
θ = coordinates, deg
ρ = density, kg/m^3
σ = surface tension, N/m

Subscripts

a = adiabatic, Region (a) in Fig. 2
aB = bottom Region (a) shown in Fig. 2
ac = liquid flow area in evaporator
aT = top Region (a) shown in Fig. 2
B = bottom
b = region (B) in Figs. 1 and 2
c = condenser, capillary
e = evaporator
eff = effective
g = gravity
h = hydraulically
i = defined by Eq. (3)
l = liquid
lv = interface of liquid-vapor
sat = saturated
T = top
tot = total
v = vapor
w = wire, wall
δa = thickness of Region (a)
δb = thickness of Region (b)

References

[1] Peterson, G. P., and Ma, H. B., 1999, "Temperature Response of Heat Transport in Micro Heat Pipe," ASME J. Heat Transfer, **121**(3), pp. 438–445.
[2] Wang, E. N., Zhang, L., Jiang, L. N., Koo, J. M., Maveety, J. G., Sanchez, E. A., Goodson, K. E., and Kenny, T. W., 2004, "Micromachined Jets for Liquid Impingement Cooling of VLSI Chips," J. Microelectromech. Syst., **13**(5), pp. 833–842.
[3] Jiao, A. J., Riegler, R., Ma, H. B., and Peterson, G. P., 2005, "Thin Film Evaporation Effect on Heat Transport Capability in a Groove Heat Pipe," Microfluid. Nanofluid., **1**(3), pp. 227–233.
[4] Jiao, A. J., Ma, H. B., and Critser, J. K., 2007, "Evaporation Heat Transfer Characteristics of Tube Heat Pipes With Micro Trapezoidal Structure Liquid Wicks," Int. J. Heat Mass Transfer, **50**(15–16), pp. 2905–2911.
[5] Kim, S. J., Seo, J. K., and Do, K. H., 2003, "Analytical and Experimental Investigation on the Operational Characteristics and the Thermal Optimization of a Miniature Heat Pipe With a Grooved Wick Structure," Int. J. Heat Mass Transfer, **46**(11), pp. 2051–2063.
[6] Ma, H. B., and Peterson, G. P., 1996, "Experimental Investigation of the Maximum Heat Transport in Triangular Grooves," ASME J. Heat Transfer, **118**(4), pp. 740–745.
[7] Ma, H. B., and Peterson, G. P., 1997, "Temperature Variation and Heat Transfer in Triangular Grooves With an Evaporating Film," J. Thermophys. Heat Transfer, **11**(1), pp. 90–97.
[8] Hanlon, M. A., and Ma, H. B., 2003, "Evaporation Heat Transfer in Sintered Porous Media," ASME J. Heat Transfer, **125**(4), pp. 644–652.
[9] Peterson, G. P., 1994, *An Introduction to Heat Pipes*, Wiley, New York.
[10] Khrustalev, D., and Faghri, A., 1994, "Thermal Analysis of a Micro Heat Pipe," ASME J. Heat Transfer, **116**(1), pp. 189–198.
[11] Hopkins, R., Faghri, A., and Khrustalev, D., 1999, "Flat Miniature Heat Pipes With Micro Capillary Grooves," ASME J. Heat Transfer, **121**(1), pp. 102–109.
[12] Stephan, P. C., and Busse, C. A., 1993, "Analysis of the Heat Transfer Coefficient of Grooved Heat Pipe Evaporator Walls," Int. J. Heat Mass Transfer, **35**(2), pp. 383–391.
[13] Demsky, S. M., and Ma, H. B., 2004, "Thin Film Evaporation on a Curved Surface," Microscale Thermophys. Eng., **8**(3), pp. 285–299.
[14] Jiao, A. J., Han, X., Critser, J. K., and Ma, H. B., 2006, "Numerical Investigations of Transient Heat Transfer Characteristics and Vitrification Tendencies in Ultra-Fast Cell Cooling Processes," Cryobiology, **52**(3), pp. 386–392.
[15] Chato, J. C., 1962, "Laminar Condensation Inside Horizontal and Inclined Tubes," ASHRAE J., **4**(1), pp. 52–60.

Heat Transfer Resulting From the Interaction of a Vortex Pair With a Heated Wall

Roland Martin
Laboratoire de Modélisation et d'Imagerie en Géosciences,
CNRS UMR 5212 and INRIA Futurs Magique3D,
Université de Pau et des Pays de l'Adour,
Bâtiment IPRA,
Avenue de l'Université,
64013 Pau, France

Roberto Zenit
Instituto de Investigaciones en Materiales,
Universidad Nacional Autónoma de México,
Apartado Postal 70-360,
Distrito Federal 04510, México

The motion of a two-dimensional vortex pair moving toward a wall is studied numerically. The case for which the wall is heated is analyzed. The equations of momentum and energy conservation are solved using a finite volume scheme. In this manner, the instantaneous heat transfer from the wall is obtained and is related to the dynamics of the fluid vortex interacting with the wall. It was found that, as expected, when the fluid vortex approaches the wall, the heat transfer increases significantly. The heat transfer changes in a nonmonotonic manner as a function of time: When the vortex first reaches the wall, a volume of heated fluid is convected from the wall; this fluid volume circulates in the vicinity of the wall, causing the rate of heat transfer to decrease slightly, to then increase again. A wide range of Prandtl and Reynolds numbers were tested. A measure of the effective heat transfer coefficient, or Nusselt number, is proposed.
[DOI: 10.1115/1.2885182]

Keywords: vortex pair, wall interaction, convective heat transfer, simulation

1 Introduction

Convective heat transfer is probably the most commonly used method to remove heat from a heated source in engineering applications. The nature of the fluid flow is, hence, the factor that determines how effective the heat removal is. In spite of its prominence, the design of convective heat transfer devices has been mainly empiric. To be able to further enhance the convective heat transfer processes, the details of the interaction between fluid flow and walls have to be fully understood.

Clearly, the fluid motion over a wall has a direct implication to the heat transfer rate, as heat is convected by the flow. Although the understanding of convective heat transfer is very well developed for the case of steady flows, the determination of unsteady heat transfer coefficients is still incipient [1]. Understanding such unsteady processes is a key factor to achieve the increasing need of fast heat removal from modern engineering applications. In particular, the unsteady motion created by vortices and its implications to the increase of heat transfer [2] is of significant importance: One of the most common techniques to enhance the convective heat transfer uses vortex generators (see, for example, Refs. [3,4] and references therein). As vortices interact with walls, an unsteady boundary layer develops, which has direct implications to the rate of heat transfer [5,6].

The interaction of vortical structures with walls has been analyzed by many authors in a variety of configurations [7]. Of particular interest, because of its apparent simplicity, is the case of a compact isolated vortex ring impinging normally over a solid wall [8]. The evolution of this flow configuration is complex: Resulting from the vortex fluid motion, an unsteady boundary layer develops on the wall. The vorticity created on the wall is convected, resulting in the formation of a secondary vortex, which interacts with the original one. These two vortical structures continue to interact with each other, creating, in some cases, a third vortex. These observations were originally obtained by experiments [8,9], but were also verified by numerical simulations [10,11].

For the case of nonisothermal flows, most investigations have been focused to understand the effect of vortical structures over the global heat transfer rate. Studies of the effect of an isolated vortex are less common. Reulet et al. [12] investigated the effect of an isolated vortex, produced by a flapping wing, convected by a turbulent stream over a heated wall. They found that the evolution of the thermal boundary layer was strongly coupled with the dynamic effects of the vortex. Romero-Méndez et al. [13] analytically calculated the effects of isolated Rankine vortices over walls in different configurations and found that in all cases an increase of the heat transfer was observed. Although this study considered an idealized flow, it gave a significant insight on the fundamental processes that occur during the interaction of vortices with walls and their implications with heat transfer.

The objective of this paper is to study the mechanism by which heat is removed from a wall resulting from the interaction of a coherent vortical structure. A simplified arrangement has been chosen to solve this problem: the normal impingement of a 2D vortex pair with a flat heated wall. We have opted to use computer simulations to be able to study the sole effect of the coherent fluid flow on the wall heat flux. An experimental study of the same problem would have an additional important complication: Natural convection would always be present; therefore, it would not be possible to study the removal of heat without this effect. The case for which both vortical motion and natural convection contribute to the rate of heat transfer could be of interest, in particular, for practical applications; however, its study lies beyond the current investigation.

Using a modified SIMPLE numerical scheme, the equations of momentum and energy are solved to find the velocity and temperature fields as a function of time. The instantaneous heat transfer from the wall is calculated and related to the motion of the fluid in the vicinity of the wall. The heat transfer rates are correlated to the convective and diffusive processes at the moment of impact of the vortex at the wall and for long periods. We first introduce the general mathematical formulation of the problem; then, the problem of study is described. The numerical method and its implementation issues are then discussed. The results are presented and discussed.

Contributed by the Heat Transfer Division of ASME for publication in the JOURNAL OF HEAT TRANSFER. Manuscript received December 4, 2006; final manuscript received July 2, 2007; published online April 8, 2008. Review conducted by Gautam Biswas.

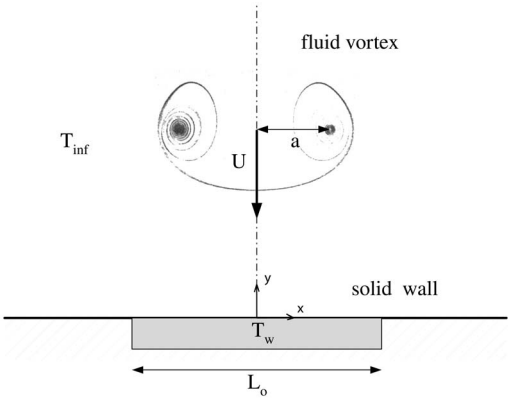

Fig. 1 The interaction of a vortex pair (or ring) with a heated wall

2 Mathematical Formulation

The flow studied here is two dimensional, unsteady, laminar, and incompressible. The dimensionless conservation equations are the continuity

$$\nabla \cdot \mathbf{u}^* = 0 \tag{1}$$

time-dependent momentum

$$\frac{\partial \mathbf{u}^*}{\partial t^*} + (\mathbf{u}^* \cdot \nabla^*)\mathbf{u}^* + \nabla^* P^* = \frac{1}{\mathrm{Re}} \nabla^{*2} \mathbf{u}^* \tag{2}$$

and energy conservation

$$\frac{\partial T^*}{\partial t^*} + (\mathbf{u}^* \cdot \nabla^*) T^* = \frac{1}{\mathrm{RePr}} \nabla^{*2} T^* \tag{3}$$

where $\mathbf{u}^* = (u^*, v^*)$ is the 2D velocity field with components in $x^* = x/a$ (horizontal) and $y^* = y/a$ (vertical), $P^* = P/\rho U^2$ is the pressure, and $t^* = t/(a/U)$ is the dimensionless time. U and a are the characteristic velocity and distance, respectively. The Reynolds number Re is defined as $\mathrm{Re} = Ua/\nu$, where ν is the kinematic viscosity. For the case of interest, a is the size of the vortex pair (defined as the initial distance between the centers of the two rectilinear vortices) and U its displacement velocity. The Prandtl number is defined as $\mathrm{Pr} = \nu/\alpha$, where α is the thermal diffusivity.

The energy equation is formulated in a nonconservative form in order to decouple it from the momentum conservation equation. The fluid is assumed to be Newtonian with constant properties. Re and Pr vary, respectively, in ranges of 250–1000 and 0.7–100 in order to investigate their influence on the heat transfer of a vortex impinging with an isothermal wall. No-slip and constant temperature conditions are considered for all walls. A segment of the lower wall (over which the vortex pair impinges) is kept at a higher constant temperature. At each time step, the temperature is computed in the computational domain and the heat flux is calculated over the heated region.

3 Problem Definition

In this investigation, the interaction of a vortex pair with a heated wall is studied. A 2D configuration is considered: a pair of counter-rotating equal-strength vortices moving at the same velocity toward a fixed heated wall. Particularly, we focus on evaluating the enhancement of the heat transfer resulting from this interaction.

The problem under investigation is depicted schematically in Fig. 1. A vortex pair (the equivalent of a vortex ring in 3D) is placed at an initial distance of $4a$ from a solid wall. The distance between the centers of the two rectilinear vortices is $2a$. The center of the pair moves initially at a velocity U in a trajectory perpendicular to the wall (y direction). At the center of the bottom solid wall, a plate of length L_o is kept at a fixed temperature T_w. The fluid is contained between four solid walls of length L. The size of the square domain is such that $L = 4L_o$. The fluid and the walls, with the exception of the heated plate, are initially at the same temperature, T_{inf}.

The initial condition of the simulation considers a 2D cut of a Hill spherical vortex [14]. This configuration allows us to directly relate the translational velocity of the pair with its size (separation distance between centers). For such a vortical structure, the vorticity is confined into the interior of a uniformly translating cylinder of radius a. The vortex lines form circles about an axis passing through the center of the disk and the streamlines lie in meridional planes. Outside the disk, the flow is irrotational. After some manipulations [15], the velocity is given by an inviscid irrotational formulation derived from a scalar function Ψ expressed as

$$\Psi = \begin{cases} \dfrac{15U}{20a^2}\left(x^4 + x^2y^2 + \dfrac{5}{3}x^2a^2\right) & \text{for } x^2 + y^2 < a^2 \\ \dfrac{Ua^3}{2}x^2(x^2 + y^2)^{-3/2} & \text{for } x^2 + y^2 > a^2 \end{cases} \tag{4}$$

where U is the translation velocity of the vortex in the y direction. Clearly, for this case $u = -\partial\Psi/\partial y$ and $u = \partial\Psi/\partial x$. Note that the coordinate system is taken to be at the center of the vortex. From Eq. (4), it is easily verified that the irrotational motion for $x^2 + y^2 > a^2$ is also described by the velocity potential

$$\Phi = -\frac{Ua^3}{2}\frac{y}{(x^2 + y^2)^{3/2}} \tag{5}$$

which is the potential function of a rigid disk moving through an ideal fluid with a y velocity U.

The initial pressure field is

$$P = P_{\mathrm{inf}} - \rho\frac{U^2a^3}{2}\left(\frac{x^2 - 2y^2}{(x^2 + y^2)^{3/2}} + \frac{a^3(x^2 + 4y^2)}{x(x^2 + y^2)^4}\right), \quad x^2 + y^2 > a^2 \tag{6}$$

Taking into account the continuity of pressure across the surface of the disk, we find

$$P = H - \rho|\mathbf{u}|^2, \quad x^2 + y^2 < a^2 \tag{7}$$

where H is the Bernoulli constant,

$$H = \frac{25U^2}{40a^2}x^2(x^2 + y^2)$$

and

$$\rho|\mathbf{u}|^2 = \frac{9U^2}{4a^4}\left(y^2x^2 + y^2(y^2 + x^2)^2 + \frac{a^2y^2}{9}\right)$$

This inviscid vortex is taken solely as the initial condition to start the numerical simulation of the problem. Clearly, as the full Navier–Stokes equations are solved in time, this condition adapts itself to that of a viscous pair moving toward a wall. Note also that this initial condition does not account for the presence of the wall.

The temperature of the vortex is initially set to be the same as the ambient temperature of the flow. The temperature of the heated patch on the wall is maintained constant and higher than the flow temperature by 45 K. The length of the isothermal plate is given by L_0. The heat flux over the isothermal heated plate is evaluated.

4 Numerical Method

In the present study, a finite volume technique is used, considering a SIMPLE-like method. For more details, the reader is referred to Ref. [16]. A linearization and an alternating direction implicit (ADI) decomposition of the momentum equations are introduced to ensure a second order and semi-implicit time stepping

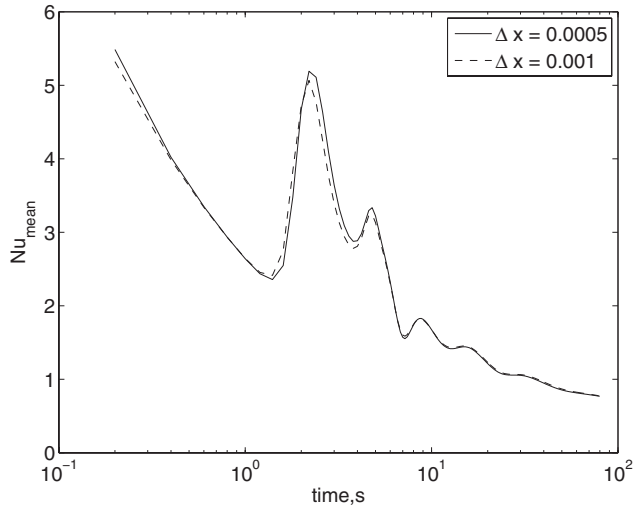

Fig. 2 Mean Nusselt number as a function of time. Simulations for two mesh sizes, considering Re=250 and Pr=0.7.

formulation of the predictor step and a semi-implicit formulation of the predictor step [17]. At each ADI step, a tridiagonal linear system is solved. A second/third order monotone upwind scheme for conservation laws (MUSCL) flux limiter is also introduced in the formulations of the convective fluxes to reduce the numerical diffusion. In the corrector step, a convergence criterion for the pressure correction algorithm is implemented to ensure a mass residual less than or equal to 10^{-4}. Then, the energy equation is solved by computing the temperature in an iterative procedure ensuring a 10^{-7} temperature accuracy. Antisymmetric conditions are implemented for velocities at the walls. Different mesh sizes were tested, and it was found that the numerical dispersion disappears for meshes of 200×200 with a mesh size of 0.0005. In all the simulations, the courant number is taken as $\max(U_{\max}\Delta t/\Delta x, \mu\Delta t/\Delta x^2)\leq 0.2$. The simulations with these mesh sizes and time steps, as will be shown in the next section, are in good agreement with other previously reported numerical results. Figure 2 shows the calculated mean Nusselt number (see the definition in Eq. (10)) for a typical flow, for two different values of the mesh size. Clearly, the results are grid independent.

Many different combinations of Reynolds and Prandtl numbers were studied. The Reynolds number ranged from 250 to 1000 to study laminar-inertial flows. The Prandtl number was varied from 1.4 to 13.3. These range of values corresponds to the physical properties of most common liquids. A few additional simulations were also performed with Prandtl numbers of 0.7 and 100 (considering only Re=250 and 1000) to cover the physical properties corresponding to gases and oils, respectively.

All the computations were performed for several characteristic time scales $t_{\text{char}}=a/U$, up to the order 15 (corresponding to approximately 50 s). Such calculations consist of approximately 500,000 time steps, corresponding to approximately 150 CPU min in a personal computer (3 GHz, Pentium IV processor). Computations are performed with the same small time step of 0.0005 s and a grid resolution of 200×200 for the same mesh size of 0.0005 m.

The physical properties of water are considered for all the calculations. The values of the thermal diffusivity α are varied artificially to achieve several values of Pr. Different values of Re are obtained, varying only the magnitude of U, keeping the relative size of the vortex (with respect to the container) fixed.

5 Results

5.1 Flow Field. Figure 3 shows the evolution of the vorticity field as the vortical structure approaches and reaches the wall. Since, for the case studied here, the flow remains symmetric, only the fields on the right side are shown. For all cases, as explained above, the energy and momentum equations are uncoupled. Hence, the isothermal velocity field is first resolved. Each image shows the vorticity field for a different time instant; additionally, isovorticity lines are shown to facilitate the identification of the vortical structures. Before the vortex pair reaches the wall ($t^*=t/(a/U)\leq 1$), the vorticity is confined within the vortex core. This is expected since a Hill vortex structure was chosen as the initial condition. When the vortex moves closer to the wall ($t^*=1.5$), the forced fluid motion over the wall creates an unsteady boundary layer ($t^*=2$). The boundary layer separates as a result of the flow-induced adverse pressure gradient. The vorticity created during the separation detaches from the wall, forming a secondary vortex ($t^*=2.5$). The primary and secondary vortices interact with each other and the wall ($2.5<t^*<4.5$). The formation of tertiary vortex can be observed for larger Re cases. The fluid motion is eventually dissipated by the effect of viscosity. The figure shows only the results for Re=250. Other simulations, for higher values of the Re, show a similar behavior.

The motion of the vortices obtained with our computer simulations can be compared with the analytical results of two counter-rotating inviscid vortices interacting with a wall. The solution of this classical problem can be found in Ref. [18]. The trajectory of the center of the vortex is given by

$$4x^2y^2 = C(x^2+y^2) \tag{8}$$

where C is an arbitrary constant that depends on the initial separation of the vortex pair (a in our case). It is interesting to note that this analytical result is independent of the circulation of the vortex pair. Figure 4 shows a comparison of the prediction of Eq. (8) and the trajectories of the center of the vortices for two different values of Re. Clearly, away from the wall, the trajectories of the simulated vortex pair are in good agreement with the inviscid theory, corresponding to times $t^*<1.5$. However, as expected, as the vortex approaches the wall, the trajectory of the vortex pair is greatly affected. From Fig. 3, it can be observed that for $t^*>1.5$, there is a significant amount of vorticity being produced at the wall; hence, the inviscid prediction is not expected to be accurate.

The rich flow physics of a viscous vortex pair (or ring) interacting with a solid wall has been reported before by several authors (see, for example, Ref. [8]). In particular, to quantitatively validate our results, a comparison with the results of Orlandi [10] is presented, who simulated the interaction of a vortex pair with a wall; as opposed to our simulations, he considered the case for which the distance between the centers of the vortices and the translation speed were independent. The trajectory of the main vortex obtained by Orlandi is shown also in Fig. 4. Despite the fact that the simulation conditions are not identical, the agreement between these results is good.

5.2 Evolution of Temperature Field. Figure 5 shows the evolution of the temperature field for the same flow shown in Fig. 3, considering a value of Pr=1.4. As in the previous figure, isovorticity lines are also shown on top of the temperature fields. When the simulation starts, the temperature of the fluid is lower than that of the plate. Even before the vortical structure reaches the wall, the heat from the plate has begun to diffuse into the fluid ($t^*=1$). When the vortex moves closer and interacts with the wall ($t^*=1.5$), heat is strongly convected away from the wall by the motion of the fluid ($1.5<t^*<3$). Subsequently, as a result of the recirculating nature of the fluid motion, the heated lump of fluid returns back to the wall ($3.5<t^*<4$), resulting in a decrease of

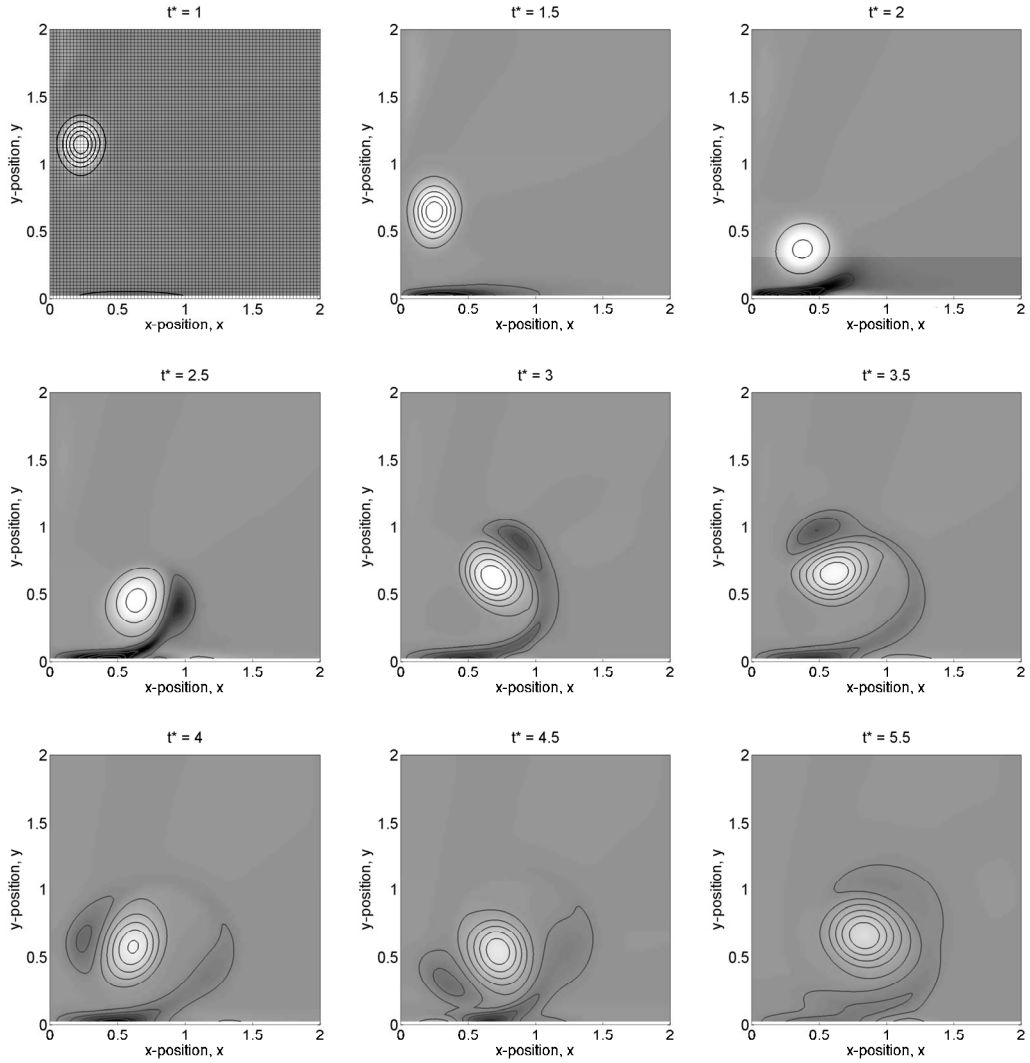

Fig. 3 Evolution of the vorticity field. Black and white levels on the figure represent values of 0.5 s^{-1} and −0.5 s^{-1} of vorticity, respectively. The solid lines show contours of isovorticity, which are used to visualize the vortical structures. The case shown is for Re=250. The time is shown in dimensionless terms: $t^*=t/(a/U)$. A unit of t^* represents the time it takes for a vortex to move, at a constant velocity U, a distance equivalent to its size. The distances are normalized by the size of the heated plate: x/L_0 and y/L_0. Note that only the right side of the simulation is shown. The mesh shown on the first image is indicative of the computational grid.

the rate of heat transfer. However, along with the heated fluid, a fresh volume of fluid is also dragged over the wall, resulting in a second increase of the heat transfer ($t^*=4.5$). The rate of heat transfer continues to decrease for subsequent times. Many simulations were conducted for a wide range of Re and Pr; a similar qualitative behavior was observed for all cases.

5.3 Wall Heat Transfer. The local wall heat transfer can be expressed in dimensionless terms as

$$\mathrm{Nu}=\frac{h(x)L_0}{k}=\frac{L_0\left.\dfrac{\partial T}{\partial y}\right|_{y=0}}{T_w-T_{\inf}} \tag{9}$$

where T_w is the temperature at the wall, $T_{\inf}$ is the initial temperature of the fluid away from the wall, L_0 is the length of the heated plate, k is the thermal conductivity of the liquid, and $h(x)$ is the local convective heat transfer coefficient.

Figure 6 shows the value of the local Nusselt number as a function of the horizontal coordinate over the length of the wall, for the simulation results shown in Figs. 3 and 5. Each line represents the dimensionless heat transfer for different instants during the interaction of the vortex with the wall. Clearly, the heat transfer increases to a maximum value when the vortex pair reaches the wall, which occurs at $t^*=2$, for that particular value of Re. Also, it is interesting to note that for most times, the Nusselt number is relatively uniform across the plate. This uniformity results from the fact that the size of the vortex pair is comparable to the size of the heated plate. Nevertheless, there is a variation of the heat transfer over the plate; therefore, to quantify the total heat transfer resulting from the vortex-wall interaction, the mean averaged Nusselt number over the heated wall can be calculated as

$$\mathrm{Nu}_{\mathrm{mean}}=\frac{1}{L_0}\int_{-L_0/2}^{L_0/2}\frac{h(x)x}{k}dx \tag{10}$$

where the local convective heat transfer coefficient $h(x)$ is defined as

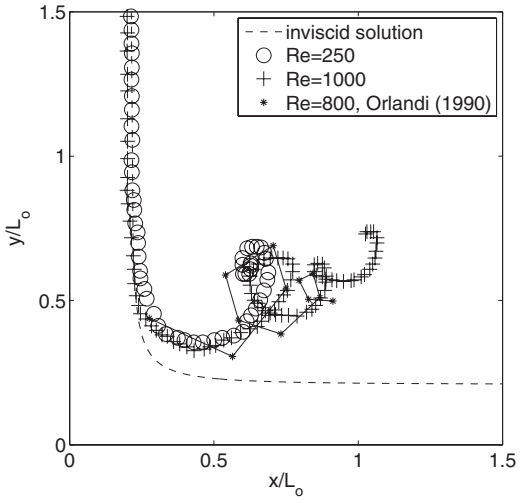

Fig. 4 Trajectory of the center of the main vortex. Two simulation cases are shown: (○) Re=250; (+) Re=1000. The dashed line is the trajectory from Eq. (8), considering C=22.9. The results of Orlandi [10] are also shown.

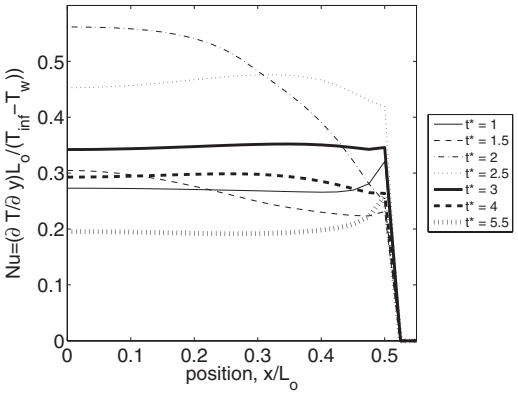

Fig. 6 Nusselt number as a function of position over the plate for different time instants. The case shown is for Re=250 and Pr=1.4. Note that only the right side of the profile is shown.

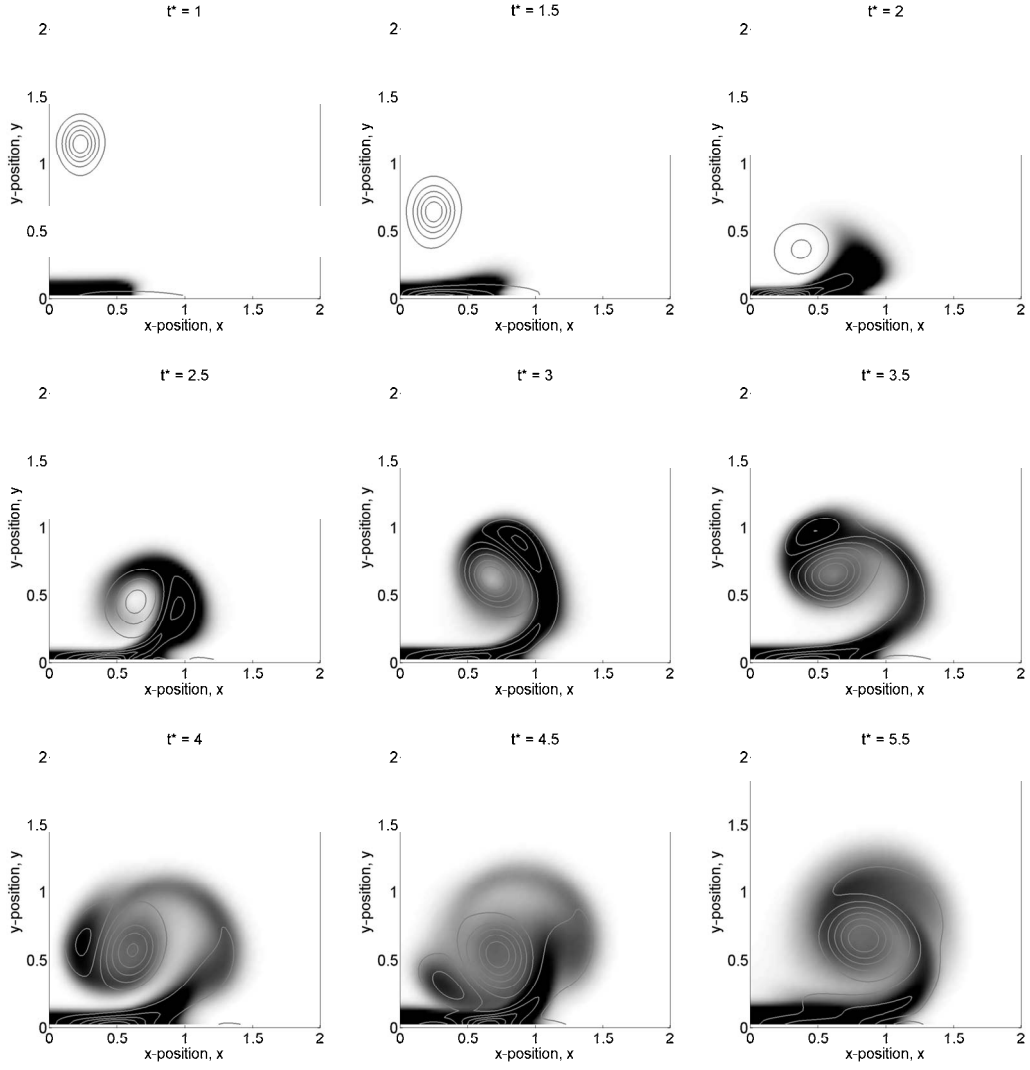

Fig. 5 Evolution of the temperature field. Black and white levels in the figure represent values of 0.9 and 1.0 of the dimensionless temperature $(T-T_w)/(T_{inf}-T_w)$, respectively. The solid lines show contours of isovorticity, which are used to visualize the vortical structures. The case shown is for Re=250 and Pr=1.4. Time and size are scaled, as in Fig. 3. Note also that only the right side of the simulation is shown.

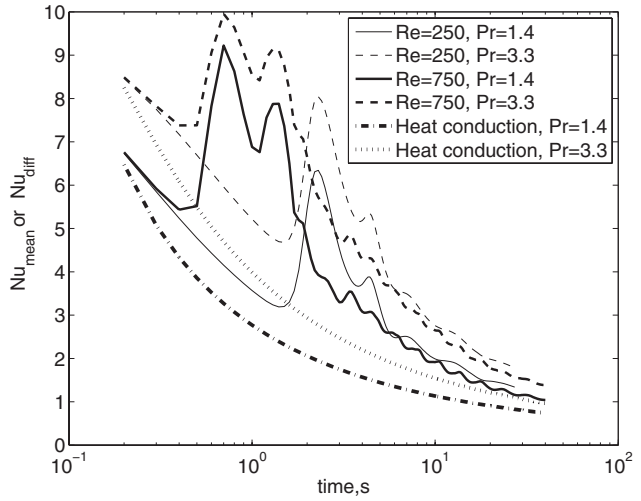

Fig. 7 Mean Nusselt number as a function of time. Simulations for two typical values of Re and Pr are shown. Also, simulations for a purely conductive system (no fluid motion) are shown for comparison.

$$h(x) = \frac{k}{T_w - T_{\inf}} \left(\frac{\partial T}{\partial y}\right)\bigg|_{y=0} \tag{11}$$

Figure 7 shows results for four typical simulations, where the mean Nusselt number Nu_{mean} is shown as a function of time. One of the cases shown (Re=250, Pr=1.4) corresponds to the simulation results shown in Figs. 3 and 5. Clearly, for early times, the Nusselt number decreases as a function of time as the heat from the wall is being diffused mainly by conduction through the fluid. When the fluid vortex approaches the wall, a sudden increase of the heat transfer is observed. The heat transfer then decreases as a result of the recirculating nature of the flow; a second increase of the Nusselt number can be observed, but with a smaller magnitude than the first. For the cases shown in the figure, the purely conductive, Nu_{diff}, solution was calculated to serve as a basis of comparison. The purely diffusive heat transfer coefficient is obtained from the solution of the same geometry considering no fluid motion; that is, $(u^*, v^*) = (0, 0)$ everywhere in the computational domain. The heat transfer for the purely conductive case is below the vortex-convected case. Hence, the enhancement of the rate of heat removal from the wall results from the interaction of the vortical structure with the wall. The same qualitative behavior is observed in all the cases shown in the figure. Figure 8 shows the calculated value of the Nusselt number by first varying the value of Pr for the same Re (a) and vice versa (b). As the Reynolds number increases, the peak of heat transfer appears earlier because the vortex pair moves faster and reaches the wall sooner. Also, the magnitude of the peak is larger for larger Re. Moreover, as the Prandtl number increases, the heat transfer also increases. Hence, for this case, the heat transfer is dominated by the convective action of the fluid motion.

5.4 Enhancement of Heat Transfer. To evaluate the amount of additional heat transferred resulting from the interaction of the vortex pair with the wall, the ratio of the vortex induced heat transfer (Nu_{mean}) and that for the purely conductive case (Nu_{diff}) is calculated. Figure 9 shows the ratio Nu_{mean}/Nu_{diff} as a function of time for several characteristic values of the Reynolds and Prandtl numbers. It can be clearly observed that during the interaction of the vortex with the wall, the heat transfer can be enhanced as much as 3.2 times the value corresponding to the conductive case. The heat transfer enhancement increases with Re and Pr.

To obtain a quantitative measurement of the enhancement, we locate the maximum value Nu_{max} of the heat transfer achieved

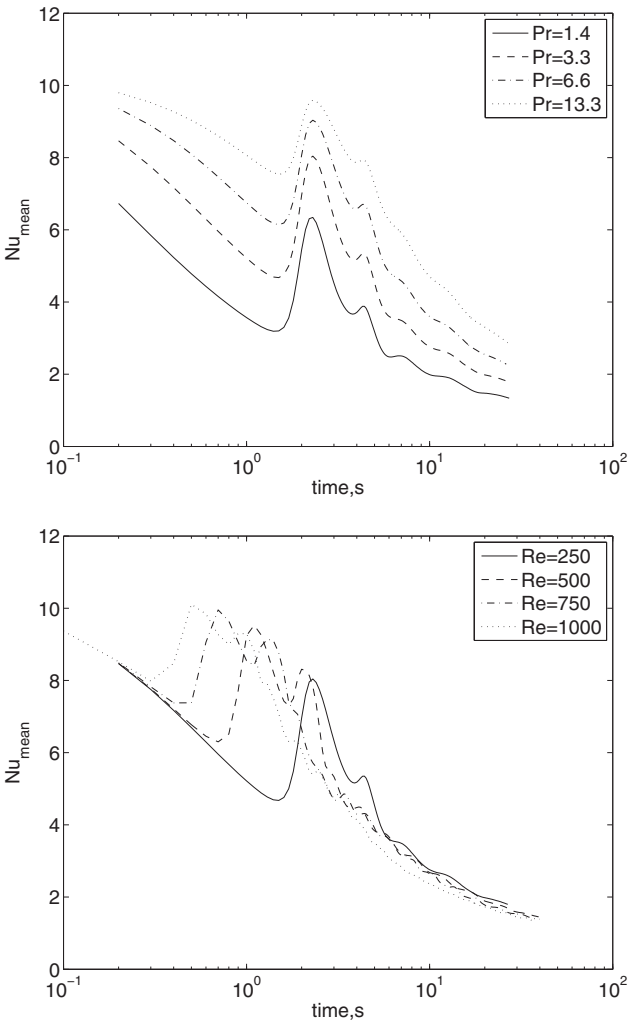

Fig. 8 Mean Nusselt number as a function of time. (*a*) Simulations keeping Re fixed and Pr varied. (*b*) Simulations keeping Pr fixed and Re varied.

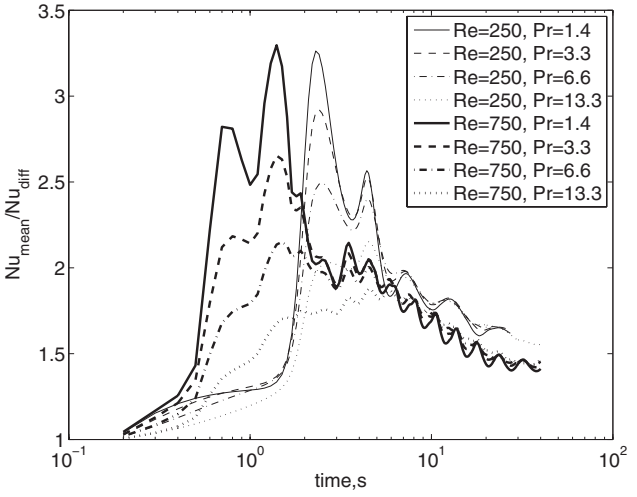

Fig. 9 Ratio of the mean convective to the purely conductive Nusselt numbers. Simulations for two typical Re numbers are shown for four values of Pr.

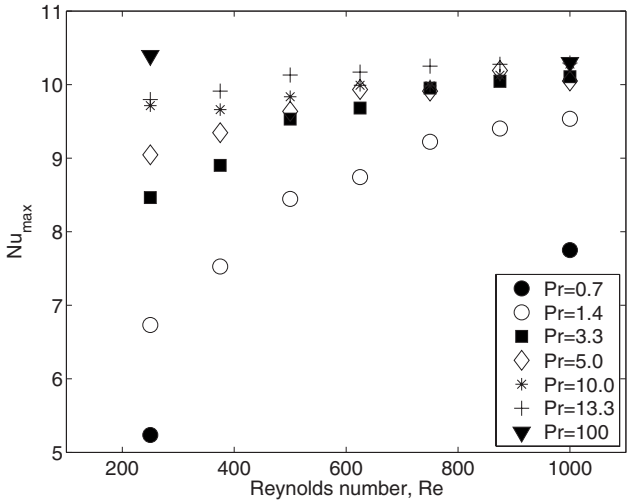

Fig. 10 Maximum of the mean Nusselt number against the Reynolds number for several values of Pr between 1.4 and 13.26. Additional results are also shown for Pr=0.7 and 100 and for Re=250 and 1000.

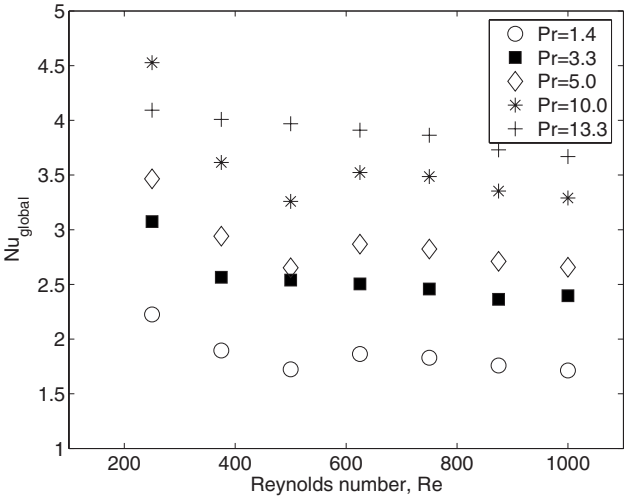

Fig. 11 Time integral of the mean Nusselt number against the Reynolds number for several values of Pr between 1.4 and 13.26

during the interaction. This value corresponds to the time instant at which the vortex first interacts with the wall. Figure 10 shows the value of $\mathrm{Nu}_{\max}$ as a function of the flow Reynolds number for a range of values of the Prandtl number. For all cases, the value of the maximum heat transfer increases with Re hence, the enhancement of heat transfer increases with the Reynolds number. The results also show that the maximum heat transfer increases with Pr, as the Prandtl number increases, the dependence with the Reynolds number becomes less important. The results presented in the figure can be fitted to the following expression:

$$\mathrm{Nu}_{\max} = 4.139\mathrm{Re}^{0.113}\mathrm{Pr}^{0.076} \tag{12}$$

This equation, however, is not very accurate for certain values of the Pr and Re since it assumes a dependence of the type $\mathrm{Re}^{\alpha}\mathrm{Pr}^{\beta}$, where α and β are constants. A better fit of the numerical results can be given by the relation

$$\mathrm{Nu}_{\max} = 27.68\mathrm{Re}^{0.0206}(1-\mathrm{Pr}^{-0.1265})\mathrm{Re}^{0.3221/\mathrm{Pr}} \tag{13}$$

This expression is more accurate than formula (12), but only for the range of parameters chosen in this investigation. Moreover, from equations like this, the functional dependence of the independent variable is not evident at first sight, and its physical meaning is not obvious.

The maximum value of the Nusselt number is clearly not the only significant parameter to quantify the enhancement of heat transfer resulting from the interaction of the vortex pair with the wall. As it has been shown above, there is a complex nonsteady fluid-wall interaction that results in continuous changes in the value of the heat transfer rate. To obtain a global measurement of the heat transfer resulting from this interaction, a time averaged Nusselt number can be calculated as

$$\mathrm{Nu}_{\mathrm{global}} = \frac{1}{T}\int_0^T \mathrm{Nu}_{\mathrm{mean}}(t)dt$$

where T is the total time during which the interaction is significant. Figure 11 shows the *global* Nusselt number as a function of Re for several values of Pr. This average value of the heat transfer coefficient decays slightly with the Reynolds number and increases with the value of the Prandtl number. By averaging over a long time, the unsteady effects of the flow are lumped into $\mathrm{Nu}_{\mathrm{global}}$, and the global heat removal is determined mainly by the fluid thermal properties; hence, one may expect a weak dependence on the flow Reynolds number considering this measure of the effective heat transfer.

Note that some variability can be observed in these measurements; this is the result of the choice of the averaging time T used in the calculations. For some combinations of Re and Pr, the duration of the interaction is very long. For practical reasons, most simulations were stopped at $t_{\mathrm{char}}=15$ (corresponding to approximately 50 s or approximately 500,000 time steps). Despite this variability, the general trend in the results is very clear.

6 Conclusions

In this investigation, the motion of a vortex pair impinging on a solid wall was studied. The fluid motion that resulted from this interaction causes an increase of the local heat transfer coefficient. Although it is clear that a forced fluid motion over a heated wall causes an increase of the heat transfer from the wall, the details of the process had not yet been investigated to date. In particular, the case of the interaction of an isolated vortex pair (or ring) with a heated wall had not been previously reported.

Our isothermal simulations were in good agreement with previously reported experimental and numerical results. The collision of a vortex pair with a flat wall results in a complex fluid-wall interaction that has direct implications to the rate of heat transfer.

The simulations showed that the heat transfer increases as a result of the vortex-wall interaction, compared to the purely conductive case. The heat transfer reaches a maximum value when the vortex first arrives at the wall, to then decrease as the flow continues to develop and a secondary vortex forms; subsequently, the heat transfer reaches a second local maximum value when the fluid, pushed by the circulating heated lump, is forced to interact with the wall. Several local maxima, of decaying relative magnitude, were observed at a frequency that is proportional to the vortex circulation. The magnitude of the heat transfer rate increases with the values of the Reynolds and Prandtl numbers.

References

[1] Goldstein, R. J., Eckert, E. R. G., Ibele, W. E., Patankar, S. V., Simon, T. W., Kuehn, T. H., Strykowski, P. J., Tamma, K. K., Bar-Cohen, A., Heberlein, J. V. R., Davidson, J. M., Bischof, J., Kulacki, F. A., Kortshagen, U., Garrick, S., and Srinivasan, V., 2005, "Heat Transfer: A Review of 2002 Literature," Int. J. Heat Mass Transfer, **48**, pp. 819–927.

[2] Fiebig, M., 1997, "Vortices and Heat Transfer," Z. Angew. Math. Mech., **77**, pp. 3–18.

[3] Valencia, A., and Sen, M., 2003, "Unsteady Flow and Heat Transfer in Plane Channels With Spatially Periodic Vortex Generators," Int. J. Heat Mass Transfer, **46**, pp. 3189–3199.

[4] Yang, S.-J., 2003, "Numerical Study of Heat Transfer Enhancement in a Chan-

nel Flow Using an Oscillating Vortex Generator," Heat Mass Transfer, **39**, pp. 257–265.
[5] Doligalski, T. L., and Walker, J. D. A., 1984, "The Boundary Layer Induced by a Convected Two-Dimensional Vortex," J. Fluid Mech., **139**, pp. 1–28.
[6] Escriva, X., and Giovannini, A., 2003, "Analysis of Convective Momentum and Wall Heat Transfer: Application to Vortex Boundary Layer Interaction," Int. J. Heat Mass Transfer, **46**, pp. 2471–2483.
[7] Doligalski, T. L., Smith, C. R., and Walker, J. D. A., 1994, "Vortex Interactions With Walls," Annu. Rev. Fluid Mech., **26**, pp. 573–616.
[8] Walker, J. D. A., Smith, C. R., Cerra, A. W., and Doligalski, T. L., 1987, "The Impact of a Vortex Ring on a Wall," J. Fluid Mech., **181**, pp. 99–140.
[9] Ersoy, S., and Walker, J. D. A., 1986, "Flow Induced at a Wall by a Vortex Pair," AIAA J., **24** (10), pp. 1597–1605.
[10] Orlandi, P., 1990, "Vortex Dipole Rebound From a Wall," Phys. Fluids A, **2**, pp. 1429–1436.
[11] Chang, T. Y., Hertzberg, J. R., and Kerr, R., M., 1997, "Three-Dimensional Vortex/Wall Interaction: Entrainment in Numerical Simulation Experiment," Phys. Fluids, **9**(1), pp. 57–66.
[12] Reulet, P., Marchand, M., and Millan, P., 1998, "Experimental Characterization of the Convective Vortex-Wall Interaction," Rev. Gen. Therm., **37**(8), pp. 661–668.
[13] Romero-Méndez, R., Sen, M., Yang, K. T., and McClain, R. L., 1998, "Enhancement of Heat Transfer in an Inviscid-Flow Thermal Boundary Layer Due to a Rankine Vortex," Int. J. Heat Mass Transfer, **41**, pp. 3829–3840.
[14] Hill, M. J. M., 1894, "On a Spherical Vortex," Philos. Trans. R. Soc. London, Ser. A, **185**, pp. 213–245.
[15] Saffman, P. G., 2001, *Vortex Dynamics*, Cambridge University Press, Cambridge, England.
[16] Patankar, S. V., 1980, *Numerical Heat Transfer and Fluid Flow*, Hemisphere, New York.
[17] Van Doormal, J. P., and Raithby, G. D., 1984, "Enhancements of the SIMPLE Method for Predicting Incompressible Fluid Flows," Numer. Heat Transfer, **7**, pp. 147–163.
[18] Lamb, H., 1995, *Hydrodynamics*, Cambridge University Press, New York..

Proposed Modification to Whole Domain Function Specification Method to Improve Accuracy of Its Estimations

Cha'o-Kuang Chen
e-mail: ckchen@mail.ncku.edu.tw

Li-Wen Wu

Yue-Tzu Yang

Department of Mechanical Engineering,
National Cheng Kung University,
Tainan 70101, Taiwan, R.O.C.

This paper investigates the inverse heat transfer problem of laminar forced convection within a circular pipe. The performances of two classical algorithms used in the whole domain function specification method (WDFSM) to obtain simultaneous estimates of the time-varying inlet temperature and outer-wall heat flux are compared. Additionally, this study proposes a modification to the linear assumption employed in the conventional WDFSM to improve its estimation performance. The WDFSM solution procedure is based on future temperature measurements at two different locations within the pipe flow. In the modified algorithm, the variations of the estimations at all time steps for various values of the future-time parameter are investigated, and if large variations in the slope of the function are detected at some time steps, the originally linear assumption for the variation of the unknowns is replaced with the assumption of a constant function at these time steps. Otherwise, the estimates at the other time steps are calculated using the linear assumption. The numerical results confirm that the proposed algorithm yields slightly more accurate estimates of the unknowns than the two classic algorithms.
[DOI: 10.1115/1.2884184]

Keywords: conjugate heat transfer, inverse method, numerical method, pipe flow

1 Introduction

Conjugate heat transfer, in which an interaction occurs between the conduction effects in a solid wall and the convection effects within a fluid flowing around it, occurs in many engineering devices. In the case of thin-walled pipes, early researchers neglected wall conduction effects and considered that the conditions acting on the external surface of the pipe were the same as those at the surface of the inner wall. However, for conjugate heat transfer in thick-walled pipes, this assumption is no longer valid. The conjugate heat transfer problem has been examined by a number of researchers [1–4]. Generally, it has been shown that a substantial amount of heat is transferred to the fluid in the unheated sections of the pipe as a result of wall conduction effects. These effects are more pronounced when the solid-to-fluid thermal conductivity ratio, k_{sf}, is high and the inner-wall to outer-wall radius ratio, $R_{\mathrm{iw}} = r_{\mathrm{iw}}/r_{\mathrm{ow}}$, is low. Under these conditions, the thermal boundary conditions existing at the internal surface are not known a priori, and hence, the energy equations must be solved by assuming conditions of temperature and heat flux continuity.

Many researchers have attempted to establish stable solutions for inverse heat conduction problems (IHCPs) using analytical and numerical approaches. For example, Su and co-workers [5,6] estimated the spatially nonuniform wall heat flux in a thermally developing hydrodynamically developed turbulent flow in a circular pipe using finite element interpolation and the Levenberg–Marquardt method. Meanwhile, Park and Lee [7] employed an inverse technique based on the Karhunen–Loève Galerkin procedure to numerically evaluate the unknown functions of the wall heat flux for laminar flow within a duct. Bokar and Özisik [8] applied the conjugate gradient method of minimization with an adjoint equation to estimate the time-varying inlet temperature for laminar flow within a parallel-plate duct. Finally, Li and Yan [9,10] applied the same inverse method to estimate the space- and time-dependent wall heat flux for unsteady turbulent forced convection within a circular tube and a parallel-plate channel, respectively. However, the approaches described above all involve lengthy iterative computational procedures and neglect the effects of axial heat conduction within the wall in the vicinity of the solid-fluid interface.

The sequential function specification method (SFSM) proposed by Beck et al. [11] uses estimates of the unknowns at several future times, $p>1$, to improve the stability of the ill-posed IHCP and to reduce the sensitivity of the estimated results to measurement errors. Yang [12,13] employed the SFSM to determine interior source and mix-typed boundary conditions. Meanwhile, Chantasiriwan [14] utilized SFSM to estimate the time-dependent Biot number. Behbahani-nia and Kowsary [15] applied the dual reciprocity boundary element method with SFSM to estimate the boundary heat flux in a two-dimensional IHCP. Kim and Lee [16] applied the SFSM to estimate the time-varying heat transfer coefficient between a tube-shaped casting and metal molds. The function specification method has the advantages of simplifying the analysis task, reducing the computational time and expense by replacing the iterative process with a future-time estimation concept, and providing simultaneous estimates of all the unknown parameters, thereby further enhancing the computational efficiency.

This study considers the problem of conjugate heat transfer within a laminar pipe flow and proposes an efficient technique combining the function specification method and the linear least-squares-error method to obtain simultaneous estimates of the unknown outer-wall heat flux and inlet temperature over the total time interval. Yang and Chen [17] verified the applicability of the linear least-squares-error method to the two-dimensional IHCPs. The inverse method applied in this study, i.e., the whole domain function specification method (WDFSM), is used to obtain simul-

[1]Corresponding author.

Contributed by the Heat Transfer Division of ASME for publication in the JOURNAL OF HEAT TRANSFER. Manuscript received August 10, 2006; final manuscript received November 15, 2007; published online April 10, 2008. Review conducted by A. Haji-Sheikh.

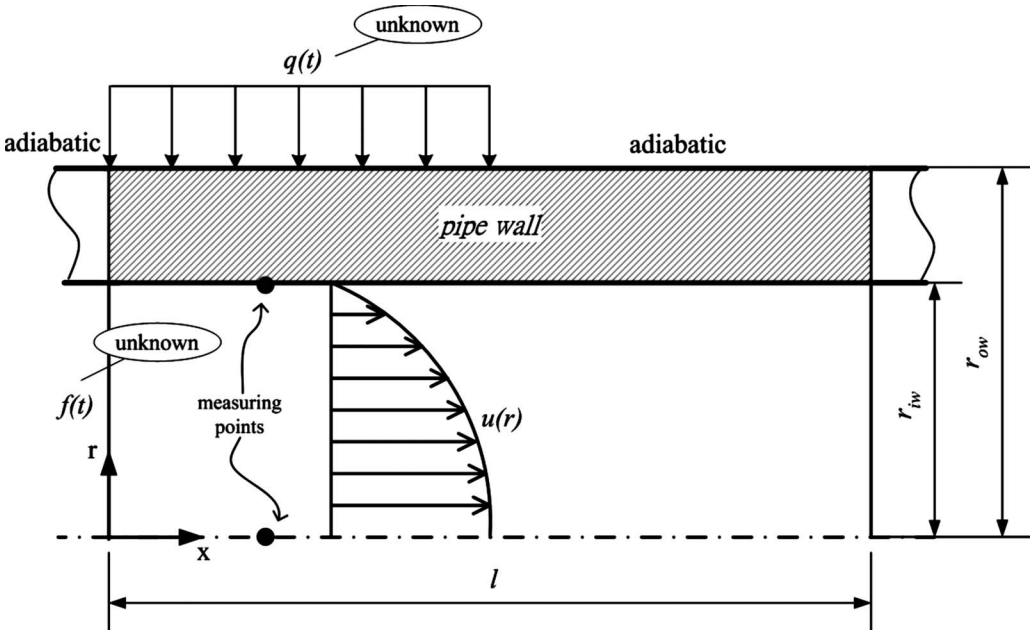

Fig. 1 System under consideration. Note that the velocity profile is fully developed and that the inlet temperature is uniform. ($q(t)$ and $f(t)$ denote the outer-wall heat flux function and the inlet temperature function, respectively.)

taneous solutions of the two-dimensional conduction equation for the pipe wall and the two-dimensional convection equation for the flowing fluid. In obtaining these results, the WDFSM is applied using two different classic algorithms to estimate the future unknown parameter values, i.e., the constant variation function and the time-dependent linear variation function, respectively. In an attempt to improve the accuracy of the estimated solutions obtained using these two algorithms, an ameliorative algorithm is developed for the WDFSM, which integrates the assumptions of the constant and time-dependent linear variation functions. The results confirm that the estimates obtained using the modified algorithm are slightly more accurate than those obtained using the original algorithms. Furthermore, it is shown that the estimates are relatively insensitive to errors in the temperature measurements.

2 Physical Model and Governing Equations

The present study considers a system in which a Newtonian fluid of constant properties flows with steady laminar motion in a circular pipe. At $X=0$, the inlet temperature, $\Theta(0,R,\tau)$, begins to vary as a function of time with the form $F(\tau)$. The heat flux imposed on the external surface of the pipe, $Q(\tau)$, also varies as a function of time. The present simulations calculate these two distributions simultaneously. Due to the symmetrical nature of the current problem, the computational domain needs only to consider one-half of the pipe flow. The following assumptions are made: (1) the flow is two dimensional; (2) the pipe wall is homogeneous and has a constant thermal conductivity, k_s, and a finite thickness; (3) the fluid is incompressible, homogeneous, and has a constant thermal conductivity, k_f; and (4) the pipe is of sufficient length so that fully developed flow exists at its entrance and exit regions.

Figure 1 presents a schematic representation of the current pipe flow and conjugate heat transfer system. The governing equations for the temperature field of the pipe flow are expressed by the following differential equations.

In the wall region,

$$\frac{\partial T}{\partial t} - \frac{\alpha_s}{r}\frac{\partial}{\partial r}\left(r\frac{\partial T}{\partial r}\right) - \alpha_s\frac{\partial}{\partial x}\left(\frac{\partial T}{\partial x}\right) = 0 \qquad (1a)$$

$$\frac{\partial T(0,r,t)}{\partial x} = 0 \quad \text{at } x=0, \quad r_{\text{iw}} \leqslant r \leqslant r_{\text{ow}}, \quad t>0 \qquad (1b)$$

$$\frac{\partial T(x,r_{\text{ow}},t)}{\partial r} = \frac{q(t)}{k_s} \quad \text{at } 0<x\leqslant l/2, \quad r=r_{\text{ow}}, \quad t>0 \qquad (1c)$$

In the fluid region,

$$\frac{\partial T}{\partial t} + u(r)\frac{\partial T}{\partial x} - \alpha_f\left[\frac{\partial^2 T}{\partial x^2} + \frac{1}{r}\frac{\partial}{\partial r}\left(r\frac{\partial T}{\partial r}\right)\right] = 0 \qquad (2a)$$

$$T(0,r,t) = f(t) \quad \text{at } x=0, \quad 0\leqslant r\leqslant r_{\text{iw}}, \quad t>0 \qquad (2b)$$

$$\frac{\partial T(x,0,t)}{\partial r} = 0 \quad \text{at } x>0, \quad r=0, \quad t>0 \qquad (2c)$$

The initial condition is expressed as

$$T(x,r,0) = T_{\text{initial}} \quad \text{at } x>0, \quad 0<r<r_{\text{ow}}, \quad t=0 \qquad (3)$$

At the interface between the pipe wall and the fluid within the pipe ($r=r_{\text{iw}}$),

$$k_f\partial T_f(x,r_{\text{iw}},t)/\partial r = k_s\partial T_s(x,r_{\text{iw}},t)/\partial r \qquad (4a)$$

$$T_s(x,r_{\text{iw}},t) = T_f(x,r_{\text{iw}},t) \qquad (4b)$$

where r_{ow} and r_{iw} are the outer and inner pipe radii, respectively. Let $u(r)$ be the fluid velocity distribution. According to the conventional Hagen–Poiseuille expression, $u(r)$ is given by

$$u(t) = 2u_m\left[1-\left(\frac{r}{r_{\text{iw}}}\right)^2\right] \qquad (5)$$

where u_m is the average velocity and can be determined from the measured flow rate.

The following scale factors are introduced to reduce the governing equations and the boundary conditions of Eqs. (1*a*)–(1*c*), (2*a*)–(2*c*), (3), (4*a*), (4*b*), and (5) to a dimensionless form:

$$\Theta(X,R,r) = \frac{T(x,r,t)-T_{\text{initial}}}{T_{\text{initial}}}, \quad F(\tau) = \frac{f(t)-T_{\text{initial}}}{T_{\text{initial}}}$$

$$Q(\tau)=\frac{q(t)r_{\mathrm{ow}}}{k_sT_{\mathrm{initial}}},\quad R=\frac{r}{r_{\mathrm{ow}}},\quad X=\frac{x}{l},\quad \tau=\frac{\alpha_f t}{r_{\mathrm{ow}}^2}$$

In these expressions, $F(\tau)$ is the dimensionless time-varying temperature at the entrance of the pipe, and $Q(\tau)$ denotes the dimensionless time-varying outer-wall heat flux. The governing parameters for conjugate conduction and laminar forced convection heat transfer in a pipe subjected to a nonuniform heat flux include the Reynolds number $\mathrm{Re}=2r_{\mathrm{iw}}u_m/\nu$, the Prandtl number Pr, the solid-to-fluid thermal conductivity ratio $k_{sf}=k_s/k_f$, and the solid-to-fluid thermal diffusivity ratio, $\alpha_{sf}=\alpha_s/\alpha_f$.

From the above, it is clear that the current problem involves many independent dimensionless parameters. A comprehensive parametric study involving all of these parameters would involve a vast set of results and is not called for in the present study. Hence, the values of some of the dimensionless parameters are specified as constants, i.e.,

$$L=l/r_{\mathrm{ow}}=20 \text{ and } R_{\mathrm{iw}}=r_{\mathrm{iw}}/r_{\mathrm{ow}}=0.8$$

$$k_{sf}=72.027 \text{ and } \alpha_{sf}=55.94$$

$$\mathrm{Pe}=7000$$

The value of the dimensionless length is sufficiently long to observe the thermal development of the flow. The dimensionless length of the unheated section ($l/2<x<l$) is long enough to account for the wall axial conduction effects and to ensure that the outlet boundary condition ($\partial T/\partial x=0$) is appropriate.

3 Numerical Method

3.1 Direct Problem. In the present study, the direct problem is analyzed using the finite-difference method. Following discretization, the dimensionless governing equations and boundary conditions given in Eqs. (1*a*)–(1*c*), (2*a*)–(2*c*), and (3) can be expressed in the following recursive forms.

In the wall region,

$$\frac{\Theta_{i,j}^n-\Theta_{i,j}^{n-1}}{\Delta\tau}-\frac{\alpha_{sf}}{R_j}\left(\frac{\Theta_{i,j+1}^n-\Theta_{i,j-1}^n}{2\Delta R}+R_j\frac{\Theta_{i,j+1}^n-2\Theta_{i,j}^n+\Theta_{i,j-1}^n}{(\Delta R)^2}\right)-\frac{\alpha_{sf}}{L^2}\left(\frac{\Theta_{i+1,j}^n-2\Theta_{i,j}^n+\Theta_{i-1,j}^n}{(\Delta X)^2}\right)=0 \tag{6a}$$

$$\frac{\Theta_{1,j}^n-\Theta_{0,j}^n}{\Delta X}=0 \quad \text{at } i=0,\quad jw\leq j\leq J,\quad n>0 \tag{6b}$$

$$\frac{\Theta_{i,J}^n-\Theta_{i,J-1}^n}{\Delta R}=Q^n \quad \text{at } 0<i\leq I/2,\quad j=J,\quad n>0 \tag{6c}$$

In the fluid region,

$$\frac{\Theta_{i,j}^n-\Theta_{i,j}^{n-1}}{\Delta\tau}+\frac{1}{R_{\mathrm{iw}}L}\mathrm{Pe}\left[1-\left(\frac{R_j}{R_{\mathrm{iw}}}\right)^2\right]\frac{\Theta_{i+1,j}^n-\Theta_{i-1,j}^n}{2\Delta X}-\frac{1}{L^2}\frac{\Theta_{i+1,j}^n-2\Theta_{i,j}^n+\Theta_{i-1,j}^n}{(\Delta X)^2}-\frac{1}{R_j}\left(\frac{\Theta_{i,j+1}^n-\Theta_{i,j-1}^n}{2\Delta R}+R_j\frac{\Theta_{i,j+1}^n-2\Theta_{i,j}^n+\Theta_{i,j-1}^n}{(\Delta R)^2}\right)=0 \tag{7a}$$

$$\Theta_{0,j}^n=F^n \quad \text{at } i=0,\quad 0\leq j\leq jw,\quad n>0 \tag{7b}$$

$$\frac{\Theta_{i,1}^n-\Theta_{i,0}^n}{\Delta R}=0 \quad \text{at } i>0,\quad j=0,\quad n>0 \tag{7c}$$

The initial condition is given by

$$\Theta_{i,j}^0=0 \quad \text{at } i>0,\quad 0<j<J,\quad n=0 \tag{8}$$

Substituting Eq. (4*b*) into the discretization equation obtained from the energy equation (Eq. (4*a*)) at the interface between the wall and the fluid inside the pipe gives the dimensionless inner-wall temperature as

$$\Theta_{i,jw}^n=\frac{k_{sf}}{k_{sf}+1}\Theta_{i,jw+1}^n+\frac{1}{k_{sf}+1}\Theta_{i,jw-1}^n \tag{9}$$

In Eqs. (6*a*)–(6*c*), (7*a*)–(7*c*), (8), and (9), ΔR and ΔX are the increments in the dimensionless spatial coordinates, $\Delta\tau$ is the increment of the temporal coordinate, i is the ith grid point along the x-coordinate direction, j is the jth grid point along the r-coordinate direction, n is the nth grid point along the temporal coordinate, and $\Theta_{i,j}^n$ is the dimensionless temperature at grid point (i,j). Meanwhile, Q^n and F^n are the uniform outer-wall heat flux and inlet temperature, respectively, at the nth grid point along the temporal coordinate. Finally, J is the grid point at the boundary, i.e., $R=1$, and jw represents the grid point at the inner wall, i.e., $R=R_{\mathrm{iw}}=0.8$.

In the inner-wall temperature expression given in Eq. (9), it is apparent that the dimensionless inner-wall temperature, $\Theta_{i,jw}^n$, expressed by $\Theta_{i,jw+1}^n$ at the first radial grid point in the pipe wall and by $\Theta_{i,jw-1}^n$ at the final radial grid point in the fluid, is eliminated during algebraic vector manipulation. In other words, the boundary conditions acting at the solid-fluid interface are avoided, which significantly simplifies the analysis task.

Using the inner-wall temperature given in Eq. (9) and the boundary conditions and initial condition given in Eqs. (6*b*), (6*c*), (7*b*), (7*c*), and (8), the recursive forms of the governing equations in Eqs. (6*a*) and (7*a*) can be rearranged in the form of the following linear model:

$$\mathbf{T}^n=\mathbf{A}^{-1}\mathbf{T}^{n-1}+\mathbf{A}^{-1}\mathbf{B}\mathbf{C}^n=\mathbf{D}\mathbf{T}^{n-1}+\mathbf{D}\mathbf{B}\mathbf{C}^n \tag{10}$$

where

$$\mathbf{D}=\mathbf{A}^{-1}$$

In the above, matrix $\mathbf{A}$ is a constant matrix constructed from the thermal properties and spatial coordinates of the system. Meanwhile, the components of vector $\mathbf{T}$ are the dimensionless temperatures at discrete points within the pipe wall and the fluid. Finally, matrix $\mathbf{B}$ is the coefficient of vector $\mathbf{C}$, which is composed of the dimensionless boundary conditions, including the inlet temperature and the heat flux acting on the external surface of the pipe.

3.2 Inverse Problem

3.2.1 Whole Domain Function Specification Method. It is advantageous to perform the current algebraic manipulations using a matrix form of the conjugate heat transfer model. Equation (10) can be written in an expanded matrix form as

$$\begin{Bmatrix}\mathbf{T}^1\\ \mathbf{T}^2\\ \vdots\\ \mathbf{T}^{N-1}\\ \mathbf{T}^N\end{Bmatrix}=\begin{bmatrix}\mathbf{D} & 0 & \cdots & & 0\\ \mathbf{D}^2 & \mathbf{D} & \ddots & & \\ \vdots & \ddots & \ddots & \ddots & \vdots\\ \mathbf{D}^{N-1} & \ddots & \ddots & \mathbf{D} & 0\\ \mathbf{D}^N & \mathbf{D}^{N-1} & \cdots & \mathbf{D}^2 & \mathbf{D}\end{bmatrix}[\mathbf{B}]\times\begin{bmatrix}\mathbf{C}^1\\ \mathbf{C}^2\\ \vdots\\ \mathbf{C}^{N-1}\\ \mathbf{C}^N\end{bmatrix}+\begin{bmatrix}\mathbf{D}\\ \mathbf{D}^2\\ \vdots\\ \mathbf{D}^{N-1}\\ \mathbf{D}^N\end{bmatrix}\{\mathbf{T}^0\} \tag{11}$$

where N is the number of time steps to be estimated. The unknown vector $\mathbf{C}$ of each time step has two components, i.e., the inlet temperature and the outer-wall heat flux. To stabilize the computational results, the future-time concept is applied. Equation

(10) can be expressed in terms of the following vectors and matrices:

$$\begin{Bmatrix} \mathbf{T}^n \\ \mathbf{T}^{n+1} \\ \vdots \\ \mathbf{T}^{n+p-2} \\ \mathbf{T}^{n+p-1} \end{Bmatrix} = \begin{bmatrix} \mathbf{D} & 0 & \cdots & & 0 \\ \mathbf{D}^2 & \mathbf{D} & \ddots & & \\ \vdots & \ddots & \ddots & \ddots & \vdots \\ \mathbf{D}^{p-1} & \ddots & \ddots & \mathbf{D} & 0 \\ \mathbf{D}^p & \mathbf{D}^{p-1} & \cdots & \mathbf{D}^2 & \mathbf{D} \end{bmatrix} [\mathbf{B}] \times \begin{bmatrix} \mathbf{C}^n \\ \mathbf{C}^{n+1} \\ \vdots \\ \mathbf{C}^{n+p-2} \\ \mathbf{C}^{n+p-1} \end{bmatrix} + \begin{bmatrix} \mathbf{D} \\ \mathbf{D}^2 \\ \vdots \\ \mathbf{D}^{p-1} \\ \mathbf{D}^p \end{bmatrix} \{\mathbf{T}^{n-1}\} \tag{12}$$

where p is a future-time parameter indicating the number of future-time measurements used as input data. Applying the assumptions given in Secs. 3.2.2 and 3.2.3, the future components $(\mathbf{C}^{n+1}, \mathbf{C}^{n+2}, \ldots, \mathbf{C}^{n+p-1})$ for times t^{n+1}, $t^{n+2}, \ldots, t^{n+p-1}$ are incorporated into the current-time component $\mathbf{C}^n$. Then, substituting Eq. (12) into Eq. (11) and simplifying the result, the whole domain equation can be rearranged into the following form:

$$\Theta = \mathrm{M}\Psi \tag{13}$$

where

$$\Theta = \begin{Bmatrix} \mathbf{T}^1 - \mathbf{D}^1\mathbf{T}^0 \\ \mathbf{T}^2 - \mathbf{D}^2\mathbf{T}^0 \\ \vdots \\ \mathbf{T}^r - \mathbf{D}^r\mathbf{T}^0 \\ \mathbf{T}^2 - \mathbf{D}^2\mathbf{T}^0 \\ \mathbf{T}^3 - \mathbf{D}^3\mathbf{T}^0 \\ \vdots \\ \mathbf{T}^{p+1} - \mathbf{D}^{p+1}\mathbf{T}^0 \\ \vdots \\ \mathbf{T}^N - \mathbf{D}^N\mathbf{T}^0 \\ \vdots \\ \mathbf{T}^{N+p-1} - \mathbf{D}^{N+p-1}\mathbf{T}^0 \end{Bmatrix}, \quad \Psi = \begin{bmatrix} \mathbf{C}^1 \\ \mathbf{C}^2 \\ \vdots \\ \vdots \\ \mathbf{C}^{N-1} \\ \mathbf{C}^N \end{bmatrix}$$

The unknown parameters at any time step can be estimated simultaneously by applying the linear least-squares-error method, i.e.,

$$\Psi = (\mathbf{M}^T\mathbf{M})^{-1}\mathbf{M}^T\Theta \tag{14}$$

where $(\mathbf{M}^T\mathbf{M})^{-1}\mathbf{M}^T$ is a reverse matrix.

This method, which combines the function specification method and the whole domain estimation technique, enables all of the unknown boundary conditions to be estimated simultaneously over the total time interval.

3.2.2 WDFSM Algorithms. The function specification method can be implemented using different algorithms, which are differentiated by the assumptions they make regarding the relationship between the future components and the current estimated components. It is worth emphasizing that even though the algorithms described below are temporarily inexact assumptions, they nonetheless provide an effective means of stabilizing the computational results. The sections below describe two classic function specification algorithms, and introduce a modified algorithm which combines the characteristics of both algorithms.

Algorithm 1: Constant Function. The future-time unknown components are temporarily estimated using a constant function form. In this function, the future components $\mathbf{C}^{n+1}$, $\mathbf{C}^{n+2}, \ldots, \mathbf{C}^{n+p-1}$ are assumed to be equal to the component being currently estimated.

$$\mathbf{C}^n = \mathbf{C}^{n+1} = \mathbf{C}^{n+2} = \cdots = \mathbf{C}^{n+p-1} \tag{15}$$

The single unknown is $\mathbf{C}^n$, since $\mathbf{C}^1, \ldots, \mathbf{C}^{n-1}$ have been calculated previously.

Algorithm 2: Linear Function. The future-time unknown components are temporarily estimated using a linear function form. Numerical experiments have determined that the assumption of a linear function form for the unknown components is superior to that of a constant function form [18]. Under the linear function form approach, it is assumed that the future components $\mathbf{C}^{n+1}$, $\mathbf{C}^{n+2}, \ldots, \mathbf{C}^{n+p-1}$ vary linearly and that $\mathbf{C}^{n+j-1}$ can be written in terms of $\mathbf{C}^n$ and $\mathbf{C}^{n-1}$ [11] as

$$\mathbf{C}^{n+j-1} = j\mathbf{C}^n - (j-1)\mathbf{C}^{n-1} \tag{16}$$

The unknown component can then be estimated at each time step by applying the measurements of future time steps.

3.2.3 Algorithm 3: Modified Algorithm. In order to improve the accuracy of the estimates obtained from the WDFSM, this study proposes a modified algorithm, which essentially combines the constant and linear functions described above. In the proposed algorithm, the variations of the unknown estimates at future time steps for various values of the future-time parameter are investigated, and if large variations in the slope of the function are detected at any time step, the originally linear assumption is replaced with the constant function assumption at these particular time steps. The time steps at which the algorithm replaces the linear assumption with the constant function are identified by establishing the intersection points of piecewise approximate slope lines constructed on the basis of the preliminary stable estimates generated using different future-time parameter values. The future unknown components at these particular time steps are then computed using the constant function rather than the original linear function. However, the future unknown components at all other time steps are still estimated using the linear algorithm. As an example of this approach, Fig. 2 shows the estimated results obtained from the WDFSM using the linear algorithm (Algorithm 2) with several future-time parameter values (i.e., $p=17$, $p=19$, and $p=21$) for a triangular heat flux profile. As described above, the time steps at which Algorithm 3 will replace the linear assumption with a constant function assumption are calculated by identifying the intersection points of piecewise approximate slope lines to the curves of the estimated results. In the present example, the relevant time steps are seen to be $\tau_1=0.00087$ and $\tau_2=0.00142$, respectively. Therefore, under the modified algorithm, the future-time components at these particular time steps will be calculated

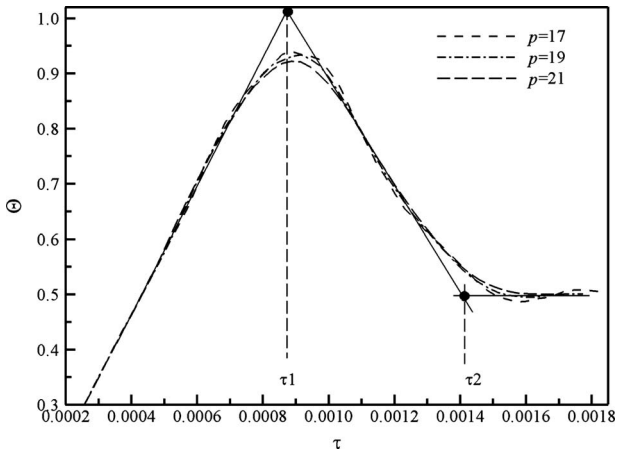

Fig. 2 Time steps for use in modified algorithm obtained from intersection points of piecewise approximate slope lines

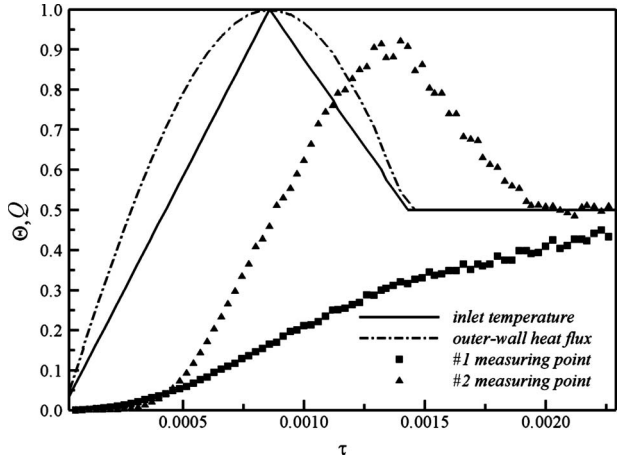

Fig. 3 The dimensionless boundary conditions and simulated measured temperatures at downstream locations with measurement error of 3%

using the constant function algorithm, while those at all other time steps will be calculated using the original linear function algorithm.

4 Results and Discussion

This paper considers the conjugate heat transfer problem of fluid flowing through a pipe. Hence, the analyzed IHCP involves determining the effect of heat conduction in the pipe wall in developing laminar forced convection flow and generating heat transfer within the pipe. The time-dependent inlet temperature, $F(\tau)$, and outer-wall heat flux distribution, $Q(\tau)$, illustrated in Fig. 3 are assumed to vary in the form

$$F(\tau) = \begin{cases} \dfrac{\tau}{8.58 \times 10^{-4}} & \text{for } 0 < \tau \leqslant 8.58 \times 10^{-4} \\ 1 - \dfrac{\tau - 8.58 \times 10^{-4}}{2 \times 5.72 \times 10^{-4}} & \text{for } 8.58 \times 10^{-4} < \tau \leqslant 1.43 \times 10^{-3} \\ 0.5 & \text{for } 1.43 \times 10^{-3} < \tau \end{cases}$$

$$Q(\tau) = \begin{cases} \sin\left(\dfrac{\pi\tau}{1.716 \times 10^{-3}}\right) & \text{for } 0 < \tau \leqslant 1.43 \times 10^{-3} \\ 0.5 & \text{for } 1.43 \times 10^{-3} < \tau \end{cases}$$

The direct problem described above in Sec. 3.1 can be solved using the finite-difference method. The total simulation time of 2.288×10^{-3} (in dimensionless terms) is divided into 80 equal time steps, corresponding to a sampling frequency of 2.86×10^{-5}. The dimensionless length and radius of the pipe are both assumed to be equal to 1 and are divided into 50 and 40 equal divisions, respectively, corresponding to $\Delta X = 0.02$ and $\Delta R = 0.025$. Temperature measurement sensors are placed on the centerline of the pipe ($R=0$) and at the inner wall ($R=R_{iw}$), respectively, at a downstream location of $X_{mea} = 10\Delta X$, as shown in Fig. 1. Using the dimensionless temperature data obtained from the direct problem, the inverse problem for the time-varying inlet temperature and outer-wall heat flux components is solved using the three algorithms described in Sec. 3.2. The quality of the estimated results obtained from each algorithm is then verified via a comparison with the above time-varying boundary conditions (exact solutions).

In practice, the temperature measurements always contain a certain degree of error. Therefore, in this study, it is considered that the simulated temperature measurements used in the inverse analysis include a measurement error component. For reasons of practicality, a random error noise is added to the exact temperature values computed in the direct problem. Hence, the measured dimensionless temperature $\Theta_{measured}$ is expressed as

$$\Theta_{measured} = \Theta_{exact}(1 + \omega\sigma) \tag{17}$$

where Θ_{exact} is the exact dimensionless temperature, σ is the amplitude of the measurement error, and ω is a random value specified between -1 and 1.

The simulated measured temperatures at two different downstream locations for an assumed measurement error of $\sigma = 3\%$ are illustrated in Fig. 3. It clearly shows that the measurements are taken at the two locations where the temperatures are significantly different from the inlet temperatures. In this study, the simulated measured temperatures are used for simultaneous estimation of the inlet temperature and the outer-wall heat flux. Figure 4 compares the exact solutions and the estimated results for the dimensionless inlet temperature. The estimated results are calculated with three different values of the future-time parameter p and an assumed measurement error of $\sigma = 3\%$ by the WDFSM using Algorithm 1 (Fig. 4(*a*)) and Algorithm 2 (Fig. 4(*b*)). In general, the estimated results are seen to be in good agreement with the exact solutions at $p=18$ and $p=22$. However, those obtained with $p=18$ are slightly less accurate than those obtained with $p=22$. When a value of $p=14$ is specified, the estimated results deviate significantly from the exact solutions. Comparing the estimated results obtained using $p=14$ in Figs. 4(*a*) and 4(*b*), respectively, it

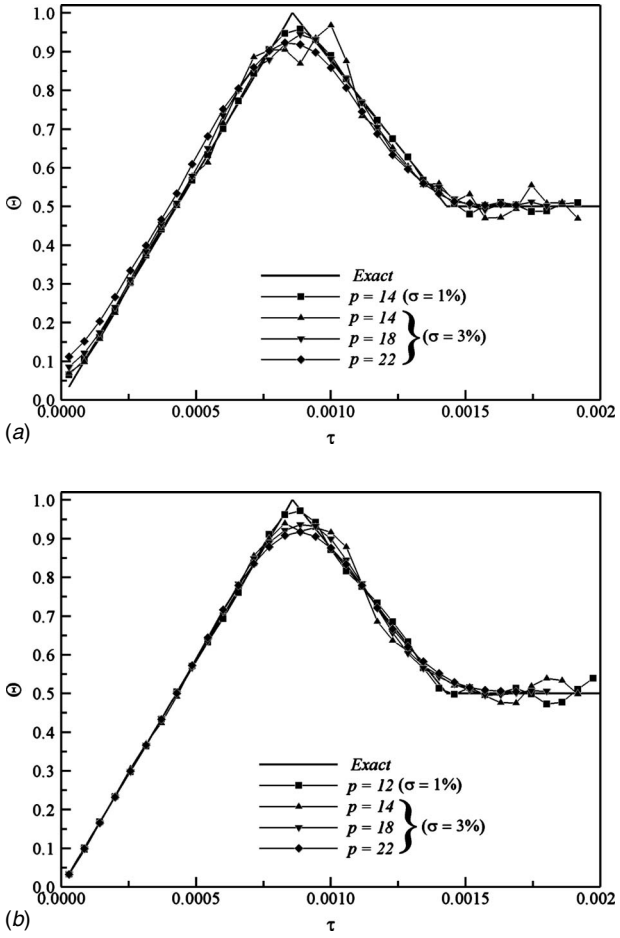

Fig. 4 Estimated dimensionless inlet temperature distributions for measurement error of 3% obtained using different values of future-time parameter in (*a*) Algorithm 1 and (*b*) Algorithm 2

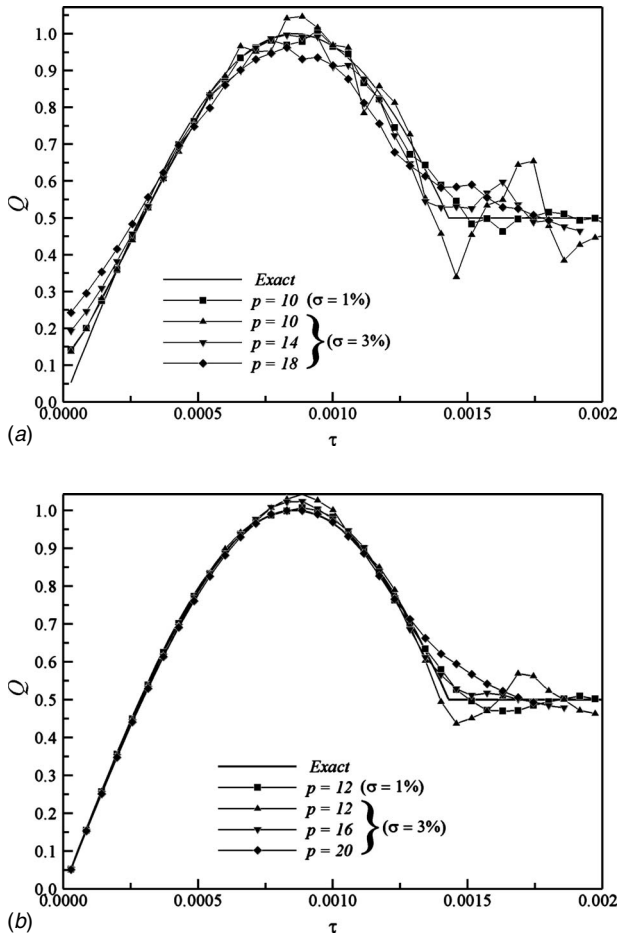

Fig. 5 Estimated dimensionless outer-wall heat flux distributions for measurement error of 3% obtained using different values of future-time parameter in (*a*) Algorithm 1 and (*b*) Algorithm 2

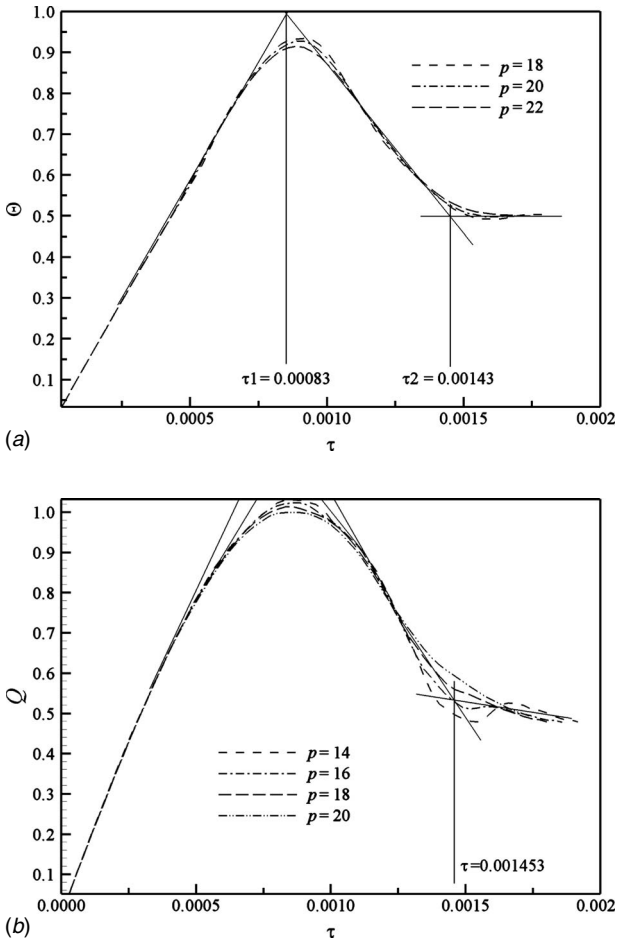

Fig. 6 Identification of time steps for use in modified algorithm

is seen that those obtained from Algorithm 2 are closer to the exact solution than those obtained from Algorithm 1. Therefore, it can be concluded that the effect of the future data in reducing the sensitivity of the estimated results to measurement errors is better in Algorithm 2 than in Algorithm 1.

Figure 5 compares the exact solutions and the estimated results for the dimensionless outer-wall heat flux, $Q(\tau)$. The estimated results are calculated with three different values of the future-time parameter p and an assumed measurement error of $\sigma=3\%$ by the WDFSM using Algorithm 1 (Fig. 5(*a*)) and Algorithm 2 (Fig. 5(*b*)). Comparing the estimated results obtained from Algorithm 1 with $p=14$ and Algorithm 2 with $p=16$, it can be seen that although both sets of estimated results provide reasonable approximations to the exact solutions, those obtained from Algorithm 2 with $p=16$ are more accurate. When measurement errors are taken into consideration, a slight deviation exists between the exact solutions and the best estimated results obtained from Algorithms 1 and 2. The extent of this deviation depends on the value of the future-time parameter. The value of the future-time parameter, which minimizes the deviation, i.e., the optimum future-time parameter, varies from algorithm to algorithm.

Figures 4 and 5 reveal that the value of the future-time parameter required to provide a close approximation of the outer-wall heat flux is significantly lower than that required to generate accurate estimations of the inlet temperature. When Algorithm 1 is applied, slight deviations in the estimated results from the exact solutions are seen immediately prior to heating (see Figs. 4(*a*) and 5(*a*)). It is observed that the magnitude of these deviations increases as the value of the future-time parameter is increased. However, these deviations are not evident under Algorithm 2 (see Figs. 4(*b*) and 5(*b*)). In other words, the estimated results presented in Figs. 4(*b*) and 5(*b*) are more exact than those in Figs. 4(*a*) and 5(*a*), respectively, since the leading error is fully eliminated. Note that the leading error observed under Algorithm 1 is caused as a result of a flawed assumption (i.e., a constant function) regarding the variation of the unknown parameters at the future time steps.

Figure 6 shows the derivation of the time steps associated with the intersection points obtained from piecewise approximate slope lines based on the results of the preliminary estimations obtained using Algorithm 2 with several future-time parameter values. As described previously, the modified algorithm replaces the linear assumption with the constant assumption at these time steps to improve the accuracy of the estimated results. In Fig. 6(*a*), which shows the inlet temperature distribution, it can be seen that the time steps at which the assumption for the unknowns must be modified are 0.00083 and 0.00143, respectively. However, in Fig. 6(*b*), which shows the outer-wall heat flux distribution, it is difficult to establish the intersection of the slope lines at the peak of the heat flux profile, and the only time step which can be identified is 0.001453.

Figures 7(*a*) and 7(*b*) present the best estimates obtained from the three algorithms for the dimensionless inlet temperature, $\Theta(\tau)$, and the dimensionless outer-wall heat flux, $Q(\tau)$, respectively. In each case, the results assume a measurement error of $\sigma=3\%$ and are obtained using the optimum value of the future-time parameter

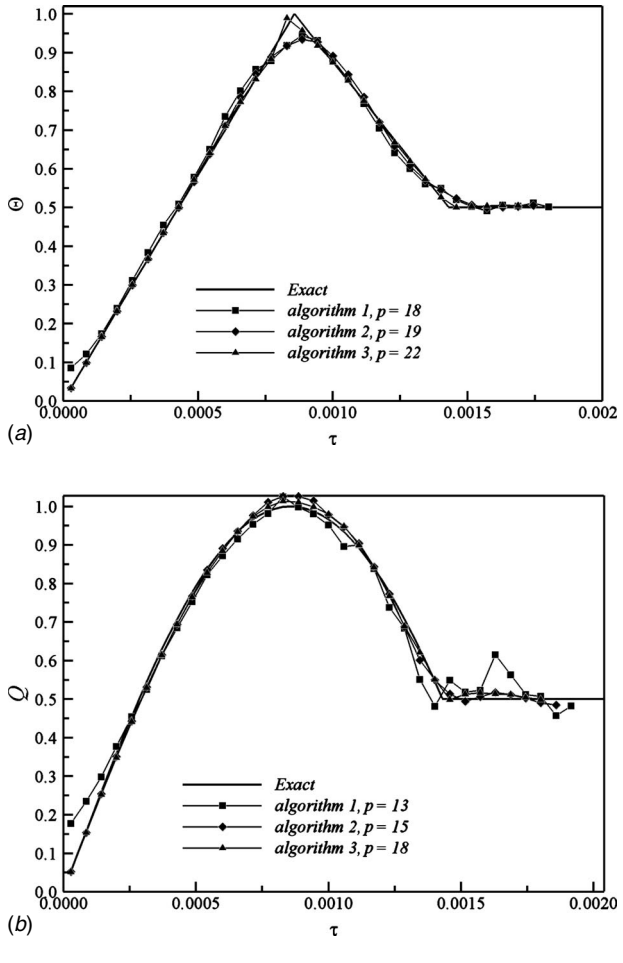

Fig. 7 Optimum estimation results obtained from three algorithms for (*a*) inlet temperature and (*b*) outer-wall heat flux with measurement error of 3%

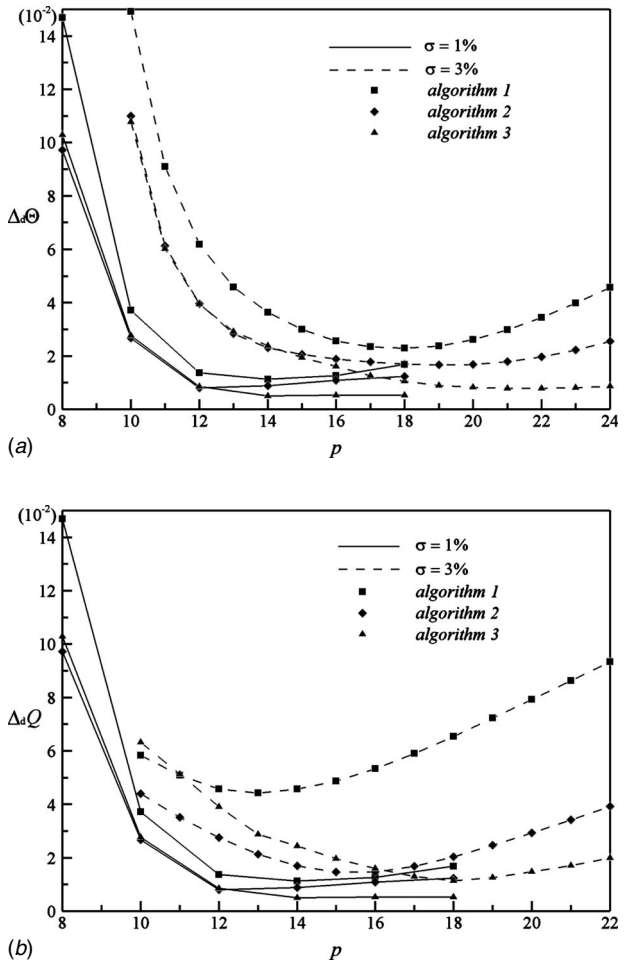

Fig. 8 Variation of rms error with future-time parameter for three algorithms for (*a*) inlet temperature, $\Delta_d\Theta$, and (*b*) outer-wall heat flux, $\Delta_d Q$, for measurement errors of 1% and 3%

in each algorithm. The exact solutions are also presented for comparison purposes. It is observed that the best estimate obtained from Algorithm 2 is more accurate than that provided by Algorithm 1. However, the solution provided by Algorithm 3 is closer to the exact solution than those of either Algorithm 1 or Algorithm 2. Hence, it can be concluded that Algorithm 3 provides a workable approach for solving the current inverse problem with high accuracy.

As stated previously, the quality of the estimated results is easily checked since the exact solution is known. In this study, the quality of the estimated solutions is assessed by $\Delta_d\mathbf{C}$, i.e., the root-mean-square (rms) error, defined as

$$\Delta_d\mathbf{C} = \sqrt{\frac{1}{N}\sum_{i=1}^{N}(\mathbf{C}^i_{\text{estimated}} - \mathbf{C}^i_{\text{exact}})^2} \tag{18}$$

Clearly, from Eq. (18), a higher rms error corresponds to a less accurate solution. This study divides the rms error, $\Delta_d\mathbf{C}$, into two groups, i.e., $\Delta_d\Theta$ (the rms error of the inlet temperature) and $\Delta_d Q$ (the rms error of the outer-wall heat flux). Figure 8 plots the variations of $\Delta_d\Theta$ (Fig. 8(*a*)) and $\Delta_d Q$ (Fig. 8(*b*)) with the future-time parameter p for a measurement error of σ=3%. The results reveal that the variations of the rms error are greatly influenced by the value of the future-time parameter in all three algorithms. In general, the sensitivity of the estimated results to measurement errors can be reduced by increasing the value of the future-time parameter. Increasing the value of p in the ranges $p \leqslant 18$, $p \leqslant 19$, and $p \leqslant 22$ yields a distinct improvement in the estimated results for the inlet temperature obtained by Algorithms 1, 2, and 3, respectively. In other words, the error of the estimations actually increases in Algorithms 1 and 2 at values of p higher than the optimum value. Regarding the estimated results for the outer-wall heat flux, the rms can be improved by increasing the value of the future-time parameter in the ranges $p \leqslant 13$, $p \leqslant 15$, and $p \leqslant 18$ for Algorithms 1, 2, and 3, respectively. From Fig. 8, it is clear that Algorithm 2 consistently produces more accurate solutions than Algorithm 1 at the same value of the future-time parameter. This confirms that the effect of the future data in minimizing the error of the estimated results is better in Algorithm 2 than in Algorithm 1. Finally, it is seen that the rms reduces significantly as the value of the future-time parameter is increased in Algorithm 3. Therefore, the most accurate estimates shown in Fig. 8 are those obtained by Algorithm 3.

On the basis of the results in Fig. 8, it can be concluded that a greater volume of future data is required to damp oscillation and to obtain a stable solution when higher measurement errors exist. The optimum value of the future-time parameter p depends on the amplitude of the measurement error and the algorithm employed.

5 Conclusion

This study has applied the WDFSM to obtain simultaneous estimates of the time-varying inlet temperature and outer-wall heat flux in laminar pipe flow based on temperature measurements taken within the pipe flow. The performances of three algorithms in the function specification method have been compared. The

function specification method has the advantage that the unknown quantities of the thermal boundary conditions can be estimated directly without changing the physics of the problem.

When fewer future-time measurements are used to estimate the heat flux component at the current time step, the estimated solution is generally unstable. However, the stability increases as the number of future measurements increases. In other words, the future-time parameter serves as a stabilizing parameter in the WDFSM. The current results have revealed that the estimated results are accurate even when a measurement error of 3% is introduced. In general, the numerical results have shown that the algorithm proposed in this study, which integrates the constant variation and time-dependent linear variation functions of the two classic algorithms, yields slightly more accurate estimates of the unknowns than either of the two classic algorithms.

Nomenclature

$\mathbf{A}$ = constant matrix constructed from thermal properties and spatial coordinates
$\mathbf{B}$ = coefficient matrix of $\mathbf{C}$
$\mathbf{C}$ = vector constructed from the unknown boundary conditions
F = dimensionless inlet temperature
$f(t)$ = function form of inlet temperature variation
k = thermal conductivity
l = length of the pipe
p = future-time parameter
Pr = Prandtl number
Q = dimensionless outer-wall heat flux
$q(t)$ = function form of the outer-wall heat flux
$\mathbf{R}$ = reverse matrix
R = dimensionless radial coordinate
Re = Reynolds number
r = radial coordinate
$\mathbf{T}$ = temperature vector
T = temperature
u = fluid axial velocity
X = dimensionless axial coordinate
x = axial coordinate

Greek Symbols

α = thermal diffusivity
ΔX = axial step size
ΔR = radial step size
$\Delta\tau$ = time step size
ν = kinematic viscosity
ω = random variable
Θ = dimensionless temperature
σ = standard deviation of the measurement error
τ = dimensionless time

Subscripts

exact = exact temperature
f = fluid
i,j,n,J = indices
initial = initial value
iw = inner wall
jw = index of radial coordinate at inner wall
m = mean value
measured = measured temperature
ow = outer wall
s = solid

References

[1] Zariffeh, E. K., Soliman, H. M., and Trupp, A. C., 1982, "The Combined Effects of Wall and Fluid Axial Conduction on Laminar Heat Transfer in Circular Tubes," *Proceedings of the Seventh International Heat Transfer Conference*, Munich, Germany, Vol. 4, pp. 131–136.

[2] Bernier, M. A., and Baliga, B. R., 1992, "Conjugate Conduction and Laminar Mixed Convection in Vertical Pipes for Upward Flow and Uniform Wall Heat Flux," Numer. Heat Transfer, Part A, **21**, pp. 313–332.

[3] Faghri, M., and Sparrow, E. M., 1980, "Simultaneous Wall and Fluid Axial Conduction in Laminar Pipe-Flow Heat Transfer," ASME J. Heat Transfer, **102**, pp. 58–63.

[4] Campo, A., and Schuler, C., 1988, "Heat Transfer in Laminar Flow Through Circular Tubes Accounting for Two-Dimensional Wall Conduction," Int. J. Heat Mass Transfer, **31**, pp. 2251–2259.

[5] Su, J., and Lopes, A. B. 2000, "Estimation of Unknown Wall Heat Flux in Turbulent Circular Pipe Flow," Int. Commun. Heat Mass Transfer, **27**(7), pp. 945–954.

[6] Su, J., and Silva Neto, A. J., 2001, "Simultaneous Estimation of Inlet Temperature and Wall Heat Flux in Turbulent Circular Pipe Flow," Numer. Heat Transfer, Part A, **40**, pp. 751–766.

[7] Park, H. M., and Lee, J. H., 1998, "A Method of Solving Inverse Convection Problem by Means of Mode Reduction," Chem. Eng. Sci., **53**(9), pp. 1731–1744.

[8] Bokar, J. C., and Özisik, M. N., 1995, "An Inverse Analysis for Estimating the Time-Varying Inlet Temperature in Laminar Flow Inside a Parallel Plate Duct," Int. J. Heat Mass Transfer, **38**(1), pp. 39–45.

[9] Li, H. Y., and Yan, W. M., 2000, "Inverse Convection Problem for Determining Wall Heat Flux in Annular Duct Flow," ASME J. Heat Transfer, **122**, pp. 460–464.

[10] Li, H. Y., and Yan, W. M., 2003, "Identification of Wall Heat Flux for Turbulent Forced Convection by Inverse Analysis," Int. J. Heat Mass Transfer, **46**, pp. 1041–1048.

[11] Beck, J. V., Blackwell, B., and Clair, C. R., 1985, *Inverse Heat Conduction-Ill-Posed Problem* Wiley, New York.

[12] Yang, C. Y., 1998, "A Sequential Method to Estimate the Strength of the Heat Source Based on Symbolic Computation," Int. J. Heat Mass Transfer, **41**, pp. 2245–2252.

[13] Yang, C. Y., 1998, "Inverse Estimation of Mix-Typed Boundary Conditions in Heat Conduction Problems," J. Thermophys. Heat Transfer, **12**, pp. 552–561.

[14] Chantasiriwan, S., 2000, "Inverse Heat Conduction Problem of Determining Time-Dependent Heat Transfer Coefficient," Int. J. Heat Mass Transfer, **42**, pp. 4275–4285.

[15] Behbahani-nia, A., and Kowsary, F., 2004, "A Dual Reciprocity BE-Based Sequential Function Specification Solution Method for Inverse Heat Conduction Problems," Int. J. Heat Mass Transfer, **47**, pp. 1247–1255.

[16] Kim, T. G., and Lee, Z. H., 1997, "Time-Varying Heat Transfer Coefficients Between Tube-Shaped Casting and Metal Mold," Int. J. Heat Mass Transfer, **40**, pp. 3513–3525.

[17] Yang, C. Y., and Chen, C. K., 1996, "The Boundary Estimation in Two-Dimensional Inverse Heat Conduction Problems," J. Phys. D, **29**, pp. 333–339.

[18] Chantasiriwan, S., 1999, "Comparison of Three Sequential Function Specification Algorithms for the Inverse Heat Conduction Problem," Int. Commun. Heat Mass Transfer, **26**, pp. 115–124.

On the Physics of Heat Transfer and Aerodynamic Behavior of Separated Flow Along a Highly Loaded Low Pressure Turbine Blade Under Periodic Unsteady Wake Flow and Varying of Turbulence Intensity

M. T. Schobeiri

B. Öztürk

The Turbomachinery Performance and Flow Research Laboratory (TPFL), Texas A&M University, College Station, TX 77843

M. Kegalj

Fachgebiet Turbomaschinen und Fluidantriebstechnik, TU-Darmstadt, D-64287 Darmstadt, Germany

D. Bensing

University Bochum, D-44780 Bochum, Germany

This paper attempts to provide a detailed insight into the heat transfer and aerodynamic behavior of a separation zone that is generated as a result of boundary layer development along the suction surface of a highly loaded low pressure turbine blade. This paper experimentally investigates the individual and combined effects of periodic unsteady wake flows and freestream turbulence intensity (Tu) on heat transfer and aerodynamic behavior of the separation zone. Heat transfer experiments were carried out at Reynolds numbers of 110,000, 150,000, and 250,000 based on the suction surface length and the cascade exit velocity. Aerodynamic experiments were performed at Re = 110,000. For the above Re numbers, the experimental matrix includes Tu's of 1.9%, 3.0%, 8.0%, and 13.0% and three different unsteady wake frequencies with the steady inlet flow as the reference configuration. Detailed heat transfer and boundary layer measurements are performed with particular attention paid to the heat transfer and aerodynamic behavior of the separation zone at different Tu's at steady and periodic unsteady flow conditions. The objectives of the research are (a) to quantify the effect of Tu on the aerothermal behavior of the separation bubble at steady inlet flow conditions, (b) to investigate the combined effects of Tu and the unsteady wake flow on the aerothermal behavior of the separation bubble, and (c) to provide a complete set of heat transfer and aerodynamic data for numerical simulation that incorporates Navier–Stokes and energy equations. The experimental investigations were performed in a large-scale, subsonic, unsteady turbine cascade research facility at the Turbomachinery Performance and Flow Research Laboratory of Texas A&M University. [DOI: 10.1115/1.2885156]

Introduction

Flow separation occurs in aircraft turbine components during the design and off-design operation. At higher Reynolds numbers (takeoff, landing: 400,000–600,000), flow separation may occur in high pressure turbine (HPT) blades as a result of incidence angle changes that are induced by adverse off-design operation conditions. On the other hand, at lower Reynolds numbers (cruise: 50,000–250,000), the laminar boundary layer along the suction surface of the low pressure turbine (LPT) passing through the minimum blade pressure encounters an adverse pressure gradient that causes the flow to separate, build up a separation bubble, and then reattach. The process of flow separation and reattachment adds to the complexity of the flow field, which makes it more difficult to reliably predict the flow field using numerical tools.

The computational fluid dynamic (CFD) tools have reached a level of maturity that enables the gas turbine designers to numerically simulate complex flow structures. CFD codes are regularly utilized for qualitative aerodynamics and heat transfer studies of HPTs at high Reynolds numbers in the absence of flow separation. It is also utilized as a powerful tool for parametric aerodynamics and heat transfer design studies. However, quantitatively, the CFD has not reached the desired level to a priori predict the flow quantities of complex structures in a reliable fashion. Separation inception, size and reattachment, total pressure loss coefficient, and efficiency are among those quantities where CFD is still not yet capable of a priori providing quantitative results that satisfactorily compare with the experiment. Furthermore, the prediction of blade surface temperature is still associated with major inaccuracy. Implementation of physically sound turbulence and transition models is still an unresolved issue.

Given the turbine inlet temperature level of the current high performance core engines, the low pressure turbine (LPT) blades are not subjected to excessive thermal stresses that require extensive heat transfer studies. However, considering the current state-of-the-art engine design and projecting its progressive trend into the near future, a thorough understanding of the underlying physics of LPT heat transfer and its quantitative prediction seems indispensable. This is, on the other hand, unmistakably concatenated with understanding the basic heat transfer physics of separated flow regime that is exposed to periodic unsteady inlet flow conditions. This circumstance constitutes the prime motivation in defining the objective of the present work that treats the heat transfer

Contributed by the Heat Transfer Division of ASME for publication in the JOURNAL OF HEAT TRANSFER. Manuscript received October 13, 2006; final manuscript received May 31, 2007; published online April 10, 2008. Review conducted by Jay M. Khodadadi.

and aerodynamic behavior of the separation zone under periodic unsteady flow conditions and varying turbulence intensity.

LPT aerodynamic aspects of separated flow under periodic unsteady inlet flow conditions have been the subject of a series of research reports published by TPFL, supported by the NASA Glenn Research Center. Very recent papers, Refs. [1,2], deal with the physics of the inception, onset, and extent of the separation bubble along a LPT blade under periodic unsteady inlet flow conditions. The study in Ref. [3] investigates the effect of Reynolds numbers and periodic unsteady wake flow conditions on boundary layer development, separation, and reattachment along the suction surface of a low pressure turbine blade. The subsequent study, Ref. [4], treats intermittent behavior of the separated boundary layer along the suction surface of a low pressure turbine blade under periodic unsteady flow conditions. The comprehensive study in Ref. [5] investigates the combined effects of wake frequency and freestream turbulence intensity of the unsteady boundary layer behavior along the suction surface of a LP turbine with particular attention given to the separation bubble aerodynamics. LPT aerodynamic research reported in Ref. [6] also deals primarily with boundary layer separation and reattachment behavior under unsteady flow conditions. Pressure surface separation aerodynamics and heat transfer was the subject of an experimental investigation reported in Ref. [7], where the separation was triggered by changing the incidence angle.

LPT aerodynamics and heat transfer aspects of a separated flow along the pressure side were treated numerically in Ref. [8]. Here, as in Ref. [7], the separation was triggered by varying the incidence angle that caused moderate to massive separation zones on the pressure surface of a highly loaded LPT blade, T106-300. This paper provides a detailed velocity, heat transfer, and pressure measurement along the pressure surface. Further intensive literature search and the subsequent communications with heat transfer experts [9,10] did not result in finding more papers that cover this topic.

HPT heat transfer aspects of gas turbine blades are reported in many papers. Detailed heat transfer and boundary layer development along the surfaces of a high Reynolds number space shuttle main engine (SSME) blade under periodic unsteady inlet flow condition is reported in Ref. [11]. The effect of periodic unsteady inlet flow conditions on a HPT blade heat transfer is reported in Refs. [12–14], where the experiments were focused on obtaining the surface heat transfer information and pressure distribution without unsteady boundary layer measurements.

Steady heat transfer aspects are the subject of many articles published prior to 1971 that dealt with heat transfer in turbomachinery, summarized in Ref. [15]. Further detailed information about gas turbine heat transfer and a critical evaluation of different heat transfer experimental and numerical methods are presented in Ref. [16]. An interesting investigation dealing with the effect of freestream turbulence on HPT blade heat transfer and pressure distribution is presented in Ref. [17]. Systematic heat transfer experiments were performed where the turbulence intensity was varied from 0.73% to 14.33% by applying different turbulence generator grids at Reynolds numbers ranging from 15,000 to 105,000. The results reveal a systematic increase in Nusselt numbers with increasing the Reynolds number at constant turbulence intensity. Furthermore, the transition start moves further upstream with increasing the Reynolds number and turbulence intensity.

The objectives of the research are (a) to quantify the effect of Tu on the aerothermal behavior of the separation bubble at steady inlet flow conditions, (b) to investigate the combined effects of Tu and the unsteady wake flow on the aerothermal behavior of the separation bubble, and (c) to provide a complete set of heat transfer and aerodynamic data for numerical simulation that incorporates Navier–Stokes and energy equations. The experimental investigations were performed in a large-scale, subsonic unsteady turbine cascade research facility at the Turbomachinery Performance and Flow Research Laboratory of Texas A&M University.

Experimental Research Facility

To investigate the effect of unsteady wake flow on turbine and compressor cascade aerodynamics, particularly on unsteady boundary layer transition, a multipurpose, large-scale, subsonic research facility was designed and has been in operation since 1993. Since the facility in its original configuration is described in Refs. [1,2,11], only a brief description of the modifications and the main components is given below. The research facility consists of a large centrifugal compressor, diffuser, settling chamber, nozzle, unsteady wake generator, and a turbine cascade test section, as shown in Fig. 1. The compressor with a volumetric flow rate of 15 m^3/s is capable of generating a maximum mean velocity of 100 m/s at the test section inlet. The settling chamber consists of five screens and one honeycomb flow straightener to control the uniformity of the flow.

A two-dimensional periodic unsteady inlet flow is simulated by the translational motion of an unsteady wake generator (see Figs. 2 and 3) with a series of cylindrical rods attached to two parallel operating timing belts driven by an electric motor. To simulate the wake width and spacing that stem from the trailing edge of rotor blades, the diameter and number of rods can be varied. The rod diameter, its distance from the LPT blade leading edge, the wake width, and the corresponding drag coefficient are chosen according to the criteria outlined by Schobeiri et al. [18]. The belt-pulley system is driven by an electric motor and a frequency controller. The wake-passing frequency is monitored by a fiber optic sensor. The sensor also serves as the triggering mechanism for data transfer and its initialization, which is required for ensemble averaging. This type of wake generator produces clean two-dimensional wakes, whose turbulence structure decays and development is, to a great extent, predictable [19].

To account for a high flow deflection of the LPT cascade, the entire wake generator and test section unit, including the traversing system, was modified to allow a precise angle adjustment of the cascade relative to the incoming flow. This is done by a hydraulic platform, which simultaneously lifts and rotates the wake generator and test section unit. The unit is then attached to the tunnel exit nozzle with an angular accuracy less than 0.05 deg, which is measured electronically.

Variation of Unsteady Wake Frequency. The special design of the facility and the length of the belts (L_{belt}=4960 mm) enables a considerable reduction of the measurement time. For unsteady boundary layer investigation, two clusters of rods with a constant diameter of 2 mm are attached to the belts, as shown in Fig. 2. The two clusters with spacings S_R=160 mm and S_R=80 mm are separated by a distance, which does not have any rods, thus, simulating steady-state case (S_R=∞). Thus, it is possible to measure sequentially the effect of three different spacings at a single boundary layer point. To clearly define the influence domain of each individual cluster with the other one, the clusters are arranged with a certain distance between each other. Figure 2 exhibits the time dependent velocities for S_R=80 mm, S_R=160 mm, and S_R=∞. As seen, the steady-state case is characterized by a constant velocity. However, the frequency of the unsteady case with S_R=80 mm is twice as high as with S_R=160 mm. Using the triggering system mentioned above and a continuous data acquisition, we define buffer zones of 100 ms equally divided between the signals originating from passing of two successive rod clusters. The data analysis program cuts the buffer zones and evaluates the data pertaining to each cluster. Comprehensive preliminary measurements were carried out to make sure that the data were exactly identical to those when the entire belt length was attached with rods of constant spacing, which corresponded to each individual cluster spacing. For the surface pressure and heat

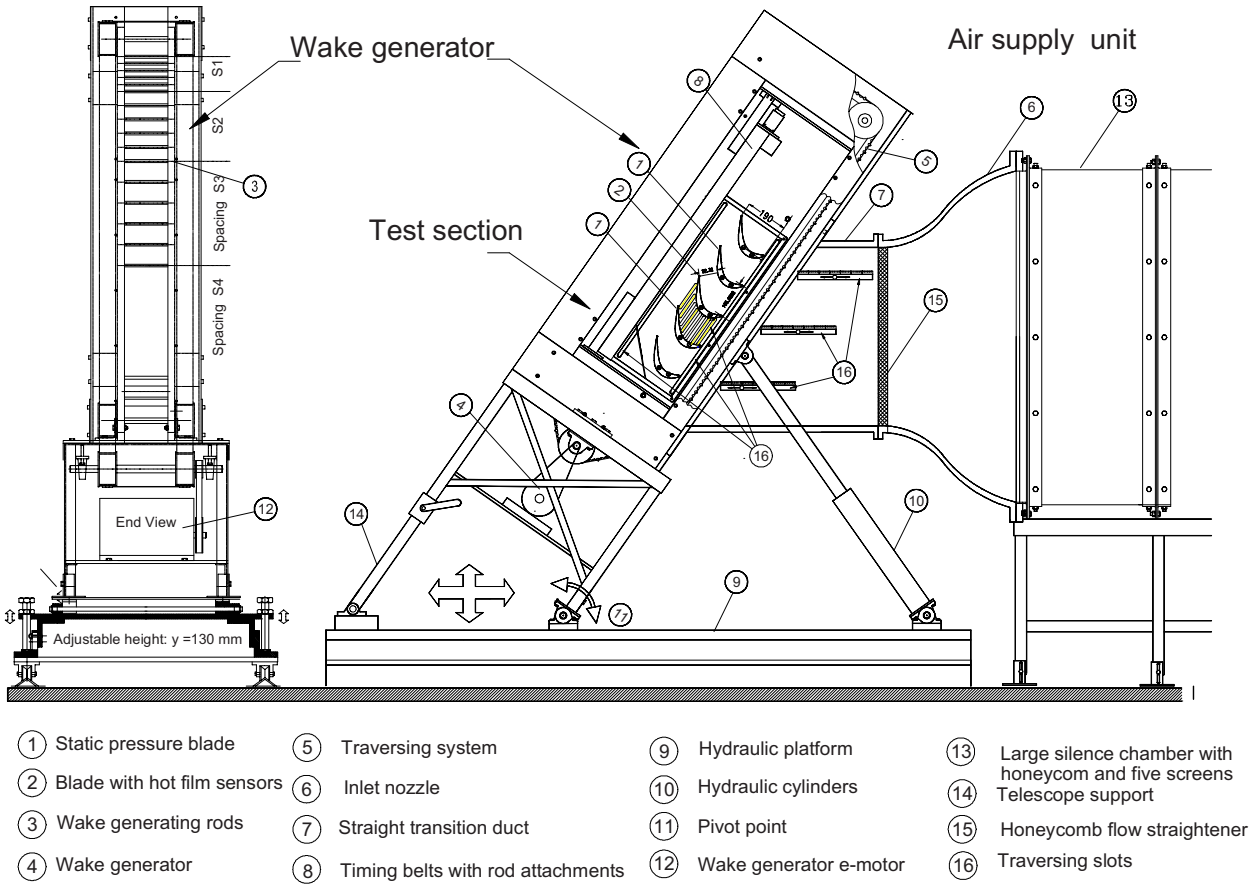

Fig. 1 Turbine cascade research facility with the components and the adjustable test section

transfer experiments, the entire belt length was attached one after the other with rods of S_R=80 mm, S_R=160 mm, and S_R=∞ (no rod, steady case), respectively. To accurately account for the unsteadiness caused by the frequency of the individual wakes and their spacings, the flow velocity, and the cascade parameters, a reduced frequency Ω that includes the cascade solidity σ, the flow coefficient Φ, the blade spacing S_B, and the rod spacing S_R is defined. Many researchers have used the Strouhal number as the unsteady flow parameter, which only includes the speed of the wake generator and the inlet velocity. However, the currently defined reduced frequency Ω is an extension of the Strouhal number in the sense that it incorporates the rod spacing S_R and the blade spacing S_B, in addition to the inlet velocity and wake generator speed. For surface pressure measurement, rods with uniform spacings, as specified in Table 1, were attached over the entire belt length. For boundary layer measurement, however, clusters of rods were attached, as mentioned previously. For the rod spacings of S_R=80 mm, S_R=160 mm, and S_R=∞ (no rod, steady case), the corresponding reduced frequencies are Ω=3.18, 1.59, and 0.0.

Variation of Turbulence Intensity, Length Scale. Three different turbulence grids were manufactured for producing inlet turbulence intensities Tu=3.0%, 8.0%, and 13.0%. The grids consist of square shaped aluminum rods with the thickness, G_T, and opening, G_O, given in Table 2. The turbulence intensity values were measured at the cascade inlet with the location from the cascade leading edge Tu_{LE} listed in Table 2. The grids were subsequently installed upstream of the wake generator with the distance form cascade leading edge G_{LE} defined in Table 2.

As mentioned at the beginning, one of the objectives of the ongoing investigation is to provide a database for subsequent CFD simulations. In this regard, comprehensive sets of experimental data dealing with the inlet flow condition, its turbulence behavior, and statistical evaluation have been provided and documented in Ref. [19].[1] Since introducing these data in their entirety is beyond the scope of this paper, we present the most essential information for description of the inlet flow condition. An adequate description of the inlet flow condition requires, in addition to the time dependent velocity distribution and freestream turbulence intensity, information about the turbulence length scale. As Bruun [20] summarized, a direct measurement of the integral length scale using two parallel hot-wire sensors is, due to the thermal (and even cold) wake interference, associated with significant errors. A recent paper by Barrett and Hollingsworth [21] summarizes different methods for calculating the length scale. The current investigations utilize an alternative solution to estimate the length scale by using relations developed by Hinze [22]. To document the turbulence length scales, one-dimensional power spectra of the velocity fluctuations were measured using a single-wire probe. The spectral measurements used 20,000 data points at 20 kHz (low-pass filter at 10 kHz). The results of the spectral calculations are shown in Fig. 4(*a*), where the power spectral distribution (PSD) is plotted versus the frequency. As seen, there is a systematic decrease in PSD with decreasing the turbulence intensity. From these data, the integral length scales Λ were calculated for each turbulence grid. The results of these calculations are presented in Fig. 4(*b*), and in Tables 1 and 2. Figure 4(*b*) indicates a decrease in length scale with increasing the freestream turbulence

[1]The entire data are available for CFD simulation; please contact the principal author.

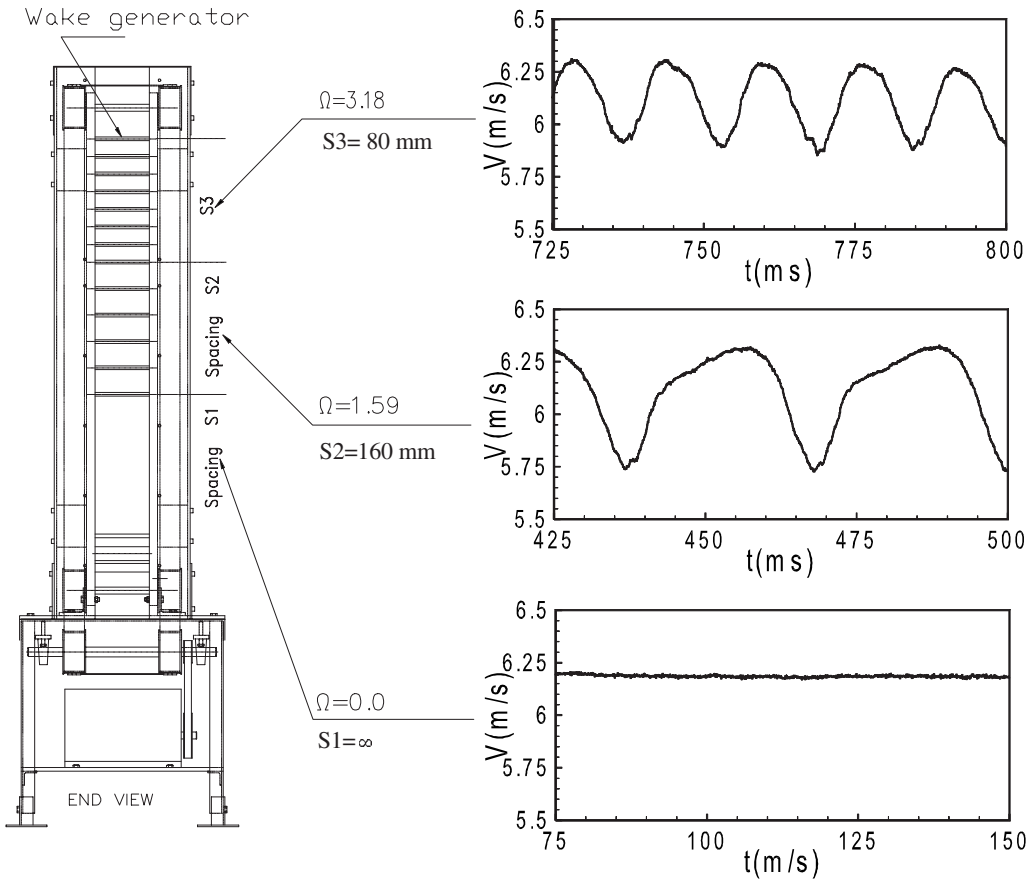

Fig. 2 Wake Generator (left), velocity distributions generated with three different reduced frequencies $\Omega=0$ (steady), 1.59, and 3.18. Location of the data measured: 30 mm upstream of the leading edge

intensity. The solid curve plotted in Fig. 4(*b*) indicates the tendency that by increasing the turbulence intensity, the length scale asymptotically approaches a constant limit.

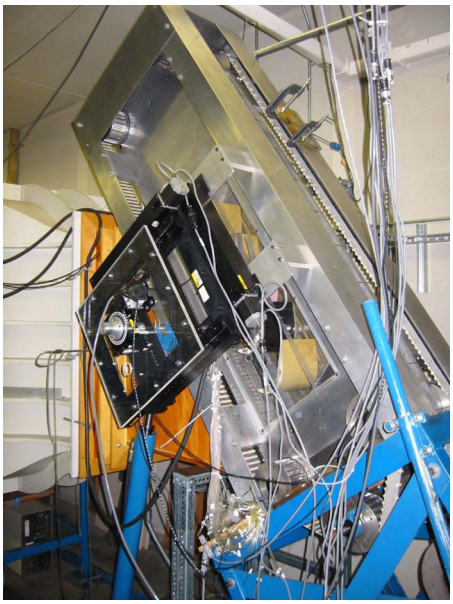

Fig. 3 Turbine cascade research facility with three-axis traversing system

LPT Blades, Aerodynamics. The cascade test section shown in Fig. 1, located downstream of the wake generator, includes five LPT blades with a height of 200.0 mm and the chord of 203.44 mm, as shown in Fig. 3. This blade number is necessary and sufficient to secure a spatial periodicity for the cascade flow. For boundary layer investigations, five identical "Pak B" airfoils, designed by Pratt and Whitney and manufactured in TPFL, were implemented whose cascade geometry is given in Table 1. The blade geometry resembles essential features such as the laminar boundary layer separation that is inherent to typical LPT blades. The blade geometry was made available to NASA researchers and academia to study the specific problems of LPT flow separation, its passive, active control and its prevention. To ensure that the periodicity requirement is fulfilled, second and fourth blades were specially manufactured and instrumented each with 48 static pressure taps. Almost identical pressure distributions measured around these two blades confirm the periodicity for steady and periodic unsteady inlet flow conditions. A computer controlled traversing system is used to measure the inlet velocities and turbulence intensities, as well as the boundary layers on suction and pressure surfaces. The traversing system (see Fig. 3) was modified to allow the probe to reach all streamwise positions along the suction and pressure surfaces. The three-axis (x, y, θ) traversing system is vertically mounted on the plexiglass sidewall. Each axis is connected to a dc stepper motor with an encoder and decoder. The optical encoder provides a continuous feedback to the stepper motor for accurate positioning of the probes. The x-y-axes are capable of traversing along the suction and pressure surfaces in small steps up to 1 μm. The θ-axis is capable of rotating the probe axis with

Table 1 Parameters of turbine cascade test section

Parameters	Values	Parameters	Values
Inlet velocity	V_{in}=4 m/s	Inlet turbulence intensity	Tu=1.9%
Rod translational speed	U=5.0 m/s	Blade Re number	Re_{ss}=110,000
Nozzle width	W=200.0 mm	Blade height	h_B=200 mm
Blade chord	c=203.44 mm	Cascade solidity	σ=1.248
Blade axial chord	c_{ax}=182.85 mm	Zweifel coefficient	ψ_A=1.254
Blade suction surf. length	L_{SS}=270.32 mm	Cascade angle	φ=55 deg
Cascade flow coefficient	Φ=0.80	Cascade spacing	S_B=163 mm
Cascade inlet flow angle	α_1=0 deg	Cascade exit flow angle	α_2=90 deg
Wake generator rod diameter	D_R=2.0 mm	Rod distance to lead. edge	L_R=122 mm
Cluster 1 (no rod, steady)	S_R=∞ mm	Ω parameter steady case	Ω=0.0
Cluster 2 rod spacing	S_R=160.0 mm	Ω parameter for Cluster 1	Ω=1.59
Cluster 3 rod spacing	S_R=80.0 mm	Ω parameter for Cluster 2	Ω=3.18

an angular accuracy of less than 0.05 deg, which is specifically required for boundary layer investigations where the measurement of the laminar sublayer is of particular interest.

The data acquisition system used to perform the present paper is the same one described in previous papers [1,2]. Two adjacent blades are used for boundary layer measurements. The unsteady data are taken by calibrated, custom designed, miniature, single hot-wire probes. At each boundary layer position, samples were taken at a rate of 20 kHz for each of 100 revolutions of the wake generator. The data were ensemble averaged at 100 revolutions with respect to the rotational period of the wake generator. Before final data were taken, the number of samples per revolution and the total number of revolutions were varied to determine the optimum settings for convergence of the ensemble-averaged data. For the steady-state case, the instantaneous velocity components are calculated from the temperature compensated instantaneous voltages by using the calibration coefficients. The instantaneous velocity, and ensemble-averaged and time-averaged velocities are determined using the standard procedure described in many papers, among others, in Refs. [11,19,20].

Table 2 Turbulence grids: Geometry, turbulence intensity, and length scale

Turbulence grid	Grid opening (%)	Grid thickness (mm)	Turbulence intensity Tu (%)	Length scale Λ (mm)
No grid	G_O=100	0	Tu_{in}=1.9	41.3
TG1	G_O=77	GT=6.35	Tu_{in}=3.0	32.5
TG2	G_O=55	GT=9.52	Tu_{in}=8.0	30.1
TG3	G_O=18	GT=12.7	Tu_{in}=13.0	23.4

Location of turbulence intensity measured from the cascade leading edge: Tu_{LE}=30.0 mm.
Grid distance from leading edge for all three grids: G_{LE}=160.0 mm.

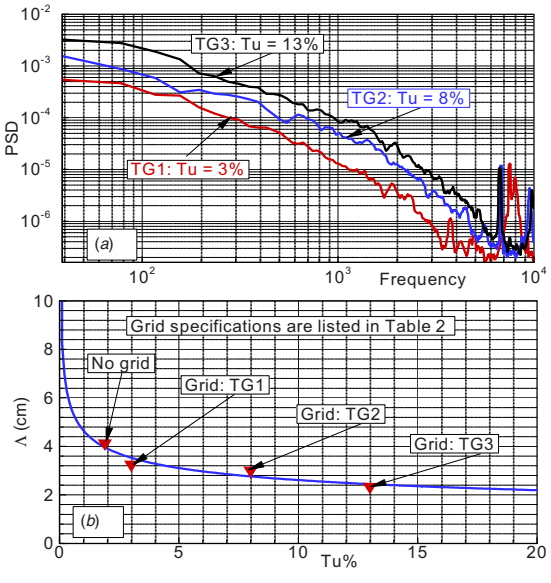

Fig. 4 (*a*) PSD as a function of frequency for three different grids described in Table 1. The results from (*a*) are used to generate the turbulence length scales as a function of turbulence intensity (*b*).

LPT Blade, Heat Transfer. Figure 6 shows the details of the heat transfer blade. A separate blade is specially manufactured from a nonconductive material with a thin Inconel heater foil attached to its surface via a two-sided temperature resistant adhesive tape. On top of this tape, a sheet of liquid crystal is attached for temperature measurements. The power required for heating the heat transfer blade is supplied by a Sytron 10 V–200 A (maximum) dc power supply. The current passing through the test blade is measured with a multimeter connected across a shunt resistor. Two separate multimeters are used to measure the voltages in the circuit. One multimeter is connected across the output leads of the power supply to measure the voltage output, and the other is connected across the blade terminals. These two measurements are used to calculate the power losses in the cable resistance. The yellow band of the liquid crystal is used to record the data. The location of the yellow band is controlled through the power supply to the blade, and the voltage and the current readings across the blade terminals are recorded for different locations of the yellow band on the turbine blade. The collected data are reduced based upon a constant heat flux analysis, which entails determining all the energy losses on a flux basis and subtracting them from the heat flux of the Inconel foil. Details of heat transfer measurements using the liquid crystal technique are presented in an extensive literature review documented in Ref. [23].

Uncertainty Analysis

Aerodynamics. The Kline and McClintock [24] uncertainty analysis method was used to determine the uncertainty of the aerodynamics, as well as heat transfer quantities described in this paper. The uncertainties in velocity for the single-wire probe after data reduction, the Re numbers, and the pressure coefficients are given in Table 3. As shown, the uncertainty in velocity increases as the flow velocity decreases. This is due to the uncertainty of the pneumatic pressure transducer at lower pressure during the calibration. The uncertainties in Re numbers and the pressure coefficients exhibit similar behavior. It is worth noting that the relatively minor Re changes caused by the uncertainty have almost no influence on boundary layer development, separation, and reat-

Table 3 Uncertainty analysis for velocity, Re number, and pressure coefficient C_p measurements

V (m/s)	Re	$\omega V/V$ (%)	$\omega \mathrm{Re}/\mathrm{Re}$ (%)	$\omega C_p/C_p$ (%)
3.6	110,000	3.939	2.361	2.205
4.9	150,000	2.127	1.684	2.057
8.16	250,000	0.772	1.362	0.693

tachment, as documented in Ref. [3]. Table 4 exhibits the uncertainties of freestream turbulence intensities at Re=110,000, 150,000, and 250,000. As described in the table caption, for each Re number, the uncertainty of the corresponding freestream turbulence intensity Tu can be found easily.

Heat Transfer. Uncertainties in heat transfer coefficients are calculated for the entire blade surface. Table 5 shows the uncertainties at each s/s_0-position for the heat input to the foil Q_{foil}, the radiative heat Q_{rad} transfer, and the heat transfer coefficient h on the suction surface. Similar values were measured for pressure surface. As seen, the uncertainties in heat transfer coefficients are approximately 4.5%. These uncertainties arise mainly due to the higher uncertainty in radiation heat loss from the blade surface. Also, uncertainties in radiation heat losses are sensitive to individual uncertainties in the measurement of yellow line temperature and the temperature of the freestream air. These values are taken to be 0.5 K, which is the uncertainty with the thermocouples used in the measurement of the freestream air. Uncertainties in the heat inputs to the blade are of the order of 0.4% and are relatively low when compared to the radiation losses.

Results and Discussion

Detailed surface pressure and boundary layer measurements were performed at a Reynolds number of 110,000. This Reynolds number, which pertains to a typical cruise operation, exhibits a representative value within LPT operating range between 75,000 and 400,000, as discussed by Hourmouziadis [25]. Furthermore, it produces separation bubbles that can be accurately measured by miniature hot-wire probes. Surface pressure measurements at Reynolds numbers of 75,000, 110,000, 125,000, and 150,000, presented in Ref. [1], show that pressure distribution for these Reynolds numbers does not differ substantially from each other. Therefore, for the boundary layer investigations, a representative Reynolds number of 110,000 was chosen. For generation of the unsteady wakes, cylindrical rods with the diameter d_R=2 mm were chosen to fulfill the criterion that requires the generation of a

Table 4 Uncertainty values for each Re number with corresponding freestream turbulence intensity Tu(%). As an example, for Re=110,000 and Tu=1.9%, the uncertainty is ωTu/Tu(%)=0.577.

Re/Tu (%)	1.9	3	8	13
110,000	0.577	0.367	0.142	0.093
150,000	0.229	0.146	0.058	0.04
250,000	0.137	0.087	0.033	0.021

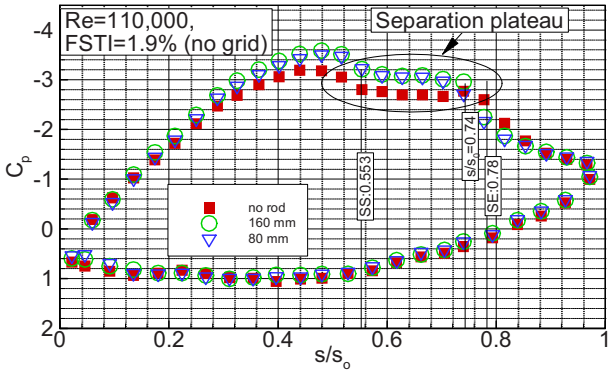

Fig. 5 Static pressure distribution in the blade midsection at Re=110,000, Tu=1.9, and reduced frequencies Ω=0,1.59,3.18 (no rod, 160 mm, 80 mm spacing), SS=separation start, SE=separation end

drag coefficient C_D that is approximately equal to the C_D of the turbine blade with the chord and spacing given in Table 1 (details are reported in Refs. [19,26]).

Results: Surface Pressure Distributions. For the Reynolds number of 110,000 with a freestream turbulence intensity of 1.9% (no grid), three different reduced frequencies, namely, Ω=0.0, 1.59, and 3.18, that correspond to the rod spacings S_R=∞, 160 mm, and 80 mm were applied. Figure 5 shows the pressure distributions along one of the static pressure blades for the steady case and two unsteady cases. The pressure signals inherently signify the time-averaged pressure because of the internal pneumatic damping effect of the connecting pipes to the transducer. It is worth noting that the pressure distribution gives reasonably good information about the extent of the flow separation. However, it does not provide the information about the exact begining and end of the separation bubble. This is due to the longitudinal spacing between the pressure taps. Furthermore, the static pressure distribution does not provide the necessary information about the lateral extent of the separation bubble. This deficiency is eliminated by traversing the boundary layer from leading edge to trailing edge, where detailed timed dependent flow velocity information is extracted.

The time-averaged pressure coefficients along the pressure and suction surfaces, in the midsection of the blade, are plotted in Fig. 5. The suction surface (upper portion) exhibits a strong negative pressure gradient. The flow accelerates at a relatively steep rate and reaches its maximum surface velocity that corresponds to the minimum C_p=−3.65 at s/s_0=0.47. Passing through the minimum pressure, the fluid particles within the boundary layer encounter a positive pressure gradient that causes a sharp deceleration until s/s_0=0.55 has been reached. In accordance with the intermittency analysis presented in Ref. [4], this point signifies the beginning of the laminar boundary layer separation and the onset of a separation bubble. As seen in the subsequent boundary layer discussion, the separation bubble characterized by a constant C_p-plateau extends up to s/s_0=0.78, thus, occupying more than 23% of the suction surface and constituting a large separation. Passing the

Table 5 Uncertainty analysis for heat transfer measurements

s/s_0	Voltage (V)	Current (A)	T_{air} (C)	$\omega_{Q_{\mathrm{rad}}}/Q_{\mathrm{rad}}$ (%)	$\omega_{Q_{\mathrm{foil}}}/Q_{\mathrm{foil}}$ (%)	ω_h/h (%)
0.1	3.50	114.9	31.3	4.384	0.408	4.387
0.3	2.401	80.8	33.2	4.961	0.426	4.973
0.5	2.10	71.3	32.8	4.827	0.435	4.847
0.7	1.949	66.5	32.4	4.700	0.441	4.727
0.9	1.793	61.5	31.7	4.494	0.441	4.533

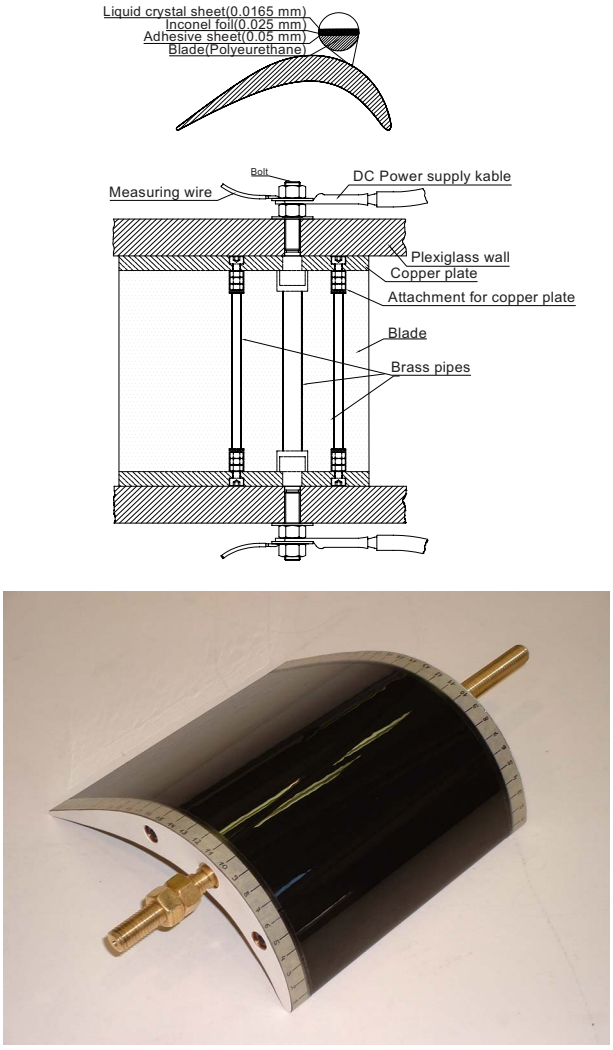

Fig. 6 Heat transfer blade with liquid crystal sheet, top detailed drawing, and bottom instrumented blade

plateau, the flow first experiences a second sharp deceleration indicative of a process of reattachment, followed by a further deceleration at a moderate rate. On the pressure surface, the flow first decelerates at a very slow rate and reaches an almost constant pressure coefficient at $s/s_0=0.3$, and starts to slowly accelerate until the trailing edge has been reached. Unlike the suction surface, the pressure surface boundary layer does not encounter any adverse positive pressure gradient that triggers separation. However, close to the leading edge, a small plateau extending from $s/s_0=0.08$ to 0.16 indicates the existence of a small-size separation bubble that might be attributed to a minor inlet flow incidence angle.

Considering the unsteady case with the reduced frequency $\Omega=1.59$ ($S_R=160$ mm), Fig. 5 exhibits a slight difference in the pressure distribution between the steady and unsteady cases. This deviation is attributed to the momentum deficiency of the main flow due to the drag forces caused by the moving rods. This momentum deficiency leads to a reduction of the total and static pressure.

For Re=110,000, the wakes have a reducing impact on the streamwise extent of the separation plateau. As seen in Fig. 5, the trailing edge of the plateau has shifted from $s/s_0=0.78$ to $s/s_0=0.74$. This shift reduced the streamwise extent of the separation plateau from 23% to 19% of the suction surface length, which is, in this particular case, close to 17% of reduction in streamwise extent of the separation bubble. Increasing the reduced frequency to $\Omega=3.18$, by reducing the rod spacing to $S_R=80$ mm, causes a slight shift of C_p-distribution compared with the $\Omega=1.59$ case. One should bear in mind that pneumatically measured surface pressure distribution represents a time integral of the pressure events only.

Results: Boundary Layer Development, Separation, Reattachment. Boundary layer measurements were performed to identify the streamwise and normal extent, as well as the deformation of the separation zone under unsteady wake flow. The steady-state case serves as the reference configuration. The experimental matrix includes the boundary layer information that covers 11 streamwise locations on the suction surface upstream, within, and downstream of the separation bubble. Measurements were performed for the Reynolds number of 110,000, for four different Tu's of 1.9%, 3.0%, 8.0%, and 13.0%, and three different reduced frequency values of $\Omega=0.0$ ($S_R=\infty$), $\Omega=1.59$ ($S_R=160$ mm), and $\Omega=3.18$ ($S_R=89$ mm). For each case, ensemble- and time-averaged velocity and turbulence fluctuation, turbulence intensity, and unsteady boundary layer parameters are generated. The discussion of the results are centered on the combined effects of the unsteady wakes and freestream turbulence intensity, and their mutual interaction. Thus, only those results that are essential for understanding the basic physics describing the combined effects mentioned above are presented.

Results: Time-Averaged Velocity and Fluctuation Distributions. The effect of wake frequency on time-averaged velocity and turbulence intensity distributions is investigated for Re=110,000 at turbulence intensity levels of Tu=1.9%, 3.0%, 8.0%, and 13%. The distribution of time-averaged velocity and turbulence fluctuations is presented for the above Tu levels. For discussing the heat transfer results, all Tu levels will be presented. Figures 7 and 8 display the velocity and fluctuation distributions at one streamwise position upstream, three positions within, and two positions downstream of the separation bubble using single hot-wire probes. The diagrams include one steady-state data for reference purposes, $\Omega=0.0$ ($S_R=\infty$), and two sets of unsteady data for $\Omega=1.59$ ($S_R=160$ mm) and $\Omega=3.18$ ($S_R=80$ mm).

Effect of Unsteady Wakes. As Figs. 7 and 8 indicate, in the upstream region of the separation bubble at $S/S_0=0.49$, the flow is fully attached. The velocity distributions inside and outside the boundary layer experience slight decreases with increasing the reduced frequency, Fig. 7(*a*). At the same positions, however, the time-averaged fluctuations shown in Fig. 7(*b*) exhibit substantial changes within the boundary layer, as well as outside it. The introduction of the periodic unsteady wakes with highly turbulent vortical cores and subsequent mixing has systematically increased the freestream turbulence intensity level from 1.9% in steady case, to almost 3% for $\Omega=3.18$ ($S_R=80$ mm). This intensity level is obtained by dividing the fluctuation velocity at the edge of the boundary layer (Fig. 7(*b*)) by the velocity at the same normal position (Fig. 7(*a*)). Comparing the unsteady cases $\Omega=1.59$ and 3.18, with the steady reference case $\Omega=0.0$, indicates that, with increasing Ω, the lateral position of the maximum fluctuation shifts away from the wall. This is due to the periodic disturbance of the stable laminar boundary layer upstream of the separation bubble. Convecting downstream, the initially stable laminar boundary layer flow experiences a change in pressure gradient from strongly negative to moderately positive, causing the boundary layer to separate. The inflectional pattern of the velocity distribution at $S/S_0=0.57$ signifies the beginning of a separation bubble that extends up to $S/S_0=0.85$, resulting in a large sized *closed separation bubble*. As opposed to open separation zones that are encountered in compressor blades and diffuser boundary layers, the closed separation bubbles are characterized by a low velocity flow circulation within the bubble, as shown in Fig. 7(*a*). Measurement of boundary layer single-wire probes along the suc-

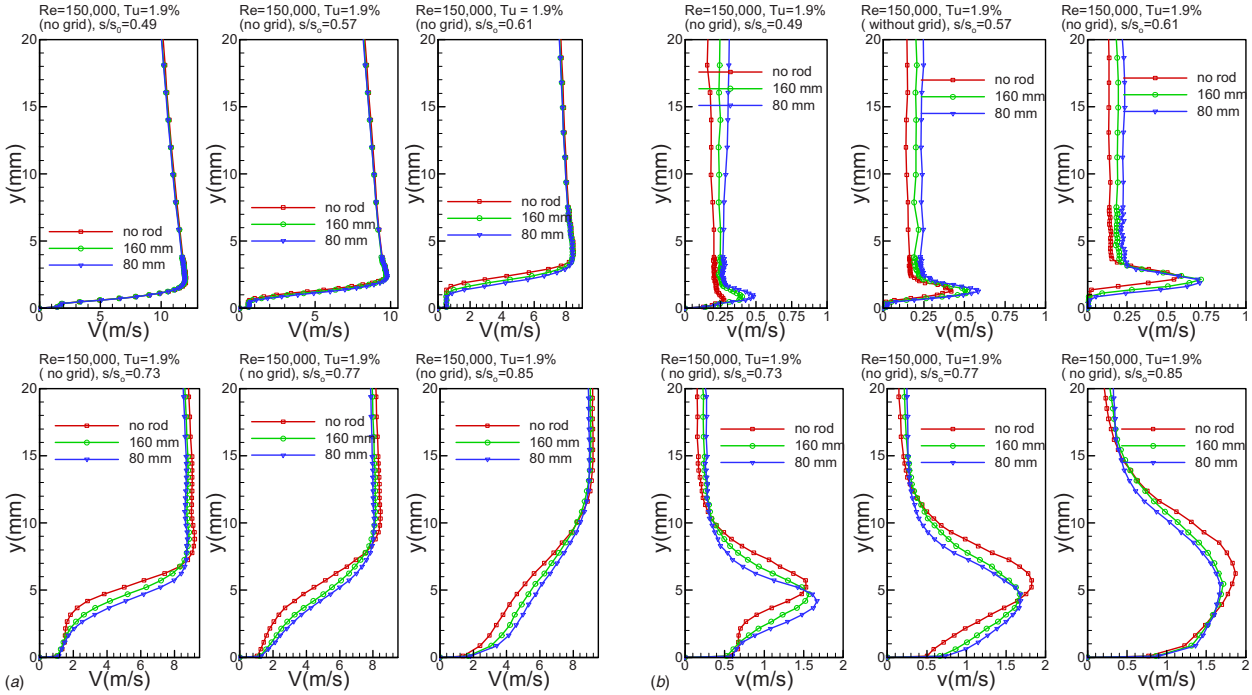

Fig. 7 Distribution of time-averaged velocity (*a*) and turbulence fluctuation rms (*b*) along the suction surface for steady case $\Omega=0$ ($S_R=\infty$) and unsteady cases $\Omega=1.59$ ($S_R=160$ mm) and $\Omega=3.18$ ($S_R=80$ mm) at Re=110,000 and freestream turbulence intensity of 1.9% (without grid)

tion surface of a Pak-B blade by many researchers, among others, Bons et al. [27], Kaszeta and Simon [6], and Roberts and Yaras [28], reveal exactly the same pattern, as shown in Fig. 7(*a*). In contrast, the single-wire measurement in an open separation zone exhibits a pronounced kink at the lateral position, where the reversed flow profile has its zero value. Despite the fact that a single-wire probe does not recognize the flow direction, the appearance of a kink in a separated flow is interpreted as the point of

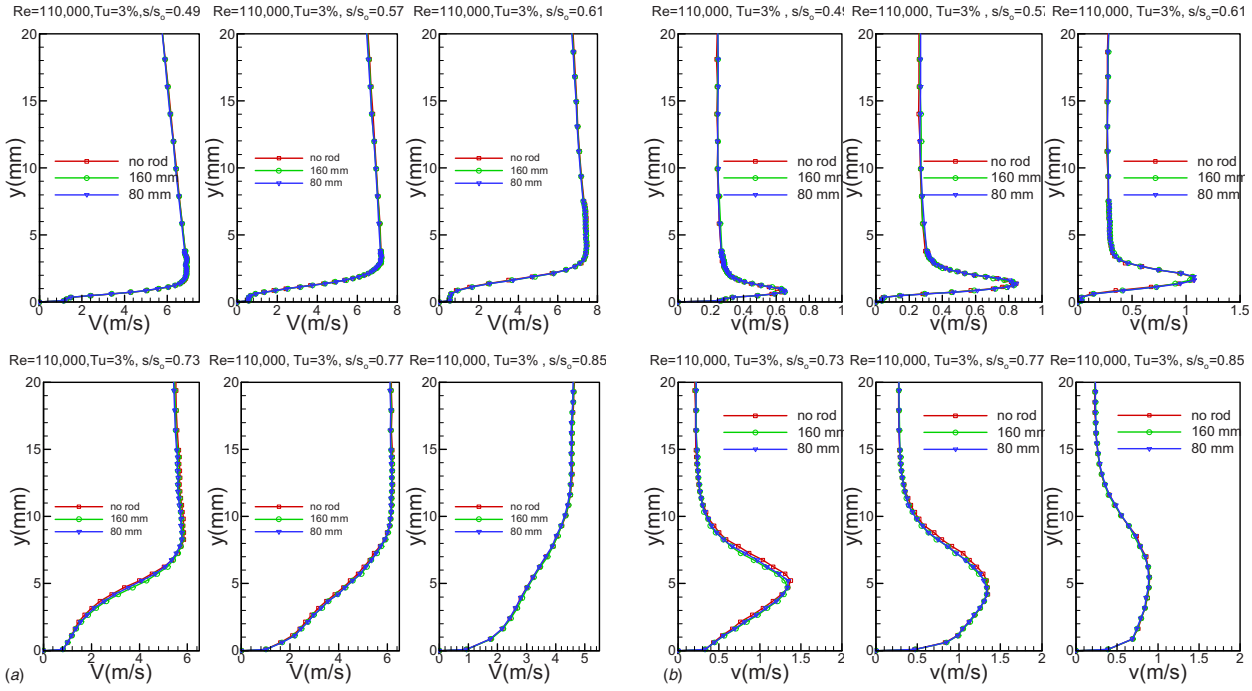

Fig. 8 Distribution of time-averaged velocity (*a*) and turbulence fluctuation rms (*b*) along the suction surface for steady case $\Omega=0$ ($S_R=\infty$) and unsteady cases $\Omega=1.59$ ($S_R=160$ mm) and $\Omega=3.18$ ($S_R=80$ mm) at Re=110,000 and Tu=3% with Grid TG1

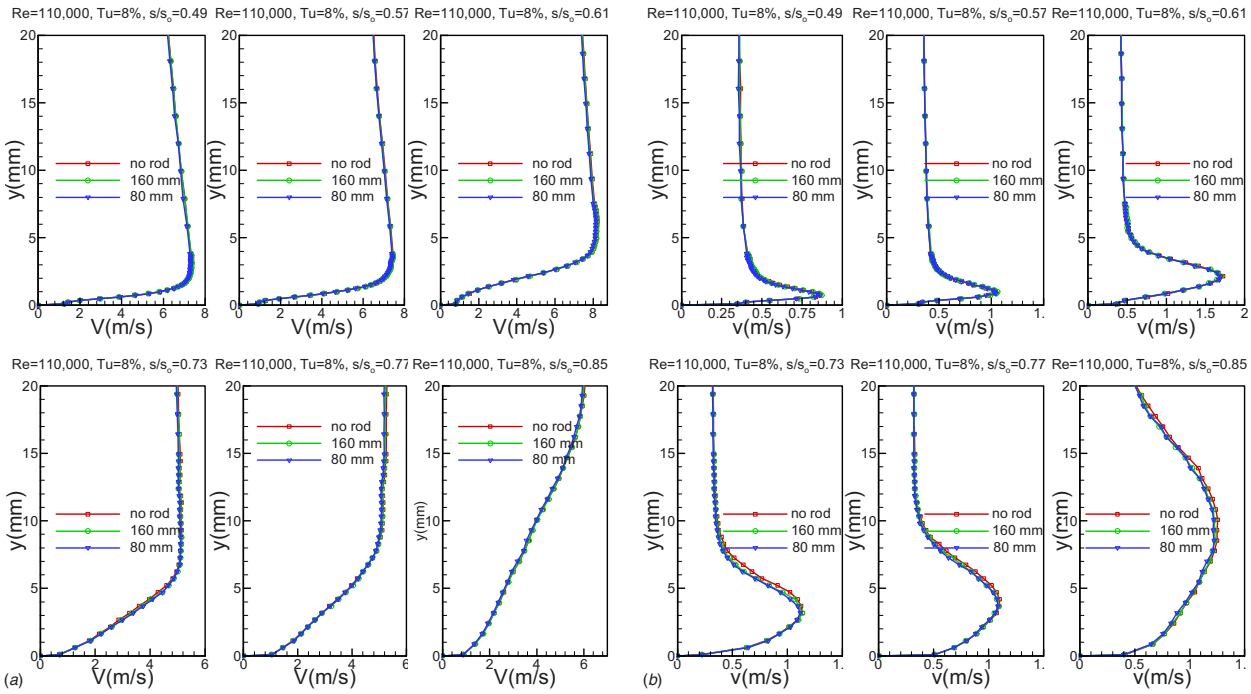

Fig. 9 Distribution of time-averaged velocity (*a*) and turbulence fluctuation rms (*b*) along the suction surface for steady case $\Omega=0$ ($S_R=\infty$) and unsteady cases $\Omega=1.59$ ($S_R=160$ mm) and $\Omega=3.18$ ($S_R=80$ mm) at Re=110,000 and Tu=8% with Grid TG2

reversal with a negative velocity.

The effect of unsteady wake frequency on boundary layer separation is distinctly illustrated in Fig. 7(*a*) at $S/S_0=0.61$, 0.73, and 0.77. While the steady flow case (no rod, $\Omega=0.0$) is fully separated, the impingement of wakes with $\Omega=1.59$ on the bubble has the tendency to reverse the separation causing a reduction of the separation height. This is due to the exchange of mass, momentum, and energy between the highly turbulent vortical cores of the wakes and the low energetic fluid within the bubble, as shown in Fig. 7(*b*). Increasing the frequency to $\Omega=3.18$ moved the velocity distribution further away from the separation, as seen in Fig. 7(*a*), $S/S_0=0.77$. Passing through the separation regime, the reattached flow still shows the unsteady wake effects on the velocity and fluctuation profiles. The fluctuation profile, Fig. 7(*b*), at $S/S_0=0.85$ depicts a decrease of turbulence fluctuation activities caused by unsteady wakes ($\Omega=1.59$ and 3.18) compared to the steady case ($\Omega=0$, no rod). This decrease is due to the calming phenomenon extensively discussed by several researchers (Refs. [29–32]).

Combined Effects of Unsteady Wakes and Turbulence Intensity. Increasing the turbulence level from 1.9% to 3%, which is produced by the turbulence grid TG1, shows that the time-averaged velocity (Fig. 8(*a*)), as well as the fluctuation distribution (Fig. 8(*b*)), hardly experience any noticeable changes with increasing the reduced frequency from $\Omega=0.0$ to 3.18. This is the first indication that the high frequency turbulence generated by TG1 is about to dictate the boundary layer development from leading edge to trailing edge. While the high frequency stochastic fluctuations of the incoming turbulence seem to overshadow the periodic unsteady wakes and the lateral extent of the separation bubble, they are not capable of completely suppressing the bubble. A similar situation is encountered at higher turbulence intensity levels of 8% produced by Grid TG2, Figs. 9(*a*) and 9(*b*). The time-averaged velocity as well as fluctuation rms do not exhibit effects of unsteady wake impingement on the suction surface throughout. In contrast to the above 3% case, the 8% turbulence intensity case, Fig. 9(*a*), seems to substantially reduce the separation bubble, where an inflection velocity profile at $S/S_0=0.61$ is still visible. An almost complete suppression is accomplished by utilizing the turbulence intensity of 13% that is produced by turbulence grid TG3, Figs. 10(*a*) and 10(*b*). In both turbulence cases of 8% and 13%, the periodic unsteady wakes along with their high turbulence intensity vortical cores seem to be completely submerged in the stochastic high frequency freestream turbulence generated by Grids TG2 and GT3.

Results: Combined Effects of Wake and Turbulence Intensity on Bubble Kinematics. To keep the amount of data presented in this paper to a reasonable size essential for understanding the physics, the ensemble-averaged velocity contours are presented for Tu=1.9 and 8.0, respectively. Thus, the contour plots pertaining to Tu=3.0% and 13% that are very similar to the ones with Tu=8% will not be discussed. The combined effects of the periodic unsteady wakes and high turbulence intensity on the onset and extent of the separation bubble are shown in Figs. 11 and 12 for the Reynolds number of 110,000. These figures display the full extent of the separation bubble and its dynamic behavior under a periodic wake flow impingement at different t/τ. For each particular point S/S_0 on the surface, the unsteady velocity field inside and outside of the boundary layer is traversed in the blade normal direction and ensemble averaged at 100 revolutions of the wake generator. To obtain a contour plot for a particular t/τ, the entire unsteady ensemble-averaged data traversed from leading to trailing edge are stored in a large-size file (of several gigabytes) and sorted for the particular t/τ under investigation. In all cases investigated, the closest physical location from the wall measured with a magnifier was about 0.1 mm.

Variation of Tu at $\Omega=1.59$. Figure 11 with a cascade Tu =1.9% exhibits the reference configuration for $\Omega=1.59$ (S_R =160 mm), where the bubble undergoes periodic contraction and

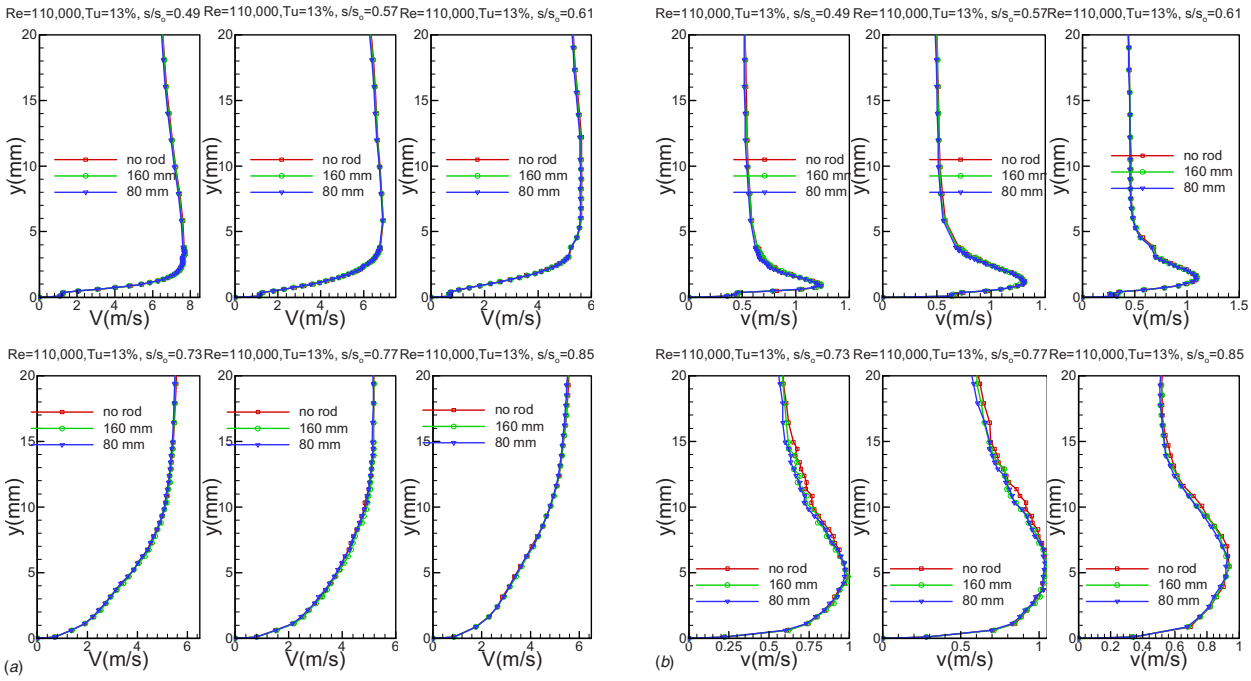

Fig. 10 Distribution of time-averaged velocity (*a*) and turbulence fluctuation rms (*b*) along the suction surface for steady case $\Omega=0$ ($S_R=\infty$) and unsteady cases $\Omega=1.59$ ($S_R=160$ mm) and $\Omega=3.18$ ($S_R=80$ mm) at Re=110,000 and Tu=13% with Grid TG3

expansion as extensively discussed in Ref. [1]. The white areas identify the separation bubble (SB) size and location. During a rod passing period, the wake flow and the separation bubble undergo a sequence of flow states, which are not noticeably different when

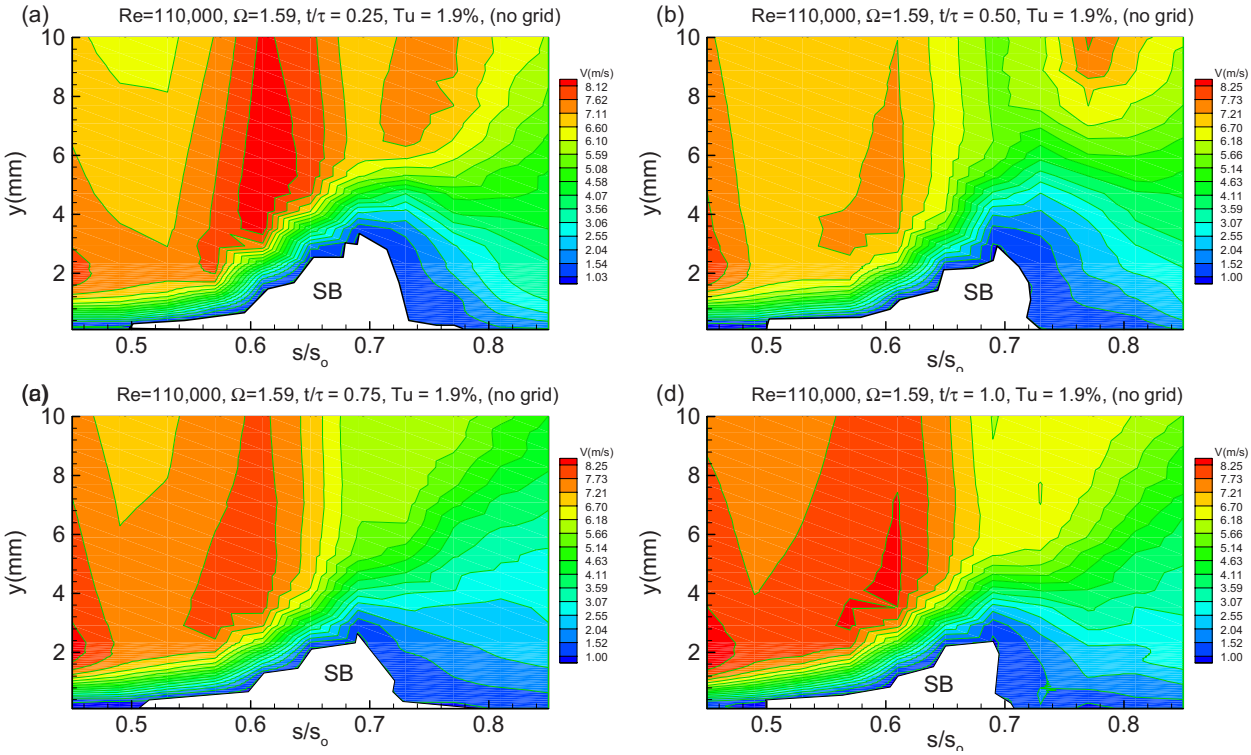

Fig. 11 Ensemble-averaged velocity contours along the suction surface for different s/s_0 with time t/τ as parameter for $\Omega=1.59$ ($S_R=160$ mm) at Re=110,000 and freestream turbulence of 1.9% (without grid). White area identifies the SB location and size.

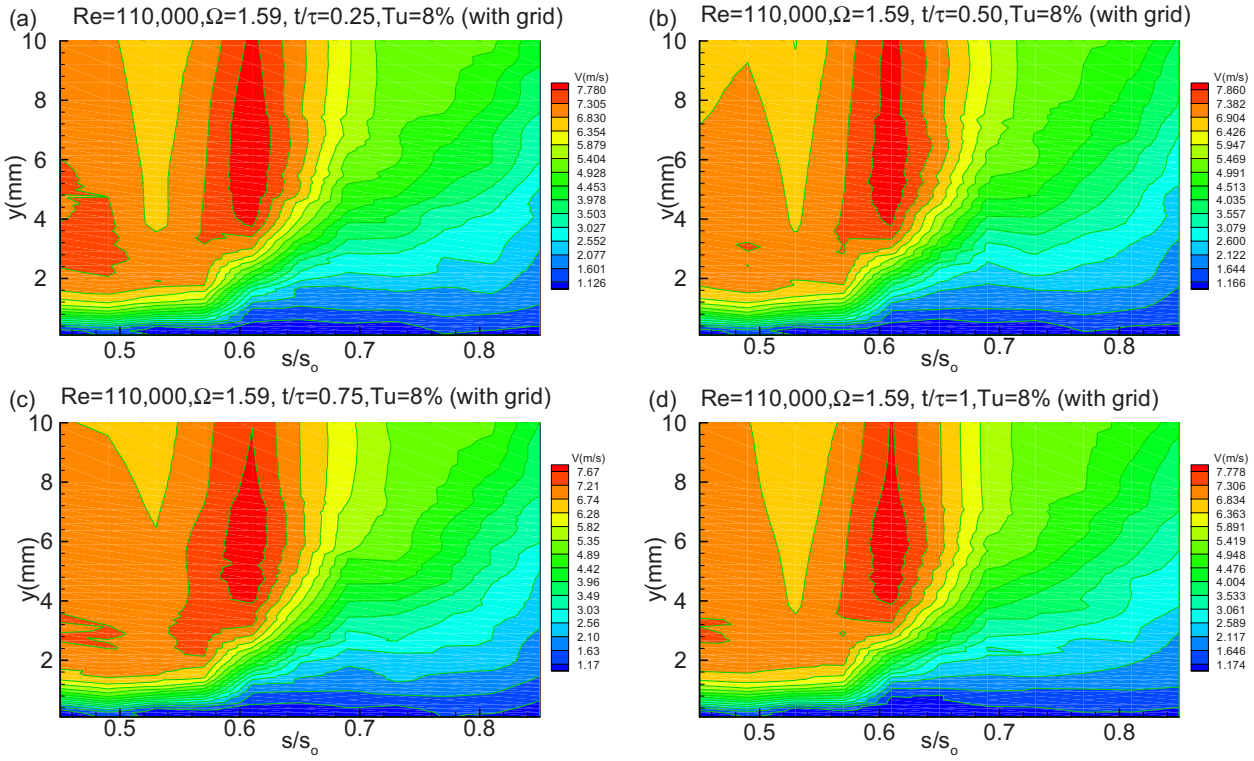

Fig. 12 Ensemble-averaged velocity contours along the suction surface for different s/s_0 with time t/τ as parameter for $\Omega=1.59$ ($S_R=160$ mm) at Re=110,000 and Tu=8% (with grid)

the unsteady data are time averaged. Starting with Re=110,000 and $\Omega=1.59$, Fig. 11(*a*) exhibits the SB in its full size at $t/\tau=0.25$. At this instant of time, the incoming wakes have not reached the separation bubble. The bubble is completely governed by the wake external flow, which is distinguished by red patches traveling above the bubble. At $t/\tau=0.5$, the wake with its highly turbulent vortical core passes over the blade and generates high turbulence kinetic energy. At this point, the wake turbulence penetrates into the bubble causing a strong mass, momentum, and energy exchange between the wake flow and the fluid contained within the bubble. This exchange causes a dynamic suppression and a subsequent contraction of the bubble, as can be recognized by comparing the SB size at $t/\tau=0.5$ with the one at $t/\tau=0.25$. As the wake travels over the bubble, the size of the bubble continues to contract at $t/\tau=0.75$ and reaches its minimum size at $t/\tau=1.0$. At $t/\tau=1$, the full effect of the wake on the boundary layer can be seen before another wake appears and the bubble moves back to the original position.

Increasing the turbulence level to 3%, 8%, and 13% by successively attaching the turbulence grids TG1, TG2, and TG3 (detail specifications are listed in Tables 1 and 2) and keeping the same reduced frequency of $\Omega=1.59$ has significantly reduced the lateral extent of the bubble. The case with Tu=8% is an appropriate representative of dynamic changes among the turbulence levels mentioned above. As shown in Fig. 12, the instance of the wake traveling over the separation bubble, which is clearly visible in Fig. 12, has diminished almost entirely. Increasing the turbulence intensity to 8% (Figs. 12(*a*)–12(*d*)) and 13%, respectively, has caused the bubble height to further reduce (the corresponding figure for 13% is very similar to the one with 8%). Although the higher turbulence level has, to a great extent, suppressed the separation bubble as Fig. 12 clearly shows, it was not able to completely eliminate it. There is still a small core of separation bubble remaining. Its existence is attributed to the stability of the separation bubble at the present Re number level of 110,000.

Variation of Tu at $\Omega=3.18$. Figures 13 and 14 represent the dynamic behavior of the separation bubble at Tu=1.9% and 8%, respectively, but at a higher reduced frequency of $\Omega=3.18$. Similar to Fig. 11, the case with the Tu=1.9% presented in Figs. 13(*a*)–13(*d*) exhibits the reference configuration for $\Omega=3.18$ ($S_R=80$ mm), where the bubble undergoes periodic contraction and expansion. The temporal sequence of events is identical with the case discussed in Fig. 11, making a detailed discussion unnecessary. In contrast to the events described in Fig. 11, the increased wake frequency in the reference configuration, Fig. 13, is associated with higher mixing and, thus, higher turbulence intensity that causes a more pronounced contraction and expansion of the bubble. This can be seen by comparing the SB size (deep blue) in Figs. 13(*a*)–13(*d*) with the ones in Fig. 11 (white area marked with SB). While the streamwise extension of the bubble along the suction surface remains unchanged, its size experiences a shrinking deformation.

As in case with $\Omega=1.59$, applying turbulence levels of 3%, 8%, and 13% by successively utilizing the turbulence grids TG1, TG2, and TG3 and keeping the same reduced frequency of $\Omega=3.18$ has significantly reduced the lateral extent of the bubble. Again, as a representative example, the case with Tu=8% is presented in Figs. 14(*a*)–14(*d*), which reveals similar behavior as discussed in Fig. 12. Further increasing the turbulence intensity to 13% has caused the bubble height to further reduce. Although the higher turbulence level has, to a great extent, suppressed the separation bubble, it was not able to completely eliminate it. There is still a small core of separation bubble remaining. Its existence is attributed to the stability of the separation bubble at the present Re-number level of 110,000.

Quantifying the Combined Effects on Aerodynamics. Figures 11–14 show the combined effects of turbulence intensity and unsteady wakes on the onset and extent of the separation bubble. Detailed information relative to the propagation of the wake and

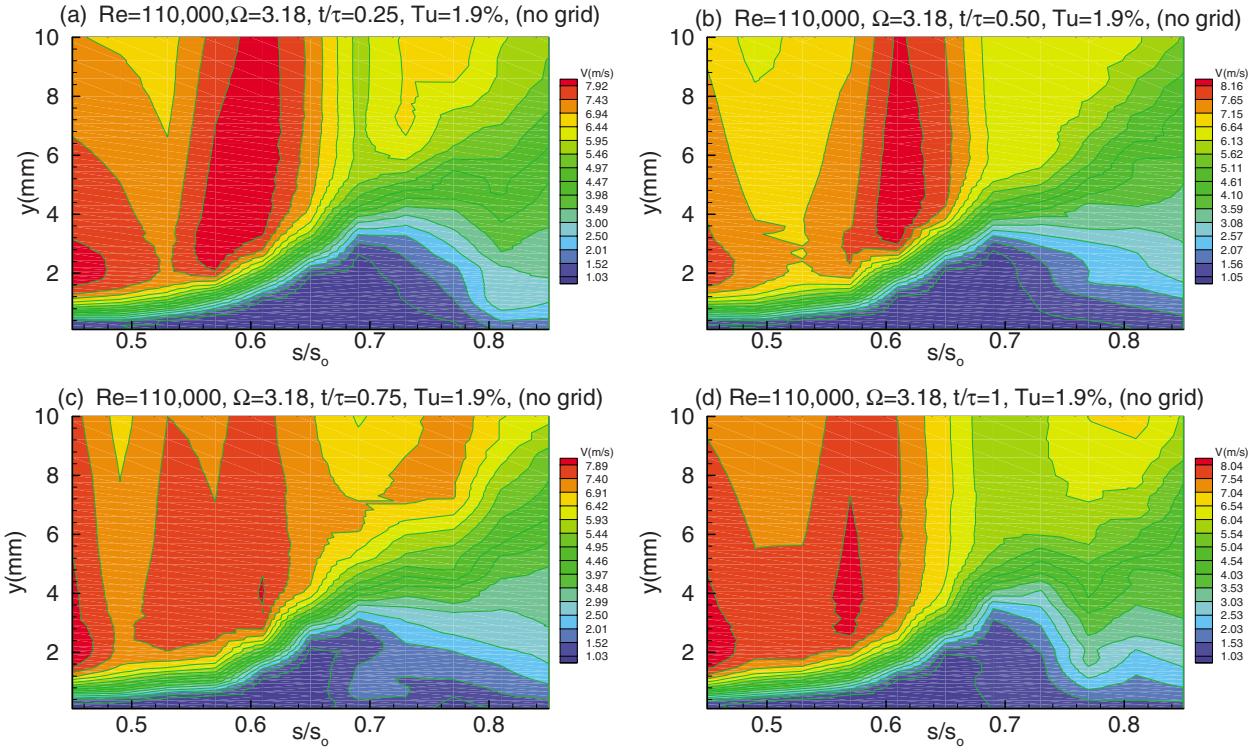

Fig. 13 Ensemble-averaged velocity contours along the suction surface for different s/s_0 with time t/τ as parameter for $\Omega=3.18$ ($S_R=80$ mm) at Re=110,000 and freestream turbulence of 1.9% (without grid)

the turbulence into the separation bubble is provided by Figs. 15(*a*)–15(*d*), where the time dependent ensemble-averaged velocities and fluctuations are plotted for Re=110,000 at a constant location $y=3.36$ mm inside the bubble for different intensities ranging from 1.9% to 13%. As Fig. 15(*a*) depicts, the wake has penetrated into the separation bubble, where its high turbulence

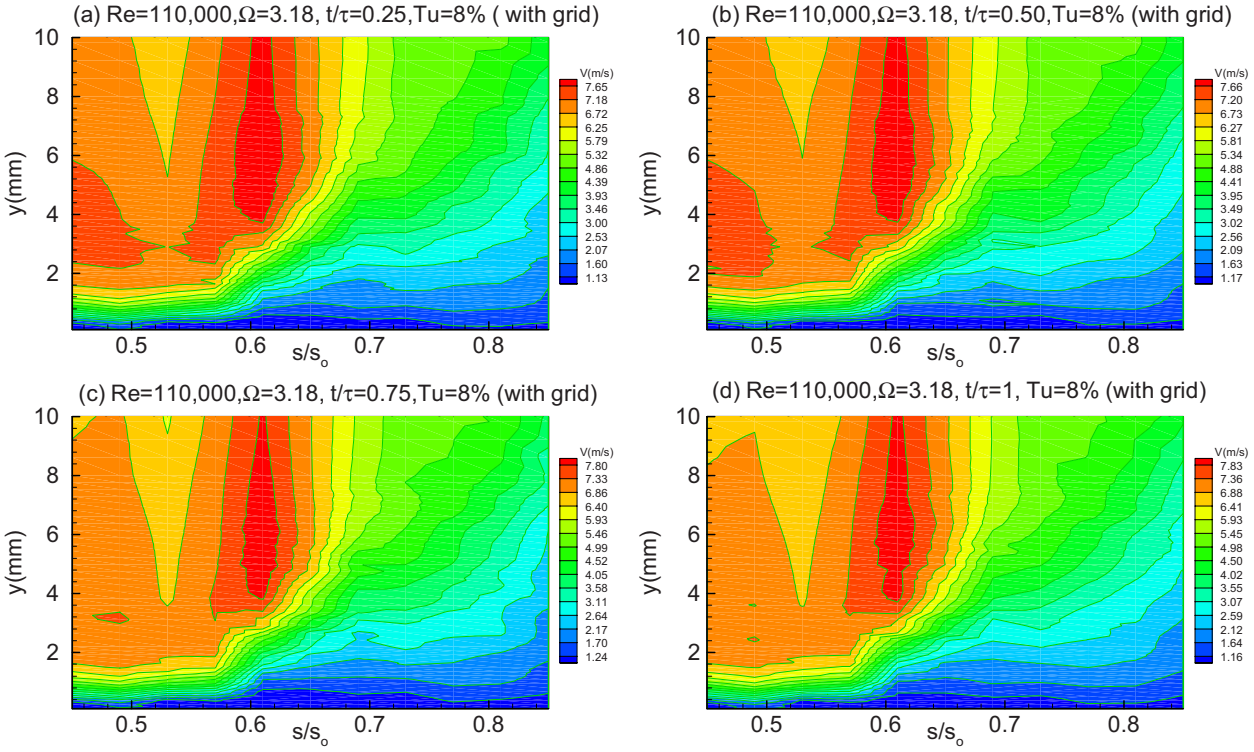

Fig. 14 Ensemble-averaged velocity contours along the suction surface for different s/s_0 with time t/τ as parameter for $\Omega=3.18$ ($S_R=80$ mm) at Re=110,000 and freestream turbulence of 8.0% (with Grid TG2)

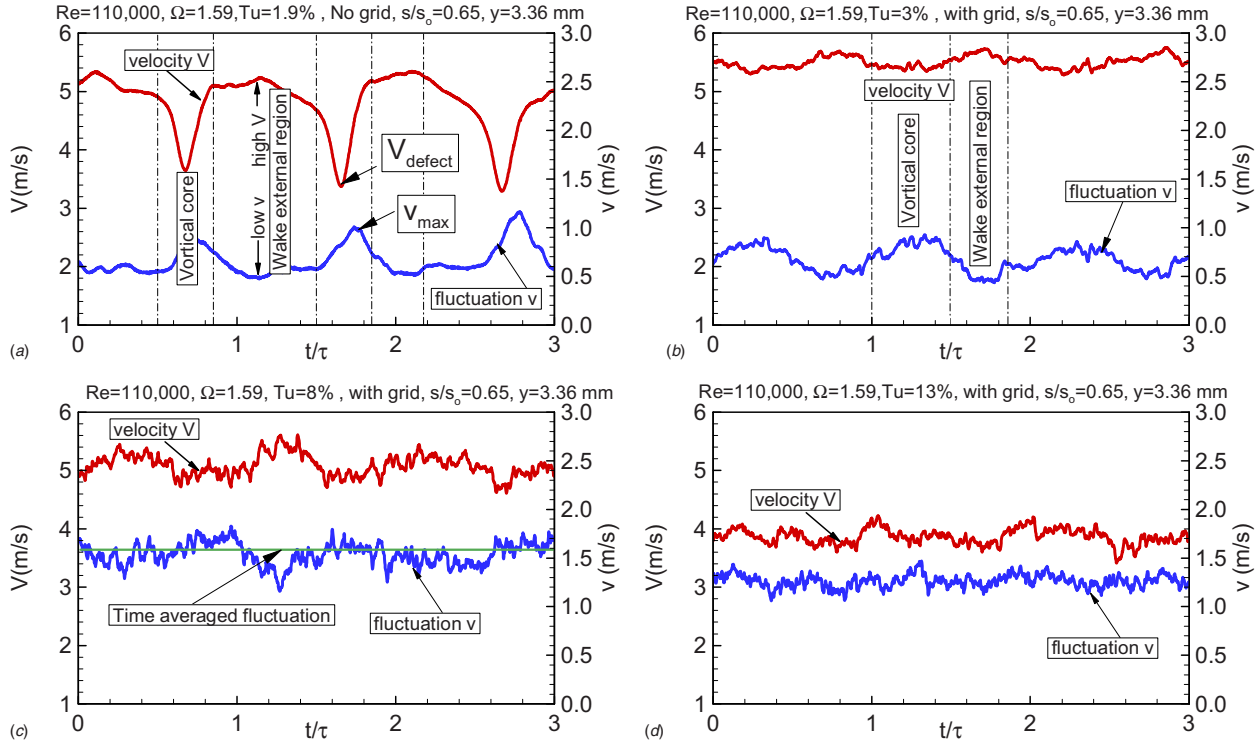

Fig. 15 ((*a*)–(*d*)) Time dependent ensemble-averaged velocities and fluctuations for Re=110,000 at a constant location s/s_0=0.65 mm inside the bubble for different inlet turbulence intensities ranging from 1.9% to 13%

vortical core and its external region are clearly visible. Lowest turbulence fluctuations occur outside the vortical core, whereas the highest is found within the wake velocity defect. The wake defect is characterized by the lowest velocity V_{min} and the highest turbulence fluctuation v_{max}, as shown in Fig. 15(*a*). The time interval for the wake passing starts at t/τ=0.5 and ends at t/τ =0.85 and repeats periodically (t/τ=1.5 and ends at t/τ=1.85, etc.).

Increasing Tu to 3%, Fig. 15(*b*), reduces the velocity amplitude of the periodic inlet flow and its turbulence fluctuations. Despite a significant decay in amplitude, the periodic nature of the impinging wake flow is unmistakably visible. Further increase of Tu to 8%, Fig. 15(*c*), shows that the footprint of a periodic unsteady inlet flow is still visible; however, the deterministic periodicity of the wake flow is being subject to the stochastic nature caused by the high turbulence intensity. Further increase of turbulence to Tu=13% causes a degradation of the deterministic wake ensemble-averaged pattern to a fully stochastic one. Comparing Figs. 15(*a*) and 15(*c*) leads to the following conclusion: The periodic unsteady wake flow definitely determines the separation dynamics as long as the level of the time-averaged turbulence fluctuations is below the maximum level of the wake fluctuation v_{max}, shown in Fig. 15(*a*). In our case, this apparently takes place at a turbulence level between 3% and 8%. Increasing the inlet turbulence level above v_{max} causes the wake periodicity to partially or totally submerge in the freestream turbulence, thus, downgrading into stochastic fluctuation, as shown in Figs. 15(*c*) and 15(*d*). In this case, the dynamic behavior of the separation bubble is governed by the flow turbulence that is responsible for complete suppression of the separation bubble. One of the striking features this study reveals is that the separation bubble has not disappeared completely despite the high turbulence intensity and the significant reduction of its size, which is reduced to a tiny bubble. At this point, the role of the stability of the laminar boundary layer becomes apparent, which is determined by the Reynolds number.

Results: Heat Transfer. As in the aerodynamic section discussed above, the steady-state case serves as the reference configuration. The matrix for heat transfer experiments includes (a) Reynolds number variations of Re=110,000, 150,000, and 250,000, (b) freestream turbulence variations of Tu=1.9%, 3.0%, 8.0%, and 13.0%, and (c) reduced frequency variations of Ω =0.0 (S_R=∞), Ω=1.59 (S_R=160 mm), and Ω=3.18 (S_R =89 mm). In presenting the heat transfer results, we prefer to use the plain heat transfer coefficient rather than the Nusselt number, which uses thermal conductivity and a constant characteristic length, such as the blade chord, to form the Nusselt number. Three sets of plots are generated to extract the effect of each individual parameter on heat transfer coefficients. Each figure includes the pressure as well as the suction surface heat transfer coefficient h (HTC) as a function of dimensionless surface length, s/s_0. While the boundary layer behavior (according to the equation of motion) is completely decoupled from thermal boundary layer behavior, the latter is through the equation of energy directly coupled with the boundary layer aerodynamics. Thus, a detailed description of heat transfer behavior is directly coupled with the aerodynamic results.

Generic Interpretation of Separation Bubble HTC Results. To present a generic interpretation of heat transfer results within the separation bubble, we consider Fig. 16, which includes the pressure distribution (a), the velocity contour (b), the fluctuation contour (c), and a representative HTC distribution for steady-state case (d). Figures 16(*a*)–16(*d*) deliver a coherent picture of SB static pressure, velocity and turbulence distribution, and heat transfer behavior. Figure 16(*a*) depicts four distinct intervals that mark different events along the suction surface. An initially strong negative pressure gradient starting from the leading edge preserves the stable laminar boundary layer until the pressure minimum at S/S_0=0.494 has been reached. The laminar boundary layer characterized by the lack of significant lateral turbulence

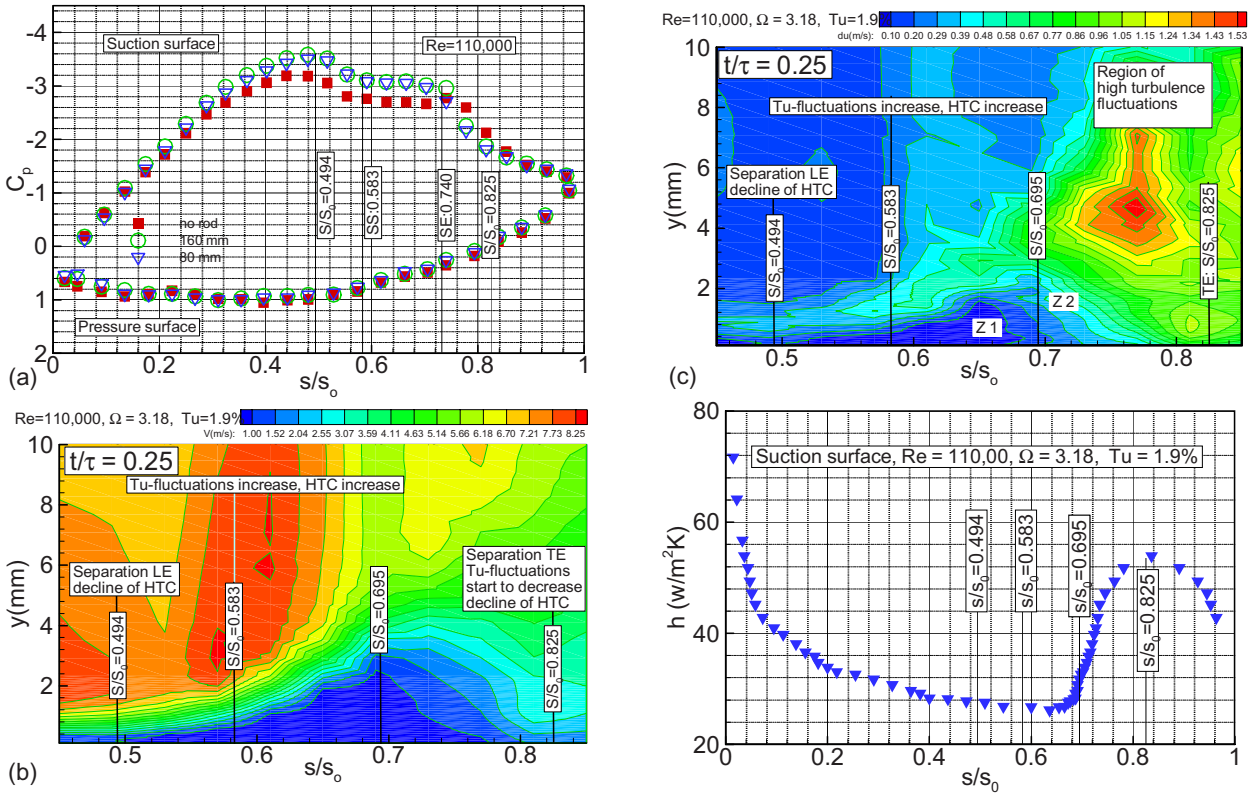

Fig. 16 Composite picture of interaction between pressure gradient, velocity, turbulence fluctuation, and heat transfer

fluctuations[2] is not capable of transferring mass, momentum, and energy to the blade surface, resulting in a steep drop of HTC from leading edge to $S/S_0=0.494$, where the pressure gradient changes the sign, Figs. 16(*a*)–16(*d*). The HTC drops further at a larger slope and assumes a minimum at the start of the separation bubble $S/S_0=0.583$. Passing through the pressure minimum, the initially stable laminar (nonturbulent) boundary layer encounters a change in pressure gradient from negative to positive, causing it to become unstable and to separate at $S/S_0=0.583$. This point marks the leading edge of the separation bubble, Figs. 16(*a*)–16(*d*). From this point on, the turbulence activities outside the bubble continuously increase, causing the heat transfer coefficient to rise.

Further increase of HTC beyond $S/S_0=0.583$ occurs at a steep rate until the separation trailing edge at $S/S_0=0.825$ has been reached. The steep increase of HTC within the separation bubble is due to an increased longitudinal and lateral turbulence fluctuation caused by the flow circulation within the bubble. As shown in Fig. 16(*c*), the extent of low turbulence envelope is much smaller than the bubble size itself, Fig. 16(*b*). This implies that the turbulence activity within the bubble is nonuniform and can be subdivided into two distinct zones, Z1 with lower fluctuation activities that occupies the bubble from the leading edge up to the location, where the bubble lateral extent reaches its maximum height, $S/S_0=0.695$ and Z2 the higher fluctuation zone beyond the maximum height, Fig. 16(*c*).

Steady Inlet Flow Condition, Variation of Re Number at Constant Tu. Starting with the steady-state case, Fig. 17, the heat transfer coefficient is plotted along the blade surface, where the Reynolds number assumes values of Re=110,000, 150,000, and 250,000. Figure 17(*a*) depicts the HTC distributions along the suction ($S/S_0>0$) and pressure surface ($S/S_0<0$) for the reference configuration, which has the lowest turbulence intensity (Tu=1.9%, no grid). Figure 17(*b*) represents the HTC distribution for steady flow with the highest Tu=13% (TG2 grid). Figure 17(*a*) shows a systematic increase of HTC by increasing the Reynolds number. On the suction side, the position $S/S_0=0.494$ for all three Re numbers indicates the location of the minimum pressure and $S/S_0=0.583$, the start of the separation bubble. The course of HTC follows the generic discussion presented above making additional discussion unnecessary.

On the pressure surface, ($s/S_0<0$), Fig. 17(*a*) reveals a qualitatively different picture. At Re=110,000 and for Tu=1.9, the HTC first drops sharply due to the governing laminar (nonturbulent) boundary layer and reaches a minimum at $S/S_0=-0.155$ that signifies the start of the transition region. During the transition process, characterized by intermittent changes of the flow pattern from laminar to turbulent and vice versa, the random fluctuations in longitudinal as well as lateral directions continuously increase leading to a lateral exchange of mass, momentum, and energy with the boundary layer, thus, increasing the HTC. For Re =110,000, the transition process seems to complete at $S/S_0\approx -0.34$. By passing the transition region, a process of relaminarization takes place, where the growth of turbulence fluctuation first decreases to arrive at a second minimum. The streamwise position of this minimum coincides with the start of the negative pressure gradient (NPG), Fig. 17(*a*). The process of transition followed by relaminarization and the distribution of the heat transfer coefficient along the suction and pressure surface of a turbine blade were reported, among others, by Giel et al. [33,34] and Arts et al. [35]. The prediction of boundary layer transition, relaminarization, and the heat transfer process along both surfaces of gas turbine blades was the subject of a comprehensive study by Boyle et al. [36]. Using the experimental results from Refs. [33,34], Boyle et al. [36] were able to numerically predict the transition as well

[2]Strictly speaking, there is no laminar flow within a turbine component. Comprehensive hot-wire measurements by many researchers have repeatedly shown that there are always random fluctuations associated with the velocity distribution. In turbine flow environment, the term "nonturbulent" may suitably replace the term "laminar."

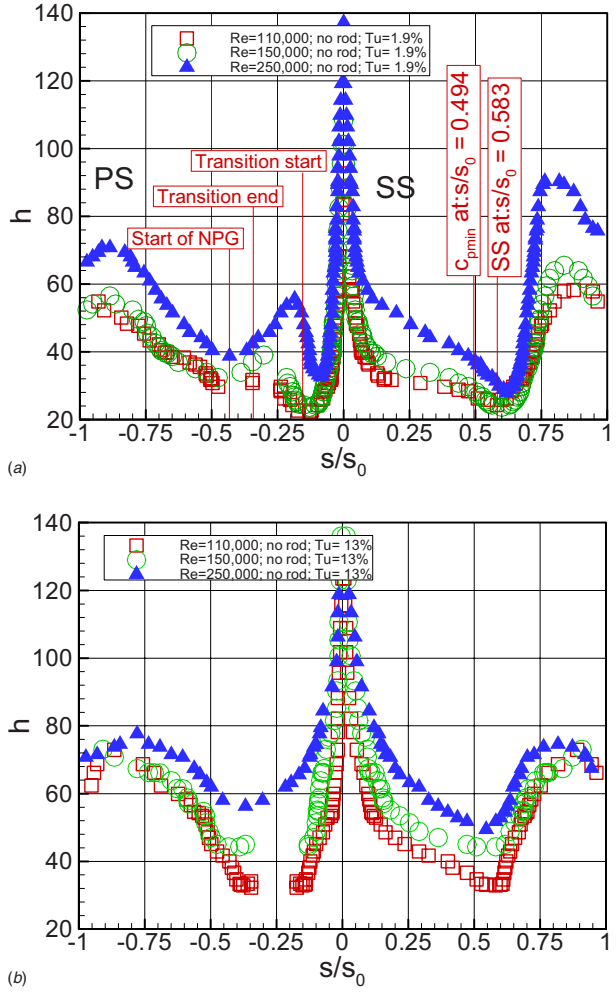

Fig. 17 Effect of Reynolds number on heat transfer coefficient, (*a*) Tu=1.9%, (*b*) Tu=13.0% for steady inlet flow condition

as the laminarization process.

Increasing the Re number shifts the transition start upstream and systematically increases the HTC. A pronounced increase in HTC is observed at higher Reynolds numbers as Fig. 17(*a*) shows. The start and end of transition and relaminarization is particularly pronounced for Re=250,000, which has the shortest transition length. While the transition start and end for all three Reynolds numbers are different, the end of relaminarization is the same due to the same start of NPG.

Subsequent installation of turbulence generator screens GT1, TG2, and TG3 has increased the freestream turbulence intensity to Tu=3.0%, 8%, and 13%. As a consequence, a pronounced exchange of mass, momentum, and energy between the outside boundary layer, flow, and the blade surface boundary layer has taken place resulting in a substantial increase in HTC. For both the suction and pressure surfaces, a systematic enhancement of HTC was achieved for all Tu cases. The HTC pattern shown in Fig. 17(*b*) with the highest turbulence intensity Tu=13% is a representative for the other two Tu cases of 3% and 8%. While on the suction surface the start of the separation bubble has not noticeably altered, on the pressure surface the transition length has substantially decreased. Here, as in Fig. 17(*a*), a systematic increase of the HTC with increasing the Reynolds number is unmistakably discernible. At all three Re cases, the heat transfer coefficient first drops sharply due to the governing nonturbulent boundary layer and reaches a minimum close to $S/S_0=-0.25$ followed by a large transitional zone that extends up to $S/S_0=-0.75$. It is apparent that the higher turbulence activities caused by a freestream turbulence of 13% washed out the transition portion completely. As Fig. 17(*b*) indicates, for Re=110,000 and 150,000 close to $S/S_0=-0.25$, few points are missing. This was due to the difficulty of locating the exact position of the liquid crystal yellow band just for this particular case.

Periodic Unsteady Inlet Flow Condition, Variation of Re Number at Constant Tu. Periodic unsteady inlet flow conditions for two different reduced frequencies are established by successively attaching rods with spacings, $S_R=160$ mm and $S_R=80$ mm, with the corresponding reduced frequencies of $\Omega=1.59$ and 3.18, Table 1. Keeping the reduced frequency and the turbulence intensity the same, heat transfer measurements were carried out for Re=110,000, 150,000, and 250,000.

HTC Results for $\Omega=1.59$. Figures 18(*a*)–18(*d*) show the HTC distribution along the suction ($s/S_0>0$) and the pressure ($s/S_0<0$) surface for a reduced frequency $\Omega=1.59$ ($S_R=160$ mm) and Tu=1.9, where the Reynolds number assumes values of Re=100,000, 150,000, and 250,000. For Re=100,000 and 150,000, Fig. 18(*a*), the HTC distributions exhibit a systematic change for all three Re cases but a substantial increase for Re=250,000. This is due to the fact that of the three Reynolds cases, the one with Re=250,000 was able to influence the laminar portion of the boundary layer and, thus, the heat HTC behavior. Comparing the periodic unsteady wake flow case in Fig. 18(*a*) with the steady flow case shown in Fig. 17(*a*) indicates only a marginal change in HTC. This is due to the fact that wakes generated by the translating rods are far apart from each other. Consequently, the turbulence activities of their vortical cores are not mutually interacting and, therefore, they are unable to substantially affect the total turbulence picture of the flow leading to almost the same HTC picture, as in Fig. 17(*a*).

Keeping the reduced frequency $\Omega=1.59$ ($S_R=160$ mm), Fig. 18(*b*), and increasing the turbulence intensity to Tu=3% have brought only a minor increase in HTC for the suction surface compared to Fig. 18(*a*). On the pressure surface, however, a major increase in HTC is clearly visible, where the transition length almost completely disappeared. In this case, it seems that the wake unsteadiness is about to submerge in the stochastic high frequency freestream turbulence generated by Grid TG1. Further increasing the turbulence intensity by subsequently attaching Grids TG2 and TG3 (grid specifications are listed in Tables 1 and 2) has not brought a substantial change compared to the case shown in Fig. 18(*b*). Results are presented in Figs. 18(*c*) and 18(*d*), where a systematic shift of HTC toward slightly higher values is shown for Re=110,000 and 150,000 and substantially higher values for Re=250,000.

HTC Results for $\Omega=3.18$. Figures 19(*a*)–19(*d*) present the HTC distribution on suction and pressure surface at Re=100,000, 150,000, and 250,000, Tu=1.9%, 3%, 8%, and 13% for a reduced frequency of $\Omega=3.18$ ($S_R=80$ mm). The HTC patterns follow closely those shown in Figs. 18(*a*)–18(*d*) with a minor increase in HTC. Increasing the reduced frequency by reducing the rod spacing from 160 mm to 80 mm, two objectives were targeted: (a) doubling the unsteady frequency and (b) reducing the distance between the wake by 50%, thereby causing an active mutual interaction and mixing of the wakes. The compounded effects of (a) and (b) superimposes additional turbulence fluctuations on the freestream turbulence raising the overall fluctuation level, thus, resulting in an increased HTC. On the suction surface, the HTC distributions pertaining to Re=110,000 and 150,000 almost coincide, while the larger Re=250,000 reveals substantially higher values. This implies that, keeping Ω and Tu constant, for the Reynolds range experimented, a substantial HTC can be achieved by substantially increasing the Re number. On the pressure surface, $s/s_0<0$, Fig. 19(*a*) reveals a qualitatively similar distribution as discussed in Figs. 17(*a*) and 18(*a*). Compared to Fig.

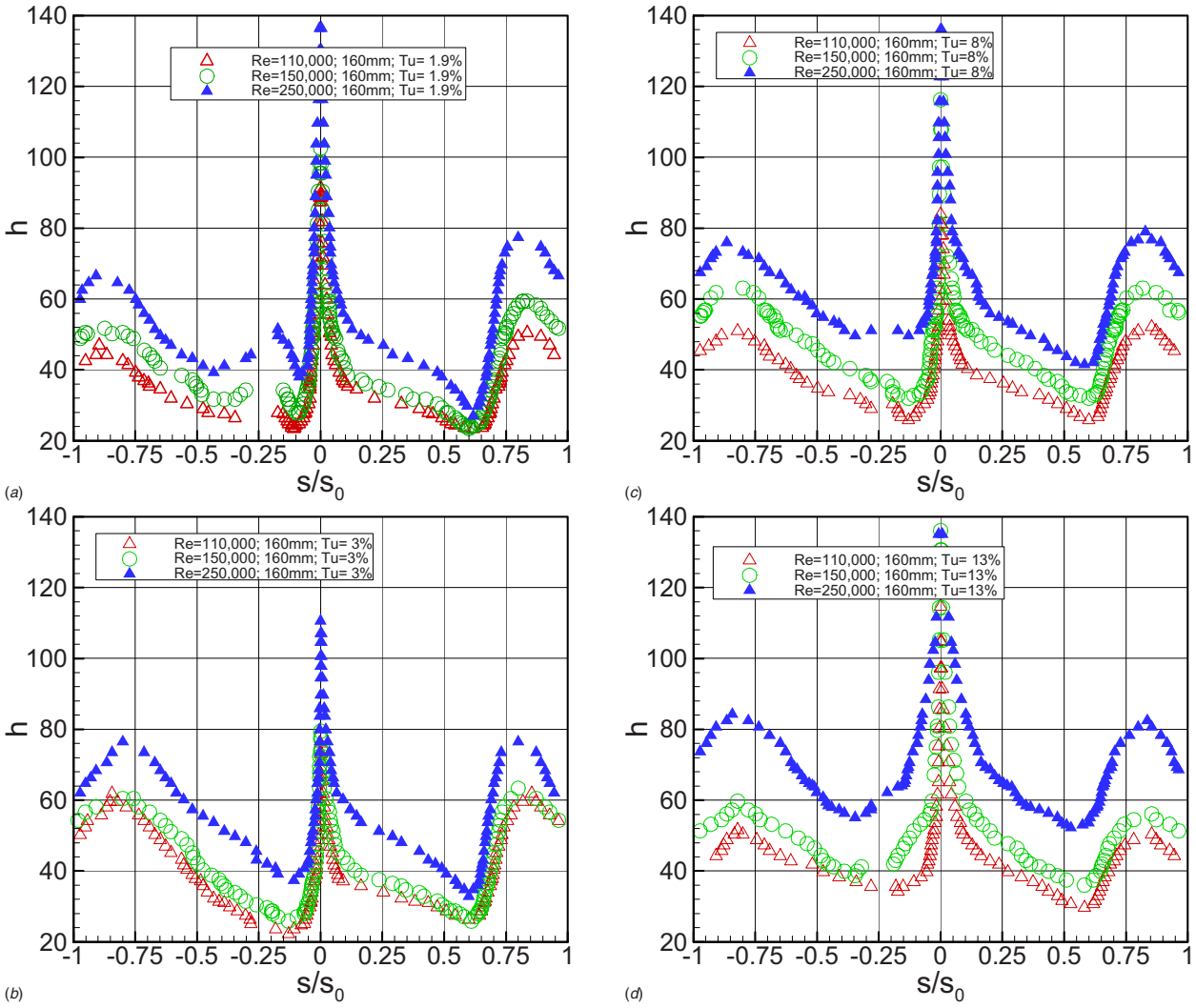

Fig. 18 Effect of Reynolds number on heat transfer coefficient, (*a*) Tu=1.9%, (*b*) Tu=3.0%, (*c*) Tu=8%, and (*d*) Tu=13% for unsteady inlet flow condition with $\Omega=\Omega=1.59$ (S_R=160 mm)

18(*a*), the transition length for all three Re cases seems to have been reduced. Keeping the reduced frequency $\Omega=3.18$ (S_R =80 mm), and successively increasing the turbulence intensity to Tu=3%, 8%, and 13%, Figs. 19(*b*)–19(*d*) have moderately increased the HTC for the suction surface compared to Fig. 19(*a*). As indicated previously, in all three Tu cases, it seems that the wake unsteadiness has submerged into the stochastic high frequency freestream turbulence generated by Grids TG2 and TG3. On the pressure surface, a major increase in HTC is clearly visible for Re=250,000, where the transition length almost completely disappears.

Effect of Unsteady Wake Frequency Ω on Heat Transfer Coefficient. The effects of unsteady wake frequency on HTC are implicitly contained in Figs. 18 and 19. However, from an aerodynamics heat transfer interaction point of view, it is of interest to present it explicitly. Figure 20 presents the results for Re =110,000 and 250,000 at constant Tu, where the reduced frequency Ω is varied from $\Omega=0.0$ ($S_R=\infty$) to $\Omega=3.18$ (S_R =80 mm). The case with Re=150,000 is very much similar to the case Re=110,000, which makes its presentation unnecessary. Figure 20(*a*) presents the HTC distribution for Re=110,000 and Tu =1.9, with the reduced frequency as a parameter. On the suction surface, only marginal changes in HTC are depicted. On the pressure surface, however, noticeable changes are observed within the transitional region, where the transition start and end moves upstream. Enlarging the pressure surface s/s_0-range of Fig. 20(*a*) from 0 to −0.5 and considering the no rod case ($\Omega=0.0$) denoted by the symbol △ as the reference case with the transition start at $s/s_0=-0.142$, the case with $\Omega=1.59$ ($S_R=160$ mm, symbol ○) has moved the transition start to $s/s_0=-0.107$. The subsequent increase of reduced frequency to $\Omega=3.18$ ($S_R=80$ mm, symbol ▼) has further moved the transition start closer to the leading edge at $s/s_0=-0.08$. The shift of the transition end reveals similar behavior. Likewise, considering the no rod case with the transition end at $s/s_0=-0.35$, increasing the reduced frequency to $\Omega=1.59$ and 3.18 moves the transition end upstream to $s/s_0=-0.175$ and $s/s_0=-0.151$, respectively.

Increasing the turbulence intensity to Tu=3%, Fig. 20(*b*), initiates the process of submerging the wake into the freestream turbulence. Little changes are observed on the suction surface. On the pressure surface, however, the first transition region is washed out due to the combined effects of turbulence intensity and unsteadiness. This is in accord with the results presented in Fig. 17(*b*). A seemingly different HTC pattern emerges when the turbulence intensity is increased. As shown in Figs. 20(*c*) and 20(*d*) with Tu=8% and 13%, respectively, the HTC distributions for both unsteady cases with $\Omega=1.59$ and 3.18 are almost identical.

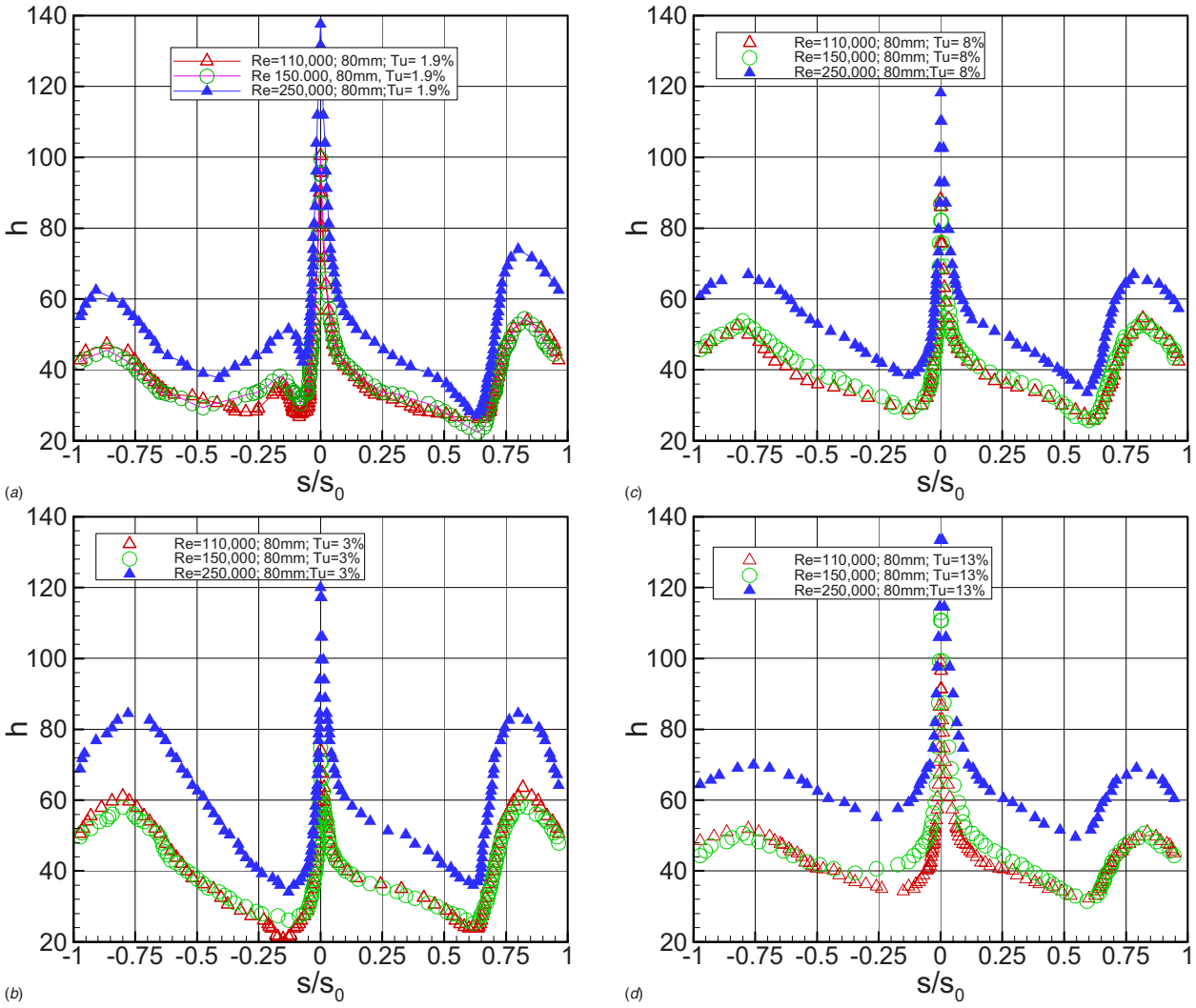

Fig. 19 Effect of Reynolds number on heat transfer coefficient, (*a*) Tu=1.9%, (*b*) Tu=3.0%, (*c*) Tu=8%, and (*d*) Tu=13% for unsteady inlet flow condition with Ω=3.18 (S_R=80.0 mm)

The steady-state case (no rod), however, shows increasingly higher HTC values towards the second half of the blade. This, at first glance, appears to be incompatible with the widespread notion that the unsteady wakes generally contribute to intensifying the turbulence activities, thus increasing the HTC. However, expediting the turbulence fluctuations for steady and unsteady cases shows that the calming effect discussed in the aerodynamics section is responsible for calming the turbulence activities, thus reducing the HTC. Similar HTC-distribution patterns are revealed for Re=250,000.

Conclusions

A detailed aerodynamic and heat transfer experimental study on the behavior of the separation bubble along the suction surface of a highly loaded LPT blade under combined effects of periodic unsteady wake flows and freestream turbulence intensity was presented. Varying the turbulence intensity levels, one steady and two different unsteady inlet wake flow conditions with the corresponding passing frequencies, the wake velocity and the turbulence intensities were investigated by utilizing a large-scale, subsonic research facility. Periodic unsteady wake flow was established by translational motion of two parallel moving timing belts on which cylindrical rods are attached. While for the aerodynamic study a representative Reynolds number of Re=110,000 was applied, for heat transfer investigations the Reynold number was varied as Re=110,000, 150,000, and 250,000. In both aerodynamics and heat transfer investigations, turbulence intensities of Tu=1.9%, 3.0%, 8.0%, 13% and unsteady parameters of Ω=0.0, 1.59, and 3.18 were applied.

Aerodynamics. A detailed unsteady boundary layer measurement identified the onset and extent of the separation bubble, as well as its behavior, under the individual and combined effects of unsteady wake flow and high turbulence intensity. It was found that the periodic unsteady wake flow definitely determines the separation dynamics as long as the level of the time-averaged turbulence fluctuation is below the maximum level of the wake fluctuation v_{max}. Increasing the inlet turbulence level above v_{max} caused the wake periodicity to totally submerge in the freestream turbulence. In this case, the separation dynamics of the bubble is governed by the flow turbulence that is responsible for partial or total suppression of the separation bubble. One of the striking features this study reveals is that the separation bubble has not disappeared completely despite the high turbulence intensity and the significant reduction of its size.

Heat Transfer. While the boundary layer behavior (according to the equation of motion) is completely decoupled from thermal boundary layer behavior, the latter is through the equation of en-

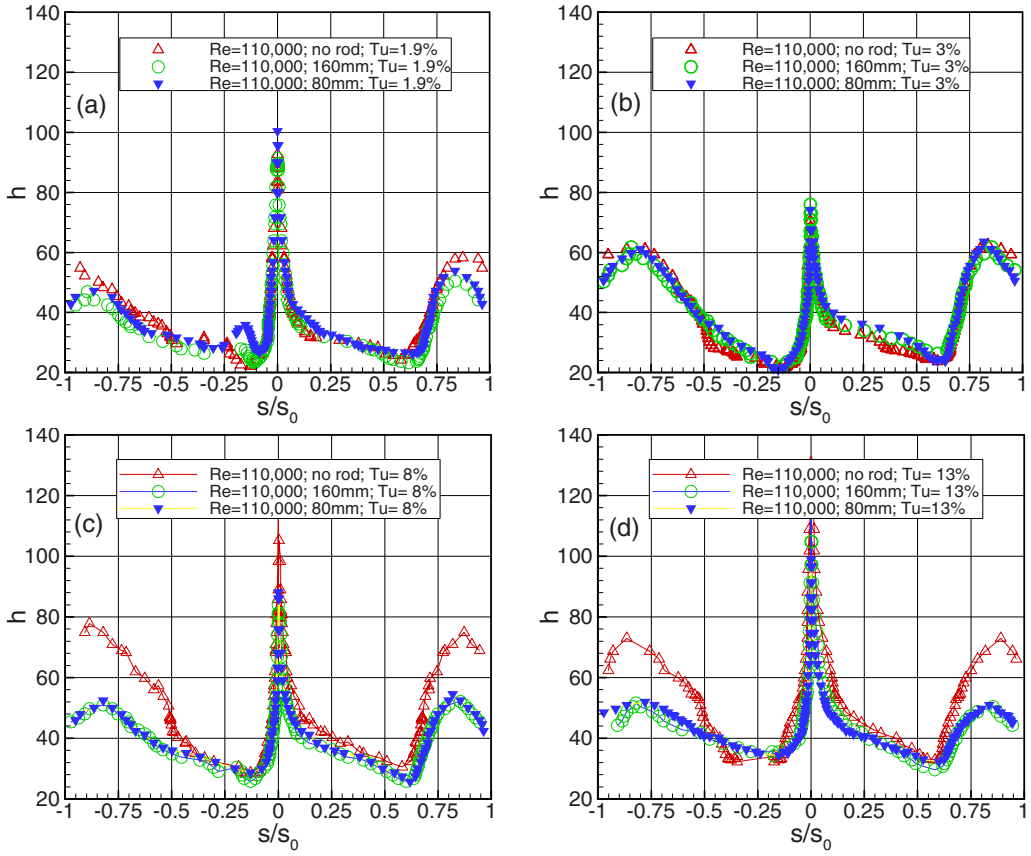

Fig. 20 Effect of unsteady wake frequency on heat transfer coefficient, (*a*) Tu=1.9%, (*b*) Tu=3.0%, (*c*) Tu=8%, and (*d*) Tu=13% for unsteady inlet flow condition with $\Omega=0.0$, 1.59, and 3.18 that correspond to $S_R=\infty$, 160 mm, and 80 mm for Re=110,000

ergy directly coupled with the boundary layer aerodynamics. Considering the aerodynamic results, the following conclusions are drawn.

1. *Individual and combined effects of Re number at constant Tu, steady inlet flow*. Increasing the Re number while keeping the turbulence intensity constant, the HTC increased systematically on both surfaces. At lower turbulence intensity, Tu=1.9%, the Reynolds number increase caused the transition start to shift upstream. Systematically increasing Tu caused the transition region to partially or totally disappear.
2. *Individual and combined effects of Re number at constant Tu, periodic unsteady inlet flow*. Increasing the Re number while keeping the turbulence intensity constant, as above, and utilizing a constant reduced frequency of $\Omega=1.59$, the HTC increased systematically on both surfaces. At a lower turbulence intensity, Tu=1.9%, the Reynolds number increase caused the transition start to shift upstream. The increase of HTC is predominantly accomplished by a higher Re number. Systematically increasing Tu caused the transition region to partially or totally disappear. Here, as in the above steady case, the wake effect on time-averaged HTC is noticeable as long as the unsteady wakes are not completely submerged in the stochastic freestream turbulence. Increasing the reduced frequency to $\Omega=3.18$ reduced the transition region and pushed the transition start further upstream.
3. *Individual and combined effects of reduced frequency* Ω *at constant Re and constant Tu*. Keeping the Reynolds number and turbulence intensity constant, the variation of reduced frequency at low Re number and turbulence intensity did not have a substantial effect on time-averaged HTC on the suction surface. On the pressure surface, however, the transition length was reduced and its start moved further upstream. Keeping the same low Re=110,000 and increasing the turbulence intensity to Tu=3.0, the wake turbulence started to submerge into the freestream turbulence leading to an increased HTC distribution on the suction side with the largest difference of about 30% in the nonturbulent region, $s/s_0 \approx 0.4$ relative to no rod case at Tu=3%. On the pressure surface, the unsteady effect was most visible in the transitional region. A seemingly different HTC pattern emerged when the turbulence intensity was increased to Tu=8% and 13%, respectively. While the HTC distributions for both unsteady cases with $\Omega=1.59$ and 3.18 were almost identical, the steady-state case (no rod) showed towards the second half of the blade increasingly higher HTC values. This, at first glance, appears to be incompatible with the widespread notion that the unsteady wakes generally contribute to intensifying the turbulence activities, thus increasing the HTC. However, expediting the turbulence fluctuations for steady and unsteady cases shows that the calming effect discussed in the aerodynamics section is responsible for calming the turbulence activities, thus reducing the HTC. Similar HTC-distribution patterns were revealed for Re=250,000.

Acknowledgment

The presented study is a part of an ongoing LPT aerodynamics project executed by the NASA Glenn Research Center. The authors were supported by NASA Cooperative Agreement No. NCC3-793 monitored by Dr. David Ashpis. The support and the permission for publication are gratefully acknowledged. The authors also gratefully acknowledge Pratt and Whitney for providing the research community with the blade coordinates.

Nomenclature

c = blade chord (mm)
c_{ax} = axial chord (mm)
C_p = pressure coefficient, $C_p=(p_i-p_s)/[(p_t-p_s)\text{inl}]$
D_R = rod diameter (mm)
E = power density function of fluctuation velocity v_{rms}
G_T = grid bar thickness (mm)
h = heat transfer coefficient, $h=Q''_{conv}/(T_{yel}-T_\infty)$ $(W/m^2\,K)$
L_{SS} = suction surface length (mm)
p_i = static pressure taps $i=1,\ldots,48$ (Pa)
p_s, p_t = static and total pressure at the inlet (Pa)
Q''_{conv} = convective heat flux, $Q''_{conv}=Q''_{foil}-Q''_{rad}-Q''_{cond}$ (W/m^2)
Q''_{cond} = conductive heat flux (W/m^2)
Q''_{foil} = heat flux of the Inconel foils heat flux $Q''_{foil}=VI/A_{foil}$ (W/m^2)
Q''_{rad} = radiation heat flux $Q''_{rad}=\varepsilon\sigma(T^4_{yel}-T^4_\infty)$ (W/m^2)
Re_{LSS} = Reynolds number based $Re=L_{ss}V_{exit}/\nu$
S_B = blade spacing (mm)
S_R = rod spacing (mm)
s = streamwise distance from the leading edge of the blade (mm)
s_0 = streamwise distance from the leading edge to the trailing edge of the blade (mm)
s_r = reattachment point of the separation bubble from blade leading edge (mm)
s_s = starting point of the separation bubble at a streamwise distance from blade leading edge (mm)
t = time (s)
$T\infty$ = air temperature (K)
T_{yel} = liquid crystal yellow band temperature $T_{yel}=44.6°C$
TG = turbulence generator grid
Tu = turbulence intensity
U = belt translational velocity
V_{ax} = axial velocity (m/s)
V_{exit} = exit velocity (m/s)
V = velocity (m/s)
$\bar{V}$ = V bartime averaged velocity (m/s)
v = fluctuation velocity (m/s)
v_{rms} = fluctuation velocity rms (m/s)
α_1, α_2 = cascade inlet and exit flow angles (deg)
γ = blades stagger angle (deg)
ε = emissivity of the liquid crystal $\varepsilon=0.85$
Λ = integral length scale $\Lambda=\bar{V}E_{(f=0)}/v^2_{rms}$ (mm)
ν = kinematic viscosity (m^2)
σ = cascade solidity, $\sigma=c/S_B$
σ = Stefan–Boltzman constant, 5.667×10^{-8} $W/m^2\,K^4$
τ = one wake-passing period (ms)
φ = flow coefficient, $\varphi=V_{ax}/U$
ψ_A = Zweifel coefficient $\psi_A=2\sin^2\alpha_2(\cot\alpha_2-\cot\alpha_1)s_B/c_{ax}$
Ω = reduced frequency $\Omega=(c/S_R)(U/V_{ax})=(\sigma/\varphi)\times(S_B/S_R)$

References

[1] Schobeiri, M. T., Öztürk, B., and Ashpis, D., 2005, "On the Physics of the Flow Separation Along a Low Pressure Turbine Blade Under Unsteady Flow Conditions," ASME Trans. J. Fluids Eng., **127**, pp. 503–513.

[2] Schobeiri, M. T., and Öztürk, B., 2004, "Experimental Study of the Effect of the Periodic Unsteady Wake Flow on Boundary Layer Development, Separation, and Re-attachment Along the Surface of a Low Pressure Turbine Blade," ASME J. Turbomach., **126**(9), pp. 663–676. 2004

[3] Schobeiri, M. T., Öztürk, B., and Ashpis, D., 2005, "Effect of Reynolds Number and Periodic Unsteady Wake Flow Condition on Boundary Layer Development, Separation, and Re-attachment Along the Suction Surface of a Low Pressure Turbine Blade," ASME Paper No. GT2005-68600.

[4] Schobeiri, M. T., Öztürk, B., and Ashpis, D., 2005, "Intermittent Behavior of the Separated Boundary Layer Along the Suction Surface of a Low Pressure Turbine Blade Under Periodic Unsteady Flow Conditions," ASME Paper No. GT2005-68603.

[5] Öztürk, B., and Schobeiri, M. T., 2006, "Effect of Turbulence Intensity and Periodic Unsteady Wake Flow Condition on Boundary Layer Development, Separation, and Re-attachment Over the Separation Bubble Along the Suction Surface of a Low Pressure Turbine Blade," ASME Paper No. GT2006-91293.

[6] Kaszeta, R. W., and Simon, T. W., 2002, "Experimental Investigation of Transition to Turbulence as Affected by Passing Wakes," NASA/CR Paper No. 2002-212104.

[7] Wolf, W., Homeyer, Lars., and Fottner, L., 2001, "Experimental Investigation of Heat Transfer in Separated Flow on a Highly Loaded Lp-Turbine Cascade," *Proceeding of the RTO/AVT Symposium and Specialists Meeting Heat Transfer and Cooling in Propulsion and Power Systems*, Loen, Norway, May 7–11.

[8] de la Calzada, P., and Alonso, A., 2005, "Numerical Investigation of Heat Transfer in Turbine Cascades With Separated Flows," ASME Paper No. GT-2002.

[9] Han, J.-C., "Gas Turbine Heat Transfer Laboratory," private communication.

[10] Ameri, A., NASA Glenn Research Center, private communication.

[11] Schobeiri, M. T., and Chakka, P., 2002, "Prediction of Turbine Blade Heat Transfer and Aerodynamics Using Unsteady Boundary Layer Transition Model," Int. J. Heat Mass Transfer, **45**, pp. 815–829.

[12] Han, J.-C., Zhang, L., and Ou, S., 1993, "Influence of Unsteady Wake on Heat Transfer Coefficient From a Gas Turbine Blade," ASME J. Heat Transfer, **115**, pp. 904–911.

[13] Dullenkopf, K., and Mayle, R. E., 1994, "The Effect of Incident Turbulence and Moving Wakes on Laminar Heat Transfer in Gas Turbines," ASME J. Turbomach., **116**, pp. 23–28.

[14] Magari, P. J., and LaGraff, L. E., 1994, "Wake-Induced Unsteady Stagnation-Region Heat Transfer Measurements," ASME J. Turbomach., **116**, pp. 29–38.

[15] Goldstein, R. J., 1971, *Film Cooling* (Advances in Heat Transfer) T. F. Irvin and J. P. Hartnett, eds., Academic, New York, Vol. 7, pp. 321–379.

[16] Han, J. C., Dutta, S., and Ekkad, S. V., 2000, *Gas Turbine Heat Transfer and Cooling Technology*, Taylor & Francis, London.

[17] Choi, J., Teng, S., Han, J.-C., and Ladeinde, F., 2004, "Effect of Free-Stream Turbulence on Blade Heat Transfer and Pressure Coefficients in Low Reynold Number Flow," Int. J. Heat Mass Transfer, **47**, pp. 3441–3452.

[18] Schobeiri, M. T., John, J., and Pappu, K., 1996, "Development of Two-Dimensional Wakes Within Curved Channels, Theoretical Framework and Experimental Investigation," ASME J. Turbomach., **118**, pp. 506–518.

[19] Schobeiri, M. T., and Özturk, B., 2004, "Turbulence Development and Decay Upstream of the LPT-Cascade," NASA GRC LPT-Project Progress Report No. 2004-2; NASA GRC Report No. 32525-61640 ME.

[20] Bruun, H. H., 1995, *Hot-Wire Anemometry*, Oxford University Press, Oxford.

[21] Barrett, M. J., and Hollingsworth, D. K., 2001, "On the Calculation of Length, Scales for Turbulent Heat Transfer Correlation," J. Heat Transfer, **123**, pp. 232–241.

[22] Hinze, J. O., 1975, *Turbulence*, 2nd ed., McGraw-Hill, New York.

[23] Wright, L., and Schobeiri, M. T., 1999, "The Effect of Periodic Unsteady Flow on Boundary Layer and Heat Transfer on a Curved Surface," ASME Trans. J. Heat Transfer, **120**, pp. 22–33.

[24] Kline, S. J., and McKlintock, F. A., 1953, "Describing Uncertainties in Single-Sample Experiments," Mech. Eng. (Am. Soc. Mech. Eng.), **75**, pp. 3–8.

[25] Hourmouziadis, J., 1989, *Blading Design for Axial Turbomachines* (Lecture Series LS-167), AGARD.

[26] Eifler, J., 1975, "Zur Frage der Freien Turbulenten Strömungen, Insbesondere Hinter Ruhenden und Bewegten Zylindern," dissertation, Technische Hochschule Darmstadt, Germany.

[27] Bons, J. P., Sondergaard, R., and Rivir, R. B., 2001, "The Fluid Dynamics of LPT Blade Separation Control Using Pulsed Jets," ASME Paper No. 2001-GT-190.

[28] Roberts, S. K., and Yaras, M. I., 2003, "Effects of Periodic-Unsteadiness, Free-Stream Turbulence and Flow Reynolds Number on Separation-Bubble Transition," ASME Paper No. GT-2003-38262.

[29] Herbst, R., 1980, "Entwicklung von Strömungsgrenzschichten bei Instationärer Zuströmung in Turbomaschinen," dissertation, Technische Hochschule Darmstadt, Germany.

[30] Pfeil, H., Herbst, R., and Schröder, T., 1983, "Investigation of the Laminar-Turbulent Transition of Boundary Layers Disturbed by Wakes," ASME J. Eng. Power, **105**, pp. 130–137.

[31] Schobeiri, M. T., and Radke, R., 1994, "Effects of Periodic Unsteady Wake Flow and Pressure Gradient on Boundary Layer Transition Along the Concave Surface of A Curved Plate," ASME Paper No. 94-GT-327.

[32] Halstead, D. E., Wisler, D. C., Okiishi, T. H., Walker, G. J., Hodson, H. P., and

Shin, H.-W., 1997, "Boundary Layer Development in Axial Compressors and Turbines: Part 3 of 4," ASME J. Turbomach., **119**, pp. 225–237.
[33] Giel, P. W., Van Fossen, G. J., Boyle, R. J., Thurman, D. R., and Civinskas, K. C., 1999, "Blade Heat Transfer Measurements and Predictions in a Transonic Turbine Cascade," ASME Paper No. 99-GT-125.
[34] Giel, P. W., Bunker, R. S., Van Fossen, G. J., and Boyle, R. J., 2000, "Heat Transfer Measurements and Predictions on a Power Generation Gas Turbine Blade," ASME Paper No. 2000-GT-0209.
[35] Arts, T., Lambert de Rouvroit, M., and Rutherford, A. W., 1990, "Aero-Thermal Investigation of a Highly Loaded Transonic Linear Turbine Guide Vane Cascade," VKI Technical Note 174.
[36] Boyle, R. J., Ames, F., and Giel, P., 2004, "Predictions for the Effects of Freestream Turbulence on Turbine Blade Heat Transfer," ASME Paper No. GT2004-54332.

Experimental and Theoretical Analysis of Transient Response of Plate Heat Exchangers in Presence of Nonuniform Flow Distribution

N. Srihari

Sarit K. Das

Department of Mechanical Engineering,
Indian Institute of Technology Madras,
Chennai, India

Transient analysis helps us to predict the behavior of heat exchangers subjected to various operational disturbances due to sudden change in temperature or flow rates of the working fluids. The present experimental analysis deals with the effect of flow distribution on the transient temperature response for U-type and Z-type plate heat exchangers. The experiments have been carried out with uniform and nonuniform flow distributions for various flow rates. The temperature responses are analyzed for various transient characteristics, such as initial delay and time constant. It is also possible to observe the steady state characteristics after the responses reach asymptotic values. The experimental observations indicate that the Z-type flow configuration is more strongly affected by flow maldistribution compared to the U-type in both transient and steady state regimes. The comparison of the experimental results with numerical solution indicates that it is necessary to treat the flow maldistribution separately from axial thermal dispersion during modeling of plate heat exchanger dynamics. [DOI: 10.1115/1.2885153]

Keywords: plate heat exchanger, flow maldistribution, axial dispersion, fluid backmixing, nonuniform flow distribution

1 Introduction

Application of plate heat exchangers (PHEs) have been extending to many industries, such as power and process sectors apart from the pharmaceutical, dairy, and brewery industries where they are predominantly used. This is mainly due to their better heat transfer characteristics having most of the features of compact heat exchangers. This motivates the researchers to investigate their performance more accurately. It is also important to develop the strategies to operate the heat exchange equipment in safe conditions (e.g., nuclear power plants or chemical industries) and avoid the industrial hazards. Transient analysis helps us to predict the behavior of the heat exchanger subjected to various operational disturbances. The disturbances may be due to sudden change in temperature or flow rates of the working fluids or failure of the process equipments. The nature of the temperature response indicates the heat exchanger performance characteristics both in steady and transient modes.

The literature available in the area of transient response of PHEs is not substantial; moreover, there are very few experimental investigations available on this theme. Initially, most of the analyses on plate heat exchangers were carried out based on the assumption of equal flow rate in all the channels [1–4], which is an ideal case with no flow maldistribution. In practical situations, the flow is distributed nonuniformly to the channels when the number of channels is more than 50 for a given plate geometry. Due to this, both thermal and hydraulic performance of the heat exchanger deviates from the existing methods of theoretical prediction. McKnight and Worley [5] pioneered the transient study on feedback control related to high velocity flow variations in a PHE. Masubuchi and Ito [6] presented a systematic analysis of static and dynamic characteristics of plate heat exchangers and suggested appropriate design and control schemes. Dynamic responses were greatly influenced by the relation between inlet and outlet passages in both counter- and parallel flow types. Zaleski and Tejszerski [7] presented the simulation of dynamic performance for cocurrent plate heat exchangers. They developed a mathematical model for the transient operation of two fluids, multichannel plate heat exchanger with parallel flow arrangement. This model is very convenient for computer-based calculation system and used for making appropriate diagrams, useful for rapid technical evaluation of the exchangers. Khan et al. [8] presented the experimental and analytical studies on countercurrent plate heat exchangers using sinusoidal and pulse inputs. It was concluded that the temperature response of the cold stream to variations in the mass flow of the hot stream most closely approaches an overdamped secondorder transfer function.

An extensive analysis was presented on dynamics of the single-pass counterflow PHEs by Das and Roetzel [9]. This model takes care of all the deviations from plug flow, like the effect of flow maldistribution and fluid backmixing, into account by introducing a dispersion term in the energy equation. Das et al. [10] conducted the experiments to analyze the transient behavior of plate heat exchangers. They found that the computation with Peclet number 3.5 gives a response that yields steady state temperature equal to that of the experiment within the limits of experimental error. Apart from the comparison with the dispersion model, parametric study was also carried out for the effects of NTU, heat capacity rate ratio, and number of plates. They suggested that first-order system can be used for control applications of the exchangers. From the general trend of the responses, the computational value of the initial delay period was on the higher side of the experimental value. They suggested, as a scope for future investigators, refinement of mathematical model by relaxing the assumption of equal flow distribution in channels. Subsequent studies by Roetzel

Contributed by the Heat Transfer Division of ASME for publication in the JOURNAL OF HEAT TRANSFER. Manuscript received September 28, 2006; final manuscript received May 11, 2007; published online April 10, 2008. Review conducted by Bengt Sunden.

and Na Ranong [11,12] and Sahoo and Roetzel [13] suggested that it is more appropriate to use axial dispersion for fluid backmixing rather than flow maldistribution. Hence, there is a need to treat flow maldistribution separately and more accurately.

On the other hand, there are a number of issues related to flow distribution. Datta and Majumdar [14,15] analyzed the effect of unequal distribution of fluid inside the channels using numerical technique and derived flow distribution equation in parallel and reverse flow manifold systems by a novel finite-difference procedure. Bassiouny and Martin [16,17] presented the analytical solutions for *U*-type and *Z*-type PHEs to describe the flow distribution and pressure drop in the channels. They derived an equation for flow distribution, characterized by the distribution parameter m^2. The parameter m^2 is positive when the channel flow rate decrease in the direction of the intake stream. The flow distribution tends to be uniform for low positive values of m^2 (≤ 0.01). The magnitude of m^2 depends on the fluid friction within the channel, free flow area of the channel and port, as well as the number of plates. The experimental analysis on flow distribution has been carried out using wooden mandrels with different port diameters by Fantu et al. [18]. This analysis presented the clear picture of the variation of pressure profiles with flow rate and port diameter and also validated Bassiouny and Martin's [16,17] model. The flow distribution parameter is incorporated in the steady state analysis by Prabhakara Rao et al. [19,20]. They presented the effect of flow distribution on thermal performance of the PHE. It was considered that the heat transfer coefficient inside the channel is a function of the velocity of the fluid stream in that particular channel. Prabhakara Rao and Das [21] conducted experiments on plate heat exchanger to study the effect of nonuniform flow distribution on pressure drop. The results show that the flow maldistribution is more severe in the *Z*-type flow configuration compared to the *U*-type PHE. Prabhakara Rao et al. [22] presented the experimental work on the effect of flow maldistribution to study the thermal performance of plate heat exchangers in the steady state. It was found that flow maldistribution decreases with the increase in port dimension. At higher NTU, it is preferable to use multipass arrangement when more number of plates is used. Theoretical analysis on transient response of PHEs, considering the effect of flow maldistribution, has been presented by Srihari et al. [23]. The flow maldistribution from the port to channel has been accounted separately and the axial dispersion was used to take care of fluid backmixing within the channel alone. However, there is no experimental evidence to validate the effect of the flow maldistribution, as suggested by their model.

The above review of literature indicates that the data available in transient analysis of the plate heat exchangers are limited. In many cases, it has been assumed that the flow distribution is uniform, which is not appropriate under practical conditions. Nonuniform flow distribution deteriorates the thermal and hydraulic performance of the heat exchanger. The effect of port to channel flow distribution on the dynamics of the PHE has not been studied experimentally. This is the main inspiration of the present work.

In the present work, detailed experimental study is carried out to analyze the transient response of PHEs under uniform and nonuniform flow conditions. The experimental results have been compared with a simple numerical theoretical model for different flow configurations. This experimental data along with the model are useful to estimate the behavior of the heat exchanger under temperature transients and helpful to design the controller for the heat exchangers.

2 Details of the Experimental Test Facility

2.1 Test Plate Heat Exchanger. The test plate heat exchanger is manufactured by Alfa Laval company and the plates are made of stainless steel with Nitrile rubber gaskets. The test unit contains 40 corrugated stainless steel plates. Geometrical features of a plate are shown in Fig. 1. The heat exchanger is initially arranged for *U*-type flow configuration and it can be modified to *Z*-type configuration. In case of multipass arrangement, the special plates are provided within the plate pack to change the direction of flow. A series of experiments have been carried out for both *U*-type and *Z*-type flow configurations of single-pass PHE and also 1–2 pass arrangement for multipass PHE.

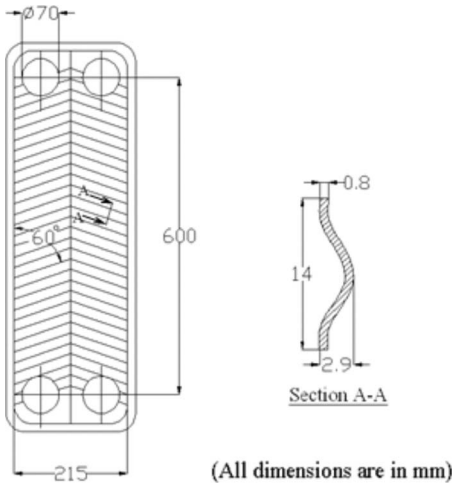

Fig. 1 Geometrical features of the plate

2.2 Transient Experimental Test Setup. The experimental test setup is designed, as shown in Fig. 2, to achieve the sudden rise in hot fluid temperature. Cold fluid receives heat from the hot fluid across the plates and is sent to the cooling tower. After the hot fluid is passed through the exchanger, it is fed back to the hot water tank. The water in this tank is heated up with help of electrical heaters of 42 kW capacity and is kept at a constant temperature using the temperature controller. Bypass lines are connected to the main pipe lines and electropneumatic valves are used to obtain the required flow directions during the experiments. The fluid flow rates can be adjusted by the flow control valves and are measured with the help of standard ASME orifice meters. *T*-type thermocouples are connected to the pipe lines to measure the temperature response at an interval of 1 s. The responses are recorded with the help of data acquisition system (HP 34970A). All the thermocouples are calibrated over the entire range of interest, using a precision thermometer and a constant temperature bath. Least count of the thermocouple is 0.1 °C and it has been estimated that the time constant is 150 ms.

3 Procedure to Conduct the Transient Experiments

The test plate heat exchanger is used to conduct the transient experiments for single-pass and multipass flow arrangements. The heat exchanger has 31 channels, out of which 16 channels carry the cold fluid and 15 carry the hot fluid. Cold fluid is always allowed to flow on the side having more number of channels to minimize the heat loss from the end plates. The experiments are conducted for uniform and nonuniform flow distribution conditions. The flow nonuniformity is created artificially by inserting the wooden mandrels (Fig. 3) into the four ports of the exchanger. Its circular groove acts as a port with reduced diameter of 24 mm instead of actual dimension of 70 mm.

Electropneumatic valves are located as per the valve position, i.e., normally open (NO) / normally closed (NC). At the beginning of the experiments, Valves V2 and V4 are closed and Valves V1, V3, and V5 are opened. Initially, hot water flows in bypass line and back to the hot water tank as Valve V2 is closed and Valve V1 opened. The cold water flows in cold water circuit and some stream of it is bypassed to hot water inlet pipe as Valve V3 is opened. At this condition, only cold water circulates in both the

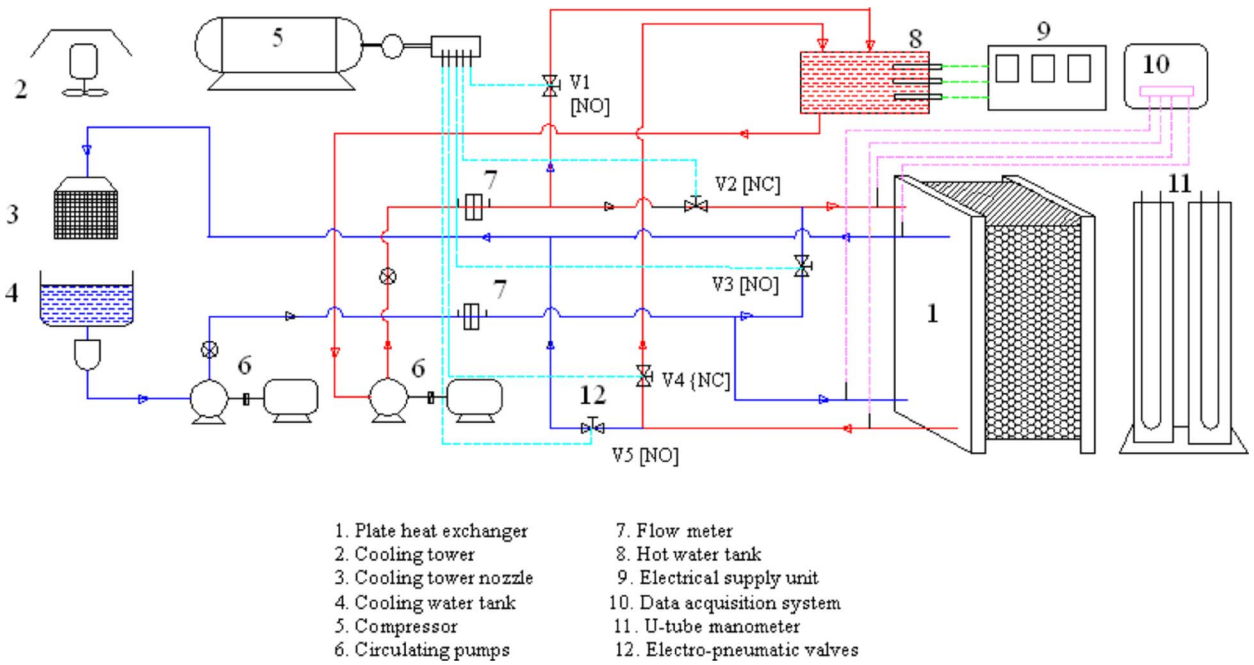

Fig. 2 Schematic diagram of the transient experimental test facility

sides and both the streams flow back to the cooling tower as Valve V5 is open. Because cold water only flows in both sides, heat transfer will not take place in the heat exchanger. Initially, all the fluid temperatures have the same value as the cold inlet temperature. All the electropneumatic valves are connected to a single main switch. When this switch is put to ON position, after the hot water reaches the predetermined steady temperature, the transient starts. As Valve V2 is opened and Valves V1 and V3 are closed, hot water pushes the existing cold water in the hot water line at the entrance of the exchanger. It produces the sudden rise in hot water temperature at the inlet and then heat transfer takes place inside the heat exchanger. As Valve V4 is opened and Valve V5 closed, the hot water coming from the exchanger goes back to the hot water tank. The accompanying variation of flow rates on both sides does not affect the test because heat transfer takes place only after the change in temperature takes place. The inlet and outlets temperatures of the fluids are recorded till the steady state is reached. The temperature response on the cold and hot outlet gradually increases and attains the steady state condition. Transient response of the particular configuration for the given flow rate is observed by analyzing the recorded data of temperatures at regular intervals of time. The procedure has been repeated for different flow arrangements and flow rates.

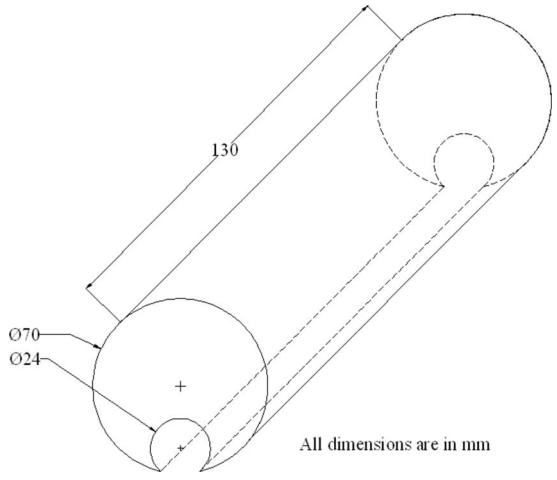

Fig. 3 Schematic diagram of the mandrel

4 Data Reduction

4.1 Experiments to Find the Friction Factor Correlation. The experiments are conducted at steady state condition for different flow rates with *U*-type flow configuration to analyze the nonuniform flow distribution using the mandrel. Initially, experiments are conducted for finding the correlation between the friction factor and Reynolds number in a single channel to know the flow resistance in a channel for varying flow rates. The following correlation for the friction factor was obtained by regression analysis of the pressure drop data.

$$f = 21.4\,\mathrm{Re}^{-0.3} \quad \text{for } 500 < \mathrm{Re} < 5000 \tag{1}$$

The channel Reynolds number is defined on the basis of twice the plate spacing b, as

$$\mathrm{Re} = \frac{U_c(2b)}{\nu} \tag{2}$$

For finding the above correlation, the range of operating flow rates were taken to have Reynolds number from 500 to 5000. This range assures turbulent flow since it is known that in PHEs above Re=400 flow is always turbulent. For evaluating the friction factor, the experimental data for a single channel pressure drop are considered. The flow distribution parameter is estimated as per the relation

$$m^2 = \frac{1}{z_c}\left[\frac{nA_c}{A_p}\right]^2 \quad \text{where } \zeta_c = 1 + C_{Td} + f\frac{l_c}{d_e} + C_{Td}{}^* \tag{3}$$

The pressure losses at the inlet and exit ports ($C_{Td}, C_{Td}{}^*$) due to changing direction of the flow are small (less than 0.5%) compared to the pressure loss due to friction inside the corrugated channel, so they are neglected.

4.2 Data Reduction for Thermal Experiments. The nondimensional time is calculated based on the residence time of the fluid flow through the channel. The time and temperature data are reduced to nondimensional form as follows. The zero point of the time axis is considered as the instant before the input temperature transient starts.

Nondimensional time:

$$z = \tau/\tau_{ra1}$$

where τ_{ra1} is the characteristic time

$$\tau_{ra1} = \frac{n_1 A_c L}{\dot{V}_{g1}}$$

Nondimensional temperature:

$$t = \frac{\theta - \theta_{g1,\text{in}}}{\theta_{g2,\text{in}} - \theta_{g1,\text{in}}} \tag{4}$$

Heat transfer correlation for the existing heat exchanger has been obtained from the previous steady state experimental test data from Prabhakara Rao et al. [22] of the same PHE as given below

$$\text{Nu} = 0.218\ \text{Re}^{0.65}\ \text{Pr}^{1/3} \tag{5}$$

All the fluid properties are taken based on the bulk mean temperature.

4.3 Uncertainty in the Measurements. The measuring equipments used for conducting the experiments are tested for the accuracy. The uncertainty in the flow rate measurement is estimated to be maximum ±3.23%. The uncertainty in the pressure drop measurement across the orifice plate is found to be ±4.5% maximum. Calibration of the thermocouples has been carried out and the uncertainty in the temperature measurement is found to be ±1.5%. More than ±90% of the heat transfer data have the energy balance within an error of ±2.0%, and a maximum of ±5.0%. The maximum uncertainty in the values of Re, f, U, and NTU are ±1.11%, ±4.39%, ±0.54%, and ±0.995%, respectively.

5 Mathematical Model

In the present work, experimental results have been compared to the theoretical model that considers the nonuniform flow distribution. A similar model with analytical study has recently been published by Srihari et al. [23]. However, the analytical model is too complex needing inversion of large matrices and complicated eigenvalue calculation. Fourier series based numerical inversions of Laplace transform is also required. The present analysis instead uses simple finite-difference model with iterative solution procedure. The coordinate system is chosen in the direction of flow through the first channel. Numbers $1,2,3,\ldots,N$ (which is chosen to be odd) represent the channels, where an odd and even number of channels will carry Fluids 1 and 2, respectively, as shown in Fig. 4. The flow within a channel is considered to be one dimensional and small elements of fluid and plate can be considered as control volumes as shown in Fig. 5. The energy balance equations are framed for Fluid 1, Fluid 2, and for all the plates considering the above assumptions. The energy equations for both the fluids in nondimensional form for the parallel flow PHE can be written as

$$\frac{(R_\tau)^{m_{i+1}}}{R_{wi}}\frac{\partial t_i}{\partial z} = \frac{1}{\text{Pe}_i}\frac{\partial^2 t_i}{\partial x^2} - \frac{\partial t_i}{\partial x} + \frac{\text{NTU}_i}{2}(R_N)^{m_{i+1}} \times (t_{Wi} + t_{Wi+1} - 2t_i) \quad (i = 1,2,3,4,\ldots,N) \tag{6}$$

For intermediate plates except the end plates,

$$R_C\frac{\partial t_{wi}}{\partial z} = K_{i-1}(t_{i-1} - t_{wi}) + K_i(t_i - t_{wi}) \quad (i = 2,3,4,\ldots,N) \tag{7}$$

For the end plates,

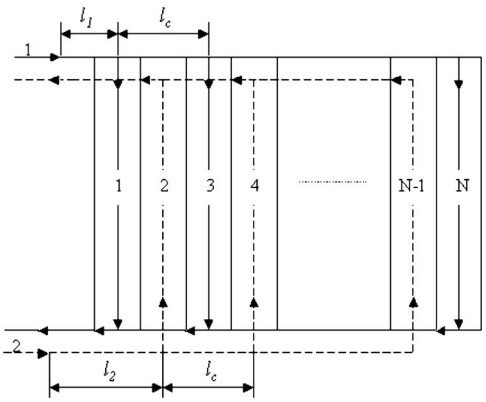

Fig. 4 *U*-type flow configuration of the plate heat exchanger

$$R_C\frac{\partial t_{w1}}{\partial z} = \frac{\text{NTU}_1}{2}R_{w1}(t_1 - t_{w1}) \tag{8}$$

$$R_C\frac{\partial t_{w,N+1}}{\partial z} = K_N(t_N - t_{w,N+1}) \tag{9}$$

where

$$K_i = \frac{\text{NTU}_i}{2}R_{wi}(R_2 \cdot R_N)^{m_{i+1}} \quad \text{and } m_j = j - 2[j/2]$$

The nondimensional form of the governing equations are reduced as

$$\frac{(R_\tau)^{m_{i+1}}}{R_{wi}}\frac{\partial t_i}{\partial z} = \frac{1}{\text{Pe}_i}\frac{\partial^2 t_i}{\partial x^2} - \frac{\partial t_i}{\partial x} + \frac{\text{NTU}_i}{2}(R_N)^{m_{i+1}} \times (t_{Wi} + t_{Wi+1} - 2t_i) \quad (i = 1,2,3,4,\ldots,N) \tag{10}$$

For the counterflow arrangement, the governing equations can be obtained from Srihari et al. [23]. With the help of the counter- and parallel flow PHE equations, it is possible to extend analysis for multipass arrangements. The flow arrangements for 1–2 pass PHE is a combination of counter- and parallel flow configuration, as shown in Fig. 6. Furthermore, the analysis can be extended to any kind of multipass arrangements, such as M-N/N-N pass PHE.

5.1 Flow Distribution From Port to Channels. The flow distribution parameter m, defined by Bassiouny and Martin [16,17], given in the expressions mainly depends on the exchanger geometry, configuration, and number of channels as given in the equation below:

$$m^2 = \left(\frac{1}{\zeta_c}\right)\left(\frac{n \cdot A_c}{A_p}\right)^2 \tag{11}$$

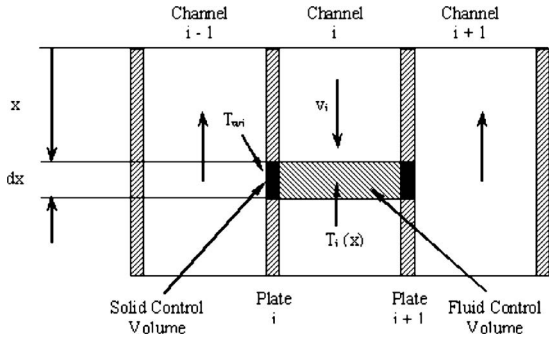

Fig. 5 Control volume of the fluid inside the channel and control volume of the plate

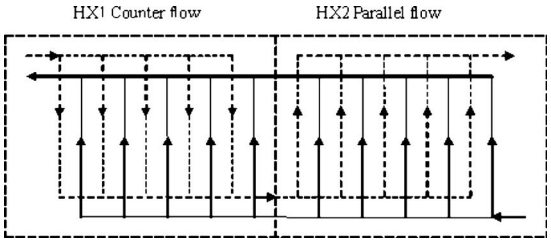

Fig. 6 Schematic diagram of 1–2 pass arrangement

Here ζ_c is the total frictional resistance of the channel.

The value of m^2 will increase with the square of the number of channels for a given port and channel size. The value of m^2 approaches zero when the flow is uniformly distributed amongst the channels. The more the flow maldistribution, the higher is the value of m^2. The channel velocity for *U*-type and *Z*-type configurations as given by Boussiony and Martin [16,17],

$$U\text{-type configuration} \quad U_c = \left(\frac{A}{nA_c}\right) m \frac{\cosh m(1-z)}{\sinh m} \tag{12}$$

$$Z\text{-type configuration} \quad U_c = \left(\frac{A}{nA_c}\right) m \frac{\cosh mz}{\sinh m} \tag{13}$$

5.2 Boundary Conditions. The boundary conditions are defined using Danckwert's [24] analysis. As per his theory, if dispersion of the fluid begins at the entrance, a sudden temperature drop will be experienced at that section. The dispersion of the fluid inside the port is not taken into consideration because it is less significant. The boundary conditions for Eqs. (6)–(9) may be written as follows:

at $x=0$:

$$t_i - \frac{1}{\mathrm{Pe}_i}\frac{\partial t_i}{\partial x} = f_1(z-\phi_i)u(z-\phi_i) \quad \left(i = 1,3,5,\ldots,2\left[\frac{N+1}{2}\right]-1\right) \tag{14}$$

$$t_i - \frac{1}{\mathrm{Pe}_i}\frac{\partial t_i}{\partial x} = f_2(z-\phi_i)u(z-\phi_i) \quad \left(i = 2,4,6,\ldots,2\left[\frac{N}{2}\right]\right) \tag{15}$$

$$\frac{\partial t_{wi}}{\partial x} = 0 \quad (i = 1,2,3,\ldots,N+1) \tag{16}$$

at $x=1$:

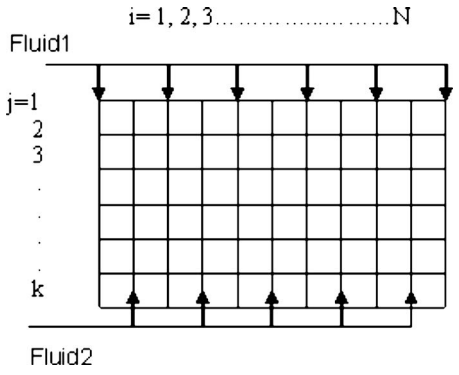

Fig. 7 Grid structure used in the finite-difference analysis

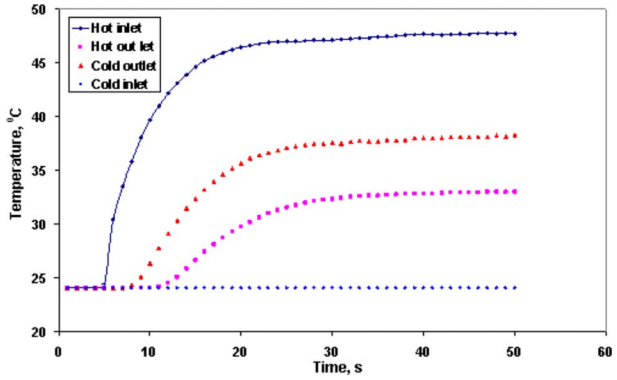

Fig. 8 Experimental results of temperature response in dimensional form

$$\frac{\partial t_i}{\partial x} = 0 \quad (i = 1,2,3,\ldots,N) \tag{17}$$

$$\frac{\partial t_{wi}}{\partial x} = 0 \quad (i = 1,2,3,\ldots,N+1) \tag{18}$$

5.3 Numerical Solution Procedure. Finite-difference technique is used to solve the governing differential equations. Gauss–Jordan scheme is used for point by point iteration. Each channel (say, $i=1,2,3,\ldots,N$) is distributed in k number of nodes ($j=1,2,3,\ldots,k$). So a nodal network of $N\times k$ is aggregated as shown in Fig. 7. Temperatures at these discrete points are denoted as $t_{i,j}$. The differential equations (6)–(9) are expressed in the form of finite difference by substituting derivatives with forward, central, and backward differences for entrance, intermediate, and exit nodes, respectively. The first and last channel finite-difference equations are different from intermediate channels. Moreover, for intermediate channels, even number of channels ($i=2,4,6,\ldots,N-1$) and odd number of channels ($i=3,5,7,\ldots,N-2$) do have different sets of equations for each node point. This temperature distribution across each nodal point acts as the initial state of the next part of the model, which takes temperature transient into account. The i and j subscripts are used to designate x and y allocations of discrete nodal points. However, in addition to being discretized in space, the problem must be discretized in time. Hence, the calculation must be performed at successive time steps. For solving the finite-difference equations, explicit method is used in such a way that the cell Peclet number is low to ensure stability of the solution. First, it solves for temperature of particu-

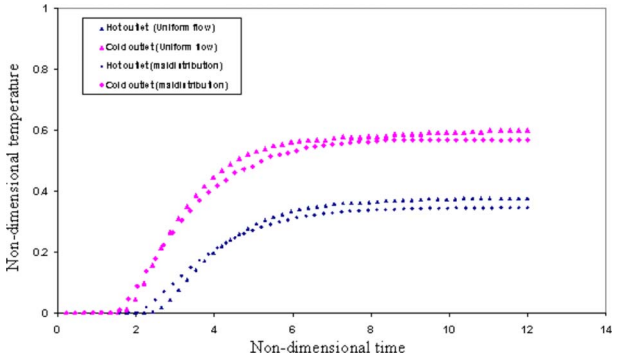

Fig. 9 Comparison of temperature response with uniform and nonuniform flow distributions ($m^2=3.8$) for *U*-type at Re=1110, $N=31$, NTU=1.6, and $R_{g2}=1$

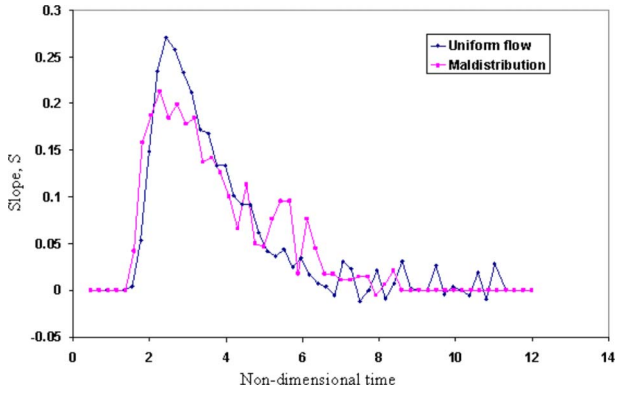

Fig. 10 Comparison of the slopes response for *U*-type with uniform and nonuniform flow distributions (m^2=3.8) for *U*-type at Re=1110, *N*=31, NTU=1.6, and R_{g2}=1

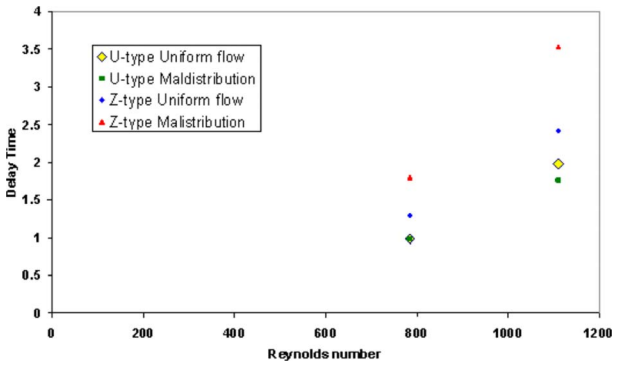

Fig. 12 Variation in initial delay for *U*-type and *Z*-type flow configurations

lar node at the current time step. After getting all nodal point temperature at one time step, we march to the next time step. In this way, the transient temperature distribution is obtained by marching out in the time. The final temperature of the combined fluid at the outlet can be calculated by considering temperature responses at the exit of each channel and corresponding phase lag, and using the weighted mean average as follows:

$$t(z) = \frac{\Sigma \dot{m}_i \, . \, t_i(z - \phi_i)}{\Sigma \dot{m}_i} \tag{19}$$

6 Results and Discussion

6.1 Experimental Study on the Transient Response. The experimental results are presented with uniform and nonuniform flow distributions for single-pass and multipass flow arrangements. The experimental observations, such as fluid temperature and time, are reduced to nondimensional form to compare with the theoretical simulations. However, Fig. 8 depicts the typical temperature responses in dimensional form. It is clear that the experiment starts at uniform temperature state, which is same as the cold fluid inlet temperature condition. The hot fluid inlet temperature suddenly increases, which results in the response of the cold and hot fluid temperatures at the outlet of the exchanger. The responses of the cold and hot fluids are delayed from the time at which the temperature disturbance is started. This represents the initial delay in the temperature response, which is different for cold and hot fluids. Both cold and hot fluid temperatures gradually increase with time and reach steady state.

Figure 9 shows the comparison of temperature responses for *U*-type flow configuration with uniform and nonuniform flow distribution (m^2=3.8) conditions at Reynolds number 1110. It is observed that the transient features such as initial delay, time constant, and time required to reach steady state temperature are influenced with the flow nonuniformity. These differences in response are difficult to distinguish in the direct time response. So another plot is made; it compares the difference in slope of the responses for cold fluid (Fig. 10). It depicts the variation of slope of the responses and maximum slope reduces with flow maldistribution, which means that response becomes slower for nonuniform flow condition. Apart from this, the comparison of the cold outlet temperatures at steady state indicates the reduction in the temperature under nonuniform flow distribution, which represents reduction in effectiveness of the exchanger.

Figure 11 shows the comparison of temperature responses for *Z*-type flow configuration with uniform and nonuniform flow distribution conditions at Reynolds number 1110. Flow nonuniformity affected more strongly on the *Z*-type flow configuration compared to its effects on the *U*-type exchanger. In this case, initial delay is more for nonuniform flow condition. By comparing the uniform and nonuniform cases, it can be stated that the reduction in nondimensional cold fluid steady state temperature (i.e., the effectiveness) reduces significantly due to the flow nonuniformity. This is mainly due to the fact that the cold and hot fluid distribute nonuniformly in opposite directions and the end channels having the maximum and minimum flow rates of cold and hot steams, respectively. This phenomenon leads to the creation of an imbalance of both the fluid flow rates on either side of each plate of the exchanger, thereby reduction in effectiveness. It is clear that in this case the flow nonuniformity also affects the thermal performance as well as the transient characteristics of the heat exchanger. Figure 12 shows the variation of initial delay for the *U*-type and *Z*-type exchangers at two Reynolds numbers. This plot indicates that the initial delay increases with Reynolds number

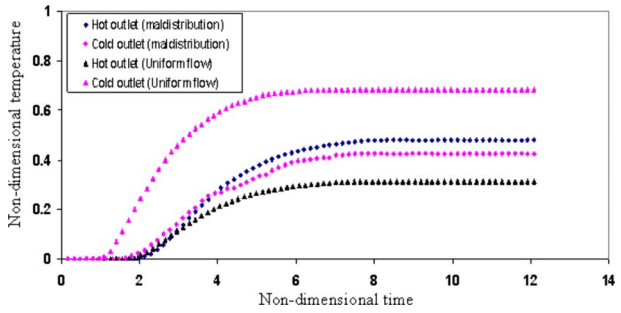

Fig. 11 Comparison of temperature response with uniform and nonuniform flow distributions (m^2=3.8) for *Z*-type at Re =1110, *N*=31, NTU=1.6, and R_{g2}=1

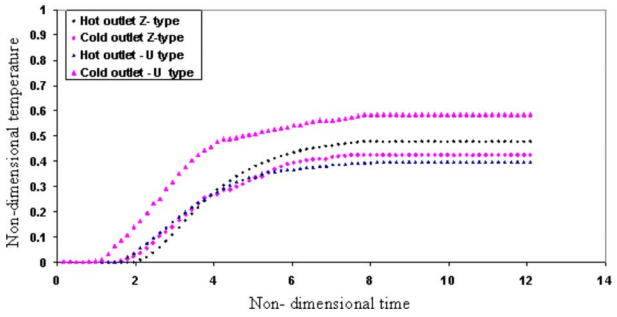

Fig. 13 Comparison of transient response for *U*-type and *Z*-type flow configurations under nonuniform flow distributions (m^2=3.8) at the Re=1110

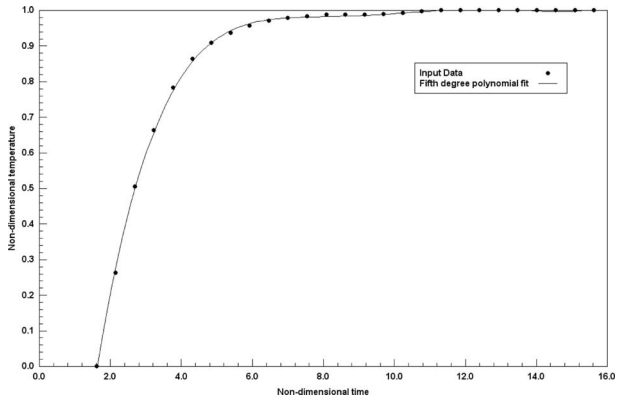

Fig. 14 Hot inlet temperature data fitted to the fifth-order polynomial with $R^2=0.9995$

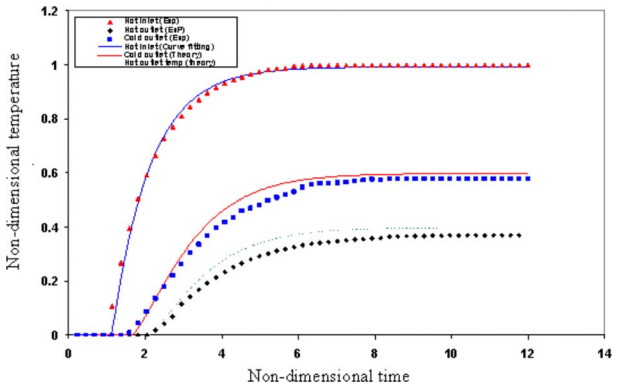

Fig. 16 Comparison of Experimental temperature response with the theoretical model for *U*-type Re=1110, *N*=31, NTU =1.6, and $R_{g2}=1$ for flow distribution $m^2=3.8$

and flow nonuniformity for *Z*-type flow configuration. The initial delay increases with Reynolds number and reduces with flow nonuniformity for *U*-type exchanger. In case of nonuniform flow distribution for *U*-type, the first channels have more flow rate which leads to the reduction of the initial delay. Figure 13 shows the comparison between the *U*-type and the *Z*-type flow configurations for nonuniform flow distribution at Reynolds number of 1110. It indicates a stronger influence of the nonuniformity for the *Z*-type compared to *U*-type flow in the transient and steady state regimes. The response time characterized by the time constant of the system critically depends on the thermal inertia of the system giving a sluggish response for a system with higher thermal inertia. The thermal inertia of the system comprises the two components, the heat capacity of the solid mass (that is the thermal plates) and the fluid holdup. Also, a part of the thick end plates contribute to the thermal inertia depending on the nature of contact between the two extreme plates and the end plates.

6.2 Comparison of Experimental Results with the Theoretical Predictions. Experimentally, the step rise in temperature of the hot fluid is not possible, it will take some time (few seconds in this study for the inlet temperature) to reach steady state due to noninstantaneous opening of the valves. So, temperature rise obtained from the experimental results can be used to fit to a curve and find the function. Figure 14 shows the temperature response on the hot fluid side fitted with suitable fifth-order polynomial. The polynomial function is transformed into Laplace domain and used as inlet temperature change in theoretical models. The resultant responses from the theoretical model are compared to the experimental results in nondimensional form. The axial dispersive Peclet number value is initially taken as 5 while comparing the theoretical responses with the experimental values at the steady and transient regions. Then, the value of Pe is gradually increased and comparison is made at regular intervals; at the value of 30 both theoretical simulations and experimental results match closely. This value of Peclet number (30) is higher than that of the value from the previous studies (3.5) by Das et al. [10], because their Peclet number takes care of both flow maldistribution and fluid backmixing. However, in the present analysis this value of Peclet number takes care of the fluid backmixing alone and flow maldistribution effects are taken care exclusively through the flow distribution model.

Figure 15 shows the comparison of the responses with the theoretical results for *U*-type flow configuration at Re=1110, *N*=31, NTU=1 and $R_{g2}=1$ under uniform flow distribution. It is observed that the responses are in good agreement with the theoretical prediction in transient and steady state regimes. The initial delay for the hot side is more than the cold side because the first channel contains the cold fluid and second channel contains the hot fluid. The initial delay for cold and hot side responses also shows the close matching with the theoretical results. Figure 16 shows that the temperature response for the *U*-type flow configuration for the same Reynolds number for nonuniform flow condition. The nonuniform flow distribution is represented by a characteristic parameter m^2, which is estimated to be 3.8. The cold and hot side responses are compared to the theoretical simulation; marginal deviations are observed in transient and steady state regimes. These deviations are small and the reason for the discrep-

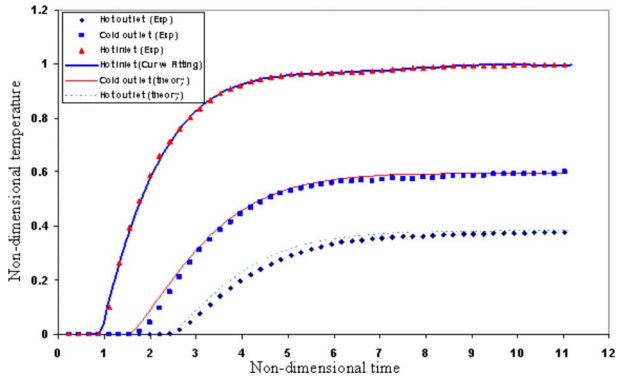

Fig. 15 Comparison of temperature response with theoretical model for *U*-type Re=1110, *N*=31, NTU=1.6, and $R_{g2}=1$ for uniform flow distributions ($m^2=0.05$)

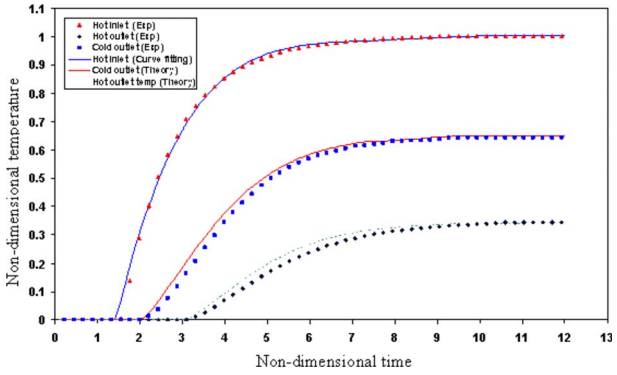

Fig. 17 Comparison of experimental temperature response with the theoretical model for *Z*-type Re=780, *N*=31, NTU=1.8, and $R_{g2}=1$ for uniform distributions ($m^2=0.05$)

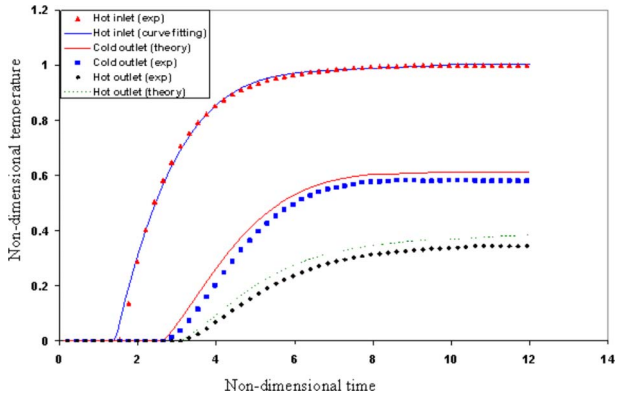

Fig. 18 Comparison of experimental temperature response with the theoretical model for *Z*-type Re=780, *N*=31, NTU=1.8, and R_{g2}=1 for flow distribution (m^2=3.5)

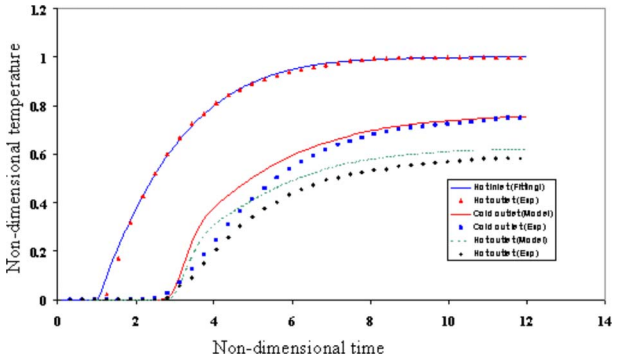

Fig. 19 Comparison of experimental temperature response with the theoretical model for 1–2 pass arrangement Re=1110, *N*=31, NTU=2.0, and R_{g2}=0.9 for flow distribution m^2=3.8

ancies is explained at the end of this section.

Figure 17 shows the responses for *Z*-type flow configuration at Re of 780 with uniform flow distribution and experimental results are in agreement with the theoretical model in transient and steady state regimes. It is observed that the initial delay is more in cold and hot fluid sides when compared to the *U*-type flow configuration, because in this case, all the fluid streams have the same flow path length between the inlet and exit. Figure 18 shows comparison for the *Z*-type flow configuration with nonuniform flow distribution condition at the same Reynolds number. The temperature responses show marginal deviation in both transient and steady state regimes.

Figure 19 shows the comparison of experimental temperature response with the theoretical simulation for the 1–2 pass arrangement. The theoretical trends show deviation in slope of the responses, which is due to the approximation of the actual (second-order) simulation results with the first-order function and obtain the transfer function for one module of the heat exchanger. This first-order function is given as input to the next module of the heat exchanger. This transformation of the data from one module to the other module of the heat exchanger may lead to this deviation. The difference in temperature between the theoretical and experimental response in the steady state is due to the same reason, which will be explained for single-pass experimental response. Marginal deviations between the experimental and theoretical responses are observed in transient and steady state regimes under nonuniform flow distribution condition. These deviations are due to the heat loss through the heat exchanger end plates and the plate edges. Because the flow distribution is nonuniform, some of the plates at the end will have very less flow rates; it leads to the imbalance in flow rates of both fluids. Even though these deviations are small, it can be estimated at the steady state. The deviations from experimental to theoretical results at steady state are almost equal to the difference in energy balance as given in Table 1. This proves that the marginal deviation of the theoretical results from experimental data is not due to inaccuracy of the model but due to the limitations of the energy balance in the experiments.

7 Conclusion

An experimental and numerical study has been carried out to investigate the effect of port to channel flow maldistribution on the transient response of plate heat exchangers. Appropriate experiments have been conducted to verify the transient numerical models for single-pass and multipass PHEs at various flow rates. The comparison between the *U*-type and *Z*-type flow configurations is also made with uniform and nonuniform distributions. The results indicate that the transient features, such as initial delay, response time, and time required to reach steady state, are affected due to the flow nonuniformity. The experimental results confirms the well known fact in the literature that the *Z*-type PHE is more strongly affected by maldistribution than the *U*-type in both transient and steady state regimes. The experimental results are in good agreement with the theoretical models, which are solved by simple finite-difference method. The theoretical model is clearly successful in predicting the transient features, such as initial delay, response time, and asymptotic values, and also agree well with the experimental observations. Hence, this analysis confirms that the flow distribution can and should be evaluated separately while axial dispersion can take care of fluid backmixing alone.

Nomenclature

English Symbols

A = heat transfer area per effective plate, m^2
A_c = free flow area in a channel, m^2
b = plate spacing, m
C = heat capacity of resident fluid(s), J K^{-1}

Table 1 Comparison of the experimental and theoretical results

S. No	Flow arrangement	Reynolds number	Flow distribution	m^2	Energy balance difference (%)	Deviation between experiment and theory (%)
1	*U*-type	1110	Uniform	0.05	0.9	1.1
2	*U*-type	1110	Nonuniform	3.8	5.0	5.3
3	*U*-type	880	Uniform	0.05	1.1	1.4
4	*U*-type	880	Nonuniform	3.6	4.2	4.4
5	*Z*-type	780	Uniform	0.05	0.8	1.1
6	*Z*-type	780	Nonuniform	3.5	7.1	7.3

C_{Td} = pressure loss coefficient at the inlet port
C_{Td}^{*} = pressure loss coefficient at the exit port
d_e = equivalent diameter of channel, $2b$, m
d_j = elements of matrix $\bar{D}$
D = axial dispersion coefficient, W m^{-1} K^{-1}
f = fanning friction factor
$f(Z)$ = inlet temperature function
h = heat transfer coefficient, W m^{-2} K^{-1}
i = square root of -1
K_i = $(\mathrm{NTU}_i/2)R_{wi}(R_2 \cdot R_N)^{m_{i+1}}$ Eq. (10)
l_c = path traversed by fluid particle between two consecutive channels, m
L = fluid flow length in a channel, m
m_j = $j-[j/2]$, where j is an integer
m = flow distribution parameter, Eq. (3)
$\dot{m}$ = mass flow rate, kg s^{-1}
n = number of channels on one side
N = number of channels
NTU_1 = number of transfer units of the heat exchanger
Nu = Nusselt number
Pe = Axial dispersive Peclet number, $\dot{w}L/A_cD$
Pr = Prandtl number
$rh(i)$ = ratio, h_i/h_a
$rv(i)$ = ratio, v_a/v_i
R_2 = Heat capacity rate ratio in the channels, $\dot{w}_{a2}/\dot{w}_{a1}$
Re = Reynolds number
R_c = wall heat capacity rate ratio, C_w/C_1
R_{g2} = heat capacity rate ratio of the combined flow, $\dot{w}_{g2}/\dot{w}_{g1}$
$R_{g\tau}$ = characteristic rate ratio of the combined flow, τ_{rg2}/τ_{rg1}
R_N = ratio U_{a2}/U_{a1}
R_{wi} = ratio, $\dot{w}_i/\dot{w}_a$
R_τ = characteristic time ratio in channels, τ_{ra2}/τ_{ra1}
S = slope, ratio of difference in dimensionless temperature to dimensionless time, $\Delta t/\Delta z$
t = non dimensional temperature, $(\theta-\theta_{g1,in})/(\theta_{g2,in}-\theta_{g1,in})$
u = unit step function
U_{a1} = $hA/\dot{w}_{a1}$
$U_{a1(2)}$ = $(hA/\dot{w}_a)_{1(2)}$
U_c = channel velocity, m/s
$\dot{w}$ = heat capacity rate of the fluid in channel, $\dot{m}C_p$
x = dimensionless space coordinate along the channel, X/L
X = space coordinate, m
y = dimensionless space coordinate along the port
z = dimensionless time τ/τ_{a1}

Greek Symbols

β_j = jth eigenvalue of matrix A
θ = temperature, K
τ = time, s
τ_{ra} = residence time in case of uniform distribution, $C/\dot{w}_a$
ζ_c = average channel friction coefficient
ϕ = dimensionless phase lag (cumulative value)
$\Delta\phi$ = dimensionless phase lag (discrete value), $\Delta\tau_i/\tau_{ra1}$
ν = viscosity of the fluid, m/s^2

Subscripts

a = the case of uniform flow distribution
g = combined flow before departing into channels
i = ith channel
W = plate
Wi = ith plate
0 = initial
1 = the fluid in odd channels
2 = the fluid in even channels

References

[1] Watson, E. L., McKillop, A. A., Dunkley, W. L., and Perry, R. L., 1960, "Plate Heat Exchanger—Flow Characteristics," Ind. Eng. Chem., **52**(9), pp. 733–744.
[2] Buonopane, R. A., Troupe, R. A., and Morgan, J. C., 1963, "Heat Transfer Design Method for Plate Heat Exchangers," Chem. Eng. Prog., Symp. Ser., **59**(7), pp. 57–61.
[3] Wolf, J., 1964, "General Solutions of the Equations of the Parallel Flow Multi Channel Heat Exchangers," Int. J. Heat Mass Transfer, **7**, pp. 901–919.
[4] Jackson, B. W., and Troupe, R. A., 1966, "Plate Heat Exchanger Design by ε-NTU Method," Chem. Eng. Prog., Symp. Ser., **62**(64), pp. 185–190.
[5] McKnight, G. W., and Worley, C. W., 1953, "Dynamic Analysis of Plate Heat Exchanger System," *ISA Proceedings*, pp. 68–75, Paper No.53-6-1.
[6] Masubuchi, M., and Ito, A., 1977, "Dynamic Analysis of Plate Heat Exchanger System," Eng. Trans., **142**, pp. 434–441.
[7] Zaleski, T., and Tajszerski, J., 1980, "Dynamics of Plate Heat Exchangers," *Chemplant '80, Computations in Design and Erection of Chemical Plants*, Vol. 2, Heviz, Sept. 3–5, Hungarian Chemical Society, Budapest, pp. 770–790.
[8] Khan, A. R., Baker, N. S., and Wardle, A. P., 1988, "The Dynamic Characteristics of a Counter-Current Plate Heat Exchanger," Int. J. Heat Mass Transfer, **31**, pp. 1269–1278.
[9] Das, S. K., and Roetzel, W., 1995, "Dynamic Analysis of Plate Heat Exchangers With Dispersion in Both Fluids," Int. J. Heat Mass Transfer, **38**, pp. 1127–1140.
[10] Das, S. K., Spang, B., and Roetzel, W., 1995, "Dynamic Behaviour of Plate Heat Exchangers—Experiments and Modelling," J. Heat Transfer, **117**, pp. 859–864.
[11] Roetzel, W., and Na Ranong, C., 1999, "Consideration of Maldistribution in Heat Exchangers Using the Hyperbolic Dispersion Model," Chem. Eng. Process., **38**, pp. 675–681.
[12] Roetzel, W., and Na Ranong, C., 2000, "Axial Dispersion Models for Heat Exchangers," Int. J. Heat Technology, Calore e Technologia, **18**, pp. 7–17 (http://termserv.casaccia.enea.it/eurotherm/H&T.html).
[13] Sahoo, R. K., and Roetzel, W., 2002, "Hyperabolic Axial Dispersion Model for Heat Exchangers," Int. J. Heat Mass Transfer, **45**, pp. 1261–1270.
[14] Datta, A. B., and Majumdar, A. K., 1980, "Flow Distribution in Parallel and Reverse Flow Manifolds," Int. J. Heat Fluid Flow, **2**(4), pp. 253–262.
[15] Datta, A. B., and Majumdar, A. K., 1980, "Flow Distribution in Parallel and Reverse Flow Manifolds," Int. J. Heat Fluid Flow, **26**(9), pp. 321–1327.
[16] Bassiouny, M. K., and Martin, H., 1984, "Flow Distribution and Pressure Drop in Plate Heat Exchangers-I, U-Type Arrangement," Chem. Eng. Sci., **39**, pp. 693–700.
[17] Bassiouny, M. K., and Martin, H., 1984, "Flow Distribution and Pressure Drop in Plate Heat Exchangers-II, Z-Type Arrangement," Chem. Eng. Sci., **39**(4), pp. 701–704.
[18] Tereda, F. A., Srihari, N., Suden, B., and Das, S. K., 2007, "Experimental Investigation on Port to Channel Flow Maldistribution in Plate Heat Exchangers," Heat Transfer Eng., **28**(5), pp. 435–442.
[19] Prabhakara Rao, B., Krishna Kumar, P., and Das, S. K., 2002, "Effect of Flow Distribution to the Channels on the Thermal Performance of a Plate Heat Exchanger," Chem. Eng. Process., **41**, pp. 49–58.
[20] Prabhakara Rao, B., and Das, S. K., 2004, "Effect of Flow Distribution to the Channels on the Thermal Performance of a Multi-Pass Plate Heat Exchanger," Heat Transfer Eng., **25**(8), pp. 48–59.
[21] Prabhakara Rao, B., and Das, S. K., 2004, "Experimental and Analytical Studies on the Influence of Flow Maldistribution on the Pressure Drop Across a Plate Heat Exchanger," ASME Trans. J. Fluids Eng., **126**, pp. 681–691.
[22] Prabhakara Rao, B., Sunden, B., and Das, S. K., 2005, "An Experimental and Theoretical Investigation of the Effect of Flow Maldistribution on the Thermal Performance of Plate Heat Exchangers," ASME Trans. J. Heat Transfer, **125**, pp. 332–443.
[23] Srihari, N., Prabhakara Rao, B., Sunden, B., and Das, S. K., 2005, "Transient Response of Plate Heat Exchangers Considering Effect of Flow Maldistribution," Int. J. Heat Mass Transfer, **48**, pp. 3231–3243.
[24] Dankwerts, P. V., 1953, "Continuous Flow Systems—Distribution of Residence Times," Chem. Eng. Sci., **2**, pp. 1–13.

M. A. Panzer
Department of Mechanical Engineering,
Stanford University,
Room 101, Building 530,
440 Escondido Mall,
Stanford, CA 94305
e-mail: mpanzer@stanford.edu

G. Zhang

D. Mann

Department of Chemistry,
Stanford University,
Room 125, William Keck Science Building,
Stanford, CA 94305

X. Hu
Intel Corporation,
5000 W Chandler Blvd.,
Chandler, AZ 85226

E. Pop
Department of Electrical and Computer Engineering,
University of Illinois at Urbana-Champaign,
Urbana, IL 61801-2918

H. Dai
Department of Chemistry,
Stanford University,
Room 125, William Keck Science Building,
Stanford, CA 94305

K. E. Goodson
Department of Mechanical Engineering,
Stanford University,
Room 101, Building 530,
440 Escondido Mall,
Stanford, CA 94305

Thermal Properties of Metal-Coated Vertically Aligned Single-Wall Nanotube Arrays

Owing to their high thermal conductivities, carbon nanotubes (CNTs) are promising for use in advanced thermal interface materials. While there has been much previous research on the properties of isolated CNTs, there are few thermal data for aligned films of single wall nanotubes. Furthermore, such data for nanotube films do not separate volume from interface thermal resistances. This paper uses a thermoreflectance technique to measure the volumetric heat capacity and thermal interface resistance and to place a lower bound on the internal volume resistance of a vertically aligned single wall CNT array capped with an aluminum film and palladium adhesion layer. The total thermal resistance of the structure, including volume and interface contributions, is $12\ m^2\ K\ MW^{-1}$. *The data show that the top and bottom interfaces of the CNT array strongly reduce its effective vertical thermal conductivity. A low measured value for the effective volumetric heat capacity of the CNT array shows that only a small volume fraction of the CNTs participate in thermal transport by bridging the two interfaces. A thermal model of transport in the array exploits the volumetric heat capacity to extract an individual CNT-metal contact resistance of* $10\ m^2\ K^1\ GW^{-1}$ *(based on the annular area* $A_a = \pi db$*), which is equivalent to the volume resistance of* 14 nm *of thermal* SiO_2. *This work strongly indicates that increasing the fraction of CNT-metal contacts can reduce the total thermal resistance below* $1\ m^2\ K\ MW^{-1}$. [DOI: 10.1115/1.2885159]

Keywords: vertically aligned carbon nanotubes, thermal interface resistance, thermoreflectance thermometry, thermal interface material, single wall carbon nanotube

Introduction

The outstanding thermal properties of carbon nanotubes (CNTs), particularly their extraordinary thermal conduction properties, have generated considerable interest and research activity. Past work investigated the thermal properties of individual single wall nanotubes [1–9], multiwalled nanotubes [10,11], bulk films of nanotubes [12,13], nanotube composites [14–19], and aligned arrays of mulitwalled nanotubes [20–22]. A very promising application is the use of vertically aligned arrays of CNTs as thermal interface materials (TIMs) for electronic systems. TIMs require a high thermal conductivity, a low thermal interface resistance with the adjacent microprocessor and heat sink, as well as significant mechanical compliance to help minimize the impact of mismatched thermal expansion coefficients. Many TIM materials, such as particle-filled organics and related composites, offer excellent mechanical compliance with the penalty of relatively poor thermal conductivity. Other materials, such as alloyed metals and eutectics, offer relatively good thermal conduction properties with the penalty of poor mechanical compliance and reliability concerns related to thermal cycling. CNT films, which consist of many flexible nanotubes, may eventually provide both high thermal conductivity and lateral compliance, a truly unique combination of properties that could be very attractive for interfaces in electronic systems. However, past work has suggested that the thermal performance of CNT films is impeded by high thermal interface resistances, indicating that more detailed measurements and improved fabrication methods will be needed.

The thermal conductivity of individual single wall CNTs (SWNTs) and multiwall CNTs (MWNTs) has been the subject of recent theoretical and experimental research activity. Experimental and molecular dynamic studies have yielded room temperature

Contributed by the Heat Transfer Division of ASME for publication in the JOURNAL OF HEAT TRANSFER. Manuscript received October 26, 2006; final manuscript received September 17, 2007; published online April 8, 2008. Review conducted by Suresh V. Garimella.

thermal conductivities of individual SWNTs in the range of 2500–6600 W m^{-1} K^{-1} [1–4]. For MWNTs, past research yielded similar values in the range of 2000–3000 W m^{-1} K^{-1} [10,11]. Theoretical works predict that ballistic transport effects, interface scattering, and modification to the phonon modes in submicron length individual SWNTs tend to reduce their thermal conductivity to values below 350 W m^{-1} K^{-1} [5–9]. Likewise, measurements of bulk CNT films yielded lower thermal conductivities in the range of 20–200 W m^{-1} K^{-1} [12,13]. The discrepancy between the thermal conductivities of individual CNTs and their value in bulk films can be attributed to various effects. In particular, tube-tube contact, tube-matrix contact, and an increased defect density due to bulk film preparation methods may reduce the phonon mean free path compared to its value in individual tubes. The tube-matrix contact has been the focus of several studies [14,15,23]. Furthermore, the defined area of heat flow through the nanoscale geometries of both the individual constituent tubes and the film itself is often ambiguous and subject to variation, directly influencing the reported values of CNT thermal conductivities. This problem is particularly acute with MWNT films, which often exhibit significant variations in individual tube cross-sectional areas within a film.

Although the bulk thermal performance of CNT films falls short of the theoretical expectations, the use of CNTs as fillers in advanced TIMs and in nanostructured composite films greatly improves the thermal performance of the material. A CNT volume fraction of 1% showed an increase in the effective thermal conductivity of 2.5 in silicon oil [16] and 125% for epoxy [17]. Similarly, by suspending SWNTs randomly oriented in a polymethyl methacrylate (PMMA) composite, Guthy et al. [18] measured a thermal conductivity enhancement that saturated at 240% for 6 vol % SWNTs. Additionally, Hu et al. [19] combined CNTs with traditional nickel fillers, creating a sevenfold increase in the effective thermal conductivity of the base fluid, twice that of a nickel nanoparticle filler alone.

Other investigations showed that creating vertically aligned CNT films better utilizes the outstanding thermal conductivity of individual CNTs. Using the 3ω method, Hu et al. [20] measured the room temperature thermal conductivity of a 13 μm thick vertically aligned MWNT film grown on silicon to be 75 W m^{-1} K^{-1}, which outperforms that of randomly oriented tube samples. However, the total thermal resistance of the aligned CNT TIM was found to be 16 m^2 K MW^{-1}, which still falls well short of theoretical expectations. Yang et al. [21] performed a similar measurement of MWNT films using a thermoreflectance technique and found the effective thermal conductivities to be around 15 W m^{-1} K^{-1}, with total thermal resistances falling in the range of 0.8–2.9 m^2 K MW^{-1}. Even accounting for porosity effects, the reduced performance of these aligned MWNT films indicates that the thermal boundary resistance between the CNT and the substrate is the problem.

Much of the variation observed in the previous data can be attributed to the impact of thermal interface resistances in CNT films. The relative importance of thermal interface resistance in CNT based TIMs was recently confirmed by Tong et al. [22] in a transient phase sensitive photothermal measurement of an aligned MWNT TIM. The TIM was formed by dry adhesion of a 7 μm thick MWNT array, grown on a Si wafer, to a glass plate. The total resistance of the TIM was measured to be 12 m^2 K MW^{-1}, which was dominated by the dry glass interface resistance of 11 m^2 K MW^{-1}. The importance of the thermal interface resistance in CNT arrays motivates its further study as well as the need for metrology that focuses on this property.

In this paper, we measure and model the room temperature thermal properties of a 28 μm thick metal-coated vertically aligned SWNT film using a nanosecond thermoreflectance technique. Our objective is to extract, model, and illuminate the governing physics of the interface resistance. A 6 ns heating pulse from a frequency doubled Q-switched Nd:YAG (yttrium aluminum garnet) laser generates a transient temperature field in the metalized film, and the combination of submicrosecond laser-reflectance thermometry and effective medium modeling extracts the vertical distribution of area-averaged thermal properties in the system. The transient time scales of the measurement provide a means to separate the relative importance of thermal resistance within the film from those of the film boundaries. Isolating the thermal boundary resistances and measurement of the CNT volumetric heat capacity enables an understanding of the low measured effective thermal conductivity of the aligned SWNTs. This study provides insight into the physical mechanisms governing the thermal resistance in aligned CNT films, which will enable innovations in fabrication technology to reduce the total thermal resistance and lead to promising interface materials.

Experimental Method

Sample Preparation. The aligned SWNT sample was prepared as follows. First, an iron film 1–2 Å thick is deposited using electron beam evaporation on a 10 nm thick thermal oxide layer grown on the silicon substrate. Subsequent annealing in oxygen at 550°C produced a monolayer of ~1.3 nm diameter iron clusters to act as catalysts for the CNT growth. The CNT synthesis was carried out in a coupled-rf chemical vapor deposition (CVD) plasma system with a mixture of methane, hydrogen, and oxygen. Additional details of the CNT growth process are discussed in Ref. [24].

The scanning electron microscopy (SEM) profile of the sample in Fig. 1(*a*) shows that the tube length is 28 μm. Raman data [24] indicate that the SWNT diameter d is in the range of 1–2 nm, with the average being close to the average catalyst diameter of ~1.3 nm. Since the SWNT growth conditions yield approximately one nanotube per iron catalyst cluster [24], we estimate the SWNT number density to be 8.7×10^{16} m^{-2} based on the thickness of the deposited catalyst layer and cluster diameter after annealing. This number density corresponds to a volume fraction of ~12% based on the average SWNT annular area $A_a=\pi db$, where we use an average diameter of $d=1.3$ nm and $b=3.4$ Å, the thickness of a graphene plane. A premetalization topographic profile, produced by scanning atomic force microscopy (AFM), of the top of the CNT film is shown in Fig. 1(*b*) and indicates that the rms roughness of the film is ~60 nm.

Prior to the evaporation of the 160 nm thick aluminum film, an initial evaporation of a 20 nm thick palladium film on the exposed CNT ends enhances the metal-CNT contact interface. A SEM image (Fig. 1(*c*)) of the top of the metal film taken after deposition shows that the surface is rough and porous on the submicron scale. The potential effects of the film porosity on its optical properties will be considered in the following section.

Experimental Setup and Procedure. The thermal properties of the metallized SWNT film are measured using a thermoreflectance technique in which a high power pump laser induces a transient temperature field in the metal film. The reflected intensity of a second low power cw probe laser, being proportional to the metal temperature, provides a dynamic measurement of the temperature response of the metal film. The thermoreflectance technique has been used in the nanosecond regime to characterize the thermal properties of thin films [21,25,26] in the picosecond regime to measure both the thermal properties of thin films and their interfaces [27–29] and in the femtosecond regime to measure electron and phonon processes [30,31].

Figure 2 is a schematic of the optical path and experimental configuration along with a schematic of the sample geometry. A 650 MHz photodiode and amplifier measure the reflected intensity of a 10 mW diode laser at 637 nm wavelength, which is focused on the sample with a spot size of approximately 10 μm. The metal film on top of the CNTs is heated using a 10 Hz, 6 ns pulse width Nd:YAG laser, frequency doubled to 532 nm.

The transient metal temperature is measured through the tem-

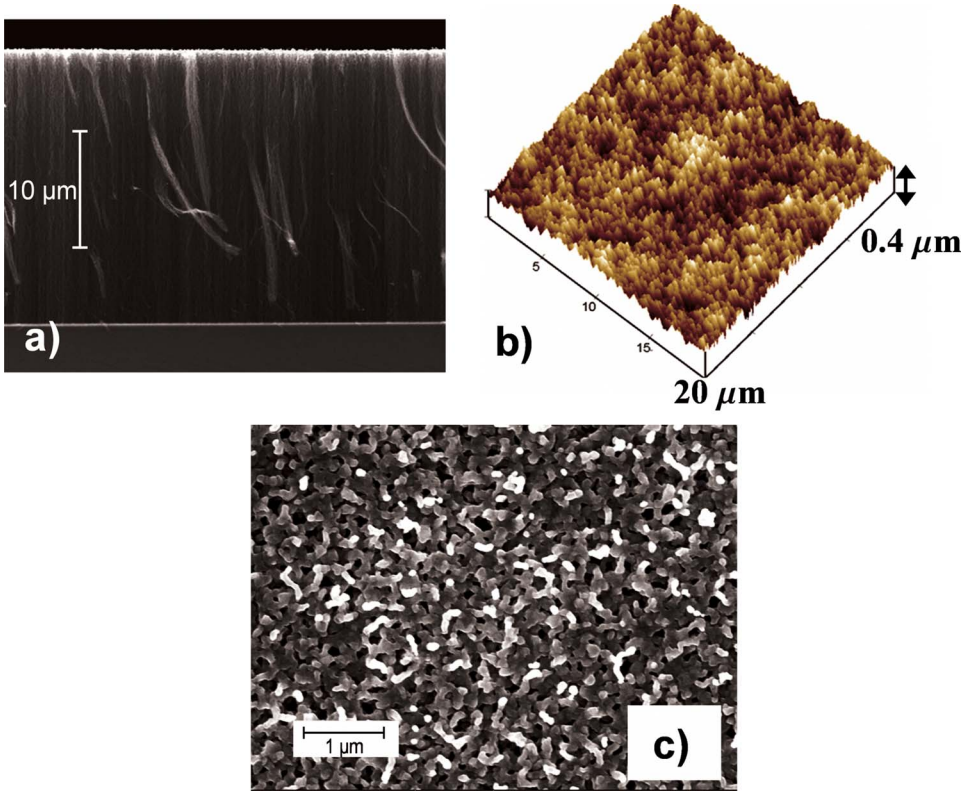

Fig. 1 (*a*) **SEM profile of aligned SWNTs grown on Si—the tube length is 28 μm. The SWNT diameter ranges between 1 nm and 2 nm, with an average of approximately 1.3 nm. (*b*) AFM topographic profile of the top of the CNT film, which indicates that the rms surface roughness is ~60 nm. (*c*) SEM of the top of the metal film after it has been deposited on CNTs. The image shows that the metal film is porous at a scale below 100 nm.**

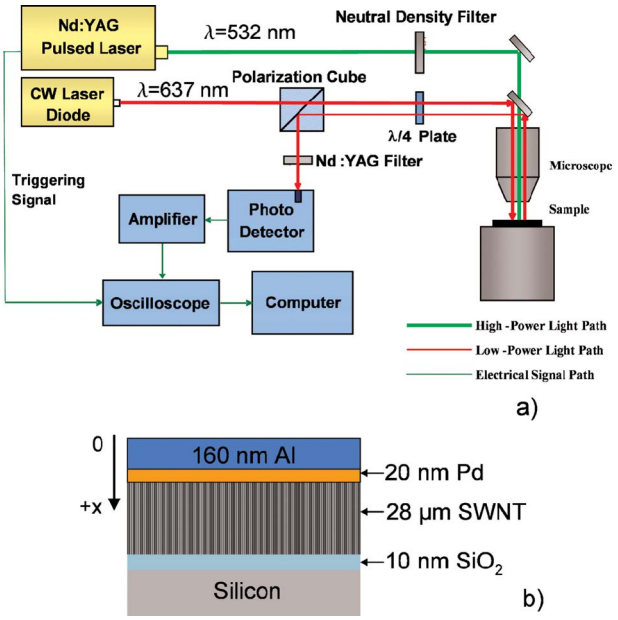

Fig. 2 (*a*) **Schematic of the thermoreflectance thermometry experimental setup including the optical and signal paths. (*b*) Schematic of the sample geometry. The initial deposition of a 20 nm thick layer of palladium on the SWNT ends forms an adhesion layer with the 160 nm thick aluminum film used for thermal reflectance thermometry.**

perature dependence of its dielectric constant [32]. The linearized temperature dependent reflectivity [33], defines the thermoreflectance coefficient C_{tr} as

$$\frac{\Delta R}{R_0} \equiv C_{tr}\Delta T \tag{1}$$

where R_0 is a reference reflectivity and T is the metal temperature.

Since for most metals, C_{tr} is approximately constant [32,34], the reflected probe intensity is proportional to the metal surface temperature.

The surface topography and porous structure of the metalized CNT films pose significant challenges for photothermal diagnostics. Due to porosity, the optical radiation may be absorbed on both the surface of the metal film and in its pores. However, since all thermal diffusion time scales in the aluminum film are subnanosecond and below the temporal resolution of the equipment, it is inconsequential whether the radiation is absorbed strictly on the metal surface or within the pores of the metal layer.

The transmission of optical radiation through the metal may lead to the possibility of energy absorption in the structure underlying the film, complicating the solution to the heat diffusion equations. Data from the image analysis of the SEM image in Fig. 1(*c*) bounds the potential unmetallized regions to less than 5%. The subwavelength of the nature of the pores further reduces the transmitted radiation by a factor of $(r/\lambda)^4$ [35,36], where r is the hole radius yielding a net energy transmission factor less than 5×10^{-4}. Furthermore, the near field radiation is appreciable only within $\sim 4r$ [36] of the hole and is thus much less than the thermal diffusion distance (~ 4 μm) into the CNT film during the laser pulse. These conclusions render the transmission of optical radiation through the metal film insignificant.

The relatively large surface roughness of the metal film

(~100 nm) augments absorption such that care must be taken to avoid damage and delamination. The mechanical compliance, porosity, and mismatched thermal expansion behavior of the metal coating and underlying CNT film may lead to significant temperature induced changes in the surface topography and associated thermoreflectance coefficient. The value of C_{tr} may also be influenced by microstructural changes in the metal film with temperature, which are related to the reflectivity through electron scattering and the plasma frequency.

We address the above concerns about photothermal interaction with the film through a strong reduction in the heating laser fluence and careful verification that C_{tr} is constant and reproducible in the temperature range of the measurement. For different laser powers, the normalized thermal response trace collapsed to a single shape that depends only on the thermal properties within the structure. Furthermore, the amplitude of the peak reflected probe intensity scaled in direct proportion to the pump power. These results indicate that the interaction of the metal with both lasers is linear and reproducible.

Data Extraction Model and Method. To extract the thermal properties of the CNT film, we fit the experimentally measured thermal response to an analytical solution of the heat diffusion equation based on effective area-averaged thermal properties. As long as heat is fully absorbed by the metal layer and is forced to conduct through the CNT film and into the substrate, the solution of the heat diffusion equation using effective area-averaged properties is a fully rigorous mathematical treatment of the physics and does not require knowledge of the CNT volume fraction. Solving the heat diffusion equation reduces to a 1D problem since the diameter of the heating pulse ($d \sim 6$ mm) is much greater than any of the thermal diffusion distances into the structure during the measurement. The governing equation in each layer is

$$\frac{\partial T_j(x,t)}{\partial t} - \alpha_j \frac{\partial^2 T_j(x,t)}{\partial x^2} = 0 \tag{2}$$

where T_j is the temperature and α_i is the thermal diffusivity of the jth material. We solve the 1D heat diffusion equation by transforming Eq. (2) to the frequency domain

$$\frac{\partial^2 \theta_j(\omega,x)}{\partial x^2} + \frac{i\omega}{\alpha_j}\theta_j(\omega,x) = 0 \tag{3}$$

where θ_j is the Fourier transform of the temperature field and which has the general solution

$$\theta_j(\omega,x) = a_j(\omega)e^{i\sqrt{i\omega/\alpha_j}x} + b_j(\omega)e^{-i\sqrt{i\omega/\alpha_j}x} \tag{4}$$

The laser heating is modeled as a heat flux boundary condition on top of the metal film with a Gaussian shaped heat pulse

$$q''_{laser}(t) = -k_{Al}\left.\frac{\partial T_{Al}(t,x)}{\partial x}\right|_0 \tag{5}$$

$$q''_{laser}(t) = \sqrt{\frac{1}{\pi\tau^2}}\rho_{Al}L_{Al}c_{p,Al}\Delta T_{max}e^{-t^2/\tau^2} \tag{6}$$

where τ is the e^{-1} laser pulse width (6 ns), ΔT_{max} is the peak temperature change, k_{Al}, ρ_{Al}, L_{Al}, and $c_{p,Al}$ is the aluminum thermal conductivity, density, thickness, and heat capacity, respectively. The silicon wafer is assumed to be semi-infinite since the thermal diffusion time through the silicon is much larger than the microsecond time scale of the measurement.

The interfaces between the aligned CNT film and both the metal film and the SiO_2 film provide four boundary conditions,

$$q''_{Al\text{-}CNT} = (R''_{CNT\text{-}Pd,eff})^{-1}(T_{Al}(L_{Al}) - T_{CNT}(0)) = -k_{Al}\left.\frac{\partial T_{Al}}{\partial x}\right|_{L_{Al}} \tag{7}$$

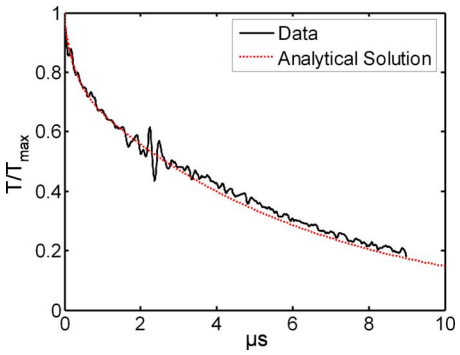

Fig. 3 Typical thermal response trace data for a particular measurement (solid) for the 28 μm sample along with the best-fit analytical solution evaluated with the average best-fit parameters summarized in Table 1 below (dashed). The data show two characteristic decay time scales during the measurement: the initial rapid decay lasting ~0.5 μs followed by a longer decay lasting ~4 μs.

$$-k_{Al}\left.\frac{\partial T_{Al}}{\partial x}\right|_{x_{Al}=L_{Al}} = -k_{CNT,eff}\left.\frac{\partial T_{CNT}}{\partial x}\right|_{x_{CNT}=0} \tag{8}$$

$$q''_{CNT\text{-}SiO_2} = (R''_{CNT\text{-}SiO_2,eff})^{-1}(T_{CNT}(L_{CNT}) - T_{SiO_2}(0)) = -k_{SiO_2}\left.\frac{\partial T_{SiO_2}}{\partial x}\right|_{x_{SiO_2}=0} \tag{9}$$

$$-k_{CNT,eff}\left.\frac{\partial T_{Al}}{\partial x}\right|_{x_{CNT}=L_{CNT}} = -k_{SiO_2}\left.\frac{\partial T_{SiO_2}}{\partial x}\right|_{x_{SiO_2}=0} \tag{10}$$

where $k_{CNT,eff}$ is the area-averaged CNT thermal conductivity and $R''_{CNT\text{-}Pd,eff}$ and $R''_{CNT\text{-}SiO_2,eff}$ are the area-averaged contact resistances between the CNTs and the palladium adhesion layer and oxide films, respectively. We define the resistance at the metallized contact as $R''_{CNT\text{-}Pd,eff}$ because the nanotubes directly contact the palladium adhesion layer underlying the aluminum film. An inverse Fourier transform converts the frequency domain solution back to the time domain, which we then fit to the experimental thermal data using a least squares curve fit algorithm.

Fitting the thermal model to the measured data is an inverse heat transfer analysis requiring the simultaneous fit of the four unknown parameters in the governing equations: $k_{CNT,eff}$, $C_{CNT,eff}$ (through $\alpha_{CNT,eff}$), $R''_{CNT\text{-}Pd,eff}$, and $R''_{CNT\text{-}SiO_2,eff}$. The impact and sensitivity of variation in each parameter on the shape of the thermal response is unique and evident at different time scales because each appears in a unique way though the governing equations (Eqs. (3) and (7)–(10)) and is localized in the vertical direction. Since the measurement is capable of resolving time scales below the thermal diffusion time through the CNT film, these properties can be accurately and individually resolved. We verified this capability by a mathematically rigorous parametric variation study of the best-fit solution of the heat diffusion equation to the experimental data.

Results and Discussion

Figure 3 shows a representative thermal response for the sample along with the least squares best-fit analytical solution evaluated with the average of the extracted properties. Nine measurements at multiple locations on the samples and at multiple laser pump powers were individually fit to the analytical heat diffusion model, and the effective parameters were averaged to produce the results shown in Table 1. Table 1 shows the corresponding rms error in the data, which is dominated by variations

Table 1 Best-fit values averaged from multiple measurements of $C_{CNT,eff}$, $R''_{CNT\text{-}Pd,eff}$, $R''_{CNT\text{-}SiO_2,eff}$, and $k_{CNT,eff}$ for the 28 μm thick sample along with their associated uncertainty. The uncertainty is calculated from the rms variation in extracted parameters individually fitted to multiple measurements.

Parameter	Average result	Uncertainty (%)
$C_{CNT,eff}$	5.2 kJ m^{-3} K^{-1}	12%
$R''_{CNT\text{-}Pd,eff}$	2.9 m^2 K^1 MW^{-1}	21%
$R''_{CNT\text{-}SiO_2,eff}$	9.1 m^2 K^1 MW^{-1}	31%
$k_{CNT,eff}$	>8 W m^{-1} K^{-1}	—

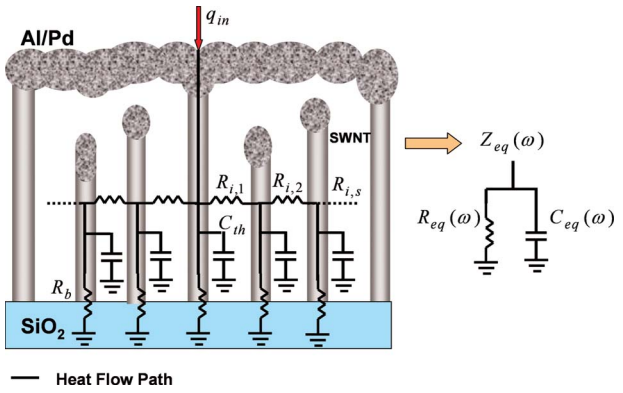

Fig. 4 Schematic illustrating the hypothesis that a subset of the CNTs is in good thermal contact with the porous and discontinuous evaporated film. The data suggest that the overwhelming majority of the heat transport is brought about by longer tubes that fully contact the metal film. We use a thermal circuit model to account for lateral thermal transport in the CNT film. The heat flows into the central tube that is in thermal contact with the metal film and then flow laterally through the intertube coupling resistance to surrounding tubes. We reduce the thermal network to a frequency dependant parallel equivalent *RC* thermal circuit, which is what is experimentally measured.

in the shape of the trace and uncertainty due to amplitude noise. Errors due to the sensitivity of the least squares fitting algorithm applied to a single thermal response trace generally contribute less than 10% error for each parameter.

An estimate of the thermal diffusion time through the CNT film qualitatively explains the particular shape of the thermal trace in Fig. 3, which displays an initial rapid decay lasting <0.5 μs followed by a second, slower decay lasting ~4 μs. The characteristic thermal diffusion time through the SWNT film is given by $t_{diff}=L^2_{CNT}/\alpha_{CNT}$, where $L_{CNT}=28$ μm is the thickness of the CNTs and α_{CNT} is the individual CNT thermal diffusivity. From the measurement of $c_p=660$ mJ g^{-1} K^{-1} by Hone et al. [37] and the CNT unit cell volume, we estimate $C_{v,a}$ to be 1.5 MJ m^{-3} K^{-1}, which is the volumetric heat capacity for an individual SWNT compatible with the area definition, $A_a=\pi db$. Combined with a value of $k_{CNT}=3600$ W m^{-1} K^{-1} [4], $\alpha_{CNT}\sim 2.4\times10^{-3}$ m^2 s^{-1} and $t_{diff}=0.33$ μs, which is in reasonable agreement with the time scale for the initial rapid decay demonstrated by the data. Consequently, the initial decay rate for times less than t_{diff} is relatively insensitive to the CNT-oxide contact resistance. A rigorous parametric variation study of the fitting parameters in the analytical model verified that the initial rapid decay rate is dominated by $R''_{CNT\text{-}Pd,eff}$ and that $R''_{CNT\text{-}SiO_2,eff}$ dominates the long-time decay characteristics.

Due to the large effective thermal interface resistances in the structure, the measurement only yields a potential lower bound of ~8 W m^{-1} K^{-1} for the area-averaged thermal conductivity of the array, which corresponds to a total CNT resistance below ~3.5 m^2 K MW^{-1}. No solution fit was attainable for thermal conductivities lower than this value, and the fit of the remaining parameters to the data trace was insensitive to conductivities at and above this value.

The data in Table 1 show that the effective CNT heat capacity is quite low, even accounting for the nanotube film porosity. Because the heat capacity is expected to be relatively insensitive to interface effects, the data suggest that only a fraction of the CNTs contribute to the volumetric specific heat. The ratio of the measured effective heat capacity to the volumetric heat capacity of an individual tube ($f_{eff,C}$) provides an estimate of the effective volume fraction of CNTs contributing to the thermal capacity in the structure,

$$f_{eff,C}=\frac{C_{CNT,eff}}{C_{v,a}}=0.0035 \tag{11}$$

which includes the contributions to the porosity occurring within an individual tube and does not require precise knowledge of the SWNT diameter. Based on an estimated average nanotube diameter of 1.3 nm, $f_{eff,C}$ corresponds to the number density of 2.5 $\times10^{15}$ m^{-2}, which is much less than the prior estimate of the SWNT yield based on the catalyst preparation conditions. A thermal model for transport within the nanotube structure presented in the subsequent section concludes that the effective volume fraction of CNTs contributing to the thermal resistance in the CNT array ($f_{eff,R}$) is nearly identical to $f_{eff,C}$. Scaling the lower bound on the area-averaged effective CNT thermal conductivity by this fraction provides an estimate of ~2300 W m^{-1} K^{-1} for the lower bound on the intrinsic conductivity of an individual SWNT measured in this study.

Since the CNT thermal resistance is small in comparison to the interface contributions, the total effective thermal resistance of the SWNT structure is determined by the sum of the boundary resistances to be $R''_{SWNT,tot}=12$ m^2 K MW^{-1}. This value is comparable to the values of 12–23 m^2 K MW^{-1} [20,22,38] for aligned MWNT array structures measured in prior work. The lower performance of the MWNT arrays may be due to the decrease in conformability of the shorter nanotubes, an increase in surface roughness of the MWNT arrays, or a significantly lower intrinsic resistance of MWNTs. Although the contact between the SWNT and the metal is probably much stronger than the van der Waal dominated contact in the MWNT experiments, the use of pressure most likely increased the number of tubes contacting the interface in the MWNT experiments.

Thermal Model for Conduction in CNT Films

In this section, we propose a hypothesis for the nanoscale SWNT-metal contact geometry that aims to explain the unexpectedly low values of the effective heat capacity and large interface resistances presented in Table 1. Related to this hypothesis, we develop an approximate thermal model of heat transport within the CNT film with the purpose of understanding the relationship between the effective volume fraction of tubes that contribute to the heat capacity and those that contribute to the thermal resistance within the CNT array. Through this understanding, we can estimate the intrinsic thermal contact resistance between an individual SWNT and a metal film from the measured data.

Since the aluminum film (Fig. 1(*c*)) is porous with its nominal thickness of 160 nm being comparable to the 60 nm rms CNT surface roughness, we believe that incomplete contact between the SWNTs and the metal film reduces the CNT volume fraction that contributes to heat conduction significantly below the 12 vol % of CNTs estimated from the catalyst preparation conditions. Figure 4 schematically illustrates our belief that the uneven CNT surface topography due to the variation in SWNT heights, combined with

the porosity of the metal film, causes the metal to make poor contact, particularly with the shorter nanotubes in the array.

To understand how the hypothesized contact geometry relates to the film thermal properties, we suggest a simple geometric model for the incomplete CNT-metal thermal contact in which we consider one individual SWNT that is in contact with the metal film and assume that the surrounding tubes are not in contact with the metal film. We will assume that heat flows into the central tube and can then couple to the surrounding tubes through an intertube coupling resistance R_i'' (m^2 K W^{-1}) (defined on the CNT perimeter area $A_p = \pi d L_{\mathrm{CNT}}$). Included in the inter-tube coupling resistance are all possible thermal transport channels, such as conduction, radiation, and occasional CNT-CNT contact between two aligned CNTs. Equating a thermal network model (Fig. 4) of heat transfer within the CNT array to an equivalent parallel effective thermal capacitance and resistance of the SWNT yields the experimentally measured effective thermal properties.

Because the interface resistance is much larger than the intrinsic SWNT resistance, we model the thermal impedance of each nanotube as a lumped thermal capacitor in parallel with a thermal boundary resistance R_b (K W^{-1}) between the SWNT and the oxide layer. The total complex thermal impedance of an individual CNT is

$$Z_{\mathrm{CNT}} = \frac{Z_C Z_b}{Z_C + Z_b} \tag{12}$$

where

$$Z_b = R_b \tag{13}$$

$$Z_C = \frac{1}{i\omega C_{\mathrm{th}}} \tag{14}$$

where $C_{\mathrm{th}} = C_{v,a} \pi d b L_{\mathrm{CNT}}$ is the total heat capacity of an individual tube. The total effective admittance of the CNT network is given by

$$\frac{1}{Z_{\mathrm{eff}}} = \frac{1}{Z_{\mathrm{CNT}}} + \frac{1}{Z_{s,\mathrm{eff}}} \tag{15}$$

where $Z_{s,\mathrm{eff}}$ is the total thermal impedance contribution from the surrounding neighboring tubes calculated below. Equating the admittance of Eq. (15) to the admittance of the equivalent parallel *RC* thermal circuit,

$$\frac{1}{Z_{\mathrm{eq}}} = \frac{1}{R_{\mathrm{eq}}(\omega)} + i\omega C_{\mathrm{th,eq}}(\omega) \tag{16}$$

yields

$$R_{\mathrm{eq}}(\omega) = \frac{1}{\mathrm{Re}\left(\frac{1}{Z_{\mathrm{eff}}}\right)} \tag{17}$$

$$C_{\mathrm{th,eq}}(\omega) = \frac{1}{\omega}\,\mathrm{Im}\left(\frac{1}{Z_{\mathrm{eff}}}\right) \tag{18}$$

A frequency-weighted average based on a representative thermal spectrum of the analytical solution of the metal temperature field yields the total R_{eq} and $C_{\mathrm{th,eq}}$ for the SWNT in contact with the metal film

$$R_{\mathrm{eq}} = \frac{\int_\omega R_{\mathrm{eq}}(\omega) X(\omega) d\omega}{\int_\omega X(\omega) d\omega} \tag{19}$$

$$C_{\mathrm{th,eq}} = \frac{\int_\omega C_{\mathrm{th,eq}}(\omega) X(\omega) d\omega}{\int_\omega X(\omega) d\omega} \tag{20}$$

where $X(\omega)$ is the amplitude of the Fourier transform of the metal thermal response.

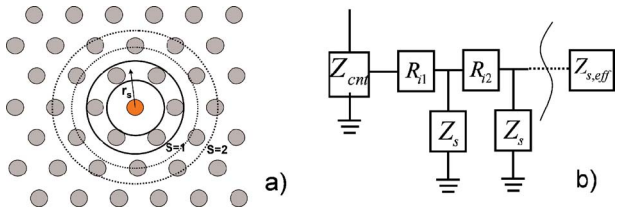

Fig. 5 (*a*) Schematic top view of a CNT in a close-pack arrangement grouped into concentric shells of neighboring tubes to calculate the effective impedance of the series of neighboring tubes, as assumed in the model. (*b*) Block diagram of impedance network modeling the linking of neighboring shells by an intershell thermal resistance.

We calculate the total impedance of the surrounding neighboring tubes, $Z_{s,\mathrm{eff}}$, by assuming a simple close-pack arrangement of the CNTs shown schematically in Fig. 5(*a*). Around the central tube contacting the metal film, we separate by the average CNT spacing the surrounding noncontacting tubes into concentric "nearest neighbor" shells. The intertube coupling resistance R_i'' links the total thermal impedance of each shell in the network (Fig. 5(*b*)).

From the CNT geometric arrangement, the total impedance of the parallel n_s tubes in the *s*th shell from the central tube is

$$Z_{\mathrm{CNT},s} = \frac{Z_{\mathrm{CNT}}}{n_s} \tag{21}$$

where the number of tubes in the *s*th shell is

$$n_s = 8s\sqrt{\frac{\pi\phi}{2\sqrt{3}}} \tag{22}$$

and where *s* is the shell label (1, 2, 3, …) and ϕ is the volume fraction ($\sim 12\%$). The total resistance between the *s*th and the $(s-1)$th, shell in terms of R_i'' is

$$R_{i,s} = R_i''\left(\frac{1}{A_{\mathrm{inner}}} + \frac{1}{A_{\mathrm{outer}}}\right) = \frac{R_i''}{\pi d L\sqrt{\frac{32\pi\phi}{\sqrt{3}}}}\left(\frac{1}{s} + \frac{1}{s-1}\right) \tag{23}$$

Combining Eqs. (21) and (23), yields the recursive relation for the total effective impedance of $Z_{s,\mathrm{eff}}$ and all shells beyond

$$Z_{s,\mathrm{eff}} = R_{i,s} + \frac{Z_{\mathrm{CNT},s} Z_{s+1,\mathrm{eff}}}{Z_{\mathrm{CNT},s} + Z_{s+1,\mathrm{eff}}} \tag{24}$$

which gives $C_{\mathrm{th,eq}}$ and R_{eq} through Eq. (15) and the subsequent relations.

In Fig. 6, we show the dependence of $C_{\mathrm{th,eq}}$ and R_{eq}, normalized to the capacitance $C_{\mathrm{th,CNT}}$ and resistance R_b of an individual tube, on R_i''. Figure 6 shows that C_{eff} and R_{eq} are essentially equivalent to the individual tube values for $R_i'' > 10^{-3}$ m^2 K W^{-1}, indicating that lateral conduction within the CNT array is negligible in this regime. Using two vertically aligned MWNT arrays pressed together in an opposing configuration, Hu et al. [39] measured $R_i'' = 1.4$ m^2 K W^{-1}, which is very large. While interpenetrating MWNTs pressed in an opposed geometry is a variant of the aligned SWNT geometry of this study, the similarity in thermal transport in aligned independent nanostructures allows for a sensible comparison. Owing to an increased CNT-CNT contact due to mechanical deformation, the MWNT intertube coupling resistance presumably provides a lower bound for the SWNT case.

Recent work using classic molecular dynamics simulations to investigate the dependence of the intertube thermal contact resistance between two aligned SWNTs on the distance between the CNT walls show that for distances larger than ~ 1.3 nm, the intertube thermal resistance is extraordinarily large

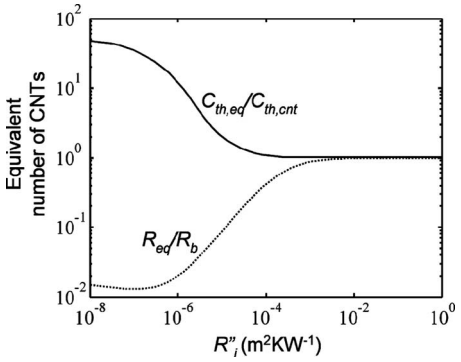

Fig. 6 The effective thermal capacity $C_{th,eq}$, and thermal resistance, R_{eq} due to intertube coupling effects normalized to that of an individual tube as a function the intertube coupling resistance R''_i

($>10^{-4}$ m^2 K W^{-1}) [40]. That the intertube resistance predicted by the simulations in Ref. [40] agrees reasonably with measurements of the interfacial thermal resistance between SWNTs and octane [23] suggests that the simulations capture the essential nanoscale physics and that a phenomenon such as near field radiation transfer is insignificant in this analysis. Based on the prior data and simulations, we believe that intertube coupling effects are insignificant in the analysis in this work. Thus, the effective thermal properties are entirely determined by the tubes that are in thermal contact with the metal film, and the tubes in poor thermal contact contribute negligibly. If intertube transport were significant, then the number of tubes that contribute to volumetric heat capacity would differ from the number of tubes that contribute to the thermal resistance and contact resistance.

If intertube coupling is negligible, the effective volume fraction of tubes contributing to conduction is nearly identical to the effective volume fraction contributing to the heat capacity. Thus,

$$f_{\text{eff},R} \approx f_{\text{eff},C} = 0.0035 \tag{25}$$

The calculation of these results exploits the directly measured volumetric heat capacity and does not depend on the precise knowledge of the true CNT film porosity, which is challenging to directly measure. This small effective volume fraction contributing to thermal transport, which we attribute to poor contact geometry, provides an explanation for the extraordinarily large thermal boundary resistances observed in most nanotube arrays.

Additionally, if intertube coupling effects are negligible, the volume fraction of tube contribution to conduction and interface resistance is the same. Scaling the area-averaged interface resistances by $f_{\text{eff},R}$ yields a value of 10 m^2 K GW^{-1} for the individual CNT-Pd contact resistance and 32 m^2 K GW^{-1} for the individual CNT-SiO_2 contact resistance, consistent with the area definition A_a. We believe that the two additional interfaces with the catalyst and SiO_2 at the base of the CNTs explain why $R''_{\text{CNT-SiO}_2}$ is about three times larger than $R''_{\text{CNT-Pd}}$.

It is useful to compare the extracted results of the intrinsic CNT-metal contact resistance with both other experimental studies and theoretical calculations. Utilizing Joule self-heating of a MWNT on a metal substrate, Kim et al. [10] measured the CNT-metal contact resistance to be 29 m^2 K^1 GW^{-1}, based on the area $A=dL_{\text{CNT}}$, where $d=14$ nm is the diameter and $L_{\text{CNT}}=1$ μm is the contact length. The reasonable agreement of Ref. [10] with those presented in this paper suggests that the mechanisms of thermal transport between a metal deposited on the end of a CNT and a CNT lying on a metal substrate may be similar.

We can provide an approximate lower bound for CNT-Pd contact resistance using the acoustic mismatch (AMM) theory of boundary resistance, reviewed in Schwartz and Pohl [41], in which phonon transport across a boundary is treated analogously to acoustic impedance mismatches. The AMM theory has been developed and applied to thermal interfaces between three dimensional materials, with insufficient development for interfaces between low dimensional structures of possibly differing dimensionalities.

A proper characterization of the nanoscale interface is critical because the complicated and ambiguous nanoscale geometry strongly dictates the mathematical structure of the AMM calculation. Although a SWNT is often treated as a quasi-1D structure, its interface with a metal includes 2D and 3D aspects. We make the approximation that the nanotubes have a quasi-2D isotropic "flat-sheet" geometry since nanotubes behave much like a 2D graphene sheet due to the strong excitation of the phonon subbands at room temperature [37]. We consider one longitudinal and two transverse acoustic polarization branches as well as model the Pd as an isotropic 2D medium. We derive the heat flux for a given temperature drop across the 2D boundary analogously to a 3D medium as in Refs. [41,42] to be

$$\dot{q}'_{\text{CNT-Pd}} = \left(\frac{1}{2\pi}\right)^2 \left(\frac{k_b T_{\text{CNT}}}{\hbar}\right)^3 \sum_{s=\text{pol}} \int_{-\pi/2}^{\pi/2} \alpha_{\text{CNT-Pd},s}(\theta) \left(\frac{\hbar}{c_s}\right) \cos(\theta) d\theta \times \int_0^{\theta_{d,\text{Pd}}/T_{\text{Pd}}} x^3 \left[\frac{1}{e^{\left(x\frac{T_{\text{CNT}}}{T_{\text{Pd}}}\right)}} - \frac{1}{e^x}\right] dx \tag{26}$$

where $\theta_{d,\text{Pd}} \sim 250$ K is the Debye temperature of the palladium, T_{CNT} and T_{Pd} are the temperatures of the CNT and Pd sides of the boundary, respectively, and $\alpha_{\text{CNT-Pd},s}(\theta)$ is the transmission coefficient computed using the AMM approximation given in Ref. [41],

$$\alpha_{\text{CNT-Pd},s}(\theta) = \frac{4\dfrac{(\rho_{\text{Pd}} c_{\text{Pd},s})}{(\rho_{\text{CNT}} c_{\text{CNT},s})}}{\left[\dfrac{(\rho_{\text{CNT}} c_{\text{CNT},s})}{(\rho_{\text{CNT}} c_{\text{CNT},s})} + \dfrac{\cos(\theta_{\text{Pd}})}{\cos(\theta_{\text{CNT}})}\right]^2} \tag{27}$$

where ρ_i is the density of material i, $c_{i,s}$ is the acoustic velocity of polarization s in material i, and θ_i is the phonon angle of incidence in side i. Computing the heat flux from the CNT side avoids critical cone considerations since it has the higher phonon velocities [42]. Assuming elastic boundary scattering with no mode conversion, the integral in Eq. (26) is limited by the lower Debye temperature (Pd) since no modes at higher frequency can be transmitted into the Pd.

From Eq. (26), the boundary resistance is defined as

$$R''_{\text{AMM}} = \frac{(T_{\text{CNT}} - T_{\text{Pd}})b}{\dot{q}'_{\text{CNT-Pd}}} \tag{28}$$

which upon numerical evaluation gives $R''_{\text{AMM}}=3.1$ m^2 K^1 GW^{-1} and is consistent with the area $A_a=\pi db$ in which the phonons in the CNT are confined. The AMM calculation predicts a boundary resistance 3.2 times lower than the extracted value for the SWNT-Pd contact, which is rather reasonable considering that AMM predictions are usually much larger at room temperature [41]. Typically, the AMM theory only applies at low temperature where the phonon wavelength is much larger that the interface roughness. However, we believe that the AMM model predicts reasonable results because the Debye temperature of the CNTs is much higher than room temperature ($\theta_{d,\text{CNT}} \sim 2500$ K), so the calculations are in the "low temperature" regime when performed from the CNT side. Also, the nanotube-metal contact is atomistic; thus, conventional surface roughness considerations in phonon transport are poorly defined and inapplicable.

The consistency of the experimental results with the AMM predictions indicates that the intrinsic conduction between an individual CNT and a metal film approaches fundamental physical limits. Thus, increasing the number of CNT-substrate contacts is

the most promising approach for improving the thermal performance of CNT-based interface materials. Moreover, the discrepancy between theory and the measured data merits future theoretical analysis, possibly considering more detailed modeling of the nanoscale dimensional effects and transport at the interface between the quasi-1D CNT and the 3D metal film.

Summary and Conclusions

This paper studies the room temperature thermal properties of metalized vertically aligned SWNTs using a nanosecond thermoreflectance technique. We measure the total thermal resistance of the TIM to be $R''_{\text{eff,tot}}=12\ \text{m}^2\ \text{K MW}^{-1}$, which we determine to be dominated by the interface resistance and not the thermal conductivity of the CNTs themselves. Images of the metal film and the CNT surface topography suggest a model for the CNT-metal contact, whereby only a subset of the CNTs are actually responsible for the thermal transport. The results show that the effective volume fraction of SWNTs contributing to thermal transports is 0.35%, which is much less than the estimation of the true volume fraction of ~12% from the catalyst deposition process. Based on the effective volume fraction, the intrinsic thermal resistance for an individual SWNT-Pd contact is $R''_{\text{CNT-Pd},a}=10\ \text{m}^2\ \text{K GW}^{-1}$ (based on the annular area, $A_a=\pi db$), which is in reasonable agreement with the upper limit predictions of the AMM theory. These results suggest that increasing the number of CNT-substrate contacts can potentially reduce the total thermal resistance of a SWNT array to less than $1\ \text{m}^2\ \text{K MW}^{-1}$. Future work toward developing practical CNT based TIMs needs to address the CNT contact geometry as well as characterize the lateral mechanical compliance of aligned nanotube arrays and their effect on the contact geometry and thermal transport, particularly during thermal cycling.

Acknowledgment

The authors gratefully acknowledge the financial support from SRC (2003-NJ-1064), DARPA (N6001-04-8916), MARCO Interconnect Focus Center, and a NSF NIRT (Award No. 1058163-1-QAXYZ). M.A.P. thanks the Stanford Graduate Fellowship program.

Nomenclature

A_a = annular area of individual CNTs, m^2
A_d = cross-sectional area of individual CNTs, m^2
b = thickness of CNT annular area, m
c_s = CNT acoustic speed of polarization s, m s^{-1}
c_p = heat capacity, $\text{J kg}^{-1}\ \text{K}^{-1}$
$C_{\text{CNT,eff}}$ = area-averaged effective volumetric heat capacity, $\text{J m}^{-3}\ \text{K}^{-1}$
C_{th} = thermal capacity, J K^{-1}
C_{tr} = thermoreflectance coefficient, K^{-1}
$C_{v,a}$ = volumetric heat capacity of individual SWNTs based on A_a, $\text{J m}^{-3}\ \text{K}^{-1}$
$C_{v,d}$ = volumetric heat capacity of individual SWNTs based on A_d, $\text{J m}^{-3}\ \text{K}^{-1}$
d = CNT diameter, m
$R''_{\text{CNT-Pd}}$ = individual Pd-CNT contact boundary resistance, $\text{m}^2\ \text{K W}^{-1}$
$R''_{\text{CNT-SiO}_2}$ = individual CNT-SiO_2 contact boundary resistance, $\text{m}^2\ \text{K W}^{-1}$
$R_{\text{CNT-Pd,eff}}$ = area-averaged effective Pd-CNT contact boundary resistance, $\text{m}^2\ \text{K W}^{-1}$
$R''_{\text{CNT-SiO}_2\text{,eff}}$ = area-averaged effective CNT-SiO_2 contact boundary resistance, $\text{m}^2\ \text{K W}^{-1}$
k_{Al} = thermal conductivity of aluminum film, $\text{W m}^{-1}\ \text{K}^{-1}$
$k_{\text{CNT,eff}}$ = effective area-averaged thermal conductivity of nanotube film, $\text{W m}^{-1}\ \text{K}^{-1}$
k_{SiO_2} = thermal conductivity of oxide layer, $\text{W m}^{-1}\ \text{K}^{-1}$
k_B = Boltzmann constant $=1.38\times10^{-23}\ \text{J K}^{-1}$
L_{Al} = thickness of aluminum, m
L_{CNT} = length of a CNT, m
n_s = number of CNTs in shell s
q'' = heat flux, W m^{-2}
R = reflectivity
R_b = total thermal boundary resistance of nanotube, K W^{-1}
R''_b = CNT thermal boundary resistance, $\text{m}^2\ \text{K W}^{-1}$
R''_{CNT} = CNT thermal resistance, $\text{m}^2\ \text{K W}^{-1}$
R_{eff} = effective resistance of an individual CNT including intertube coupling, K W^{-1}
R''_i = intertube thermal coupling resistance, $\text{m}^2\ \text{K W}^{-1}$
$R_{i,s}$ = shell s intertube thermal resistance, K W^{-1}
s = shell number
t = time, s
T_i = temperature of the ith material, K
x = position, m
Z_b = thermal interface impedance of individual CNT-substrate contacts K W^{-1}
Z_C = thermal capacitance impedance of individual SWNTs, K W^{-1}
Z_{CNT} = total SWNT thermal impedance, K W^{-1}
Z_{eff} = effective thermal impedance of CNT thermal network model, K W^{-1}
Z_{eq} = thermal impedance of an equivalent parallel RC thermal network, K W^{-1}
$Z_{s,\text{eff}}$ = total effective thermal impedance of s concentric shells of CNTs, K W^{-1}
Z_s = total thermal impedance of shell s, K W^{-1}

Greek Symbols

α_i = thermal diffusivity of the ith material, $\text{m}^2\ \text{s}^{-1}$
$\alpha_{\text{CNT-Pd}}$ = phonon boundary transmission coefficient
θ_i = Fourier transform of the temperature of the ith material, K
θ_d = Debye temperature, K
ρ = density, kg m^{-3}
τ = laser temporal pulse width, s
ϕ = volume fraction
ω = frequency, rad/s

References

[1] Osman, M. A., and Srivastava, D., 2001, "Temperature Dependence of the Thermal Conductivity of Single-Wall Carbon Nanotubes," Nanotechnology, **12**, pp. 21–21.
[2] Berber, S., Kwon, Y.-K., and Tománek, D., 2000, "Unusually High Thermal Conductivity of Carbon Nanotubes," Phys. Rev. Lett., **84**, pp. 4613–4616.
[3] Maruyama, S., 2003, "A Molecular Dynamics Simulation of Heat Conduction of a Finite Legth Single-Walled Carbon Nanotube," Microscale Thermophys. Eng., **7**, pp. 41–50.
[4] Pop, E., Mann, D., Wang, Q., Goodson, K., and Dai, H., 2006, "Thermal Conductance of an Individual Single-Wall Carbon Nanotube Above Room Temperature," Nano Lett., **6**(1), pp. 96–100.
[5] Lukes, J. R., and Zhong, H., 2007, "Thermal Conductivity of Individual Single-Wall Carbon Nanotubes," ASME J. Heat Transfer, **129**(6), pp. 705–716.
[6] Padgett, C. W., and Brenner, D. W., 2004, "Influence of Chemisorption on the Thermal Conductivity of Single-Wall Carbon Nanotubes," Nano Lett., **4**(6), pp. 1051–1053.
[7] Mingo, N., and Broido, D. A., 2005, "Length Dependence of Carbon Nanotube Thermal Conductivity and the 'Problem of Long Waves'," Nano Lett., **5**(7), pp. 1221–1225.
[8] Mingo, N., and Broido, D. A., 2005, "Carbon Nanotube Ballistic Thermal Conductance and Its Limits," Phys. Rev. Lett., **95**(9), pp. 096105.
[9] Pan, R., Xu, Z., Zhu, Z., and Wang, Z., 2007, "Thermal Conductivity of Functionalized Single-Wall Carbon Nanotubes," Nanotechnology, **18**(28), p. 285704.
[10] Kim, P., Shi, L., Majumdar, A., and McEuen, P. L., 2001, "Thermal Transport Measurements of Individual Multiwalled Nanotubes," Phys. Rev. Lett.,

87(21), p. 215502.
[11] Fujii, M., Zhang, X., Xie, H., Ago, H., Takahashi, K., Ikuta, T., Abe, H., and Shimizu, T., 2005, "Measuring the Thermal Conductivity of a Single Carbon Nanotube," Phys. Rev. Lett., **95**, p. 065502.
[12] Hone, J., Llaguno, M. C., Nemes, N. M., and Johnson, A. T., 2000, "Electrical and Thermal Transport Properties of Magnetically Aligned Single Wall Carbon Nanotube Films," Appl. Phys. Lett., **77**, pp. 666–668.
[13] Yi, W., Lu, L., Dian-lin, Z., Pan, Z. W., and Xie, S. S., 1999, "Linear Specific Heat of Carbon Nanotubes," Phys. Rev. B, **59**, pp. R9015–R9018.
[14] Shenogin, S., Xue, L., Ozisik, R., Keblinski, R., and Cahill, D., 2004, "Role of Thermal Boundary Resistance on the Heat Flow in Carbon-Nanotube Composites," J. Appl. Phys., **95**, pp. 8136–8144.
[15] Xue, Q. Z., 2006, "Model for the Effective Thermal Conductivity of Carbon Nanotube Composites," Nanotechnology, **17**(6), pp. 1655–1660.
[16] Choi, S. U. S., Zhang, Z. G., Yu, W., Lockwood, F. E., and Grulke, E. A., 2001, "Anomalous Thermal Conductivity Enhancement in Nanotube Suspensions," Appl. Phys. Lett., **79**, pp. 2252–2254.
[17] Biercuk, M. J., Llaguno, M. C., Radosavljevic, M., Hyun, J. K., Johnsond, A. T., and Fischer, J. E., 2002, "Carbon Nanotube Composites for Thermal Management," Appl. Phys. Lett., **80**, pp. 2767–2769.
[18] Guthy, C., Du, F., Brand, S., Winey, K. I., and Fischer, J. E., 2007, "Thermal Conductivity of Single-Walled Carbon Nanotube/PMMA Nanocomposites," ASME J. Heat Transfer, **129**(8), pp. 1096–1099.
[19] Hu, X., Jiang, L., and Goodson, K. E., 2004, "Thermal Conductance Enhancement of Particle-Filled Thermal Interface Materials Using Carbon Nanotube Inclusions," *Proceedings of the Intersociety Conference on Thermal and Thermo-Mechanical Phenomena in Electronic Systems*, pp. 63–69.
[20] Hu, X. J., Padilla, A. A., Xu, J., Fisher, T. S., and Goodson, K. E., 2006, "3-Omega Measurements of Vertically Oriented Carbon Nanotubes on Silicon," ASME J. Heat Transfer, **128**(11), pp. 1109–1113.
[21] Yang, D. J., Zhang, Q., Chen, G., Yoon, S. F., Ahn, J., Wang, S. G., Zhou, Q., Wang, Q., and Li, J. Q., 2002, "Thermal Conductivity of Multiwalled Carbon Nanotubes," Phys. Rev. B, **66**, p. 165440.
[22] Tong, T., Zhao, Y., Delzeit, L., Kashani, A., Meyyappan, M., and Majumdar, A., 2007, "Dense Vertically Aligned Multiwalled Carbon Nanotube Arrays as Thermal Interface Materials," IEEE Trans. Compon. Packag. Technol., **30**(1), pp. 92–100.
[23] Huxtable, S. T., Cahill, D. G., Shenogin, S., Xue, L., Ozisik, R., Barone, P., Usrey, M., Strano, M. S., Siddons, G., Shim, M., and Keblinski, P., 2003, "Interfacial Heat Flow in Carbon Nanotube Suspensions," Nat. Mater., **2**(11), pp. 731–734.
[24] Zhang, G., Mann, D., Zhang, L., Javey, A., Li, Y., Yenilmez, E., Wang, Q., McVittie, J. P., Nishi, Y., Gibbons, J., and Dai, H., 2005, "Ultra-High-Yield Growth of Vertical Single-Walled Carbon Nanotubes: Hidden Roles of Hydrogen and Oxygen," Proc. Natl. Acad. Sci. U.S.A., **102**, pp. 16141–16145.
[25] Chu, D., Touzelbaev, M., Babin, S., Pease, R. F., and Goodson, K. E., 2001, "Thermal Conductivity Measurements of Thin-Film Resist," J. Vac. Sci. Technol. B, **19**, pp. 2874–2877.
[26] Kading, O. W., Skurk, H., and Goodson, K. E., 1994, "Thermal Conduction in Metallized Silicon-Dioxide Layers on Silicon," Appl. Phys. Lett., **65**(13), pp. 1629–1631.
[27] Smith, A., Hostetler, D., and Norris, P., 2000, "Thermal Boundary Resistance Measurements Using a Transient Thermoreflectance Technique," Microscale Thermophys. Eng., **4**, pp. 51–60.
[28] Stoner, R., and Maris, H., 1993, "Kapitza Conductance and Heat Flow Between Solids at Temperature From 50 to 300 K," Phys. Rev. B, **48**, pp. 16373–16387.
[29] Paddock, C. A., and Eesley, G. L., 1986, "Transient Thermoreflectance From Thin Metal Films," J. Appl. Phys., **60**, pp. 285–290.
[30] Schoenlein, R. W., Lin, W. Z., Fujimoto, J. G., and Eesley, G. L., 1987, "Femtosecond Studies of Nonequilibrium Electronic Processes in Metals," Phys. Rev. Lett., **58**(16), pp. 1680–1683.
[31] Elsayed-Ali, H. E., Norris, T. B., Pessot, M. A., and Mourou, G. A., 1987, "Time-Resolved Observation of Electron-Phonon Relaxation in Copper," Phys. Rev. Lett., **58**(12), pp. 1212–1215.
[32] Ujihara, K., 1972, "Reflectivity of Metals at High Temperatures," J. Appl. Phys., **43**, pp. 2376–2383.
[33] Guidotti, D., and Wilman, J., 1991, "Novel and Nonintrusive Optical Thermometer," Appl. Phys. Lett., **60**, pp. 524–526.
[34] Clemens, B., Eesley, G., and Paddock, C., 1988, "Time-Resolved Thermal Transport in Compositionally Modulated Metal Films," Phys. Rev. B, **37**, pp. 1085–1096.
[35] Bethe, H. A., 1944, "Theory of Diffraction by Small Holes," Phys. Rev., **66**, pp. 163–182.
[36] Jin, E. X., and Xu, X., 2005, "Radiation Transfer Through Nanoscale Apertures," J. Quant. Spectrosc. Radiat. Transf., **93**(1–3), pp. 163–173.
[37] Hone, J., Batlogg, B., Benes, Z., Johnson, A. T., and Fischer, J. E., 2000, "Quantized Phonon Spectrum of Single-Wall Carbon Nanotubes," Science, **289**(5485), pp. 1730–1733.
[38] Xu, J., and Fisher, T., 2004, "Thermal Contact Conductance Enhancement Using Carbon Nanotube Arrays," ASME Paper No. IMECE2004-60185.
[39] Hu, X. J., Panzer, M. A., and Goodson, K. E., 2007, "Infrared Microscopy Thermal Characterization of Opposing Carbon Nanotube Arrays," ASME J. Heat Transfer, **129**, pp. 91–93.
[40] Zhong, H., and Lukes, J. R., 2006, "Interfacial Thermal Resistance Between Carbon Nanotubes: Molecular Dynamics Simulations and Analytical Thermal Modeling," Phys. Rev. B, **74**(12), p. 125403.
[41] Schwartz, E., and Pohl, R., 1989, "Thermal Boundary Resistance," Rev. Mod. Phys., **61**, pp. 605–668.
[42] Phelan, P., 1998, "Application of Diffuse Mismatch Theory to the Prediction of Thermal Boundary Resistance in Thin-Film High-Tc Superconductors," ASME J. Heat Transfer, **120**, pp. 37–43.

Correlating Equations for Laminar Free Convection From Misaligned Horizontal Cylinders in Interacting Flow Fields

Massimo Corcione[1]
Mem. ASME
e-mail: massimo.corcione@uniroma1.it

Claudio Cianfrini

Emanuele Habib

Gino Moncada Lo Giudice

Dipartimento di Fisica Tecnica,
University of Rome "La Sapienza,"
via Eudossiana 18, Rome I 00184, Italy

Steady laminar free convection in air from a pair of misaligned, parallel horizontal cylinders, i.e., a pair of parallel cylinders with their axes set in a plane inclined with respect to the gravity vector, is studied numerically. A specifically developed computer code based on the SIMPLE-C algorithm is used for the solution of the dimensionless mass, momentum, and energy transfer governing equations. Results are presented for different values of the center-to-center cylinder spacing from 1.4 up to 10 diameters, the tilting angle of the two-cylinder array from 0 deg to 90 deg*, and the Rayleigh number based on the cylinder diameter in the range between* 10^3 *and* 10^7*. It is found that the heat transfer rates at both cylinder surfaces may in principle be traced back to the combined contributions of the so-called plume effect and chimney effect, which are the mutual interactions occurring in the vertical and horizontal alignments, respectively. In addition, at any misalignment angle, an optimum spacing between the cylinders for the maximum heat transfer rate, which decreases with increasing the Rayleigh number, does exist. Heat transfer dimensionless correlating equations are proposed for any individual cylinder and for the pair of cylinders as a whole.* [DOI: 10.1115/1.2780183]

Keywords: free convection, misaligned horizontal cylinders, flow interactions, numerical analysis, correlating equations

1 Introduction

Free convection heat transfer from arrays of horizontal cylinders set in free space has a considerable relevance to several engineering applications, e.g., heat exchangers, storage devices, and electronic components, to name a few. In fact, although free convection is less effective than forced convection for the same geometry, in many situations, heat transfer designers prefer to avoid the use of mechanical fans or other active equipment for the fluid circulation due to power consumption, excessive noise, or reliability concerns.

Most of the investigations conducted in this field are substantially oriented toward the study of the thermal performance of vertical arrays of horizontal cylinders [1–7]. A detailed review of these studies is reported in a recent paper by Corcione [8], who derived numerical heat transfer dimensionless correlations for such geometry in the range $5\times10^2\leqslant \mathrm{Ra}\leqslant 5\times10^5$. A smaller degree of attention has instead been devoted to the more general case of tilted cylinder arrays, whose few related studies available in the open literature refer to quite narrow ranges of the Rayleigh number and relatively large cylinder spacings.

The first documented work on this subject was executed by Lieberman and Gebhart [2], who carried out experiments on the thermal behavior of a flat array of ten wires of 0.127 mm diameter with six spacings from 37.5 to 225 wire diameters and four orientation angles from 0 deg to 90 deg, for a single Grashof number of 1.75×10^{-2} under the assumption of uniform heat flux. They found that a peak for the average Nusselt number occurred at optimum spacings around 120, 80, 60, and 55 diameters for tilting angles with respect to gravity of 0 deg, 30 deg, 60 deg, and 90 deg, respectively. Subsequently, Sparrow and Boessneck [9] performed an experimental study on the mutual interactions occurring between two misaligned, parallel horizontal cylinders of 3.787 cm diameter set in free air one above the other at the same temperature for Rayleigh numbers in the range between 2×10^4 and 2×10^5. The geometry of the assembly was varied through independent modifications of the vertical and horizontal center-to-center separation distances in the ranges between 2 and 9 diameters and between 0 and 4.5 diameters, respectively, which correspond to tilting angles with respect to the gravity vector from 0 deg to nearly 78 deg. It was found that for all the cases investigated, the lower-cylinder Nusselt number was virtually identical to that for a single cylinder, which was already well known for the bottom element of vertical arrays, at least for intercylinder spacings larger than the cylinder diameter. In contrast, at small vertical separation distances, transverse offsets below the cylinder diameter caused an increase up to 27% for the upper-cylinder Nusselt number, compared with that for the perfect vertical alignment, while transverse offsets larger than the cylinder diameter had no significant effect. On the other hand, at large vertical separation distances, the upper cylinder displayed degradations in Nusselt number by even 20% at large transverse offsets while showing negligible changes for reduced offsetting. No type of correlation was proposed in the paper.

Leaving aside the numerical study conducted by Farouk and Guceri [10] on the thermal performance of single and double infinite rows of horizontal cylinders set in free air, which has a bearing on this subject only on a purely qualitative point of view, no other significant study expressly dedicated to free convection from unconfined, misaligned horizontal cylinders was readily found in the literature.

In this background, the aim of the present paper is to carry out a numerical investigation of free convection heat and momentum transfer from a pair of parallel horizontal cylinders with their axes set in a plane inclined with respect to the gravity vector, with the

[1]Corresponding author.

Contributed by the Heat Transfer Division of ASME for publication in the JOURNAL OF HEAT TRANSFER. Manuscript received March 8, 2007; final manuscript received May 10, 2007; published online March 27, 2008. Review conducted by Giulio Lorenzini.

horizontal and vertical positions as special cases, so as to derive heat transfer dimensionless correlating equations for any individual cylinder and for the pair of cylinders as a whole. The study is performed in air under the assumption of steady, two-dimensional laminar flow for center-to-center separation distances from 1.4 up to 10 diameters, tilting angles of the two-cylinder array from 0 deg to 90 deg, and values of the Rayleigh number based on the cylinder diameter in the range between 10^3 and 10^7.

2 Mathematical Formulation

Two horizontal parallel cylinders with their axes set in a plane inclined an angle φ with respect to the gravity vector are considered. The diameter D of the cylinders and their center-to-center separation distance S are assigned. Free convection heat transfer occurs between each cylinder surface, kept at uniform temperature t_w, and the surrounding undisturbed fluid reservoir, assumed at uniform temperature t_∞.

The buoyancy-induced flow is considered to be steady and laminar. The cylinders are assumed to be much longer than their diameter, which implies that the end effects can be reasonably neglected and the temperature and velocity fields can be considered two dimensional. The flow is assumed to be incompressible, with constant fluid properties and negligible viscous dissipation and pressure work. The buoyancy effects on momentum transfer are taken into account through the Boussinesq approximation.

Once the above assumptions are employed in the conservation equations of mass, momentum, and energy, the following set of dimensionless governing equations is obtained:

$$\nabla \cdot \mathbf{V} = 0 \tag{1}$$

$$(\mathbf{V} \cdot \nabla)\mathbf{V} = -\nabla p + \nabla^2 \mathbf{V} - \frac{\mathrm{Ra}}{\mathrm{Pr}} T \frac{\mathbf{g}}{g} \tag{2}$$

$$(\mathbf{V} \cdot \nabla)T = \frac{1}{\mathrm{Pr}} \nabla^2 T \tag{3}$$

where $\mathbf{V}$ is the velocity vector having dimensionless velocity components U and V normalized with ν/D, T is the dimensionless temperature excess over the uniform temperature of the undisturbed fluid reservoir normalized with the temperature difference $(t_w - t_\infty)$, p is the dimensionless pressure normalized with $\rho_\infty \nu^2/D^2$, $\mathrm{Ra} = g\beta(t_w - t_\infty)D^3/\alpha\nu$ is the Rayleigh number based on the cylinder diameter, $\mathbf{g}$ is the gravity vector, and $\mathrm{Pr} = \nu/\alpha$ is the Prandtl number.

The related boundary conditions are $T=1$ and $\mathbf{V}=0$ at any cylinder surface and $T=0$ and $\mathbf{V}=0$ at very large distance from the cylinders.

3 Computational Domain and Discretization Grid System

The finite-difference solution of the governing equations (1)–(3) with the boundary conditions stated above requires that a discretization grid system be established across the integration domain, taken as a rectangle, which includes the pair of cylinders and extends sufficiently far from them. A cylindrical polar grid is employed in the proximity of any cylinder, while a Cartesian grid is used to fill the remainder of the computational domain, as drawn in Fig. 1, where the r-θ and X-Y coordinate systems adopted are also represented. In the polar systems, U is the radial velocity component, and V is the tangential velocity component. In the Cartesian system, U is the velocity component along the X axis and V is the velocity component along the Y axis. According to the discretization scheme originally proposed by Launder and Massey [11], the cylindrical polar grids and the Cartesian grid, which are entirely independent of one another, overlap with no attempt of node matching. Their connection is provided by a set of false nodes, one for each neighboring grid, located beyond their intersection, as sketched in Fig. 2. Additional details on the matching regions can be found in Ref. [8].

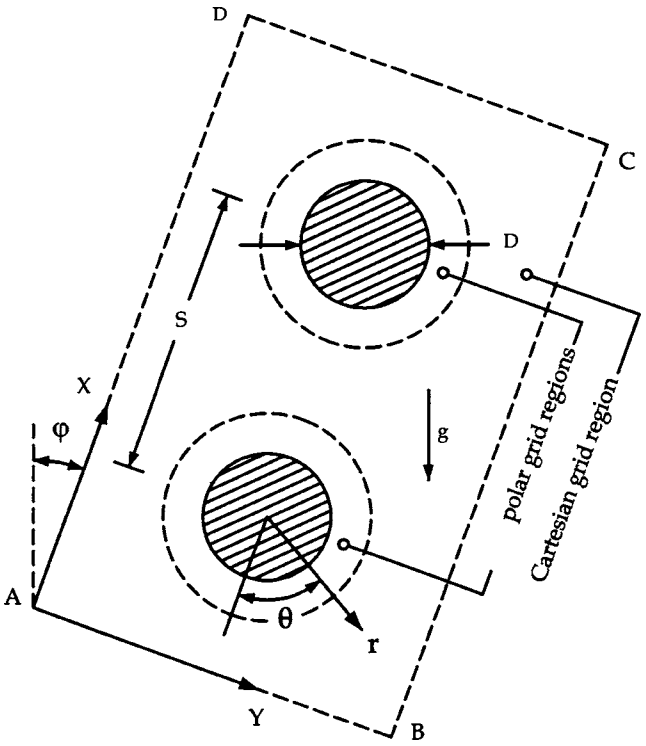

Fig. 1 Sketch of the geometry, coordinate systems, and integration domain (out of scale)

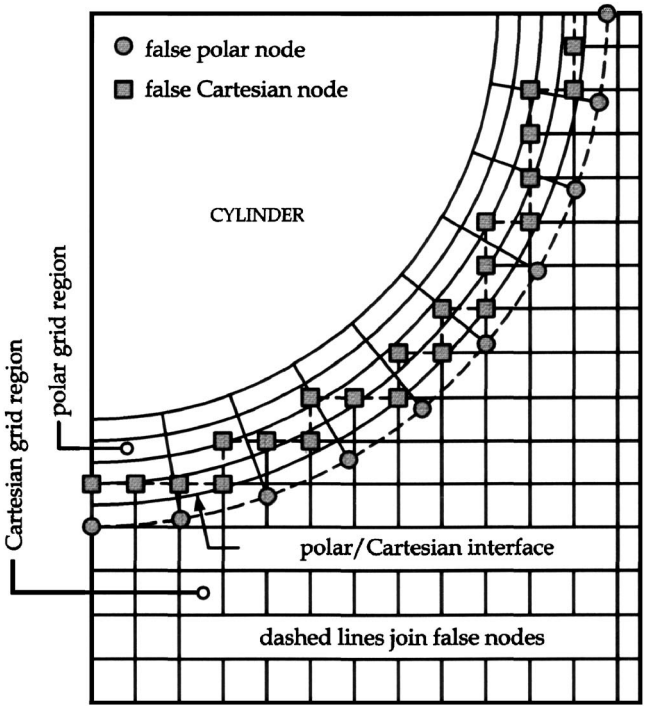

Fig. 2 Sketch of the interface between polar and Cartesian discretization grids

4 Boundary Conditions

The boundary conditions required for the numerical solution of the governing equations (1)–(3) have to be specified at any cylinder surface and at the four boundary lines enclosing the two-dimensional integration domain defined above. In particular, once such boundary lines are placed sufficiently far from the cylinders, the motion of the fluid entering or leaving the computational domain may reasonably be assumed to occur normally to them. The entering fluid is assumed at the undisturbed free field temperature. As regards the leaving fluid, whose temperature is not known a priori, a zero temperature gradient normal to the boundary line is assumed.

Thus, the following boundary conditions are applied:

(a) at any cylinder surface,

$$U = 0 \quad V = 0 \quad T = 1 \tag{4}$$

(b) at boundary line $A-B$,

$$\frac{\partial U}{\partial X} = 0 \quad V = 0 \quad T = 0 \text{ if } U > 0 \text{ or } \frac{\partial T}{\partial X} = 0 \text{ if } U \leqslant 0 \tag{5}$$

(c) at boundary line $B-C$,

$$U = 0 \quad \frac{\partial V}{\partial Y} = 0 \quad T = 0 \text{ if } V < 0 \text{ or } \frac{\partial T}{\partial Y} = 0 \text{ if } V \geqslant 0 \tag{6}$$

(d) at boundary line $C-D$,

$$\frac{\partial U}{\partial X} = 0 \quad V = 0 \quad T = 0 \text{ if } U < 0 \text{ or } \frac{\partial T}{\partial X} = 0 \text{ if } U \geqslant 0 \tag{7}$$

(e) at boundary line $A-D$,

$$U = 0 \quad \frac{\partial V}{\partial Y} = 0 \quad T = 0 \text{ if } V > 0 \text{ or } \frac{\partial T}{\partial Y} = 0 \text{ if } V \leqslant 0 \tag{8}$$

Moreover, as far as the intersections between polar and Cartesian grids are concerned, the value of each of the dependent variables at any false node of one of the two neighboring grids is obtained by a linear interpolation of the values of the same variable at the four surrounding real nodes of the other grid (see Ref. [8] for further details).

5 Solution Procedure and Additional Considerations

The set of governing equations (1)–(3) with the boundary conditions (4)–(8) is solved through a control-volume formulation of the finite-difference method. The pressure-velocity coupling is handled by the SIMPLE-C algorithm by Van Doormaal and Raithby [12], which is essentially a more implicit variant of the SIMPLE algorithm by Patankar and Spalding [13]. The advection fluxes are evaluated by the QUICK discretization scheme by Leonard [14]. Details of the SIMPLE procedure may be found in Refs. [15,16].

Fine uniform mesh spacings are used for the discretization of both the polar grid regions and the Cartesian grid region. Starting from assigned first-approximation fields of the dependent variables, the discretized governing equations are solved iteratively through a line-by-line application of the THOMAS algorithm, enforcing under-relaxation to ensure convergence. The solution is considered to be fully converged when the maximum absolute values of both the mass source and the percentage changes of the dependent variables at any grid node from iteration to iteration are smaller than the prescribed values, i.e., 10^{-4} and 10^{-6}, respectively.

After convergence is attained, the local and average Nusselt numbers $\mathrm{Nu}_i(\theta)$ and Nu_i for the bottom and top cylinders (denoted by subscripts 1 and 2, respectively) are calculated:

$$\mathrm{Nu}_i(\theta) = \frac{qD}{k(t_w - t_\infty)} = -\left.\frac{\partial T}{\partial r}\right|_{r=0.5} \tag{9}$$

$$\mathrm{Nu}_i = \frac{Q}{\pi k(t_w - t_\infty)} = -\frac{1}{2\pi}\int_0^{2\pi} \left.\frac{\partial T}{\partial r}\right|_{r=0.5} d\theta \tag{10}$$

where q is the heat flux and Q is the heat transfer rate, and the temperature gradients at any cylinder surface are evaluated through a second-order profile among each wall node and the next corresponding two fluid nodes. The average Nusselt number Nu of the pair of cylinders is then obtained as the arithmetic mean value of the average Nusselt numbers of the individual cylinders, $(\mathrm{Nu}_1 + \mathrm{Nu}_2)/2$.

Tests on the dependence of the results obtained on the mesh spacing of both the polar and the Cartesian discretization grids, as well as on the thickness of the polar grid regions and on the extent of the whole computational domain, have been performed for several combinations of values of S/D, φ, and Ra. The optimal grid-size values, as well as the optimal positions of both the polar/Cartesian interfaces and the boundary lines used for computations (representing a good compromise between solution accuracy and computational time), are such that further grid refinements or boundary displacements do not yield noticeable modifications neither in the heat transfer rates nor in the flow field, that is, the percentage changes of $\mathrm{Nu}_i(\theta)$ and Nu_i, and the percentage changes of the maximum value of the tangential velocity components at $\theta=(90 \text{ deg}+\varphi)$ and $(270 \text{ deg}+\varphi)$ for any cylinder are smaller than the prescribed accuracy values, i.e., 1% and 2%, respectively. Typical features of the integration flow domain may be summarized as follows: (a) the number of nodal points $(r \times \theta)$ of the polar discretization grids lies in the range between 45×72 and 180×108, (b) the thickness of the polar grid regions varies between 1/20 and three times the cylinder diameter, and (c) the extent of the computational domain ranges between 4 and 20 cylinder diameters upward, between 2 and 4 cylinder diameters downward, and between 3 and 8 cylinder diameters sideward depending on the Rayleigh number, the cylinder spacing, and the tilting angle. As far as the validation of both the numerical code and the meshing procedure is concerned, a comparison between the local and average Nusselt numbers $\mathrm{Nu}_0(\theta)$ and Nu_0 obtained for a single cylinder at several Rayleigh numbers and the corresponding benchmark numerical results by Saitoh et al. [17] is reported in Table 1. Moreover, in order to test the reliability of the composite polar/Cartesian grid system at close spacing between the cylinders, the results obtained for a two-cylinder vertical array have been compared with the experimental data by Tokura et al. [5] for $\mathrm{Ra}=8.5 \times 10^4$ and S/D in the range between 1.1 and 2, as shown in Table 2. Many additional details on the validation of the numerical code and the composite-grid discretization scheme of the integration domain are available in Ref. [8]. Finally, the results obtained for the top cylinder of a two-cylinder inclined array at $\mathrm{Ra}=6 \times 10^4$, 10^5, and 2×10^5 for different cylinder spacings and tilting angles with respect to the gravity vector are compared with the experimental data by Sparrow and Boessneck [9], as shown in Table 3, where a good degree of agreement may be observed.

6 Results and Discussion

Numerical simulations are performed for $\mathrm{Pr}=0.71$, which corresponds to air, and different values of (a) the Rayleigh number Ra in the range between 10^3 and 10^7, (b) the tilting angle of the array, φ, in the range between 0 deg and 90 deg, and (c) the center-to-center dimensionless cylinder spacing S/D in the range between 1.4 and 10.

Table 1 Comparison of the present solutions for the local and average Nusselt number of a single cylinder with the benchmark solutions of Saitoh et al. [17]

Ra		$Nu_0(\theta)$ θ=0 deg	θ=30 deg	θ=60 deg	θ=90 deg	θ=120 deg	θ=150 deg	θ=180 deg	Nu_0
10^3	Present	3.789	3.755	3.640	3.376	2.841	1.958	1.210	3.023
	Saitoh et al. [17]	3.813	3.772	3.640	3.374	2.866	1.975	1.218	3.024
10^4	Present	5.986	5.931	5.756	5.406	4.716	3.293	1.532	4.819
	Saitoh et al. [17]	5.995	5.935	5.750	5.410	4.764	3.308	1.534	4.826
10^5	Present	9.694	9.595	9.297	8.749	7.871	5.848	1.989	7.886
	Saitoh et al. [17]	9.675	9.577	9.278	8.765	7.946	5.891	1.987	7.898

The heat transfer results are presented in relative terms, i.e., in terms of the ratio between the Nusselt number Nu_i or Nu and Nu_0, so as to highlight in what measure the convective interactions occurring between the cylinders either enhance or degrade the heat transfer performance of any cylinder or the whole array in comparison with that typical for the single cylinder.

6.1 Heat Transfer From a Single Cylinder. The numerical results obtained for the average Nusselt number Nu_0 of the single cylinder in the range $10^3 \leqslant Ra \leqslant 10^7$ may be correlated to the Rayleigh number by the following binomial algebraic equation of the Churchill–Chu type [18]:

$$Nu_0 = 0.714 + 0.411Ra^{0.25} \tag{11}$$

with a 0.82% standard deviation of error and a range of error from −1.71% to +1.74%, as shown in Fig. 3.

6.2 Heat Transfer From a Pair of Cylinders Aligned Vertically. The effects of the independent variables Ra and S/D on the heat transfer performance of the bottom and top cylinders when the two cylinders are aligned one above the other, i.e., the two-cylinder array is vertical (φ=0 deg), are pointed out in Figs. 4 and 5, and in Fig. 6, where the distributions of Nu_1/Nu_0 versus S/D and Nu_2/Nu_0 versus S/D, respectively, are reported for different values of the Rayleigh number. In particular, Fig. 5 is a close-up of Fig. 4 for S/D in the range between 1.1 and 3.

It may be seen that the heat transfer rate at the surface of the bottom cylinder is affected by the presence of the top cylinder only at small intercylinder separation distances. In fact, at close spacing the buoyant flow promoted by the bottom cylinder cannot penetrate completely the narrow space between the cylinders. The smaller is the spacing and/or the Rayleigh number, the weaker is the penetration strength of the flow between the cylinders, which leads to an enlargement of the stagnation region at the rear of the bottom cylinder, and thus to a degradation in its Nusselt number Nu_1.

In contrast, the heat transfer performance of the top cylinder is always affected by the presence of the bottom cylinder, showing either an enhancement or a degradation with respect to the case of the single cylinder depending mainly on the cylinder spacing. In fact, two opposite effects, which originate from the warm plume spawned by the bottom cylinder, must be taken into due account. On one side, the hot buoyant flow from the bottom cylinder acts as a forced convection field wherein the top cylinder is embedded. On the other side, the upward-moving warm plume causes a decrease in the temperature difference between the surface of the top cylinder and the adjacent fluid. The first effect, which tends to increase the heat transfer rate at the top cylinder, prevails at large spacings. The second effect, which instead tends to decrease the heat transfer rate, is of major importance at close spacings. This may be explained through the theoretical results obtained by Gebhart et al. [19], who demonstrated that for a plume above a horizontal line source, the centerline temperature decreases as the inverse of the three-fifths power of the distance above the source, while the centerline velocity increases as the fifth power of the distance above the source. Hence, from a given distance, the velocity effect outweighs the temperature effect, which leads to the cited enhancement of the Nusselt number Nu_2 of the top cylinder at large separation distances.

Finally, it seems worth observing that the relative heat transfer performance increases with Ra much more for the top cylinder than for the bottom cylinder. Furthermore, as mentioned above, Nu_1/Nu_0 does not depend on the Rayleigh number at large spacings, as the bottom cylinder is not affected by the presence of the top cylinder, and its thermal performance is substantially identical to that for a single cylinder.

Local solutions are presented in Fig. 7, where equispaced isotherm lines are plotted at, e.g., $Ra=10^5$ and S/D=1.6 (typical for close cylinder spacings) and 3 (typical for larger cylinder spacings).

The results obtained for Nu_1, Nu_2, and Nu may be expressed through the following correlating equations:

Table 2 Comparison of the present solutions for the average Nusselt number of any individual cylinder in a two-cylinder vertical array with the experimental data of Tokura et al. [5]

Two-cylinder vertical array at $Ra=8.5\times10^4$		Nu/Nu_0 S/D=1.1	S/D=1.3	S/D=1.5	S/D=2
Bottom cylinder	Present	0.908	0.965	0.996	1.008
	Tokura et al. [5]	0.890	0.940	1.000	1.010
Top cylinder	Present	0.614	0.661	0.726	0.853
	Tokura et al. [5]	0.610	0.680	0.740	0.870
Whole array	Present	0.761	0.813	0.861	0.930
	Tokura et al. [5]	0.750	0.810	0.870	0.940

Table 3 Comparison of the present solutions for the average Nusselt number of the top cylinder of a pair of misaligned cylinders with the experimental data of Sparrow and Boessneck [9]

			Nu/Nu_0	
Ra	S/D	φ (deg)	Sparrow and Boessneck [9]	Present
6×10^4	2.0	0	0.84	0.86
	2.1	14	0.93	0.94
	2.2	27	1.04	1.03
	5.0	0	1.13	1.16
	5.1	11	1.04	1.04
	5.4	22	1.03	1.04
1×10^5	2.0	0	0.85	0.88
	2.1	14	0.93	0.96
	2.2	27	1.03	1.04
	5.0	0	1.18	1.18
	5.1	11	1.04	1.04
	5.4	22	1.03	1.04
2×10^5	2.0	0	0.87	0.90
	2.1	14	0.94	0.97
	2.2	27	1.03	1.04
	5.0	0	1.21	1.20
	5.1	11	1.04	1.05
	5.4	22	1.03	1.04

$$Nu_1 = 0.687 + 0.42Ra^{0.25}\tanh\left[\frac{(S/D)Ra^{0.134}}{5.76} + 0.84\right] \quad (12)$$

for $10^3 \leqslant Ra \leqslant 10^7$ and $1.4 \leqslant S/D \leqslant 10$, with a 1.28% standard deviation of error and a range of error from −1.6% to +2.3% with a 95% level of confidence;

$$Nu_2 = Ra^{0.25}\left\{0.38\ln\left[\frac{(S/D)^{0.4}}{1.866}\right] + 0.508\right\} \quad (13)$$

for $10^3 \leqslant Ra \leqslant 10^7$ and $1.4 \leqslant S/D \leqslant 10$, with a 4.33% standard deviation of error and a range of error from −7.6% to +6.6% with a 95% level of confidence;

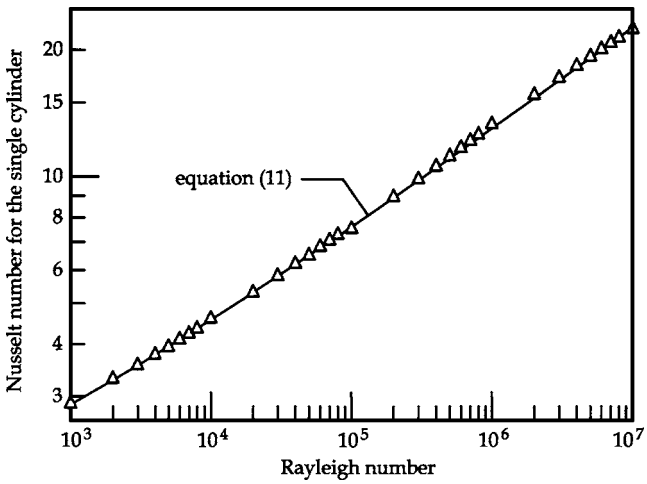

Fig. 3 Distribution of the average Nusselt number Nu_0 versus the Rayleigh number Ra for the single cylinder

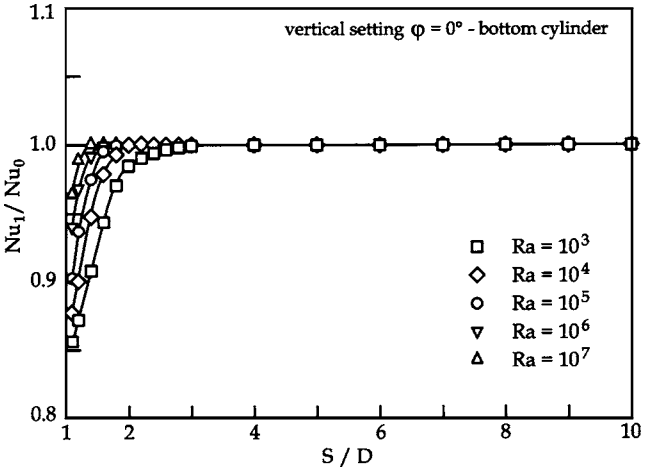

Fig. 4 Distributions of the ratio Nu_1/Nu_0 versus S/D for the bottom cylinder of a two-cylinder vertical array at different Rayleigh numbers

$$Nu = Ra^{0.25}\left\{0.17\ln\left[\frac{(S/D)^{0.49}}{1.581}\right] + 0.431\right\} \quad (14)$$

for $10^3 \leqslant Ra \leqslant 10^7$ and $1.4 \leqslant S/D \leqslant 10$, with a 4.31% standard deviation of error and a range of error from −8.8% to +7.7% with a 95% level of confidence.

6.3 Heat Transfer From a Pair of Cylinders Aligned Horizontally. The effects of the independent variables Ra and S/D on the heat transfer rate from both cylinders when the two cylinders are set side by side, i.e., the two-cylinder array is horizontal (φ=90 deg), are pointed out in Fig. 8, where the distributions of Nu/Nu_0 versus S/D are reported for different values of the Rayleigh number (it is worth noticing that for the special case of a horizontal array, $Nu_1 = Nu_2 = Nu$).

As expected, for large cylinder spacings, the average Nusselt number of any cylinder approaches that for a single cylinder. As S/D decreases, Nu/Nu_0 increases up to a point, and this is due to the increased flow rate drawn between the cylinders by the "chimney effect." The S/D value corresponding to the peak of Nu/Nu_0 is defined as the optimum cylinder spacing $(S/D)_{opt}$. It may be seen that the impact of the chimney effect is moderately higher at higher values of the Rayleigh number. Moreover, the value of

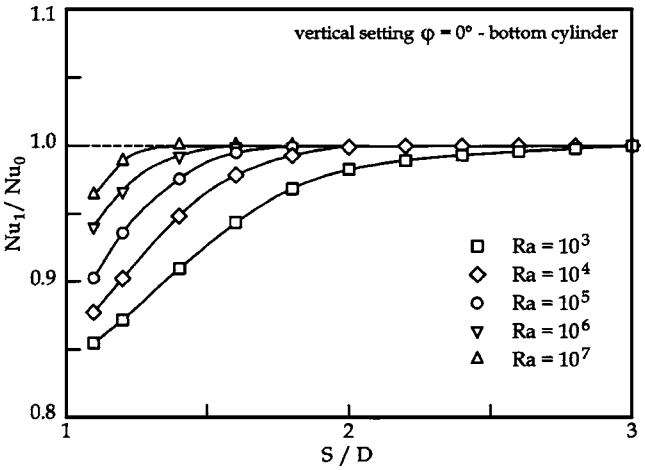

Fig. 5 Close-up of the distributions of Nu_1/Nu_0 versus S/D for the bottom cylinder of a two-cylinder vertical array at different Rayleigh numbers

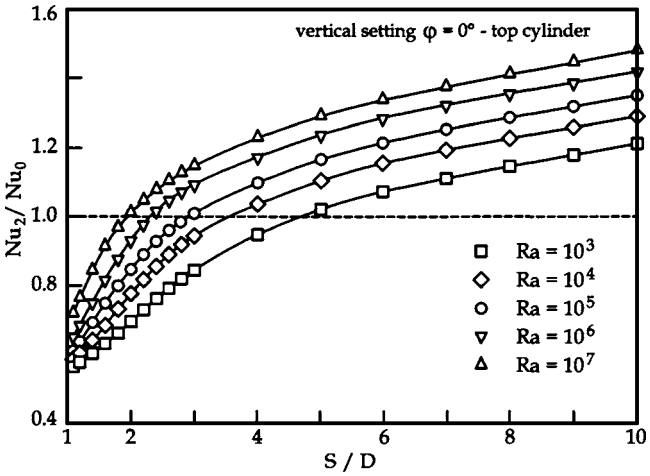

Fig. 6 Distributions of the ratio Nu_2/Nu_0 versus S/D for the top cylinder of a two-cylinder vertical array at different Rayleigh numbers

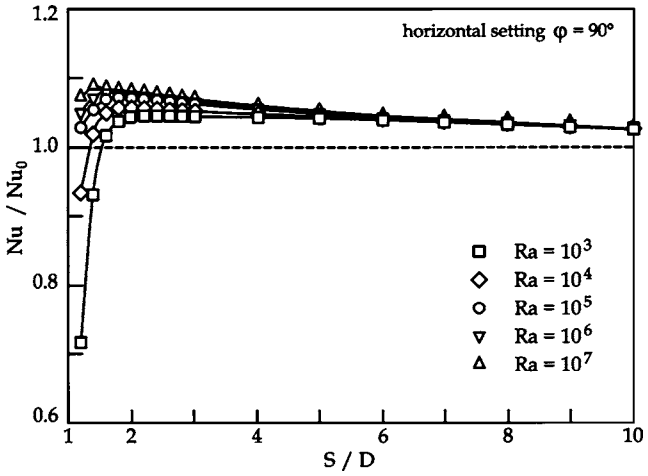

Fig. 8 Distributions of the ratio Nu/Nu_0 versus S/D for a two-cylinder horizontal array at different Rayleigh numbers

$(S/D)_{opt}$ decreases with increasing Ra, which is due to the corresponding decrease in the boundary layer thickness. As S/D is further decreased below $(S/D)_{opt}$, the full merging of the two boundary layers leads to a heat transfer decrease, which becomes significantly sharp at very close spacing. In fact, as the two cylinders are surrounded by a unique boundary layer, the amount of heat transferred to the quasimotionless fluid located between them reduces drastically. In addition, the flow configuration no longer resembles two plumes arising from individual cylinders but a single plume originated by a single source. This reflects the widening of the region of the rear stagnation point for both cylinders, which implies a decrease in the amount of heat exchanged at their upper surface.

Local solutions are presented in Fig. 9, where equispaced isotherm lines are plotted at, e.g., $Ra=10^5$ and $S/D=1.4$, 2 (at which the maximum of Nu takes place), and 5.

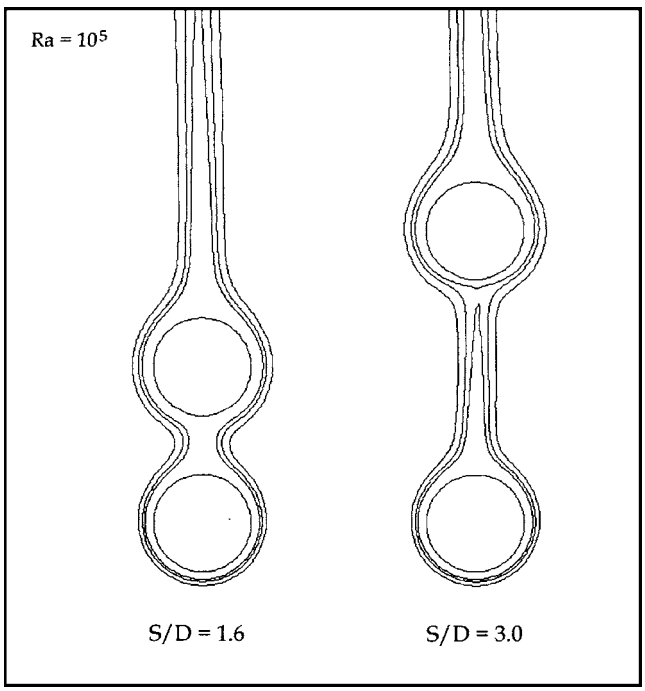

Fig. 7 Isotherm contour plots for a two-cylinder vertical array at $Ra=10^5$ and $S/D=1.6$ and 3

The results obtained for $(S/D)_{opt}$ and the corresponding Nusselt number Nu_{max}, as well as for Nu at any value of S/D, may be expressed through the following correlating equations:

$$(S/D)_{opt} = 3.39 - 0.267 \log(Ra) \tag{15}$$

for $10^3 \leqslant Ra \leqslant 10^7$, with a 4.85% standard deviation of error and a range of error from −7.1% to +4.3% with a 95% level of confidence;

$$Nu_{max} = 0.635 Ra^{0.228} \tag{16}$$

for $10^3 \leqslant Ra \leqslant 10^7$, with a 2.72% standard deviation of error and a range of error from −3.3% to +3.6% with a 95% level of confidence;

$$Nu = Ra^{0.235}[0.18(S/D) + 0.49] \tag{17}$$

for $10^3 \leqslant Ra \leqslant 10^7$ and $1.4 \leqslant S/D \leqslant (S/D)_{opt}$, with a 3.98% standard deviation of error and a range of error from −5.4% to +7.5% with a 95% level of confidence;

$$Nu = Ra^{0.223}[0.12e^{-0.6(S/D)} + 0.65] \tag{18}$$

for $10^3 \leqslant Ra \leqslant 10^7$ and $(S/D)_{opt} < S/D \leqslant 10$, with a 2.66% standard deviation of error and a range of error from −3.8% to +3.9% with a 95% level of confidence.

6.4 Heat Transfer From a Pair of Misaligned Cylinders. The geometry effects on the heat transfer rate from any individual cylinder when the two cylinders are misaligned, i.e., the two-cylinder array is inclined (0 deg $< \varphi <$ 90 deg), are displayed in Fig. 10, and in Figs. 11 and 12, where the distributions of Nu_1/Nu_0 versus S/D and Nu_2/Nu_0 versus S/D, respectively, are reported for different tilting angles at, e.g., $Ra=10^5$. In particular, Fig. 11 refers to tilting angles with respect to gravity up to 15 deg, while Fig. 12 is related to inclinations above 15 deg.

As expected, when the array is inclined, the heat transfer rate at any cylinder surface derives from the combined contributions of the two different types of mutual interactions occurring at $\varphi = 0$ deg and at $\varphi = 90$ deg discussed above, i.e., the "plume effect" and the chimney effect, respectively. As the misalignment angle φ increases from 0 deg to 90 deg, the contribution of the chimney effect increases, while that of the plume effect decreases.

Indeed, some clarification is required. In fact, since the plume spawned by the bottom cylinder is effective only as long as it impinges upon the top cylinder surface, the plume effect dies out almost abruptly as soon as the tilting angle exceeds a "critical" value, which depends mainly on geometrical factors. This means that the thermal behavior of the pair of cylinders may actually be

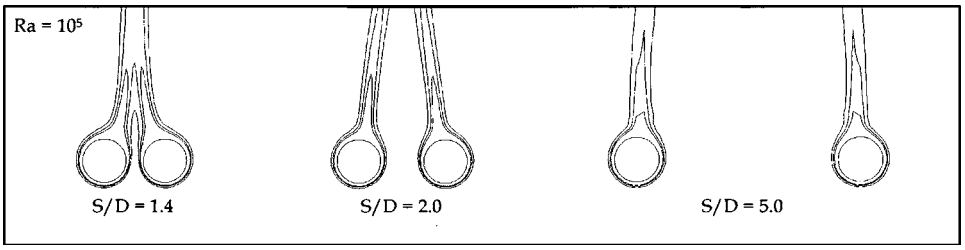

Fig. 9 Isotherm contour plots for a two-cylinder horizontal array at Ra=10^5 and S/D=1.4, 2, and 5

ascribed to the combined contributions of the plume effect and the chimney effect only for moderately inclined geometries, i.e., geometries inclined not more than 10–15 deg, which we could name "quasivertical configurations." In contrast, for pairs of cylinders with misalignments above such critical inclination angle, the mutual interactions occurring between the cylinders are governed exclusively by the chimney effect, which tends to make the thermal behavior of the bottom and top cylinders practically the same already for inclination angles of the order of 50 deg. For this reason, such geometries may be denoted as "quasihorizontal configurations."

As far as the effects of S/D and φ are specifically concerned, those related to the cylinder spacing will be examined first.

On account of what has been discussed in the section dedicated to the horizontal configuration, the contribution of the chimney effect implies that at any assigned tilting angle, a peak for the heat transfer rate from any cylinder occurs. However, in many situations, the peak for the heat transfer rate from the bottom cylinder occurs at a cylinder spacing different from that at which the peak for the heat transfer rate from the top cylinder takes place. For this reason, it seems more appropriate and interesting from the point of view of the engineering applications to focus the attention on the peak for the overall heat transfer rate from the whole cylinder array to the surrounding fluid and determine the corresponding optimum cylinder spacing $(S/D)_{opt}$, whose distributions versus φ for two different Rayleigh numbers are reported in Fig. 13. It may be noticed that, as for the horizontal configuration, $(S/D)_{opt}$ decreases with increasing Ra. In addition, $(S/D)_{opt}$ decreases with increasing φ, up to the value typical for the horizontal configuration already for inclination angles of the order of 50 deg. Actually, such decrease shows a pronounced sawtooth discontinuity, which reflects the abrupt break off of the plume effect cited above.

The angle φ^* at which such discontinuity occurs is a weak function of the Rayleigh number, which may be expressed through the following correlating equations, as displayed in Fig. 14:

$$\varphi^* = 0.175 \text{ (rad)} \quad \text{if } \mathrm{Ra} < 10^5 \tag{19}$$

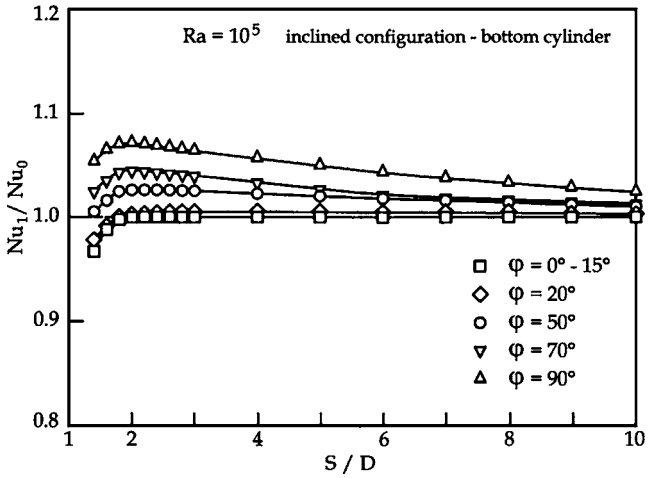

Fig. 10 Distributions of the ratio Nu_1/Nu_0 versus S/D for the bottom cylinder of a two-cylinder inclined array at Ra=10^5 and different tilting angles in the range 0 deg$<\varphi<$90 deg

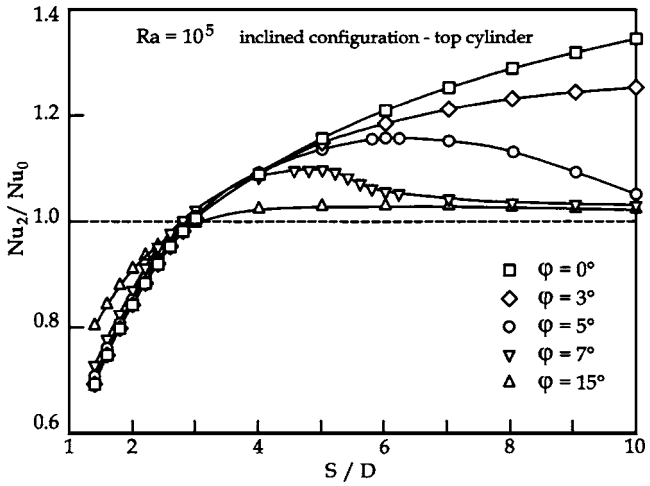

Fig. 11 Distributions of the ratio Nu_2/Nu_0 versus S/D for the top cylinder of a two-cylinder inclined array at Ra=10^5 and different tilting angles in the range 0 deg$<\varphi\leqslant$15 deg

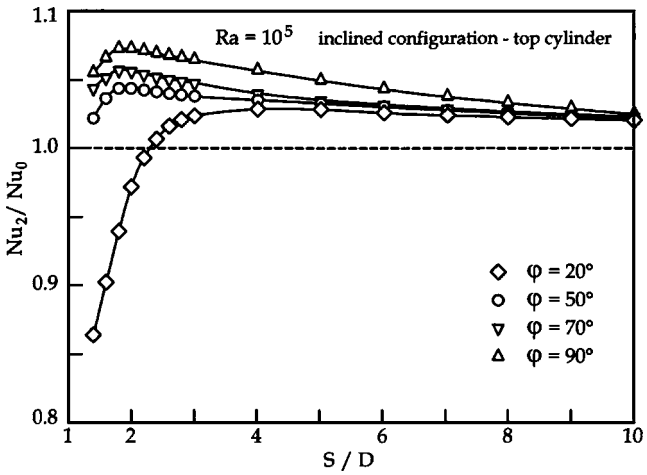

Fig. 12 Distributions of the ratio Nu_2/Nu_0 versus S/D for the top cylinder of a two-cylinder inclined array at Ra=10^5 and different tilting angles in the range 15 deg$<\varphi<$90 deg

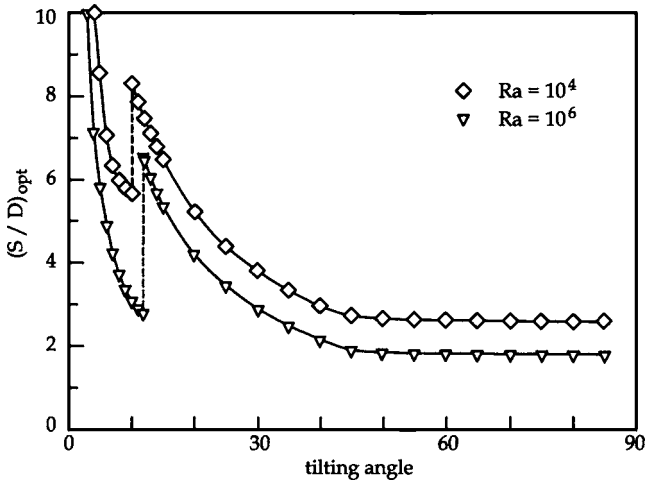

Fig. 13 Distributions of $(S/D)_{opt}$ versus φ for Ra=10^4 and 10^6

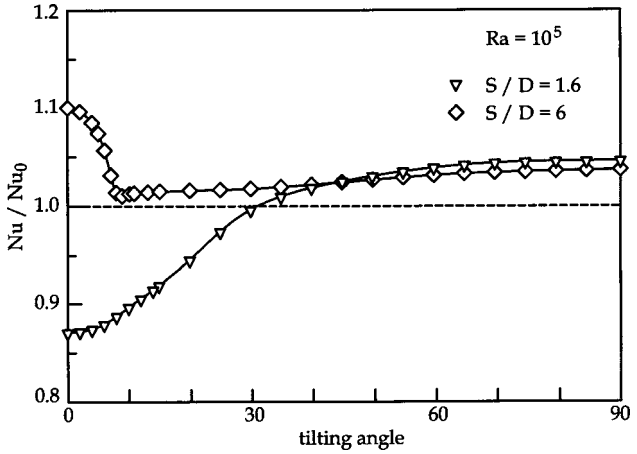

Fig. 15 Distributions of the ratio Nu/Nu_0 versus φ for Ra =10^5 and S/D=1.6 and 6

$$\varphi^* = 0.075\mathrm{Ra}^{0.075}\ (\mathrm{rad}) \quad \text{if } \mathrm{Ra} \geqslant 10^5 \tag{20}$$

for $10^3 \leqslant \mathrm{Ra} \leqslant 10^7$, with a 0.71% standard deviation of error and a range of error from −0.75% to 0.87%. Note that in both Eqs. (19) and (20), φ^* is given in radians, while in Fig. 14, the discontinuity angle φ^* is reported in degrees.

The effects of the misalignment angle will now be discussed.

Two different situations have to be considered in order to correctly take into account the dependence of the overall heat transfer rate from the whole cylinder array on the tilting angle. In fact, as mentioned in the section dedicated to the vertical configuration, the plume effect implies degradations in the heat transfer rate from the top cylinder at small separation distances and enhancements at large separation distances. This means that, since the contribution of the plume effect decreases with increasing the tilting angle φ, in the point of view of the heat transfer performance of the top cylinder, such decrease is advantageous at close cylinder spacings and unfavorable at large cylinder spacings. In contrast, the increasing contribution of the chimney effect, which occurs as the misalignment angle increases, is always propitious for the enhancement of the heat transfer performance of both cylinders. Thus, at close cylinder spacing, the positive circumstances produced by the increasing contribution of the chimney effect and by the decreasing contribution of the plume effect sum up. This leads to a distribution of Nu/Nu_0, which increases with φ, as shown in Fig. 15 for, e.g., S/D=1.6 and Ra=10^5. On the other hand, at large cylinder spacing, the positive circumstance produced by the increasing contribution of the chimney effect is countervailed by the negative circumstance produced by the decreasing contribution of the plume effect. Indeed, as long as the plume effect plays a dominant role, which occurs for very small misalignments, i.e., for tilting angles of the cylinder array lower than about 5 deg, the negative circumstance definitely prevails upon the positive one, and the distribution of Nu/Nu_0 decreases significantly with increasing φ up to a smooth minimum, as shown in Fig. 15 for, e.g., S/D=6 and Ra=10^5.

Finally, as far as the influence of the Rayleigh number on the heat transfer performance of the cylinder array is concerned, it is obvious that the Nusselt number increases with increasing Ra, owing to the increase in the buoyancy-driven flow. However, what happens to the relative heat transfer performance is definitely more interesting, as displayed in Fig. 16, where the distributions of Nu/Nu_0 versus S/D at Ra=10^3, 10^5, and 10^7 are reported for eight different misalignment angles from 2 deg to 80 deg. It may be noticed that for quasivertical alignments (that is, up to nearly φ=10 deg) and sufficiently large separation distances (that is, $S/D \geqslant 5$), the relative heat transfer performance of the whole cylinder array decreases moderately as the Rayleigh number increases.

Local solutions are presented in Fig. 17, where equispaced isotherm lines are plotted at, e.g., Ra=10^5 and S/D=3 for different tilting angles, so as to highlight the main physical facts described above.

The numerical results obtained for the optimum cylinder spacing $(S/D)_{opt}$ may be expressed through the following set of correlating equations:

$$(S/D)_{\mathrm{opt}} = \frac{0.44}{\tan\varphi} + 27.65\mathrm{Ra}^{-0.236} - 0.4 \tag{21}$$

for $10^3 \leqslant \mathrm{Ra} \leqslant 10^7$ and $0\ \mathrm{deg} < \varphi < \varphi^*$, with a 4.25% standard deviation of error and a range of error from −8.6% to +8.6% with a 95% level of confidence;

$$(S/D)_{\mathrm{opt}} = 6.3\ \mathrm{Ra}^{-0.1} + 9.8e^{-3.61\tan\varphi} \tag{22}$$

for $10^3 \leqslant \mathrm{Ra} \leqslant 10^7$ and $\varphi^* < \varphi \leqslant 45$ deg, with a 3.28% standard deviation of error and a range of error from −5.5% to +5.2% with a 95% level of confidence;

$$(S/D)_{\mathrm{opt}} = 1.135 + 7.4\mathrm{Ra}^{-0.185} \tag{23}$$

for $10^3 \leqslant \mathrm{Ra} \leqslant 10^7$ and $45\ \mathrm{deg} < \varphi < 90$ deg, with a 5.18% standard deviation of error and a range of error from −6.9% to +7.8% with a 95% level of confidence.

The numerical results obtained for the Nusselt number Nu_{max},

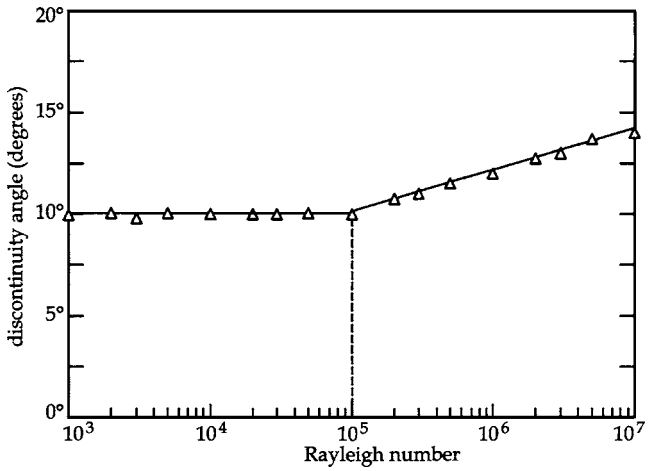

Fig. 14 Distribution of the discontinuity angle φ^* (in degrees) versus Ra

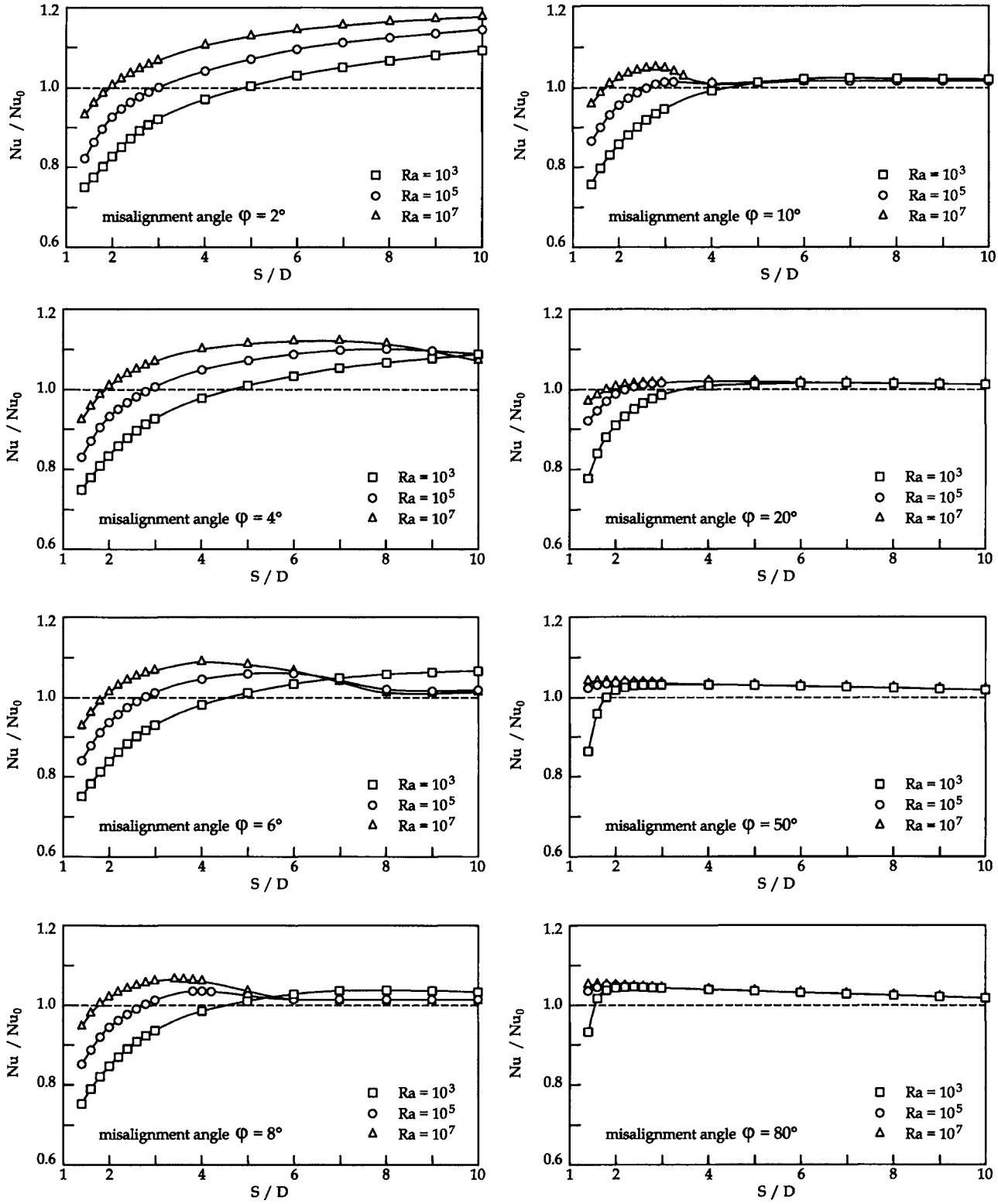

Fig. 16 Distributions of the ratio Nu/Nu_0 versus S/D at $Ra=10^3$, 10^5, and 10^7 and different tilting angles

which corresponds to the optimum cylinder spacing $(S/D)_{opt}$, may be expressed through the following set of correlating equations:

$$Nu_{max} = 0.6 + (0.86\cos^{2.73}\varphi - 0.386)Ra^{0.25} \quad (24)$$

for $10^3 \leqslant Ra \leqslant 10^7$ and $0 \text{ deg} < \varphi < \varphi^*$, with a 1.73% standard deviation of error and a range of error from −2.8% to +2.9% with a 95% level of confidence;

$$Nu_{max} = 0.61 + 0.085\cos^4\varphi + 0.431Ra^{0.25} \quad (25)$$

for $10^3 \leqslant Ra \leqslant 10^7$ and $\varphi^* < \varphi \leqslant 90$ deg, with a 1.79% standard deviation of error and a range of error from −3.6% to +2.3% with a 95% level of confidence.

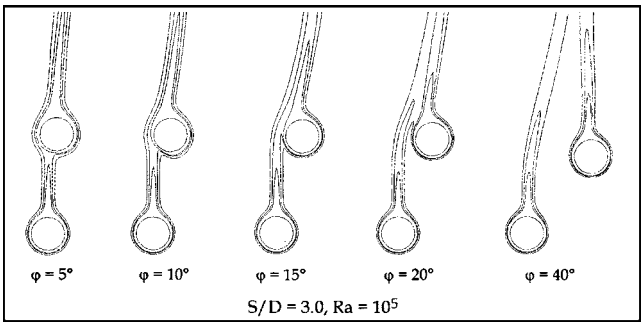

Fig. 17 Isotherm contour plots for a two-cylinder inclined array at Ra=10^5, S/D=3, and different tilting angles

The numerical results obtained for the Nusselt number Nu of the pair of cylinders as a whole may be expressed through the following set of correlating equations:

$$\mathrm{Nu} = 0.389\mathrm{Ra}^{0.25}(S/D)^{0.17}\tan^{0.01}\varphi \tag{26}$$

for $10^3 \leq \mathrm{Ra} \leq 10^7$, $0 \text{ deg} < \varphi < \varphi^*$, and $1.4 \leq S/D < (S/D)_{\mathrm{opt}}$, with a 3.46% standard deviation of error and a range of error from −7.2% to +7.1% with a 95% level of confidence;

$$\mathrm{Nu} = 0.72 + \left[0.416 + \frac{0.0012}{(S/D)^{1.24}\tan^{2.3}\varphi}\right]\mathrm{Ra}^{0.25} \tag{27}$$

for $10^3 \leq \mathrm{Ra} \leq 10^7$, $0 \text{ deg} < \varphi < \varphi^*$, and $(S/D)_{\mathrm{opt}} \leq S/D \leq 10$, with a 1.47% standard deviation of error and a range of error from −2.8% to +2.9% with a 95% level of confidence;

$$\mathrm{Nu} = 0.57 + \left\{0.259 + 0.2\left(\frac{\cos\varphi}{\cos\varphi^*}\right)^{0.01}\left[\frac{(S/D)}{(S/D)_{\mathrm{opt}}}\right]^{0.4}\right\}\mathrm{Ra}^{0.25} \tag{28}$$

for $10^3 \leq \mathrm{Ra} \leq 10^7$, $\varphi^* < \varphi \leq 90$ deg, and $1.4 \leq S/D < (S/D)_{\mathrm{opt}}$, with a 3.65% standard deviation of error and a range of error from −5.6% to +6.8% with a 95% level of confidence;

$$\mathrm{Nu} = 0.71 + 0.434(\sin^{0.02}\varphi)\left[\frac{(S/D)_{\mathrm{opt}}}{(S/D)}\right]^{0.02}\mathrm{Ra}^{0.25} \tag{29}$$

for $10^3 \leq \mathrm{Ra} \leq 10^7$, $\varphi^* < \varphi \leq 90$ deg, and $(S/D)_{\mathrm{opt}} \leq S/D \leq 10$, with a 0.75% standard deviation of error and a range of error from −1.4% to +1.1% with a 95% level of confidence.

The numerical results obtained for the Nusselt number of the bottom cylinder, Nu_1, for tilting angles smaller than the discontinuity angle φ^* may be expressed through the following correlating equation:

$$\mathrm{Nu}_1 = 0.687 + 0.42\mathrm{Ra}^{0.25}\tanh\left[\frac{(S/D)\mathrm{Ra}^{0.134}}{5.76\cos\varphi} + 0.84\right] \tag{30}$$

for $10^3 \leq \mathrm{Ra} \leq 10^7$ and $0 \text{ deg} < \varphi < \varphi^*$, with a 1.22% standard deviation of error and range of error from −1.6% to +1.5% with a 95% level of confidence.

The numerical results obtained for the Nusselt number of the top cylinder, Nu_2, for tilting angles smaller than the discontinuity angle φ^* may be expressed through the following set of correlating equations:

$$\mathrm{Nu}_2 = \frac{0.28\mathrm{Ra}^{0.26}(S/D)^{0.3}}{\cos^{3.04}\varphi} \tag{31}$$

for $10^3 \leq \mathrm{Ra} \leq 10^7$, $0 \text{ deg} < \varphi < \varphi^*$, and $1.4 \leq S/D < (S/D)_{\mathrm{opt}}$, with a 4.85% standard deviation of error and a range of error from −8.1% to +8.3% with a 95% level of confidence;

$$\mathrm{Nu}_2 = 0.80 + \left(0.413 + \frac{0.0015}{(S/D)\tan^{2.3}\varphi}\right)\mathrm{Ra}^{0.25} \tag{32}$$

for $10^3 \leq \mathrm{Ra} \leq 10^7$, $0 \text{ deg} < \varphi < \varphi^*$, and $(S/D)_{\mathrm{opt}} \leq S/D \leq 10$, with a 2.48% standard deviation of error and a range of error from −4.7% to +5% with a 95% level of confidence.

As far as the Nusselt numbers of the bottom and top cylinders, Nu_1 and Nu_2, for tilting angles larger than the discontinuity angle φ^* are concerned, they are practically the same, i.e., $\mathrm{Nu}_1 \cong \mathrm{Nu}_2 \cong \mathrm{Nu}$, which implies that Eqs. (28) and (29) may be also used for their evaluation, with the same orders of both the standard deviation and the range of error.

7 Conclusions

Free convection in air from a pair of parallel, horizontal cylinders with their axes set in a plane inclined with respect to the gravity vector has been studied numerically for the steady laminar regime by a computer code based on the SIMPLE-C algorithm. Simulations have been performed for center-to-center separation distances from 1.4 up to 10 diameters, tilting angles of the two-cylinder array from 0 deg to 90 deg, and Rayleigh numbers from 10^3 to 10^7. Heat transfer dimensionless correlating equations with acceptable percentage values of both the standard deviation and the range of error have been developed for any individual cylinder and for the pair of cylinders as a whole.

The main results obtained in the present study may be summarized as follows:

(a) for moderately tilted configurations, i.e., up to nearly 10–15 deg of inclination with respect to gravity, the heat transfer rates derive from the combined contributions of the plume effect (typical for the vertical setting) and the chimney effect (typical for the horizontal setting);
(b) for larger inclinations, the mutual interactions occurring between the cylinders are governed exclusively by the chimney effect;
(c) at any misalignment angle, an optimum cylinder spacing for the maximum heat transfer rate, which decreases with increasing the Rayleigh number, does exist;
(d) increases in the heat transfer performance relative to that typical for a single cylinder up to values of the order of 10–15% may be achieved;
(e) leaving aside the quasivertical settings, whose typical values of the optimum cylinder spacing is of the order of 8–10 cylinder diameters, it is worth to point out that for quasihorizontal configurations, i.e., for misalignment angles larger than 40–50 deg, increases of the order of 5–7% may be obtained with spacings of the order of 1.5–2 cylinder diameters, which is of significant relevance when the compactness of the heat transfer equipment is of primary importance.

Nomenclature

D = diameter of the cylinders
$\mathbf{g}$ = gravity vector
g = gravitational acceleration
k = thermal conductivity of the fluid
Nu = average Nusselt number of the pair of cylinders
$\mathrm{Nu}(\theta)$ = local Nusselt number
Nu_0 = average Nusselt number of the single cylinder
Nu_1 = average Nusselt number of the lower cylinder
Nu_2 = average Nusselt number of the upper cylinder
p = dimensionless pressure
Pr = Prandtl number= ν/α
Q = heat transfer rate
q = heat flux

r = dimensionless radial coordinate normalized with D
Ra = Rayleigh number based on the cylinder diameter $= g\beta(t_w - t_\infty)D^3/\alpha\nu$
S = center-to-center separation distance
T = dimensionless temperature
t = temperature
U = dimensionless radial or X-wise velocity component
$\mathbf{V}$ = dimensionless velocity vector
V = dimensionless tangential or Y-wise velocity component
X, Y = dimensionless Cartesian coordinates normalized with D

Greek Symbols

α = thermal diffusivity of the fluid
β = coefficient of volumetric thermal expansion of the fluid
φ = tilting angle of the two-cylinder array
ν = kinematic viscosity of the fluid
θ = dimensionless polar coordinate
ρ = density of the fluid

Subscripts

i = ith cylinder
opt = optimum value
max = maximum value
w = cylinder surface
∞ = undisturbed fluid

References

[1] Eckert, E. R. G., and Soehngen, E. E., 1948, "Studies on Heat Transfer in Laminar Free Convection With the Zehnder–Mach Interferometer," AF Technical Report No. 5747, USAF Air Material Command, Wright-Patterson Air Force Base, Ohio.

[2] Lieberman, J., and Gebhart, B., 1969, "Interaction in Natural Convection From an Array of Heated Elements, Experimental," Int. J. Heat Mass Transfer, **12**, pp. 1385–1396.

[3] Marsters, G. F., 1972, "Arrays of Heated Horizontal Cylinders in Natural Convection," Int. J. Heat Mass Transfer, **15**, pp. 921–933.

[4] Sparrow, E. M., and Niethammer, J. E., 1981, "Effect of Vertical Separation Distance and Cylinder-to-Cylinder Temperature Imbalance on Natural Convection for a Pair of Horizontal Cylinders," ASME J. Heat Transfer, **103**, pp. 638–644.

[5] Tokura, I., Saito, H., Kisinami, K., and Muramoto, K., 1983, "An Experimental Study of Free Convection Heat Transfer From a Horizontal Cylinder in a Vertical Array Set in Free Space Between Parallel Walls," ASME J. Heat Transfer, **105**, pp. 102–107.

[6] Sadeghipour, M. S., and Asheghi, M., 1994, "Free Convection Heat Transfer From Arrays of Vertically Separated Horizontal Cylinders at Low Rayleigh Numbers," Int. J. Heat Mass Transfer, **37**, pp. 103–109.

[7] Chouikh, R., Guizani, A., Maalej, M., and Belghith, A., 1999, "Numerical Study of the Laminar Natural Convection Flow Around an Array of Two Horizontal Isothermal Cylinders," Int. Commun. Heat Mass Transfer, **26**, pp. 329–338.

[8] Corcione, M., 2005, "Correlating Equations for Free Convection Heat Transfer From Horizontal Isothermal Cylinders Set in a Vertical Array," Int. J. Heat Mass Transfer, **48**, pp. 3660–3673.

[9] Sparrow, E. M., and Boessneck, D. S., 1983, "Effect of Traverse Misalignment on Natural Convection From a Pair of Parallel, Vertically Stacked, Horizontal Cylinders," ASME J. Heat Transfer, **105**, pp. 241–247.

[10] Farouk, B., and Guceri, S. I., 1983, "Natural Convection From Horizontal Cylinders in Interacting Flow Fields," Int. J. Heat Mass Transfer, **26**, pp. 231–243.

[11] Launder, B. E., and Massey, T. H., 1978, "The Numerical Prediction of Viscous Flow and Heat Transfer in Tube Banks," ASME J. Heat Transfer, **100**, pp. 565–571.

[12] Van Doormaal, J. P., and Raithby, G. D., 1984, "Enhancements of the Simple Method for Predicting Incompressible Fluid Flows," Numer. Heat Transfer, **11**, pp. 147–163.

[13] Patankar, S. V., and Spalding, D. B., 1972, "A Calculation Procedure for Heat, Mass and Momentum Transfer in Three-Dimensional Parabolic Flows," Int. J. Heat Mass Transfer, **15**, pp. 1787–1797.

[14] Leonard, B. P., 1979, "A Stable and Accurate Convective Modelling Procedure Based on Quadratic Upstream Interpolation," Comput. Methods Appl. Mech. Eng., **19**, pp. 59–78.

[15] Patankar, S. V., 1980, *Numerical Heat Transfer and Fluid Flow*, Hemisphere, Washington, DC.

[16] Patankar, S. V., 1988, "Recent Developments in Computational Heat Transfer," ASME J. Heat Transfer, **110**, pp. 1037–1045.

[17] Saitoh, T., Sajiki, T., and Maruhara, K., 1993, "Bench Mark Solutions to Natural Convection Heat Transfer Problem Around a Horizontal Circular Cylinder," Int. J. Heat Mass Transfer, **36**, pp. 1251–1259.

[18] Churchill, S. W., and Chu, H. H. S., 1975, "Correlating Equations for Laminar and Turbulent Free Convection from a Horizontal Cylinder," Int. J. Heat Mass Transfer, **18**, pp. 1049–1053.

[19] Gebhart, B., Pera, L., and Schorr, A. W., 1970, "Steady Laminar Natural Convection Plumes Above a Horizontal Line Heat Source," Int. J. Heat Mass Transfer, **13**, pp. 161–171.

Natural Convection Heat Transfer in a Partially Open Square Cavity With a Thin Fin Attached to the Hot Wall

Abdullatif Ben-Nakhi[1]
Mechanical Power & Refrigeration Department,
College of Technological Studies,
PAAET,
P.O. Box 3665,
Salmiya 22037, State of Kuwait
e-mail: abdnakhi@yahoo.com

M. M. Eftekhari

D. I. Loveday

Department of Civil and Building Engineering,
Loughborough University,
Loughborough, Leicestershire LE11 3TU, UK

A computational study of steady, laminar, natural convective fluid flow in a partially open square enclosure with a highly conductive thin fin of arbitrary length attached to the hot wall at various levels is considered. The horizontal walls and the partially open vertical wall are adiabatic while the vertical wall facing the partial opening is isothermally hot. The current work investigates the flow modification due to the (a) attachment of a highly conductive thin fin of length equal to 20%, 35%, or 50% of the enclosure width, attached to the hot wall at different heights, and (b) variation of the size and height of the aperture located on the vertical wall facing the hot wall. Furthermore, the study examines the impact of Rayleigh number $(10^4 \leqslant \mathrm{Ra} \leqslant 10^7)$ *and inclination of the enclosure. The problem is put into dimensionless formulation and solved numerically by means of the finite-volume method. The results show that the presence of the fin has counteracting effects on flow and temperature fields. These effects are dependent, in a complex way, on the fin level and length, aperture altitude and size, cavity inclination angle, and Rayleigh number. In general, Nusselt number is directly related to aperture altitude and size. However, after reaching a peak Nusselt number, Nusselt number may decrease slightly if the aperture's size increases further. The impact of aperture altitude diminishes for large aperture sizes because the geometrical differences decrease. Furthermore, a longer fin causes higher rate of heat transfer to the fluid, although the equivalent finless cavity may have higher heat transfer rate. In general, the volumetric flow rate and the rate of heat loss from the hot surfaces are interrelated and are increasing functions of Rayleigh number. The relationship between Nusselt number and the inclination angle is nonlinear.*
[DOI: 10.1115/1.2885166]

Keywords: natural convection, laminar flow, square enclosure, partially open cavity, thin fin

Introduction

The study of natural convection in open cavities has been the subject of many experimental and numerical investigations during the past two decades. This is due to its importance in several thermal engineering problems, such as the design of electronic devices and open cavity solar thermal receivers. These investigations have been motivated by recent advances in electronics technology and the need for efficient cooling techniques. Natural convection is favored for cooling of electronic devices because it is cheap, inherently reliable, simple, and quiet. Papers published in the archival literature have investigated the effect on flow and heat transfer for different Rayleigh numbers, aspect ratios, and tilt angles. Also, these works studied the occurrence of transition and turbulence and how the boundary conditions in the aperture are considered.

Various authors experimentally studied natural convection in open cavities. For example, Bejan and Kimura [1] performed experimental investigations in order to validate their theoretical study of free convection penetration into a rectangular cavity. They demonstrated that the flow consists of a horizontal counterflow, which penetrates the cavity over a distinct length. Hess and Henze [2] determined the characteristics of two- and three-dimensional natural convection flows in constrained and unconstrained cavities by means of dye flow visualization. The aperture was centrally located and had a dimensionless size of 0.5, and the Rayleigh number (Ra) ranging from 10^7 to 10^{11} in the laminar and turbulent regimes. Chan and Tien [3] experimentally investigated the effect of an open boundary on steady laminar, natural convection in a horizontal fully open rectangular cavity with an aspect ratio of 0.143, with water as the working fluid, and Rayleigh number ranging from 10^6 to 10^7. Chakroun [4] performed an experimental investigation to study the effect of wall conditions as well as its tilt angle on heat transfer for a fully open tilted cavity. His study contains seven different wall configurations over an inclination angle (measured from the vertical direction) range from −90 deg to +90 deg. It was concluded that the tilt angle, wall configuration, and number of hot walls are all factors that strongly affect the natural convection inside the fully open cavity. Rojas and Avila [5] analyzed, both numerically and experimentally, transient natural convection in an open cavity with one inclined wall that is heated in such a way that the wall temperature increases uniformly according to a hyperbolic tangent function.

Others studied theoretically laminar, natural convection heat transfer in fully open cavities. Le Quere et al. [6] investigated thermally driven laminar natural convection in inclined rectangular enclosures with three isothermal sides and covered a Grashof number range from 10^4 to 10^7. Penot [7] analyzed a similar problem using stream function-vorticity formulation in order to study the effects of Grashof number and inclination of the cavity on flow characteristics. Unsteady solutions were observed for

[1]Corresponding author.

Contributed by the Heat Transfer Division of ASME for publication in the JOURNAL OF HEAT TRANSFER. Manuscript received November 19, 2006; final manuscript received August 25, 2007; published online April 10, 2008. Review conducted by Jay M. Khodadadi.

Grashof number larger than 10^5 and cavity aperture facing upward. Chan and Tien [3] tested the validity of approximate boundary conditions at the opening for a computational domain restricted to the cavity instead of using an extended domain. They concluded that for a square open cavity having an isothermal vertical side facing the opening and two adiabatic horizontal sides, satisfactory heat transfer results could be obtained by the restricted domain. Mohamad [8] presented the numerical results for cavities similar to those considered by Chan and Tien [3] over Ra range from 10^3 to 10^7, but he employed different approximate boundary conditions at the opening plane by setting gradients of both velocity components to zero. It was found that heat transfer was not sensitive to the inclination angle and the flow was unstable at high Rayleigh numbers and small inclination angles. Polat and Bilgen [9] numerically studied inclined fully open shallow cavities in which the side facing the opening was heated by constant heat flux, and two adjoining walls being adiabatic over Ra values ranging from 10^3 to 10^{10}. The opening was in contact with a reservoir at constant temperature and pressure, and the computational domain was restricted to the cavity. They concluded that the inclination angle of the hot plate is an important parameter affecting volumetric flow rate and heat transfer. Unlike the previous studies, Miyamoto et al. [10] numerically studied partially and fully open square cavities. All three solid walls of the cavities were isothermal and various inclination angles were considered and an extended computational domain was used. In the case of the partially open cavity, the aperture was centrally located and its dimensionless size was 0.5. Their Rayleigh number ranged from 0.7 to 7×10^5 for horizontal cavities and from 7×10^3 to 7×10^4 for inclined cavities. They clarified the effects of an aperture and cavity orientation, with respect to the direction of gravity, on natural convection heat transfer in the cavity. Bilgen and Oztop [11] numerically analyzed heat transfer by natural convection within a partially open inclined cavity by employing a computation domain restricted to the cavity. The wall facing the opening was isothermally heated while the remaining walls were adiabatic. Their study covered a Rayleigh number range from 10^3 to 10^6. They concluded that the volumetric flow rate and Nusselt number to be increasing functions of Rayleigh number and aperture size and location.

Modification of heat transfer in cavities due to the presence of fins attached to cavity walls has received attention in recent years due to the many possible practical applications. Some of these applications can be found in solar collectors, nuclear reactors, heat exchangers, and electronic equipment. Heat transfer rate through the enclosure may be controlled by altering fin configuration [12]. A full literature review on heat transfer by natural convection within cavities with a thin fin attached to one of the cavity walls is presented by Ben-Nakhi and Chamkha [13].

The objective of the work presented in this paper is to study the effects of attaching a perfectly conductive thin fin to the isothermally hot wall of the cavity considered by Bilgen and Oztop [11], as shown in Fig. 1. The scope of the current work is to investigate the effects of the thin fin length and level for different combinations of the aperture size and altitude, and enclosure tilt angles.

Mathematical Model

Consider steady laminar, two-dimensional, natural convection inside a partially open square enclosure in the presence of a highly conductive thin fin of arbitrary length c attached to a vertical isothermally heated wall at arbitrary height b from the enclosure base, as shown in Fig. 1. The thickness of the fin is assumed to be very small compared to the computational grid size. The other vertical wall contains a partial opening (aperture) whose size is h and its centerline is at an altitude d from the enclosure base. The energy from the hot surfaces is dissipated by convection of ambient fluid at T_∞ through the opening. As explained by Shi and Khodadadi [12], a special coordinate system s along the walls is adopted with its origin at $x=0$ and $y=L$, as shown by the dotted

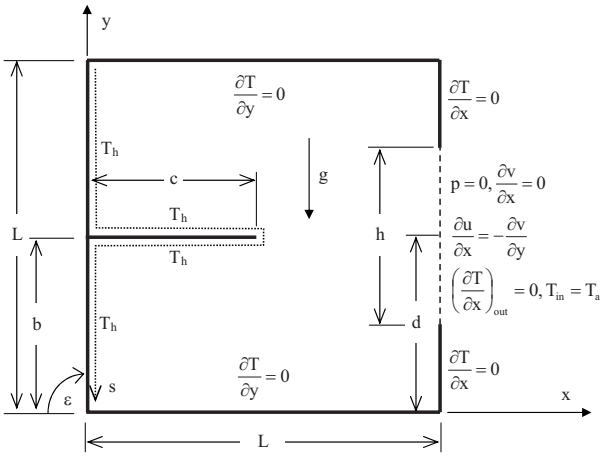

Fig. 1 Schematic diagram and coordinate system for a partially open square enclosure with thin fin

line in Fig. 1. The fluid is assumed to be incompressible, viscous, Newtonian, and having constant thermophysical properties.

The governing equations for this problem are based on the balance laws of mass, momentum, and energy. Although the current study is concerned with steady state behavior, a transient mathematical model is employed in order to accommodate the nonlinearities of the problem. Taking into account the assumptions mentioned above, and applying the Boussinesq approximation for the body force terms in the momentum equations, the governing equations for the fluid region of the domain can be written in dimensionless formulation as

$$\frac{\partial U}{\partial X}+\frac{\partial V}{\partial Y}=0 \tag{1}$$

$$\frac{\partial U}{\partial \tau}+U\frac{\partial U}{\partial X}+V\frac{\partial U}{\partial Y}=-\frac{\partial P}{\partial X}+\mathrm{Pr}\left(\frac{\partial^2 U}{\partial X^2}+\frac{\partial^2 U}{\partial Y^2}\right)+\mathrm{Ra}\ \mathrm{Pr}\ \theta\cos\varepsilon \tag{2}$$

$$\frac{\partial V}{\partial \tau}+U\frac{\partial V}{\partial X}+V\frac{\partial V}{\partial Y}=-\frac{\partial P}{\partial Y}+\ \mathrm{Pr}\left(\frac{\partial^2 V}{\partial X^2}+\frac{\partial^2 V}{\partial Y^2}\right)+\mathrm{Ra}\ \mathrm{Pr}\ \theta\sin\varepsilon \tag{3}$$

$$\frac{\partial \theta}{\partial \tau}+U\frac{\partial \theta}{\partial X}+V\frac{\partial \theta}{\partial Y}=\left(\frac{\partial^2 \theta}{\partial X^2}+\frac{\partial^2 \theta}{\partial Y^2}\right) \tag{4}$$

In writing Eqs. (1)–(4), the following dimensionless parameters and definitions are used:

$$X=\frac{x}{L},\quad Y=\frac{y}{L},\quad U=u\frac{L}{\alpha},\quad V=v\frac{L}{\alpha},\quad P=\frac{(p-p_a)L^2}{\rho\alpha^2},$$
$$\tau=\alpha\frac{t}{L^2},\quad \mathrm{Pr}=\frac{\nu}{\alpha},\quad \theta=\frac{(T-T_a)}{(T_h-T_a)},\quad \mathrm{Ra}=\frac{g\beta(T_h-T_a)L^3}{\alpha\nu} \tag{5}$$

where the dimensionless parameters appearing in the above equations are given in the Nomenclature.

Motionless fluid (i.e., $U=V=0$), $P=0$, and cold isothermal state (i.e., $\theta=0$) are assumed as the initial condition (i.e., $\tau=0$). The boundary conditions can be written as follows:

On all solid surfaces,

$$U=V=0,\quad \frac{\partial P}{\partial N}=0 \tag{6a}$$

On the hot wall and thin fin,

$$\theta = 1 \tag{6b}$$

On the horizontal walls,

$$\left(\frac{\partial \theta}{\partial Y}\right) = 0 \tag{6c}$$

On the partially open wall,

$$\left(\frac{\partial \theta}{\partial X}\right) = 0 \tag{6d}$$

On the opening,

$$P = 0, \quad \frac{\partial V}{\partial X} = 0, \quad \frac{\partial U}{\partial X} = -\frac{\partial V}{\partial Y}, \quad \left(\frac{\partial \theta}{\partial X}\right)_{\text{out}} = 0, \quad \theta_{\text{in}} = 0 \tag{6e}$$

The stream function can be defined as

$$v = -\frac{\partial \Psi}{\partial x}, \quad u = \frac{\partial \Psi}{\partial y}, \quad \psi = \frac{\Psi}{\alpha} \tag{7}$$

The local, total, and average Nusselt numbers (Nu, Nu_t, and $\overline{\mathrm{Nu}}$, respectively) for the hot surfaces (i.e., left wall and both sides of the thin fin) are given by

$$\mathrm{Nu} = -\left(\frac{\partial \theta}{\partial N}\right)_{N=0} \tag{8a}$$

$$\mathrm{Nu}_t = \int_0^Z \mathrm{Nu}\, dS, \quad Z = 1 + 2C \tag{8b}$$

$$\overline{\mathrm{Nu}} = \frac{1}{Z}\int_0^Z \mathrm{Nu}\, dS = \frac{\mathrm{Nu}_t}{Z}, \quad Z = 1 + 2C \tag{8c}$$

where $S = s/L$ and s is a coordinate adopted for distance along the hot solid-fluid interfaces and $N = n/L$, where n is the local distance normal to the s axis.

The dimensionless volumetric flow rate $\dot{V}$ is calculated by

$$\dot{V} = \int_{X=1} U_{\text{in}} dY, \quad U_{\text{in}} = \begin{cases} -U_{X=1} & \text{if } U_{X=1} < 0 \\ 0 & \text{if } U_{X=1} \geq 0 \end{cases} \tag{9}$$

Numerical Algorithm

The governing equations (1)–(4) of laminar two-dimensional natural convection heat transfer in the partially open square enclosure with thin fin, shown in Fig. 1, were discretized using the second-order upwind scheme for the convection terms and by employing the SIMPLEC pressure correction algorithm [14]. The resulting algebraic equations were solved by utilizing the alternating direction implicit (ADI) control volume method presented by Patankar [15] along with under-relaxation factors for temperature, pressure, and velocities. Steady state results were reached for all cases considered in the current paper. The convergence criterion employed for each time step Δ_{ts} and the convergence criterion employed to reach the steady-state solution Δ_{ss} were the standard relative error, which is based on the maximum norm given by

$$\Delta_{\text{ts}} = \max\left\{\frac{\|{}^{i}P - {}^{i-1}P\|_\infty}{\|{}^{i}P\|_\infty}, \frac{\|{}^{i}\theta - {}^{i-1}\theta\|_\infty}{\|{}^{i}\theta\|_\infty}, \frac{\|{}^{i}U - {}^{i-1}U\|_\infty}{\|{}^{i}U\|_\infty}, \frac{\|{}^{i}V - {}^{i-1}V\|_\infty}{\|{}^{i}V\|_\infty}\right\} \leq 10^{-8} \tag{10a}$$

$$\Delta_{\text{ss}} = \max\left\{\frac{\|{}^{j}\mathrm{Nu}_t - {}^{j-1}\mathrm{Nu}_t\|_\infty}{\|{}^{j}\mathrm{Nu}_t\|_\infty}, \frac{\|{}^{j}\Delta\psi - {}^{j-1}\Delta\psi\|_\infty}{\|{}^{j}\Delta\psi\|_\infty}\right\} \leq 10^{-6} \tag{10b}$$

where the operator $\|\eta\|_\infty$ indicates the maximum absolute value of the variable over all grid points in the computational domain. The indices i and $i-1$ represent the current and previous iterations, respectively, within each time step. The indices j and $j-1$ represent the current and preceding time steps, respectively, during simulation time.

Since different sizes and locations for the thin fin and aperture are considered in the current study, a uniform structured grid of quadrilateral mesh elements was employed in order to minimize truncation error differences between different cases. Grid tests were conducted to ensure that the results were independent of grid resolution by monitoring the average Nusselt number at the hot surfaces and the flow rate at the aperture. Grid convergence was studied for several cases with grid density from 30×30 to 200×200 at $\mathrm{Ra} = 10^5$. Grid independence was achieved with grid density of 100×100 within 1.8% in Nusselt number and 3.7% in volumetric flow rate with respect to the results obtained with a 200×200 mesh. The mesh quality of the numerical model adopted in the current study was evaluated by analyzing the aspect ratio, the equiangle skew, and the equisize skew of each cell within the domain [16]. Since a uniform structured mesh was implemented in the current work, the aspect ratio, equiangle skew, and equisize skew indices have ideal values, namely, 1.0, 0.0, and 0.0, respectively. However, a uniform mesh was not possible for all cases considered in the current study. This is because, in some cases, the uniform mesh grids do not align with the aperture's edges. For such cases, some of the mesh lines were slightly moved, to coincide with the aperture's edges, in a way that ensured the deviations of the mesh quality indices from their ideal values to be minimal. In general, the requirements for high quality meshes are satisfied in all cases considered in the current paper. In order to reduce round-off errors, double precision computation was employed in the analysis.

The accuracy of the numerical scheme was assessed by applying it to a case studied by Shi and Khodadadi [12], who considered a cavity configuration similar to that being considered in this paper but without the opening, and good agreement was observed and reported elsewhere [13]. Another test was performed by using the numerical scheme to study cases considered by Bilgen and Oztop [11]. They numerically studied laminar natural convection in a cavity similar to that considered in the current work but without the thin fin. Excellent agreement was achieved as can be seen from the streamline and temperature contours in Fig. 2 for different Ra and ε values. Furthermore, in order to examine the validity of the boundary conditions employed in the current study at the aperture when a fin is attached at the hot surface, the results of the extended domain were compared with those for the limited domain. The configurations of the extended and limited domains are similar to those defined by Chan and Tien [3] except that $\mathrm{Ra} = 10^5$ and a thin fin (with $B = 0.5$ and $C = 0.5$) is attached to the left wall. The results are presented in Fig. 3 and show good agreement. These favorable comparisons lend confidence in the numerical results to be presented in the next section.

Results and Discussion

In this section, numerical results for the streamline and temperature contours for various values of the dimensionless fin length C and dimensionless aperture altitude D are reported. In addition, representative results for volumetric flow rate $\dot{V}$ and local, average, and total Nusselt numbers (Nu, $\overline{\mathrm{Nu}}$, and Nu_t) at various configurations are presented and discussed. All results are computed for Prandtl number $\mathrm{Pr} = 0.7$.

Figures 4–6 present steady-state contour plots of the streamline and temperature for various values of thin fin length ($C = 0.0, 0.2, 0.35, 0.5$), Rayleigh number $\mathrm{Ra} = 10^5$, aperture size $H = 0.25$, and three different aperture altitudes D, namely, high, central, and low, respectively. In the absence of the thin fin, a clockwise-rotating vortex is formed, as shown in Figs. 4–6. This is because of the rise of the fluid due to the buoyancy effects produced by heating from the left wall of the enclosure. The warm fluid is discharged from the upper section of the aperture and the

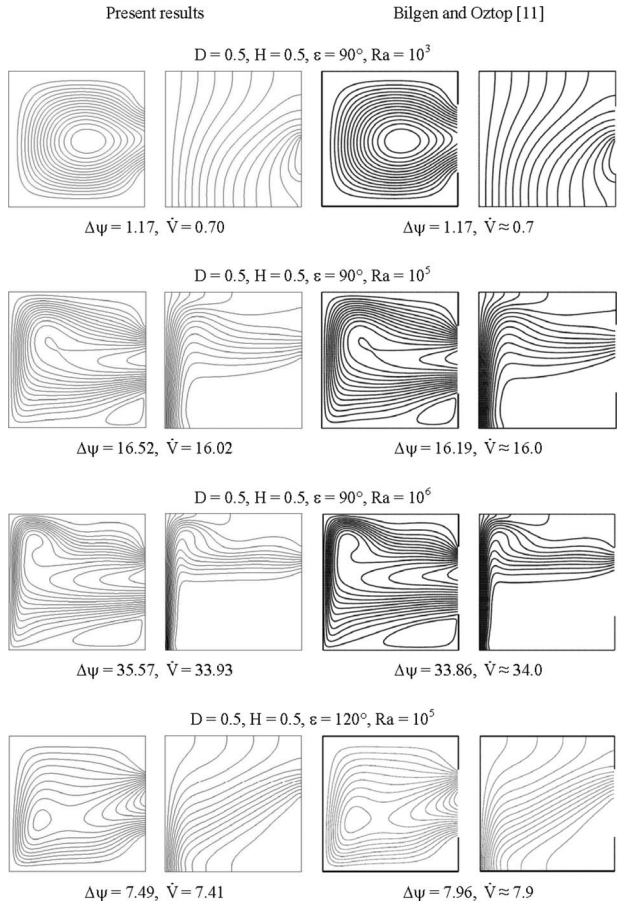

Fig. 2 Comparison of stream functions and isotherms with those of Bilgen and Oztop [11]

cold fluid is entrained from the lower part of the aperture. The size of exit and entrance sections of the fluid at the aperture can be observed by referring to the streamline contours. In general, the presence of a perfectly conductive fin attached to the hot wall of the enclosure has counteracting effects on the flow and temperature fields. The attachment of the fin strengthens the driving potential for natural convection by increasing the area of heat transfer into the fluid, while the existence of the fin tends to create a blockage to flow movement close to the hot wall, causing a weakening of the primary vortex. By comparing the cases shown in Figs. 4–6, it can be seen that the presence of a fin at $B=0.5$ redirects the flow and weakens the fluid speed within the area above the fin. This can be seen by observing the intensity of streamline and temperature contours. These contour plots indicate that longer fins have more significant effects on flow and temperature fields. On the other hand, Figs. 4–6 show that higher aperture (i.e., greater D) produces higher heat transfer rates between the hot surfaces (i.e., left side of the enclosure and both sides of the fin) and the fluid (Nu_t). This is because the fluid that is exiting from the cavity is warm, hence tends to rise. In other words, in an enclosure with lower aperture, the warm fluid should be pushed downward against the buoyancy effects for a longer distance, hence causing more obstruction to the natural convection. Nu_t is directly related to D for the four fin lengths considered in the current paper (i.e., $C=0.0,0.2,0.35,0.5$). Beside Nu_t values and the contour plots of streamlines and temperature, Figs. 4–6 present the values of the dimensionless stream function strength $\Delta\psi$ and the dimensionless volumetric flow rate into the cavity

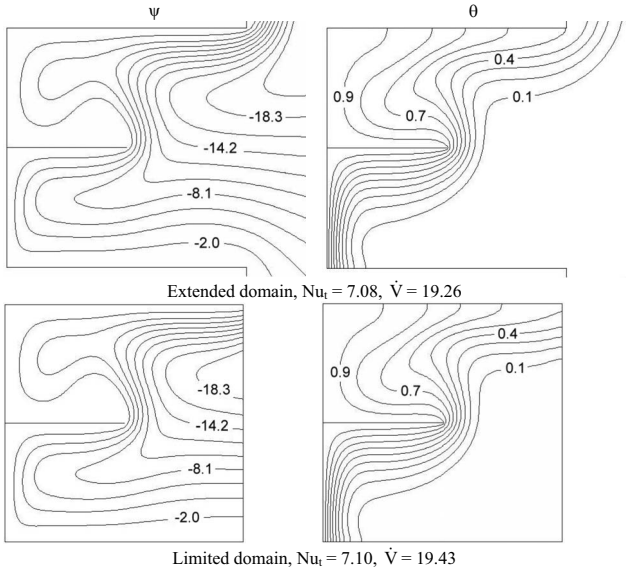

Fig. 3 Comparison of results from extended and limited domains for $B=0.5$, $C=0.5$, $H=1.0$, $\varepsilon=90$ deg, Pr=0.7, and Ra $=10^5$

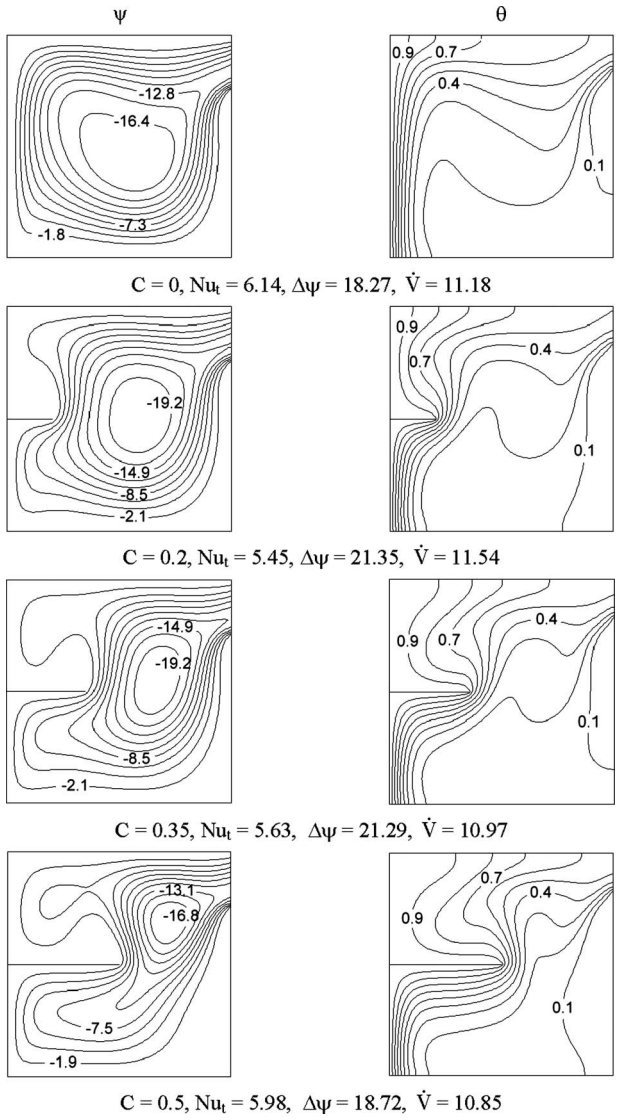

Fig. 4 Effects of C on the contour maps of the streamlines and isotherms for $B=0.5$, $D=0.875$, $H=0.25$, $\varepsilon=90$ deg, and Ra$=10^5$

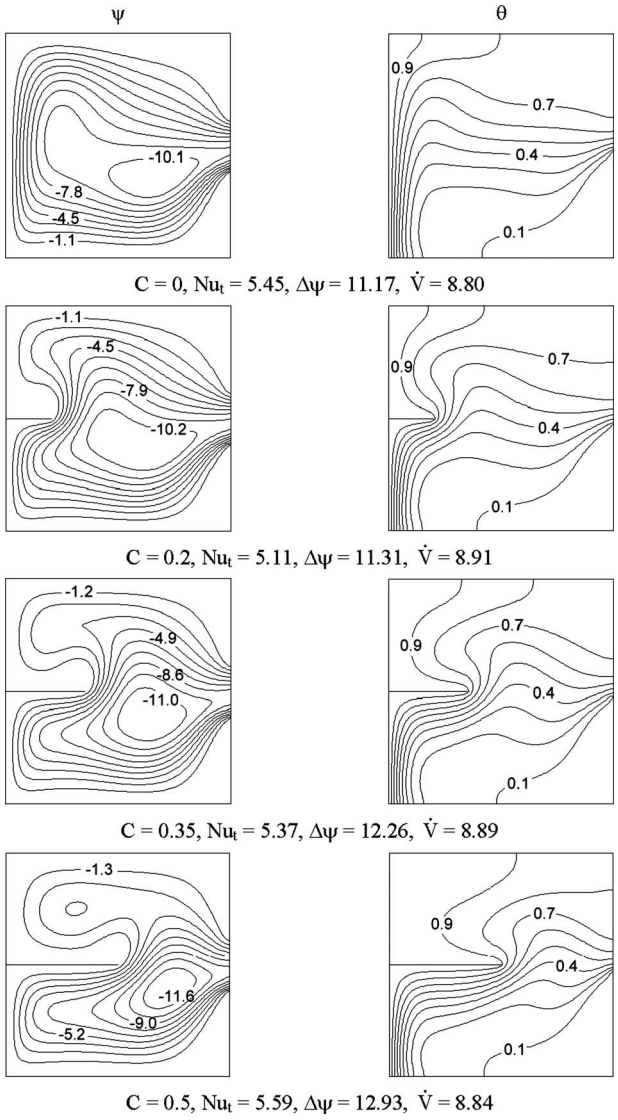

Fig. 5 Effects of *C* on the contour maps of the streamlines and isotherms for *B*=0.5, *D*=0.5, *H*=0.25, ε=90 deg, and Ra=10^5

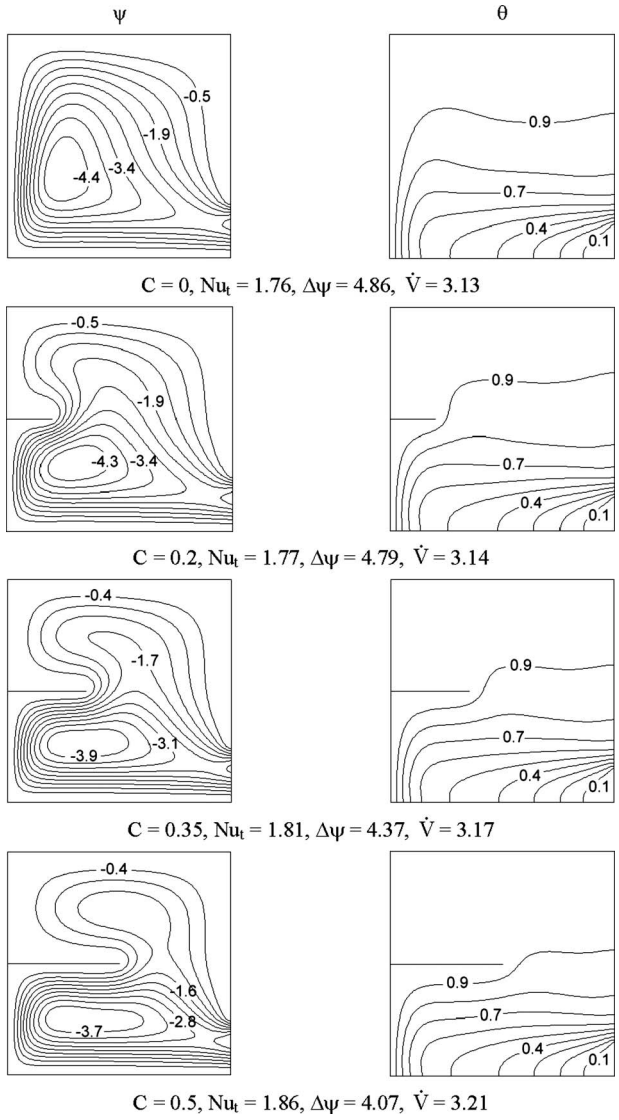

Fig. 6 Effects of *C* on the contour maps of the streamlines and isotherms for *B*=0.5, *D*=0.125, *H*=0.25, ε=90 deg, and Ra=10^5

through the aperture $\dot{V}$. These two variables are of great significance not only because they help in envisioning the fluid flow features but also because they are normally directly related to Nu_t for a given problem configuration. While results show that higher aperture is associated with higher $\Delta\psi$ and $\dot{V}$ values, these two variables are related to fin length C in a complex manner. For example, in a central aperture cavity, increasing C within the range of 0.2–0.5 intensifies $\Delta\psi$ despite the associated drop in $\dot{V}$. This is because fin length together with aperture altitude and size delineates the area available for the circulation of the main vortex. In other words, the increase in $\Delta\psi$ due to the reduction in the available area for main vortex circulation is greater than the decrease in $\Delta\psi$ due to the drop in $\dot{V}$.

Figure 7 illustrates the effects of dimensionless aperture altitude D and dimensionless fin length C on the local Nusselt number Nu at the hot wall including both sides of the fin for dimensionless fin altitude B=0.5, dimensionless aperture size H=0.25, and Ra=10^5. The upper section of the hot wall is defined by $0 \leqslant S \leqslant 0.5$, while the lower section of the wall is defined by $0.5+2C \leqslant S \leqslant 1.0+2C$. Similarly, the upper and lower parts of the fin are defined by $0.5 < S \leqslant 0.5+C$ and $0.5+C \leqslant S < 0.5+2C$, respectively. In the absence of the thin fin, the local Nusselt number Nu increases as the dimensionless distance S increases, with a slight drop close to the lower insulated wall of the enclosure. However, in the presence of a fin, the local Nusselt number exhibits a sharp reduction at the location of the wall/fin intersection, where it becomes a minimum due to the flow stagnation. In principle, the attachment of a fin in the middle of the hot wall always reduces the local Nusselt number for the hot wall by an amount that is inversely related to the fin length C. As mentioned before, this is due to the fact that the fin blocks the flow near the hot wall. The relationship between the local Nusselt number and C is more complex for the fin surfaces. The peak value of Nu, which occurs at the fin tip, is inversely related to C, whereas Nu_t, which is the area under Nu curve, for the fin is directly related to C. Furthermore, heat transfer at the lower surface of the fin is higher than that at the upper surface of the fin by a ratio directly dependent on C. Figure 7 also shows that the lowest thermal performance (i.e., small Nu and Nu_t) is associated with the low aperture. Furthermore, the best thermal performance is associated with the high aperture, although the central aperture produces higher Nu values

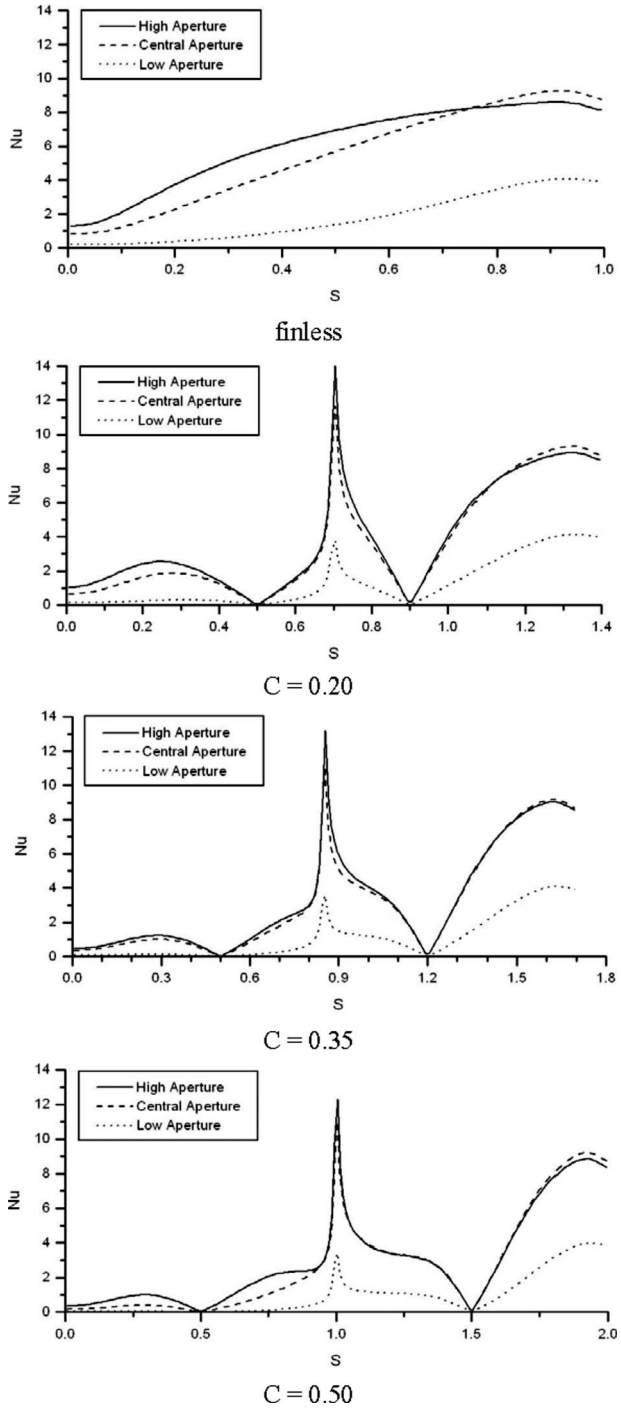

Fig. 7 Effects of *C* and *D* on the local Nusselt number at the hot wall and fin for *B*=0.5, *H*=0.25, ε=90 deg, and Ra=10^5

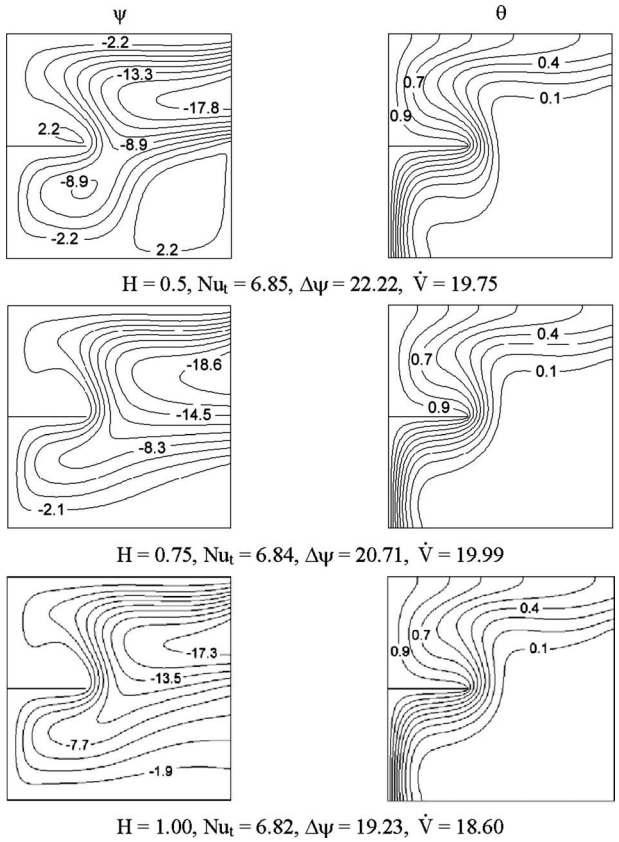

Fig. 8 Effects of *H* on the contour maps of the streamlines and isotherms for high aperture, *B*=0.5, *C*=0.35, ε=90 deg, and Ra=10^5

at the lower segment of the left wall compared to the high aperture. These observations are in agreement with Nu_t values reported in Figs. 4–6.

Figure 8 presents the contour maps of the streamlines and isotherms for $B=0.5$, $C=0.35$, for the high aperture with various sizes ($H=0.50$, 0.75, and 1.00). The contour maps of the streamlines and isotherms for the high aperture with $H=0.25$ are shown in Fig. 4. By comparing the contour maps and the monitored variables, it can be concluded that increasing H enhances heat loss from the hot surfaces until the peak in the Nu_t value is reached, after which increasing H value causes small decrease in Nu_t value.

The H value at which Nu_t profile peaks depend on case configuration, such as C and Ra values. For the cases considered in Fig. 8, the peak Nu_t value occurs at $0.25<H<0.75$. Identifying H values corresponding to peak Nu_t value is beyond the scope of the current work. It is clearly observed from Fig. 8 that increasing H from 0.25 to 0.5 improved Nu_t by allowing higher volumetric flow rate $\dot{V}$. However, Nu_t for $H=0.75$ is slightly less than that for $H=0.5$ although $\dot{V}$ for $H=0.75$ is slightly higher than that for $H=0.5$. Furthermore, by increasing H from 0.75 to 1.0, both $\dot{V}$ and the speed of the fluid near the hot surfaces decrease, hence Nu_t decreases. It is clear that the relation between H and Nu_t is complex. This is because the relationship between H and the local Nusselt number Nu is space dependent. That is to say, increasing the size of an aperture may improve Nu at some segments of the hot surfaces, but this can be at the expense of degrading Nu at other segments of the hot surfaces. For example, Nu at the upper half of the left wall for $H=0.5$ is higher (i.e., the temperature contours are more packed in the nearby area) than that for $H=0.25$, whereas Nu at the lower half of the left wall for $H=0.5$ is lower than that for $H=0.25$.

Figure 9 shows the influence of the dimensionless fin length C and dimensionless aperture altitude D and size H on the average Nusselt number at the hot surfaces $\overline{Nu}$ for $B=0.5$ and Ra=10^5. It is easily observed that C, D, and H have significant effects on $\overline{Nu}$. In general, the dependence of $\overline{Nu}$ on C and D decreases as H value increases because the geometrical differences lessen as the aperture size increases. On the whole, the average Nusselt number $\overline{Nu}$ increases as the aperture altitude is increased. However, the increase in $\overline{Nu}$ due to raising the aperture from the low to the central level is greater than that between the central and high

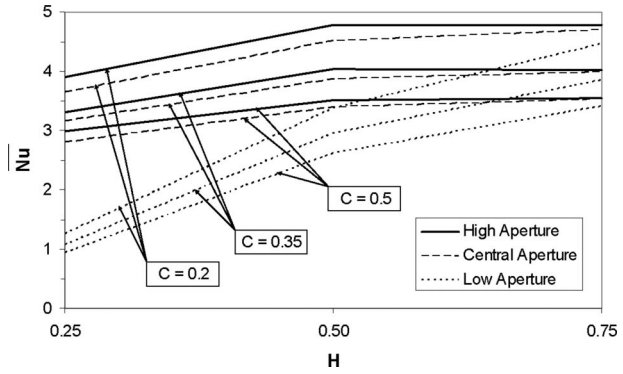

Fig. 9 $\overline{Nu}$ as a function of *C*, *D*, and *H* for *B*=0.5, ε=90 deg, and Ra=10^5

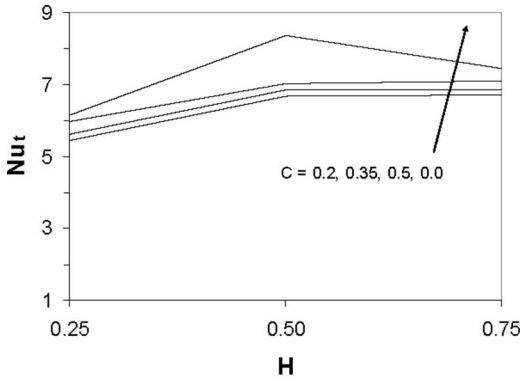

High Aperture

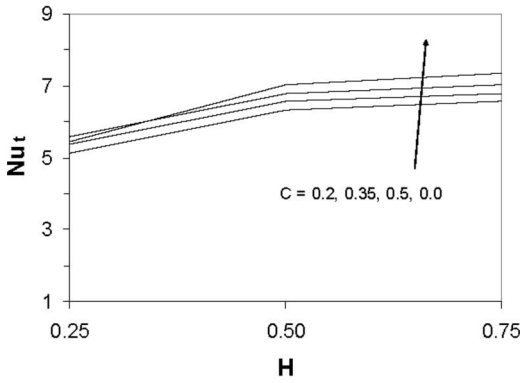

Central Aperture

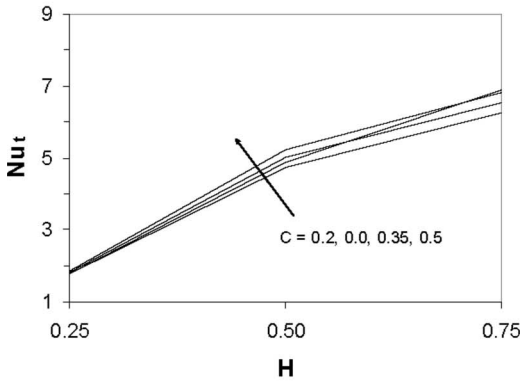

Low Aperture

Fig. 10 Nu_t as a function of *C*, *D*, and *H* for *B*=0.5, ε=90 deg, and Ra=10^5

altitudes. This may be because of the guidance effect of the centrally positioned fin (i.e., $B=0.5$), which improves $\overline{Nu}$ for cavities with central apertures. On the other hand, the average Nusselt number tends to increase appreciably as the fin length decreases. Wider apertures have stronger inverse relationships between $\overline{Nu}$ and C. This does not mean that increasing fin length will reduce the rate of heat transfer from the hot surfaces to the fluid. This fact is demonstrated in Fig. 10, which presents the effects of C, D, and H on the total Nusselt number for the hot surfaces Nu_t. Cavities with longer fins have higher Nu_t value for all combinations of D and H considered in this figure. However, finless cavity may have higher Nu_t value than that for a cavity with a fin depending on the combination of C, D, and H values. Furthermore, a finless cavity with wider aperture has higher Nu_t value regardless of the aperture altitude. The only exception is the finless cavity with high aperture and $H=0.5$, for which Nu_t value is greater than that for $H=0.75$. The values of Nu_t for the three finless cavities (i.e., high, central, and low) with aperture size $H=0.75$ are approximately equal because the effect of aperture altitude D diminishes at $H=0.75$, as shown in Fig. 9. Hence, Nu_t value for the finless cavity with high aperture and $H=0.75$ is reasonable. The reason for the awkward Nu_t value for the finless cavity with high aperture and $H=0.5$ is that a strong vortex ($\Delta\psi=53.92$) is created at the center of the cavity causing high volumetric flow rate through the opening ($\dot{V}=20.48$) and very high flow speed ($\psi=-3.6$) near the hot wall.

The impact of fin level B on Nu_t is presented in Fig. 11 for a central aperture ($D=0.5$), $\varepsilon=90$ deg, Ra=10^5, and various values of fin length ($C=0.0, 0.2, 0.35, 0.5$) and aperture size ($H=0.25, 0.5, 0.75$). The graph for a central fin is presented in Fig. 10. The results show that the fin level B is a factor that strongly affects Nu_t. For a cavity with a central aperture, the lowest Nu_t value is associated with $B=0.5$ among the levels considered in the current work, whereas the highest Nu_t value usually occurs at $B=0.75$. This is because the high fin heats up the flowing fluid after having been warmed by about 75% of the hot wall, whereas for the other two fin levels the fluid is in contact with shorter segment of the hot wall prior to reaching the fin, and a large portion of the fluid is being heated up and forced upward before reaching the segment of the hot wall past the fin. The only exception for the peak value of Nu_t is when $C=0.2$ and $H=0.75$ as the highest Nu_t value occurs at $B=0.25$. This is because, for that configuration, the fin is not sufficiently long to drive the flow away from the hot wall beyond it, while the fluid entering through the aperture pushes the fluid, passing around the fin, toward the hot wall. In addition, the buoyancy force, produced by the fin and the hot wall preceding it, is not strong enough to drive the fluid upward before reaching the remaining segment of the hot wall. For the configurations included in Fig. 11, the lowest Nu_t value occurs at $B=0.5$, $C=0.2$, and $H=0.25$, while the highest Nu_t value occurs at $B=0.75$, $C=0.35$, and $H=0.5$.

The effects of Rayleigh number Ra on the average Nusselt number at the hot surfaces $\overline{Nu}$ and volumetric flow rate through the aperture $\dot{V}$ are presented in Fig. 12 for $B=0.5$, $C=0.35$, $D=0.5$ (central aperture), $H=0.5$, and $\varepsilon=90$ deg. As expected, both

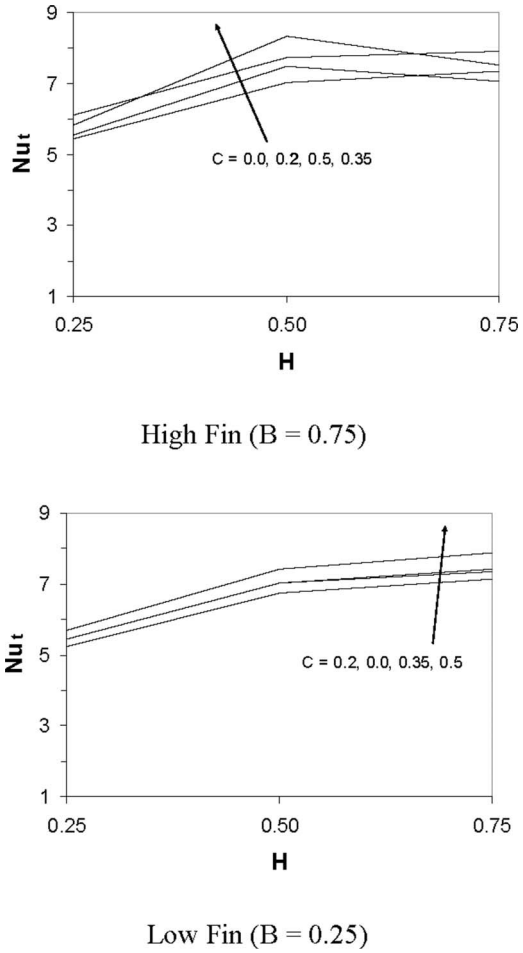

Fig. 11 Nu_t as a function of *B*, *C*, and *H* for *D*=0.5, ε=90 deg, and Ra=10^5

$\overline{Nu}$ and $\dot{V}$ increase as Ra increases and the degree of dependence increases as Ra increases. Furthermore, $\overline{Nu}$ and $\dot{V}$ curves show that they are interrelated.

Figure 13 illustrates the dependence of $\overline{Nu}$ and $\dot{V}$ on the inclination angle of the hot wall from the horizontal ε for B=0.5, C=0.35, D=0.5, H=0.5, and Ra=10^5. Both $\overline{Nu}$ and $\dot{V}$ increase rapidly with increasing ε from 0 deg to about 30 deg; thereafter the rate of increase downgrades until they reach their peak value around ε=75 deg. After that, $\dot{V}$ decreases steeply while $\overline{Nu}$ decreases gradually until roughly ε=90 deg; afterwards $\overline{Nu}$ decreases sharply. The profiles of $\overline{Nu}$ and $\dot{V}$ can be comprehended by considering the two extreme inclination angles considered in the current work, namely, ε=0 deg and 150 deg. At ε=0 deg, the hot wall will be the bottom wall and the aperture will be within the top wall. Both $\overline{Nu}$ and $\dot{V}$ are low because the rising warm fluid will directly repress the entrance of cold fluid. By increasing ε, the repression effect decreases, hence $\dot{V}$ and $\overline{Nu}$ increase. On the other hand, when the aperture is facing almost downward, say, at ε=150 deg, the warm fluid will face difficulty in exiting the enclosure due to the buoyancy forces; thus $\dot{V}$ and $\overline{Nu}$ will be low. By decreasing ε, this difficulty decreases.

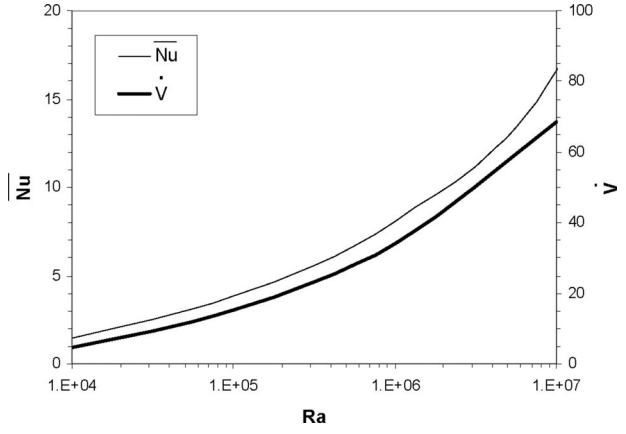

Fig. 12 Effects of Ra on $\overline{Nu}$ and $\dot{V}$ for *B*=0.5, *C*=0.35, *D*=0.5, *H*=0.5, and ε=90 deg

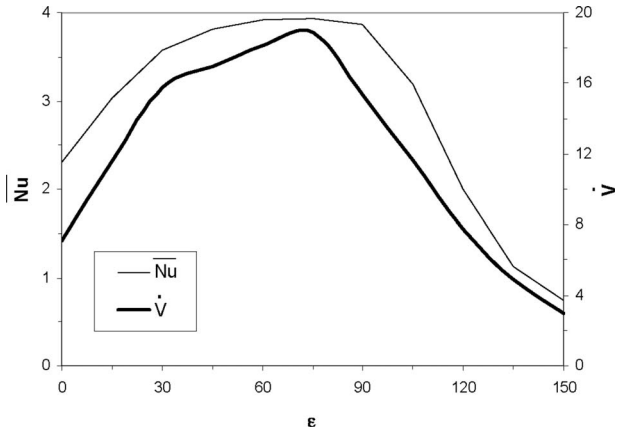

Fig. 13 Effects of ε on $\overline{Nu}$ and $\dot{V}$ for *B*=0.5, *C*=0.35, *D*=0.5, *H*=0.5, and Ra=10^5

Conclusions

Natural convection heat transfer in a partially open inclined square enclosure in the presence of a perfectly conductive thin fin of arbitrary length attached to the hot wall at various levels was studied numerically. The governing equations for this investigation were put into dimensionless formulation and were solved by the finite-volume technique. Graphical results for the streamlines and temperature contours for various parametric conditions were presented and discussed. Based on the findings in this study, it was concluded that the attachment of a perfectly conductive thin fin to the hot wall of the enclosure has counteracting effects on flow and thermal performance of the partially open cavity. These effects are dependent, in a complex way, on the thin fin level and length, aperture altitude and size, cavity inclination angle, and Rayleigh number. Although fin attachment tends to increase heat transfer at a given Ra because of the active area added, the existence of the fin may lower thermal performance of the enclosure because it blocks flow movement close to the hot wall and it could direct the flow to suppress incoming cold fluid. The results also show that a longer fin causes higher rate of heat transfer to the fluid, although the equivalent finless cavity may have higher heat transfer rate. On the whole, heat loss from the hot surfaces increases as the aperture altitude increases. This is because apertures positioned near the enclosure ceiling allow the outside fluid, which is cold, to fill the enclosure and sweep the hot wall and fin while rising due to the buoyancy effects. Moreover, heat transfer from the hot surfaces to the fluid generally improves as the aperture size increases until a peak value is reached; afterwards heat transfer may decline slightly. The impact of aperture altitude diminishes at large aperture sizes because the geometrical differ-

ences decrease. In general, the volumetric flow rate and the rate of heat loss from the hot surfaces are interrelated and are increasing functions of Rayleigh number. The relationship between Nusselt number and the inclination angle is nonlinear. Generally, the inclination angle associated with the peak Nusselt number is away from both ends of the inclination range considered in this work (i.e., 0 deg and 150 deg). This is because, at inclination angles close to 0 deg, the rising warm fluid will directly repress the entrance of cold fluid, while at inclination angles near 150 deg the outgoing warm fluid has difficulty in exiting the cavity through a downward facing aperture. Depending on the application, heat transfer can be optimized (i.e., maximized or minimized) for a given Rayleigh number by selecting appropriate parameters, namely, fin level and length, aperture altitude and size, and cavity inclination angle.

Nomenclature

b = thin fin altitude from enclosure base (m)
B = dimensionless altitude of thin fin $=b/L$
c = thin fin length (m)
C = dimensionless length of thin fin $=c/L$
d = vertical distance between aperture centerline and enclosure base (m)
D = dimensionless altitude of aperture centerline $=d/L$
g = gravitational acceleration (m/s^2)
h = aperture size (m)
H = dimensionless size of aperture $=h/L$
L = length of enclosure sides (m)
n = distance normal to s axis (m)
N = dimensionless n coordinate $=n/L$
Nu = local Nusselt number at hot surfaces
$\underline{\mathrm{Nu}}_t$ = total Nusselt number at hot surfaces
$\overline{\mathrm{Nu}}$ = average Nusselt number at hot surfaces
Pr = Prandtl number $=\nu/\alpha$
Ra = thermal Rayleigh number $=g\beta(T_h-T_a)L^3/(\alpha\nu)$
s = coordinate adopted for distance along enclosure surfaces (m)
S = dimensionless coordinate $=s/L$
T = temperature (K)
u = x component of velocity (m/s)
U = dimensionless x component of velocity $=uL/\alpha$
v = y component of velocity (m/s)
V = dimensionless y component of velocity $=vL/\alpha$
$\dot{V}$ = dimensionless volumetric flow rate into the enclosure through the aperture
x = distance along insulated walls (m)
X = dimensionless distance along insulated walls $=x/L$
y = distance normal to insulated walls (m)
Y = dimensionless distance normal to insulated walls $=y/L$

Greek Symbols

ε = inclination angle of the hot wall from negative X axis (deg)
α = thermal diffusivity (m^2/s)
β = thermal expansion coefficient ($1/K$)
ν = kinematic viscosity (m^2/s)
θ = dimensionless temperature $=(T-T_a)/(T_h-T_a)$
ρ = density (kg/m^3)
ψ = dimensionless stream function $=\Psi/\alpha$
$\Delta\psi$ = strength of dimensionless stream function $=|\psi_{\max}-\psi_{\min}|$
Ψ = stream function (m^2/s)
∇^2 = Laplacian operator

Subscripts

a = ambient
h = hot surfaces
in = into cavity
out = out of cavity

References

[1] Bejan, A., and Kimura, S., 1981, "Penetration of Free Convection Into a Lateral Cavity," J. Fluid Mech., **103**, pp. 465–478.
[2] Hess, C. F., and Henze, R. H., 1984, "Experimental Investigations of Natural Convection Losses From Open Cavities," ASME J. Heat Transfer, **106**, pp. 333–338.
[3] Chan, Y. L., and Tien, C. L., 1985, "A Numerical Study of Two-Dimensional Laminar Natural Convection in Shallow Open Cavities," Int. J. Heat Mass Transfer, **28**, pp. 603–612.
[4] Chakroun, W., 2004, "Effect of Boundary Wall Conditions on Heat Transfer for Fully Opened Tilted Cavity," ASME J. Heat Transfer, **126**, pp. 915–923.
[5] Rojas, J., and Vila, F., 1995, "Numerical and Experimental Study of Transient Natural Convection in an Inclined Wall Cavity," Int. Commun. Heat Mass Transfer, **22**, pp. 693–704.
[6] Le Quere, P., Humphrey, J. A. C., and Sherman, F. S., 1981, "Numerical Calculation of Thermally Driven Two-Dimensional Unsteady Laminar Flow in Cavities of Rectangular Cross Section," Numer. Heat Transfer, **4**, pp. 249–283.
[7] Penot, F., 1982, "Numerical Calculation of Two-Dimensional Natural Convection in Isothermal Open Cavities," Numer. Heat Transfer, **5**, pp. 421–437.
[8] Mohamad, A. A., 1995, "Natural Convection in Open Cavities and Slots," Numer. Heat Transfer, Part A, **27**, pp. 705–716.
[9] Polat, O., and Bilgen, E., 2002, "Laminar Natural Convection in Inclined Open Shallow Cavities," Int. J. Therm. Sci., **41**, pp. 360–368.
[10] Miyamoto, M., Kuehn, T. H., Goldstein, J., and Katoh, Y., 1989, "Two-Dimensional Laminar Natural Convection Heat Transfer From a Fully or Partially Open Square Cavity," Numer. Heat Transfer, Part A, **15**, pp. 411–430.
[11] Bilgen, E., and Oztop, H., 2005, "Natural Convection Heat Transfer in Partially Open Inclined Square Cavities," Int. J. Heat Mass Transfer, **48**, pp. 1470–1479.
[12] Shi, X., and Khodadadi, J. M., 2003, "Laminar Convection Heat Transfer in a Differentially Heated Square Cavity Due to a Thin Fin on the Hot Wall," ASME J. Heat Transfer, **125**, pp. 624–634.
[13] Ben-Nakhi, A., and Chamkha, A., 2006, "Effect of Length and Inclination of a Thin Fin on Natural Convection in a Square Enclosure," Numer. Heat Transfer, Part A, **50**, pp. 389–407.
[14] Vandoormaal, J. P., and Raithby, G. D., 1984, "Enhancements of the Simple Method for Predicting Incompressible Fluid Flows," Numer. Heat Transfer, **7**, pp. 147–163.
[15] Patankar, S. V., 1980, *Numerical Heat Transfer and Fluid Flow*, Hemisphere, New York.
[16] Ben-Nakhi, A., and Mahmoud, M., 2007, "Conjugate Natural Convection in the Roof Cavity of Heavy Construction Building During Summer," Appl. Therm. Eng., **27**, pp. 287–298.

Combined Effect of Temperature Modulation and Magnetic Field on the Onset of Convection in an Electrically Conducting-Fluid-Saturated Porous Medium

B. S. Bhadauria
Department of Mathematics,
Faculty of Science,
Banaras Hindu University,
Varanasi 321005, India
e-mail: drbsbhadauria@yahoo.com

The effect of temperature modulation on the onset of thermal convection in an electrically conducting fluid-saturated-porous medium, heated from below, has been studied using linear stability analysis. The amplitudes of temperature modulation at the lower and upper surfaces are considered to be very small. The porous medium is confined between two horizontal walls and subjected to a vertical magnetic field; flow in porous medium is characterized by Brinkman–Darcy model. Considering only infinitesimal disturbances, and using perturbation procedure, the combined effect of temperature modulation and vertical magnetic field on thermal instability has been studied. The correction in the critical Rayleigh number is calculated as a function of frequency of modulation, Darcy number, Darcy Chandrasekhar number, magnetic Prandtl number, and the nondimensional group number χ. The influence of the magnetic field is found to be stabilizing. Furthermore, it is also found that the onset of convection can be advanced or delayed by proper tuning of the frequency of modulation. The results of the present model have been compared with that of Darcy model. [DOI: 10.1115/1.2885871]

Keywords: temperature modulation, rayleigh number, magnetic field, chandrasekhar number, porous medium

1 Introduction

The subject of thermal instability in a porous medium under the influence of an imposed magnetic field has gained momentum for the past few decades due to its relevance and applications in engineering and technology. For example, the above study is useful in commercial production of the magnetic fluids. Other applications are in geophysics to study the earth's core and to understand the performance of petroleum reservoir [1]. A detailed review of most of the related findings has been given by Nield and Bejan [2]. Although the research field is quite interesting, only limited literature is available; Patil and Rudraiah [3] have studied the problem of setting up convection currents in a layer of viscous, electrically conducting fluid in the presence of a magnetic field, using linear and nonlinear theories, and investigated the combined effect of magnetic field, viscosity, and permeability on the stability of flow through porous medium. Rudraiah and Vortmeyer [4] have investigated the above problem for stability of finite-amplitude and overstable convection of a conducting fluid through a fixed porous bed. Using linear and nonlinear analysis, Rudraiah [5] has studied the problem of magnetoconvection in a sparsely packed porous medium. Alchaar et al. [6,7] and Bian et al. [8,9] have also investigated the magnetoconvection in porous media for different physical models. Oldenburg et al. [10] and Borglin et al. [11] have carried out numerical and experimental investigations on the flow of ferrofluids in porous media. Sekar et al. [12,13] considered the problem of convective instability of a magnetized ferrofluid in a porous medium and studied the effect of rotation on it. Desaive et al. [14] have studied linear stability problem of thermoconvection in a ferrofluid saturating a rotating porous layer by considering Brinkman model and using modified Galerkin method, and discussed both stationary and overstable convections. Sunil et al. [15,16] have investigated the effects of rotation and magnetic fields on thermosolutal convection in a ferromagnetic fluid saturating a porous medium. Recently, Saravanan and Yamaguchi [17] performed a linear analysis to study the influence of magnetic field on the onset of centrifugal convection in a magnetic fluid filled porous layer placed in zero-gravity environment and established the stability criterion. However, in most of the above studies, uniform temperature gradient has been considered.

However, we find many practically important situations in which temperature gradient is a function of both space and time. For example, in solidification of metallic alloys, time-dependent temperature gradient can be used to control the quality and structure of the resulting solid by influencing the transport process. Therefore, we assume that the temperature gradient is a function of both space and time, and can use it to study the effect of temperature modulation on the onset of thermal instability. Venezian [18] was the first to study the effect of temperature modulation on the onset of thermal instability in an ordinary fluid layer. Some other studies on temperature modulation of convective flow in an ordinary fluid layer are those of Rosenblat and Tanaka [19], Roppo et al. [20], Bhadauria and Bhatia [21], and Bhadauria [22]. Also, the studies related to the effect of temperature modulation on thermal instability in a porous medium are those of Chhuon and Caltagirone [23], Rudraiah and Malashetty [24], Malashetty and Basavaraja [25], and Bhadauria [26–28]. However, to the best of author's knowledge, no literature is available in which combined effect of both magnetic field and temperature modulation has been investigated on thermal instability in a porous medium considering free-free boundaries.

Therefore, the main object of the present investigation is to study the combined effect of temperature modulation and mag-

Contributed by the Heat Transfer Division of ASME for publication in the JOURNAL OF HEAT TRANSFER. Manuscript received December 11, 2006; final manuscript received September 18, 2007; published online April 10, 2008. Review conducted by Jamal Seyed-Yagoobi.

netic field on the stability of convective flow through a porous medium considering free-free boundaries. Brinkman–Darcy model has been considered, and sinusoidal function is taken to modulate the walls' temperature. The results of the present paper are expected to bridge the gap between the results valid for magnetoconvection in an ordinary fluid layer and for Darcy model, and have implication on convection in earth's core.

2 Statement of the Problem

Consider a porous medium saturated with an electrically conducting fluid and confined between two parallel horizontal walls at $z=0$ and $z=d$. The walls are infinitely extended in the x and y directions and are free. A constant magnetic field has been applied in the vertical direction, and an adverse temperature gradient is maintained across the fluid layer by heating from below. For temperature modulation, we use the following externally imposed wall temperatures:

$$T(t) = T_R + \frac{\Delta T}{2}[1 + \varepsilon \cos \omega t] \quad \text{at } z = 0 \tag{2.1a}$$

$$= T_R - \frac{\Delta T}{2}[1 - \varepsilon \cos(\omega t + \phi)] \quad \text{at } z = d \tag{2.1b}$$

Here, ε represents the amplitude of modulation, which is very small, ΔT is the temperature difference, ω is the modulation frequency, ϕ is the phase angle, and T_R represents the reference temperature. The fluid is supposed to be essentially incompressible insofar as its density may change by thermal expansion; therefore, for small departure from its reference temperature T_R, the fluid density under Boussinesq approximation is given by

$$\rho_f = \rho_R[1 - \alpha(T - T_R)] \tag{2.2}$$

where ρ_R is the reference density (constant) and α is the coefficient of thermal expansion. In the above considered configuration, a basic hydrostatic state is possible in which the isothermal surfaces are horizontal and therefore parallel to the equipotential surfaces of the vertical gravitational force. The basic temperature field $T_b(z,t)$ satisfies the following one-dimensional unsteady diffusion equation:

$$\gamma \frac{\partial T_b}{\partial t} = \kappa_T \frac{\partial^2 T_b}{\partial z^2} \tag{2.3}$$

where $\gamma = (\rho c_p)_m / (\rho c_p)_f$ and $\kappa_T = \kappa_m / (\rho c_p)_f$ the effective thermal diffusivity, while κ_m is the effective thermal conductivity of the porous medium. The equation for the pressure field, which balances the gravitational force, is not required explicitly. The solution of Eq. (2.3) subject to the boundary conditions (2.1) is given by

$$T_b(z,t) = T_S(z) + \in \mathrm{Re}\{T_O(z,t)\} \tag{2.4a}$$

such that

$$T_S(z) = T_R + \frac{\Delta T}{2}\left(1 - \frac{2z}{d}\right) \tag{2.4b}$$

$$T_O(z,t) = [a(\lambda)e^{\lambda z/d} + a(-\lambda)e^{-\lambda z/d}]e^{-i\omega t} \tag{2.4c}$$

where

$$\lambda^2 = -i\gamma\omega d^2/\kappa_T \text{ and } a(\lambda) = \frac{\Delta T}{2}\frac{e^{-i\phi} - e^{-\lambda}}{e^{\lambda} - e^{-\lambda}} \tag{2.4d}$$

In Eq. (2.4*a*), $T_S(z)$ is the steady temperature field, and T_O is its oscillating part, while Re stands for the real part.

3 Governing Equations

The nondimensional, linear governing equations for the vertical component of the velocity w, the temperature θ, and the vertical component of the magnetic field h_z are (Appendix A) given as follows:

$$\left(\chi\frac{\partial}{\partial t} - V_r \mathrm{D_a}\nabla^2 + 1\right)\nabla^2 w = \mathrm{R}\nabla_1^2\theta - \mathrm{QPr}_m\nabla^2\left(\frac{\partial h_z}{\partial z}\right) \tag{3.1}$$

$$\left(\gamma\frac{\partial}{\partial t} - \nabla^2\right)\theta = -w\left(\frac{\partial T_b}{\partial z}\right) \tag{3.2}$$

$$\left(\frac{\partial}{\partial t} - \mathrm{Pr}_m\nabla^2\right)h_z = \left(\frac{\partial w}{\partial z}\right) \tag{3.3}$$

where $\mathrm{R} = \alpha g \Delta T k d/\nu\kappa_T$ is the Darcy Rayleigh number, $\mathrm{Q} = \mu_m H_k^2 k/\rho_R \nu\eta$ is the Darcy Chandrasekhar number, and $V_r = \mu_e/\mu_f$ is the viscosity ratio. χ is a dimensionless group of Prandtl number $\mathrm{Pr} = \nu/\kappa_T$, Darcy number $\mathrm{D_a} = K/d^2$, and the porosity δ, and is defined by

$$\chi = \frac{\mathrm{D_a}}{\delta \mathrm{P_r}} \tag{3.4}$$

which is nothing but the reciprocal of Vadasz number [$\mathrm{Va} = \delta\,\mathrm{Pr}/\mathrm{Da}$]. As pointed out by Vadasz [29], there are many real situations in which the value of Va is very large, i.e., χ very small; therefore, one can neglect the time-derivative term in Brinkman–Darcy equation (3.1). Furthermore, he points out that there are, however, some modern porous medium applications, such as mushy layer in solidification of binary alloys and fractured porous medium, where the value of Va and so χ may be considered of the order unity; therefore, we retain the time-derivative term in the present study. Furthermore, for simplicity, we assume $V_r = 1$, that is, the effective viscosity μ_e is equal to the fluid viscosity μ_f; however, in general it is not so. Experimentally, it has been demonstrated by Givler and Altobelli [30] that the effective viscosity is five to ten times larger than the fluid viscosity. Now, combining Eqs. (3.1)–(3.3), we obtain

$$\left(\chi\frac{\partial}{\partial t} - \mathrm{D_a}\nabla^2 + 1\right)\left(\gamma\frac{\partial}{\partial t} - \nabla^2\right)\left(\frac{\partial}{\partial t} - \mathrm{Pr}_m\nabla^2\right)\nabla^2 w = -\mathrm{R}\left(\frac{\partial}{\partial t} - \mathrm{Pr}_m\nabla^2\right)\left(\frac{\partial T_b}{\partial z}\nabla_1^2 w\right) + \mathrm{QPr}_m\left(\gamma\frac{\partial}{\partial t} - \nabla^2\right)\nabla^2\left(\frac{\partial^2 w}{\partial z^2}\right) \tag{3.5}$$

The temperature gradient $\partial T_b/\partial z$, which appears in the above equation, can be obtained from the nondimensional form of Eq. (2.4) as

$$\frac{\partial T_b}{\partial z} = -1 + \varepsilon f \tag{3.6}$$

where $f = \mathrm{Re}[A(\lambda)e^{\lambda z} + A(-\lambda)e^{-\lambda z}]e^{-i\omega t}$, $A(\lambda) = (\lambda/2)[(e^{-i\phi} - e^{-\lambda})/(e^{\lambda} - e^{-\lambda})]$, and $\lambda^2 = -i\gamma\omega$. The boundaries of a porous medium can be either free or rigid. We know that under laboratory conditions, free boundaries are less accessible to the experiments; therefore, one has to consider the rigid boundaries. However, in real situations like geothermal regions, the porous layer under consideration cannot be isolated from the surrounding region to avoid the penetration of the fluid; therefore, we have to consider only free surfaces. The boundary conditions for the free-free and perfect heat conducting surfaces are as follows:

$$\theta = w = \frac{\partial^2 w}{\partial z^2} = \frac{\partial^4 w}{\partial z^4} = \cdots = 0 \quad \text{at } z = 0, 1$$

4 Method of Solution

By using perturbation procedure, we seek the eigenvalues R and the eigenfunctions w for the system (3.5), and the basic temperature gradient (3.7) that departs from the linear profile $\partial T_b/\partial z=-1$ by quantities of order ε, which is very small. We write [31]

$$(w,\mathrm{R}) = (w_0,\mathrm{R}_0) + \varepsilon(w_1,\mathrm{R}_1) + \varepsilon^2(w_2,\mathrm{R}_2) + \cdots \tag{4.1}$$

The above expression (4.1) was first used by Malkus and Veronis [32] in studying the effects of finite-amplitude convection in a convection problem. Here, w_0 and R_0 correspond to the unmodulated system, while w_i and R_i $(i \geq 1)$ are the corrections due to modulation, each of w_i must satisfy the boundary conditions (3.15). The marginally stable solutions from Eq. (B1) are given by

$$w_0^{(n)} = \sin(n\pi z) \tag{4.2}$$

and

$$\mathrm{R}_0^{(n)} = \frac{(n^2\pi^2+a^2)}{a^2}\left[\{\chi\sigma + \mathrm{D_a}(n^2\pi^2+a^2)+1\}(\gamma\sigma+\pi^2+a^2) + \frac{n^2\pi^2 Q\mathrm{Pr}_m(\gamma\sigma+n^2\pi^2+a^2)}{[\sigma+\mathrm{Pr}_m(n^2\pi^2+a^2)]}\right] \tag{4.3}$$

where $a=(a_x^2+a_y^2)^{1/2}$ is the horizontal wave number and σ is the frequency of perturbation, which may be complex. The least eigenvalue, for a fixed value of the parameters, is obtained when $n=1$, corresponding to

$$w_0 = \sin(\pi z) \tag{4.4}$$

Up to order ε^2, the critical values of the Rayleigh number R and the wave number a are calculated by the expressions

$$\mathrm{R}_c = \mathrm{R}_{0c} + \varepsilon^2\mathrm{R}_{2c} \tag{4.5}$$

$$a_c = a_{0c} + \varepsilon^2 a_{2c} \tag{4.6}$$

where a_{0c} is that value of the wave number at which R_{0c} is minimum. We use a_{0c} to calculate R_c up to order ε^2. It is only when one calculates R_{4c} that a_{2c} has to be taken into account. From (B25), the expression for R_2 is given as

$$\mathrm{R}_2 = \frac{a^2\mathrm{R}_0^2}{2\,\mathrm{Pr}_m(\pi^2+a^2)}\,\mathrm{Re}\left[C_1\sum_{n=1}^{\infty}\frac{|A_n(\lambda)|^2 C_{1n}^* L^*(\omega,n)}{|L(\omega,n)|^2} - 4\,\mathrm{Pr}_m^2\,\omega\pi^2\sum_{n=1}^{\infty}\frac{nB_n(\lambda)C_n^*(\lambda)L^*(\omega,n)}{|L(\omega,n)|^2}\right] \tag{4.7}$$

where

$$|A_n(\lambda)|^2 = \frac{4n^2\pi^4\omega^2 C}{[\omega^2+(n-1)^4\pi^4][\omega^2+(n+1)^4\pi^4]} \tag{4.8}$$

and " *" denotes the complex conjugate. The constant C takes the values 4, 4, and 1, respectively, for Cases (a), (b), and (c). The expressions for C_1, $C_n(\lambda)$, $L(\omega,n)$, $B_n(\lambda)$, and C_{1n} are given by Eqs. (B8), (B16), (B19), (B21), and (B24), respectively.

5 Marginally Stable State

Stationary Convection. The marginally stable state of the stationary convection is characterized by $\sigma=0$; therefore, from Eq. (4.9), we obtain

$$\mathrm{R}_{0c}^{(s)} = \frac{(\pi^2+a^2)}{a^2}[(\pi^2+a^2)\{1+\mathrm{D_a}(\pi^2+a^2)\}+\mathrm{Q}\pi^2] \tag{5.1}$$

Calculating the values of $\mathrm{R}_{0c}^{(s)}$ and $a_c^{(s)}$ for different values of Darcy Chandrasekhar number Q, we find that $\mathrm{R}_{0c}^{(s)}$ increases on increasing Q, thus showing that the effect of magnetic field is to inhibit the convective flow in a porous medium. Furthermore, we find that even for a small change in the value of Darcy Chandrasekhar number, there is a relative large change in the value of $\mathrm{R}_{0c}^{(s)}$, which is not so in the case of magnetoconvection in an ordinary fluid layer (Ref. [33], p. 170). When the value of Da is large, we obtain the magnetoconvection results in an ordinary fluid layer, while at small values of Da, we recover Darcy results (the Darcy model can be obtained by deleting the Brinkman viscous term (last term) from Eq. (A1)).

Oscillatory Convection. We consider $\sigma=\sigma_r+i\sigma_i$ in Eq. (4.3) with the possibility that the imaginary part σ_i would allow the oscillatory behavior of the motion at marginally stable state. With this in mind, we substitute $\sigma=i\sigma_i$ $(\sigma_r=0)$, where σ_i is real, and find that for assigned values of a, Q, Pr_m, χ, γ, and σ_i, the Rayleigh number consists of real and imaginary parts. Since R_0 has to be real, therefore, for its imaginary part to be zero, we have

$$\sigma_i\left[[\chi(\pi^2+a^2)+\gamma\{1+\mathrm{D_a}(\pi^2+a^2)\}] + \frac{\pi^2 Q\,\mathrm{Pr}_m(\mathrm{Pr}_m\,\gamma-1)(\pi^2+a^2)}{\sigma_i^2+\mathrm{Pr}_m^2(\pi^2+a^2)^2}\right]=0 \tag{5.2}$$

If $\mathrm{Q}=0$, then $\sigma_i=0$, so no overstability. Now, for overstable convection (convection through oscillatory motion) to occur, we must have the condition $\sigma_i^2>0$, which is possible from Eq. (5.2) only when $\mathrm{Pr}_m\gamma<1$ and

$$\mathrm{Q} > \frac{\mathrm{Pr}_m(\pi^2+a^2)[\gamma+(\chi+\gamma\mathrm{D_a})(\pi^2+a^2)]}{\pi^2(1-\mathrm{Pr}_m\,\gamma)} \tag{5.3}$$

Subject to the above conditions, the values of the Rayleigh number and the frequency σ_i for the oscillations at marginal stability are given by

$$\mathrm{R}_0^{(o)} = \frac{(\pi^2+a^2)\{(\chi\,\mathrm{Pr}_m+\mathrm{D_a})(\pi^2+a^2)+1\}}{a^2}\left[(\pi^2+a^2)(1+\gamma\,\mathrm{Pr}_m) + \frac{\pi^2\gamma^2\mathrm{Q}\,\mathrm{Pr}_m}{\gamma+(\chi+\gamma\mathrm{D_a})(\pi^2+a^2)}\right] \tag{5.4}$$

and

$$\sigma_i^2 = \frac{\pi^2\mathrm{Q}\,\mathrm{Pr}_m(1-\gamma\,\mathrm{Pr}_m)(\pi^2+a^2)}{\chi(\pi^2+a^2)+\gamma[1+\mathrm{D_a}(\pi^2+a^2)]} - \mathrm{Pr}_m^2(\pi^2+a^2)^2 \tag{5.5}$$

Let $\mathrm{R}_{0c}^{(o)}$ and $a_c^{(o)}$ be the critical values of the Rayleigh number and the corresponding wave number for overstable convection. For simplification, we consider $\gamma=1.0$ in our calculations. In Figs. 1(*a*) and 1(*b*), we present the characteristic curves at $\mathrm{Q}=10.0$ and $\mathrm{Q}=100.0$ for different values of χ; the values of other parameters are $\mathrm{Da}=0.1$ and $\mathrm{Pr}_m=0.1$. From the curves, we can clearly identify the points where both stationary and oscillatory convections occur simultaneously, and at these points, oscillatory solutions branch off the stationary solution. The effect of the Darcy Chandrasekhar number can also be seen clearly from Figs. 1(*a*) and 1(*b*).

In Figs. 2(*a*) and 2(*b*), we depict the neutral stability curves at $\mathrm{Q}=10.0$ and $\mathrm{Q}=100.0$, respectively, for different values of Da; the other parameters are at $\chi=1.0$, $\mathrm{Pr}_m=0.1$. In both Figs. 2(*a*) and 2(*b*), the results are qualitatively similar, but the values of R_0 in Fig. 2(*b*) are greater than those in Fig. 2(*a*), which is due to the fact that results in Fig. 2(*b*) correspond to a large value of Q.

We observe that for the overstable solution, the condition $\sigma_i^2>0$ must be satisfied; however, it is not a sufficient condition. For the overstable convection to occur, we require that the overstable critical Rayleigh number should be less than the corresponding stationary critical Rayleigh number, i.e., $\mathrm{R}_{0c}^{(o)} \leq \mathrm{R}_{0c}^{(s)}$. Although the curves presented in Figs. 1(*a*), 1(*b*), 2(*a*), and 2(*b*) satisfy this condition, we need to draw a more accurate stability map for better prediction of overstable and stationary convection. Therefore, in Fig. 3, we consider (Q, χ) plane and divide the stability

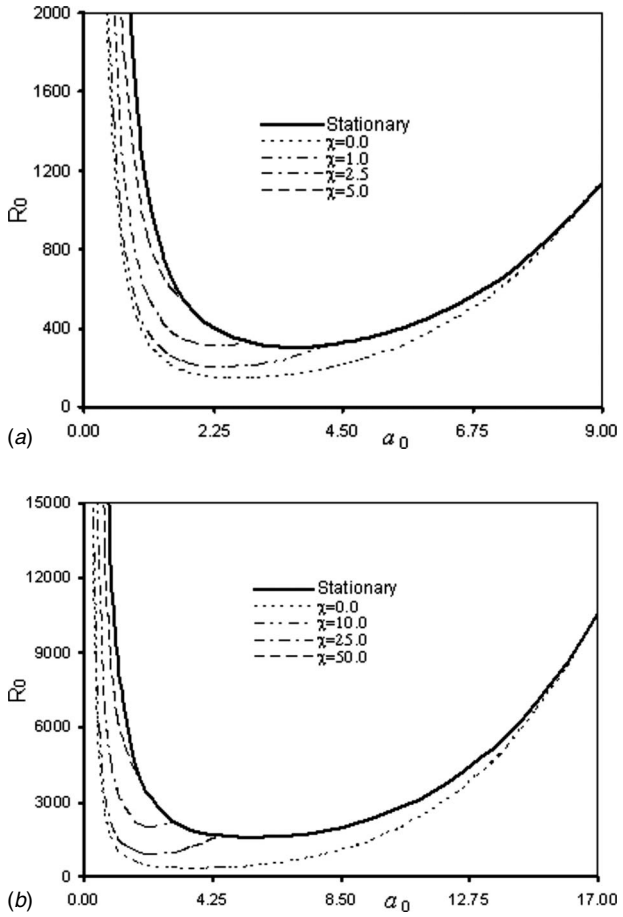

Fig. 1 (*a*) The curves representing the marginal stability limit for Q=10.0, Pr_m=0.1, and Da=0.1; (*b*) As in (*a*) but for Q =100.0

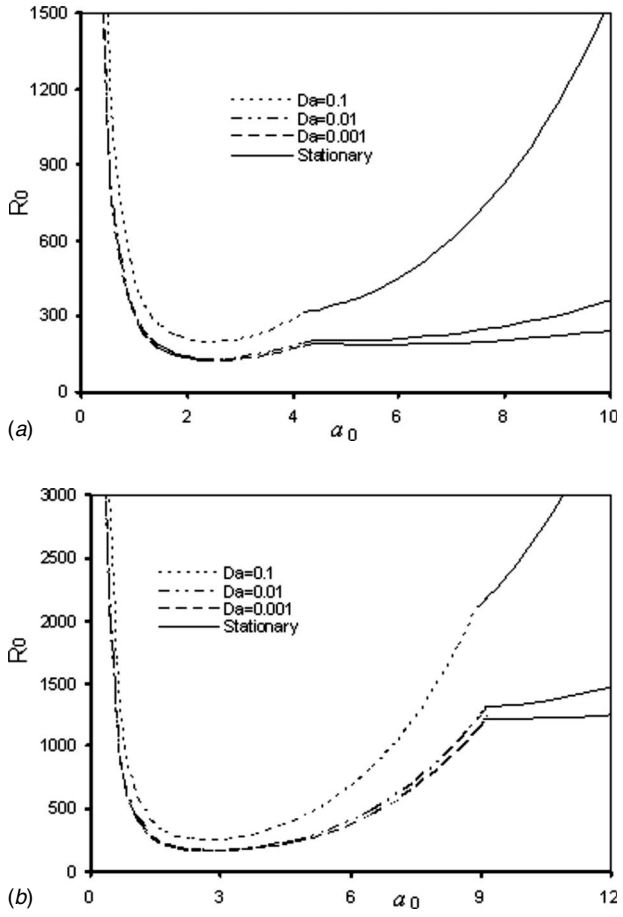

Fig. 2 (*a*) The curves representing the marginal stability limit for Q=10.0, Pr_m=0.1, and χ=1.0; (*b*) As in (*a*) but for Q=100.0

region into different zones. We find that for the zone below the dotted line instability sets in as stationary convection, and for the zone above the continuous line instability sets in as overstable convection. However, for the zone below the continuous line but above the dotted line, both stationary and overstable solutions are possible but since $R_{0c}^{(s)} < R_{0c}^{(o)}$, therefore overstable convection will not occur.

6 Results and Discussion

Now, to find the effect of temperature modulation on the onset of thermal convection, we consider $\varepsilon \neq 0$ and calculate the correction in R_{0c}, i.e., R_{2c}. The value of R_{2c} has been calculated in the following three cases: (a) When the walls' temperature is modulated in phase, i.e., ϕ=0, (b) when the modulation is out of phase, i.e., $\phi=\pi$, and (c) when only the lower wall temperature is modulated, the upper wall is held at fixed constant temperature, i.e., $\phi=-i\infty$.

The results have been presented in Figs. 4–10. From the figures, we observe that the value of R_{2c} may be positive or negative. A positive value of R_{2c} corresponds to the stabilizing effect of temperature modulation as here the value of R_c would be greater than R_{0c} (Eq. (4.5)). Similarly, in the case of a negative value of R_{2c}, we find that the value of R_c would be less than R_{0c}; therefore, the effect of temperature modulation is to destabilize the system that convection will take place at an early point. In Figs. 4–10, we depict the variation of R_{2c} with ω at different values of the other parameters. In the figures, we detect two special frequencies: one corresponding to the maximum destabilizing effect of temperature modulation, where the value of R_{2c} is found to be most negative. The other frequency corresponds to the maximum stabilizing effect of the modulation as R_{2c} is positive and maximum at this frequency. Let these frequencies, which correspond to the maximum destabilizing and maximum stabilizing effects of modulation, be denoted by ω_1 and ω_2, respectively. At a very large value of ω, the value of R_{2c} becomes zero, and therefore the effect of modulation disappears altogether.

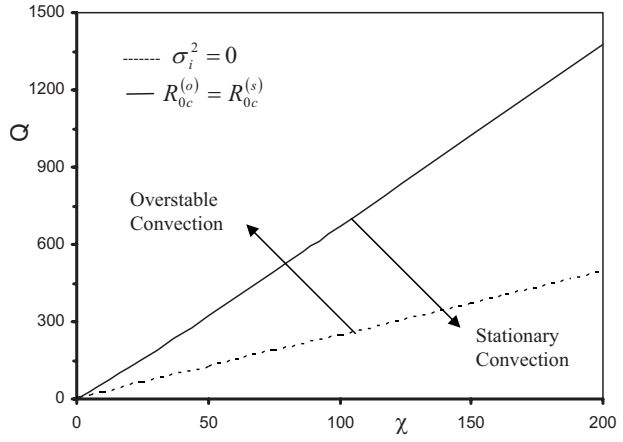

Fig. 3 The stability map showing the division of the (Q, χ) plane into the zones of stationary and overstable

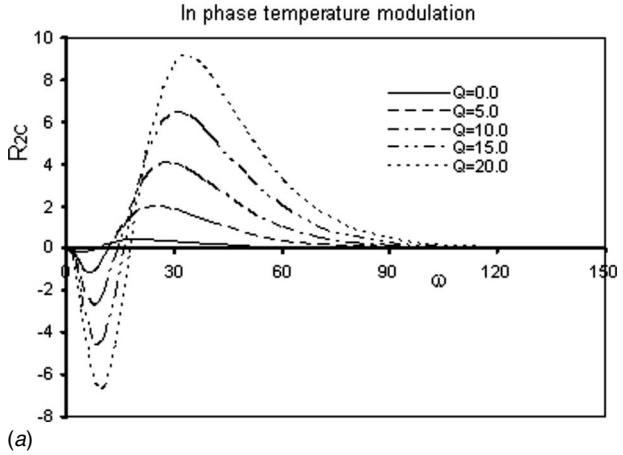

(*a*)

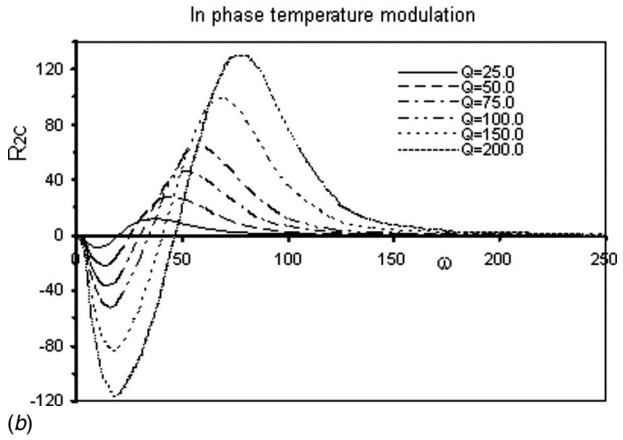

(*b*)

Fig. 4 (*a*). Variation of R_{2c} with ω; $\chi=1.0$, $Pr_m=1.0$, and Da =0.1 and (*b*) variation of R_{2c} with ω; $\chi=1.0$, $Pr_m=1.0$, and Da =0.1

First, we consider Figs. 4–6 corresponding to the in phase modulation of the walls' temperature. From the figures, we see that at $\omega=0$, the value of R_{2c} is zero, and so the effect of modulation is zero, which is also evident from the thermal conditions (2.1) that in this case, the temperature gradient ΔT is the same as in the unmodulated case. In Figs. 4(*a*) and 4(*b*), we have shown the variation of R_{2c} with ω for different values of the Darcy Chandrasekhar number Q at $\chi=1.0$, $Pr_m=1.0$ and Da=0.1. From the figusres, we find that initially when ω is small, the effect of modulation is also small, and destabilizing. This destabilizing effect increases on increasing the value of ω, and then at frequency ω_1, it becomes maximum. Further increasing the value of the frequency, the modulation stabilizes the system, and then at frequency ω_2, its effect becomes maximum stabilizing. For intermediate values of the frequency, the effect of temperature modulation decreases, and finally becomes zero at large values of ω. In both Figs. 4(*a*) and 4(*b*), we find qualitative similar results. It has been observed in these figures that as the value of the Darcy Chandrasekhar number increases, there is a shift toward the right in the frequencies ω_1 and ω_2. Therefore, the range of the frequencies corresponding to the destabilizing effect of temperature modulation increases while that corresponding to the stabilizing effect of modulation decreases. Also, it is evident from the figures that an increase in the value of Q increases the magnitude of R_{2c}.

In Fig. 5, we consider the variation of R_{2c} with ω for different values of Da at $\chi=1.0$, Q=25.0, and $Pr_m=1.0$. In this figures, we find qualitative similar results, as obtained in Figs. 4(*a*) and 4(*b*); however, the effect of decreasing the value of Da is found to decrease the magnitude of R_{2c}. In Fig. 6, we depict the variation

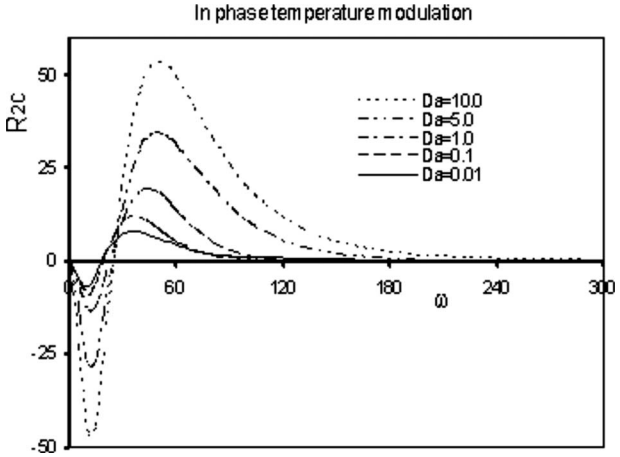

Fig. 5 Variation of R_{2c} with ω; $\chi=1.0$, $Pr_m=1.0$, and Q=25.0

of R_{2c} with ω for different values of the group number χ; the values of other parameters are Q=25.0, $Pr_m=1.0$, and Da=0.1. From the figures, we see that for small values of ω, the effect of modulation is destabilizing but small. Then, for intermediate values of the frequencies ω_1 and ω_2, we get, respectively, maximum destabilizing and stabilizing effects of temperature modulation. Increasing the value of ω, the modulation effect decreases and finally disappears as ω goes to infinity. We observe from Fig. 6 that decreasing the value of χ, the magnitude of R_{2c} decreases.

Now, we consider Figs. 7–9, which correspond to the out of phase modulation of the walls' temperature, and depict the variation of R_{2c} with ω for different parameters. Here, we see that at $\omega=0$, the value of R_{2c} is negative maximum, and so the effect of modulation is most destabilizing, which may be due to the fact that at $\omega=0$, the temperature gradient between the walls is $\Delta T[1+\varepsilon]$ greater than ΔT (in unmodulated case); therefore, the convection takes place at an early point. Furthermore, we see that for small values of ω, the effect of modulation is destabilizing, it becomes stabilizing at some frequency, and then attains a maximum stabilization at frequency ω_2. The effect of modulation decreases on further increasing the value of ω, and finally becomes zero ($R_{2c}=0$) as the frequency goes to infinity. From Figs. 7(*a*) and 7(*b*), we find that an increment in the value of Q increases the magnitude of R_{2c}, widens the range of the frequency corresponding to the destabilizing effect, and shifts the frequency ω_2 toward the right side. The results in Fig. 8 are qualitatively similar to those obtained in Figs. 7(*a*) and 7(*b*); however, the magnitude of

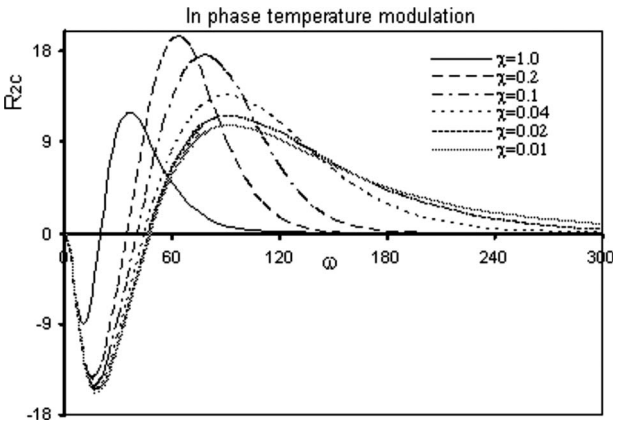

Fig. 6 Variation of R_{2c} with ω; Q=25.0, $Pr_m=1.0$, and Da=0.1

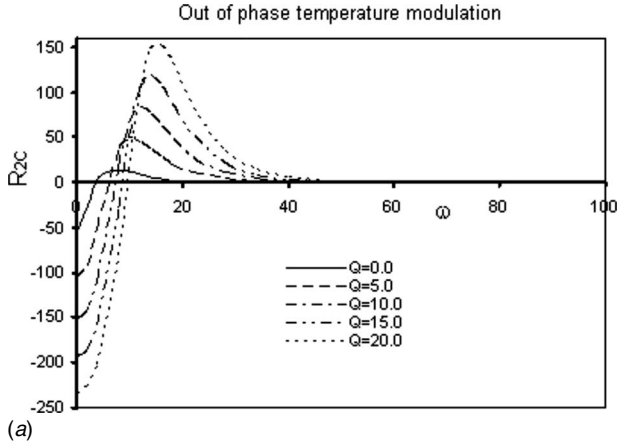

(*a*)

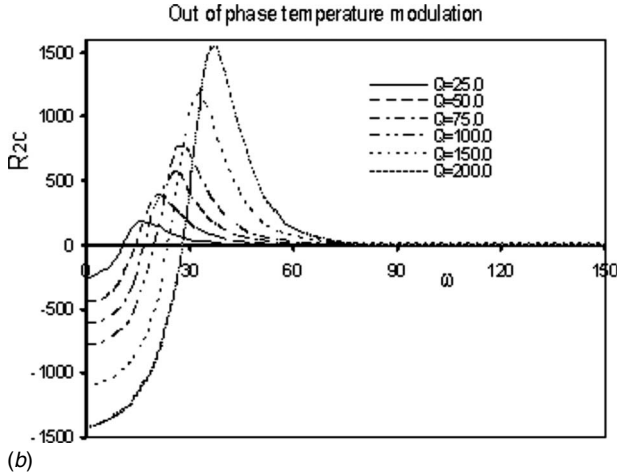

(*b*)

Fig. 7 (*a*). Variation of R_{2c} with ω; $\chi=1.0$, $Pr_m=1.0$, and Da =0.1; (*b*) Variation of R_{2c} with ω; $\chi=1.0$, $Pr_m=1.0$, and Da=0.1

R_{2c} decreases on decreasing the value of the Darcy number. In Fig. 9, we observe that a decrease in the value of χ first increases and then decreases the magnitude of R_{2c}, also frequency ω_2 shifts toward the right side.

The above results have also been calculated for case (c), that is, when only lower wall's temperature is modulated, and the upper wall is held at fixed constant temperature. Although the magnitude of R_{2c} in this case is found to be less than that in case (b), the

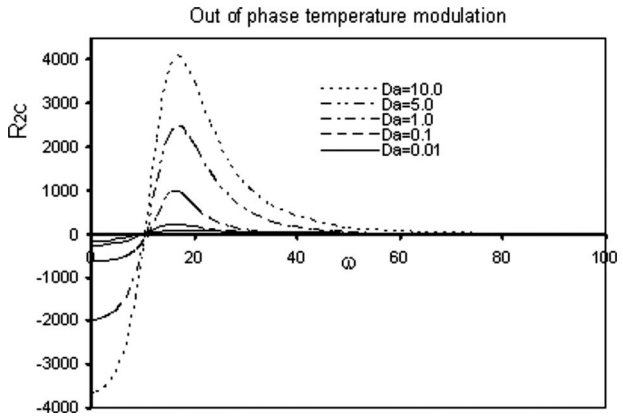

Fig. 8 Variation of R_{2c} with ω; $\chi=1.0$, $Pr_m=1.0$, and Q=25.0

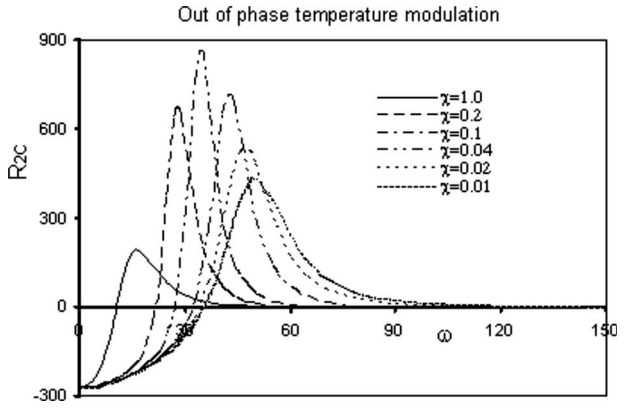

Fig. 9 Variation of R_{2c} with ω; Q=25.0, $Pr_m=1.0$, and Da=0.1

results are qualitatively similar to that of case (b); therefore, it does not seem to be appropriate to present these results again.

We know that when the frequency of modulation is small, the effect of modulation is felt throughout the porous layer. Also, the temperature profile consists of the steady straight-line section plus a parabolic profile that oscillates with time. As the amplitude of the modulation increases, the parabolic part of the profile becomes more and more significant. It is known that a parabolic profile is subject to finite-amplitude instabilities [34,35] so that convection occurs at lower Rayleigh number than that predicted by the linear theory with steady temperature gradient. Also, it is very much clear that at high frequency, modulation becomes very fast; therefore, the temperature in the porous layer remains unaffected by modulation except for a thin layer; so, we find almost the same value of the critical Rayleigh number as for zero modulation. Thus, the effect of temperature modulation is almost negligible at large values of ω.

Lastly, we calculate the variation of R_{2c} with ω, for both Brinkman and Darcy models, and depict the results in Figs. 10(*a*)–10(*c*). The results have been calculated at different values of the Darcy number, and shown for all the three types of modulation. It is found that although the results of Brinkman's model corresponding to the different Darcy numbers are very close to that of Darcy results, a very good agreement is reached at $D_a = 10^{-8}$. Thus, at $D_a = 10^{-8}$, the results of the Brinkman and Darcy models are almost the same. Similarly, for large values of D_a, we can recover the magnetoconvection results in an ordinary fluid layer.

Comparing the various results of Figs. 5 and 10(*a*), we find that for large values of D_a, the effect of modulation is destabilizing at small ω. The destabilizing effect decreases as D_a decreases, and then becomes stabilizing on further decreasing the value of D_a (Fig. 10(*a*)). This may be due to the fact that in a densely packed porous medium, propagation of the convective waves would be faster; therefore, higher temperature gradient is required for the onset of convection. Thus, the value of the critical Rayleigh number is higher in this case. However, for large ω, we find qualitative similar results in both the figures.

7 Conclusion

In the present paper, combined effect of temperature modulation and magnetic field on the onset of convection in an electrically conducting-fluid-saturated porous medium, which is confined between two free boundaries, has been studied in making a linear stability analysis. The perturbation procedure is applied and the results have been obtained under the assumptions that the disturbances are infinitesimal, and the amplitude of the primary temperature field is small. The following conclusions are drawn.

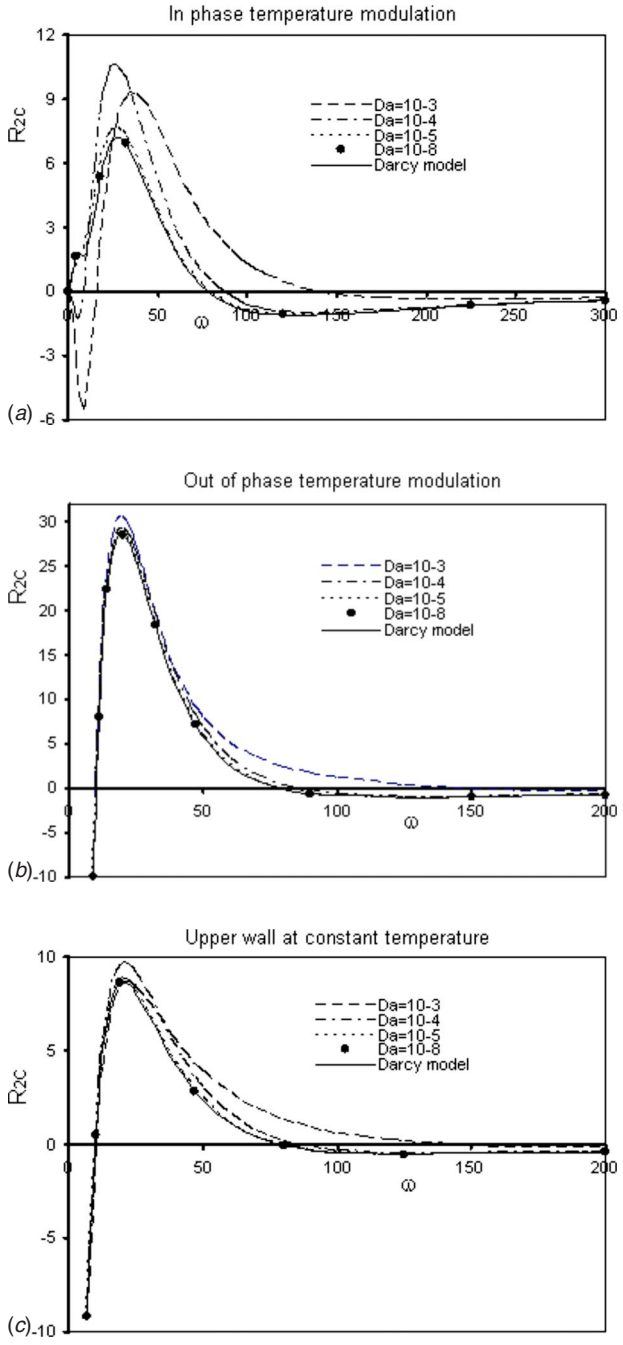

Fig. 10 (*a*) **Variation of R_{2c} with ω; χ=1.0, Pr_m=1.0, and Q =25.0; (*b*) variation of R_{2c} with ω; χ=1.0, Pr_m=1.0, and Q=25.0; and (*c*) variation of R_{2c} with ω; χ=1.0, Pr_m=1.0, and Q=25.0**

(i) The effect of temperature modulation is found to stabilize or destabilize the system depending on the values of the parameters.

(ii) For in phase modulation, it is found that at $\omega=0$, the effect of modulation is zero. When ω is small, the modulation effect is destabilizing, the effect increases with ω and becomes most destabilizing at ω_1. Further increasing the value of the frequency, it becomes most stabilizing at ω_2. Then, for intermediate values of ω, the effect decreases, and finally becomes zero for large values of ω.

(iii) For out of phase modulation or when only the lower wall temperature is modulated, the effect of modulation is found to be most destabilizing at $\omega=0$. The destabilizing effect decreases and becomes most stabilizing at ω_2, and finally modulation effect goes off when ω tends to infinity.

(iv) We find that increasing the value of the Darcy Chandrasekhar number, the magnitude of R_{2c} increases, while decreasing the value of D_a, the magnitude of R_{2c} decreases. Also, we find that decreasing the value of χ from 1.0 to 0.01, the magnitude of R_{2c} first increases and then decreases.

(v) Comparing the results for Brinkman and Darcy models, it is found that there is a very good agreement between them at $D_a=10^{-8}$.

(vi) The results of the present model can be used to bridge the gap between the results of the magnetoconvection in an ordinary viscous fluid layer and that corresponding to the Darcy limit.

Appendix A

The governing equations, for the study of magnetoconvection in an electrically conducting-fluid-saturated porous medium, under Boussinesq approximation are

$$\frac{1}{\delta}\frac{\partial \mathbf{V}}{\partial t} - \frac{\mu_m}{\rho_R}\mathbf{H}\cdot\nabla\mathbf{H} = -\frac{1}{\rho_R}\nabla p + \frac{\rho_f}{\rho_R}\mathbf{g} - \frac{\mu_f}{\rho_R}\frac{1}{k}\mathbf{V} + \frac{\mu_e}{\rho_R}\nabla^2\mathbf{V} \tag{A1}$$

$$(\rho C_p)_m\frac{\partial T}{\partial t} + (\rho C_p)_f\mathbf{V}\cdot\nabla T = \kappa_m\nabla^2 T \tag{A2}$$

$$\frac{\partial \mathbf{H}}{\partial t} + \mathbf{V}\cdot\nabla\mathbf{H} - \mathbf{H}\cdot\nabla\mathbf{V} = \eta\nabla^2\mathbf{H} \tag{A3}$$

$$\nabla\cdot\mathbf{V} = 0 \tag{A4}$$

$$\nabla\cdot\mathbf{H} = 0 \tag{A5}$$

where all constants and variables have their usual meanings and defined in the nomenclature. Initially, the fluid is at rest; the basic state is given by

$$\mathbf{V} = (u,v,w) = (0,0,0), \quad T = T_b(z,t), \quad p = p_b(z,t), \quad \rho_f = \rho_b(z,t) \tag{A6}$$

Let the basic state be slightly perturbed, then

$$\mathbf{V} = \mathbf{V}' = (u',v',w'), \quad T = T_b(z,t) + \theta', \quad p = p_b(z,t) + p',$$

$$\rho_f = \rho_b + \rho', \quad \mathbf{H} = \mathbf{H_k} + \mathbf{h}' \tag{A7}$$

A constant magnetic field $H_k=|\mathbf{H_k}|$ is maintained externally in the vertical direction of a unit vector $\hat{k}$ and $\mathbf{h}'$ is the perturbation in the magnetic field caused by the motions and the induced currents in the field. Here, we assume that the magnetic permeability and thermal conductivity of the fluid are constants and do not vary with the operating conditions, e.g., with temperature and pressure. $\mathbf{V}'$, θ', P', and ρ' are the perturbed quantities, which are considered to be infinitesimal. We introduce Eq. (A7) into Eqs. (A1)–(A5) and linearize with respect to the quantities $\mathbf{V}'$, θ', and $\mathbf{h}'$. The reduced equations are then nondimensionalized using the following scaling:

$$\mathbf{r}' = d\mathbf{r}^*, \quad t' = \frac{d^2}{\kappa_T}t^*, \quad T_b = \Delta T T_b^*, \quad \theta' = \Delta T\theta^*$$

$$\mathbf{V}' = \frac{\kappa_T}{d}\mathbf{V}^*, \quad p' = \frac{\rho_R\kappa_T\nu}{d^2}p^*, \quad \mathbf{h}' = H_k\mathbf{h}^*, \quad \omega = \frac{\kappa_T}{d^2}\omega^* \tag{A8}$$

Henceforth the asterisks will be dropped. The nondimensional form of the equations is given by Eqs. (3.1)–(3.3).

Appendix B

Introducing Eq. (4.1) into Eq. (3.5) and equating the terms of different powers of ε on both sides, we obtain

$$Lw_0 = 0 \tag{B1}$$

$$Lw_1 = -\mathrm{R}_0 L_3(f\nabla_1^2 w_0) + \mathrm{R}_1 L_3(\nabla_1^2 w_0) \tag{B2}$$

$$Lw_2 = \mathrm{R}_2 L_3(\nabla_1^2 w_0) - \mathrm{R}_0 L_3(f\nabla_1^2 w_1) - \mathrm{R}_1 L_3(f\nabla_1^2 w_0) + \mathrm{R}_1 L_3(\nabla_1^2 w_1) \tag{B3}$$

where

$$L \equiv L_1 L_2 L_2 \nabla^2 - \mathrm{R}_0 L_3 \nabla_1^2 - \mathrm{QP}_m L_2 D^2 \nabla^2 \tag{B4}$$

$$L_1 \equiv \left(\chi\frac{\partial}{\partial t} - \mathrm{D_a}\nabla^2 + 1\right), \quad L_2 \equiv \left(\gamma\frac{\partial}{\partial t} - \nabla^2\right), \quad L_3 \equiv \left(\frac{\partial}{\partial t} - \mathrm{Pr}_m\nabla^2\right) \tag{B5}$$

For the solutions of Eqs. (B1)–(B3), we use normal mode and write

$$w(x,y,z,t) = w(z)\exp[i(a_x x + a_y y) + \sigma t] \quad \text{etc.} \tag{B6}$$

where $a=(a_x^2+a_y^2)^{1/2}$ is the horizontal wave number and σ is the frequency of perturbation, which may be complex.

The solution of Eq. (B2) poses a problem due to the presence of resonance term, for its solution to exist its right-hand side must be orthogonal to the null space of the operator L. This solubility condition requires that the time-independent part on the right-hand side of Eq. (B2) should be orthogonal to $\sin \pi z$; therefore, we get $\mathrm{R}_1=0$. In fact, all odd coefficients $\mathrm{R}_1, \mathrm{R}_3, \mathrm{R}_5, \ldots$ are zero. Equation (B2) reduces to

$$Lw_1 = a^2\mathrm{R}_0\,\mathrm{Re}[C_1 f w_0 + (-2\mathrm{Pr}_m)(Df)(Dw_0)] \tag{B7}$$

where

$$C_1 = \mathrm{Pr}_m(\pi^2 + a^2) + i\omega(\mathrm{Pr}_m - 1) \tag{B8}$$

Now, to solve Eq. (B7), we expand its right-hand side in Fourier series

$$e^{\lambda z}\sin m\pi\pi = \sum_{n=1}^{\infty} g_{nm}(\lambda)\sin n\pi z \tag{B9}$$

$$e^{\lambda z}\cos m\pi\pi = \sum_{n=1}^{\infty} f_{nm}(\lambda)\cos n\pi z \tag{B10}$$

where

$$g_{nm}(\lambda) = 2\int_0^1 e^{\lambda z}\sin m\pi z \sin n\pi z dz \tag{B11}$$

and

$$f_{nm}(\lambda) = 2\int_0^1 e^{\lambda z}\cos m\pi z \cos n\pi z dz \tag{B12}$$

The integrals in Eqs. (B11) and (B12) can be evaluated directly. Using Eqs. (B9) and (B10), we write

$$f\sin \pi z = \mathrm{Re}\left[\sum_{n=1}^{\infty} A_n(\lambda)\sin n\pi z e^{-i\omega t}\right] \tag{B13}$$

$$Df\sin \pi z = \mathrm{Re}\left[\sum_{n=1}^{\infty} \lambda C_n(\lambda)\sin n\pi z e^{-i\omega t}\right] \tag{B14}$$

where

$$A_n(\lambda) = A(\lambda)g_{n1}(\lambda) + A(-\lambda)g_{n1}(-\lambda) \tag{B15}$$

and

$$C_n(\lambda) = A(\lambda)g_{n1}(\lambda) - A(-\lambda)g_{n1}(-\lambda) \tag{B16}$$

Also,

$$L\{\sin n\pi z e^{-i\omega t}\} = L(\omega,n)\sin n\pi z e^{-i\omega t} \tag{B17}$$

$$L\{\cos n\pi z e^{-i\omega t}\} = L(\omega,n)\cos n\pi z e^{-i\omega t} \tag{B18}$$

where

$$L(\omega,n) = \omega^2 \mathrm{Q}_n[\gamma(\mathrm{D}_a\mathrm{Q}_n + 1) + \chi(\gamma\mathrm{Pr}_m + 1)\mathrm{Q}_n] - \mathrm{Pr}_m\mathrm{Q}_n^3(\mathrm{D}_a\mathrm{Q}_n + 1) - \mathrm{QPr}_m\mathrm{Q}_n^2(n^2\pi^2) + i\omega[-\chi\gamma\mathrm{Q}_n\omega^2 + \chi\mathrm{Pr}_m\mathrm{Q}_n^3 + \mathrm{Q}_n^2(\gamma\mathrm{Pr}_m + 1)(\mathrm{D}_a\mathrm{Q}_n + 1) - a^2\mathrm{R}_0 + \mathrm{QPr}_m\gamma\mathrm{Q}_n(n^2\pi^2)] \tag{B19}$$

and

$$\mathrm{Q}_n = n^2\pi^2 + a^2$$

Then, in order to obtain the solution of Eq. (B7), we invert the operator L term by term and get

$$w_1 = a^2\mathrm{R}_0\,\mathrm{Re}\left[C_1\sum_{n=1}^{\infty}\frac{A_n(\lambda)}{L(\omega,n)}\sin n\pi z e^{-i\omega t} - 2\pi\lambda\mathrm{Pr}_m\sum_{n=1}^{\infty}\frac{B_n(\lambda)}{L(\omega,n)}\cos n\pi z e^{-i\omega t}\right] \tag{B20}$$

$$B_n(\lambda) = A(\lambda)f_{n1}(\lambda) - A(-\lambda)f_{n1}(-\lambda) \tag{B21}$$

Equation (B3) for w_2 reduces to the form

$$Lw_2 = -a^2\mathrm{R}_2\mathrm{Pr}_m(\pi^2 + a^2)\sin \pi z + a^2\mathrm{R}_0 L_3(f w_1) \tag{B22}$$

or

$$Lw_2 = -a^2\mathrm{R}_2\mathrm{Pr}_m(\pi^2 + a^2)\sin \pi z + a^2\mathrm{R}_0\,\mathrm{Re}[C_{1n} f w_1 + (-2\mathrm{Pr}_m)(Df) \times (Dw_1)] \tag{B23}$$

where

$$C_{1n} = \mathrm{Pr}_m(n^2\pi^2 + a^2) + i\omega(\mathrm{Pr}_m - 2) \tag{B24}$$

Again, for the solution of Eq. (B23), we need that the right-hand side of it should be orthogonal to $\sin \pi z$; therefore, we get

$$\mathrm{R}_2 = \frac{2\mathrm{R}_0}{\mathrm{Pr}_m(\pi^2 + a^2)}\,\mathrm{Re}\left[C_{1n}\int_0^1 \overline{f w_1}\sin \pi z dz + (-2\mathrm{Pr}_m)\int_0^1 \overline{(Df)(Dw_1)}\sin \pi z dz\right] \tag{B25}$$

bar denotes a time average. Using Eqs. (B17) and (B18) in Eq. (B25), we get the expression for R_2, which is given in Eq. (4.7).

Nomenclature

a = horizontal wave number $(a_x^2+a_y^2)^{1/2}$
a_c = critical wave number
d = depth of the porous layer
g = gravitational acceleration
k = permeability of the porous medium
$\mathbf{V}$ = mean filter velocity (u,v,w)
p = pressure
T = temperature
θ = perturbed temperature
$\mathbf{H}$ = magnetic field (H_1,H_2,H_3)
h_z = perturbed magnetic field along the z axis
ΔT = temperature difference between the walls
R_c = critical Rayleigh number
$\mathrm{D_a}$ = Darcy number, k/d^2
$\mathrm{P_r}$ = Prandtl number, ν/κ_T

V_r = viscosity ratio, μ_e/μ_f
Pr_m = magnetic Prandtl number ν/η
R = Rayleigh number, $\alpha g \Delta T k d/\nu\kappa_T$
Q = Chandersekhar number, $\mu_m H_k^2 k/\rho_R \nu\eta$
χ = nondimensional number, $(\mathrm{D_a}/\delta \mathrm{P_r}) \times(\mu_f/\mu_e)$
x, y, z = space coordinates
ρ = density
$(\rho c_p)_f$ = heat capacity of the fluid
$(\rho c_p)_{\mathrm{so}}$ = heat capacity of the solid
$(\rho c_p)_m = \delta(\rho c_p)_f + (1-\delta)(\rho c_p)_{\mathrm{so}}$ = relative heat capacity of the porous medium

Superscripts

$/$ =
$*$ =

Greek Symbols

α = coefficient of thermal expansion
ε = amplitude of modulation
δ = porosity
σ = electrical conductivity
μ_m = magnetic permeability
η = magnetic viscosity, $1/\mu_m\sigma$
γ = heat capacity ratio $(\rho c_p)_m/(\rho c_p)_f$
κ_f = thermal conductivity of the fluid
κ_{so} = thermal conductivity of the solid
$\kappa_m\ \delta\kappa_f + (1-\delta)\kappa_{\mathrm{so}}$ = effective thermal conductivity of porous media
μ_e = effective viscosity of the medium
μ_f = fluid viscosity
ν = kinematic viscosity, μ_f/ρ_R
κ_T = effective thermal diffusivity $\kappa_m/(\rho c_p)_f$
ω = modulation frequency
ϕ = phase angle
σ = growth rate (a complex number)

Other Symbols

$\nabla_1^2 = (\partial^2/\partial x^2) + (\partial^2/\partial y^2)$
$\nabla^2 = \nabla_1^2 + (\partial^2/\partial z^2)$
$D = \partial/\partial z$

Subscripts

b = basic state
c = critical
f = fluid
R = reference value

References

[1] Wallace, W. E., Pierce, C. I., and Sawyer, W. K., 1969, "Experiments on the Flow of Mercury in Porous Media in a Transverse Magnetic Field," Bureau of Mines, Report No. RI-7259(PB-184327).
[2] Nield, D. A., and Bejan, A., 2006, *Convection in Porous Media*, Springer-Verlag, New York.
[3] Patil, R. P., and Rudraiah, N., 1973, "Stability of Hydromagnetic Thermoconvective Flow Through Porous Medium," ASME J. Appl. Mech., **E40**, pp. 879–884.
[4] Rudraiah, N., and Vortmeyer, D., 1978, "Stability of Finite-Amplitude and Overstable Convection of a Conducting Fluid Through Fixed Porous Bed," Waerme- Stoffuebertrag., **11**, pp. 241–254.
[5] Rudraiah, N., 1984, "Linear and Non-Linear Megnetoconvection in a Porous Medium," Proc. Indian Acad. Sci., Math. Sci., **93**, pp. 117–135.
[6] Alchaar, S., Vasseur, P., and Bilgen, E., 1995, "Effect of a Magnetic Field on the Onset of Convection in a Porous Medium," Heat Mass Transfer, **30**, pp. 259–267.
[7] Alchaar, S., Vasseur, P., and Bilgen, E., 1995, "Hydromagnetic Natural Convection in a Tilted Rectangular Porous Enclosure," Numer. Heat Transfer, Part A, **27**, pp. 107–127.
[8] Bian, W., Vasseur, P., and Bilgen, E., 1996, "Effect of an External Magnetic Field on Buoyancy Driven Flow in a Shallow Porous Cavity," Numer. Heat Transfer, Part A, **29**, pp. 625–638.
[9] Bian, W., Vasseur, P., Bilgen, E., and Meng, F., 1996, "Effect of an Electromagnetic Field on Natural Convection in an Inclined Porous Layer," Int. J. Heat Fluid Flow, **17**, pp. 36–44.
[10] Oldenburg, C. M., Borglin, S. E., and Moridis, G. J., 2000, "Numerical Simulation of Ferrofluid Flow for Subsurface Environmental Engineering Applications," Transp. Porous Media, **38**, pp. 319–344.
[11] Borglin, S. E., Moridis, G. J., and Oldenburg, C. M., 2000, "Experimental Studies of Flow of Ferrofluid in Porous Media," Transp. Porous Media, **41**, pp. 61–80.
[12] Sekar, R., Vaidyanathan, G., and Ramanathan, A., 1993, "The Ferroconvection in Fluids Saturating a Rotating Densely Packed Porous Medium," Int. J. Eng. Sci., **31**(2), pp. 241–250.
[13] Sekar, R., and Vaidyanathan, G., 1993, "Convective Instability of a Magnetized Ferrofluid in a Rotating Porous Medium," Int. J. Eng. Sci., **31**(8), pp. 1139–1150.
[14] Desaive, T., Hennenberg, M., and Dauby, P. C., 2004, "Stabilite Thermomagneto-Convective d'un Ferrofluide dans une Couche Poreuse en Rotation," Mecanique & Industries, **5**, pp. 621–625.
[15] Sunil, Divya, and Sharma, R. C., 2005, "The Effect of Magnetic Field Dependent Viscosity on Thermosolutal Convection in a Ferromagnetic Fluid Saturating a Porous Medium," Transp. Porous Media, **60**, pp. 251–274.
[16] Sunil, Divya, and Sharma, R. C., 2004, "Effect of Rotation on Ferromagnetic Fluid Heated and Soluted From Below Saturating a Porous Media," J. Geophys. Eng., **1**, pp. 116–127.
[17] Saravanan, S., and Yamaguchi, H., 2005, "Onset of Centrifugal Convection in a Magnetic-Fluid-Saturated Porous Medium," Phys. Fluids, **17**, p. 084105.
[18] Venezian, G., 1969, "Effect of Modulation on the Onset of Thermal Convection," J. Fluid Mech., **35**(2), pp. 243–254.
[19] Rosenblat, S., and Tanaka, G. A., 1971, "Modulation of Thermal Convection Instability," Phys. Fluids, **14**(7), pp. 1319–1322.
[20] Roppo, M. N., Davis, S. H., and Rosenblat, S., 1984, "Benard Convection With Time-Periodic Heating," Phys. Fluids, **27**(4), pp. 796–803.
[21] Bhadauria, B. S., and Bhatia, P. K., 2002, "Time-Periodic Heating of Rayleigh-Benard Convection," Phys. Scr., **66**(1), pp. 59–65.
[22] Bhadauria, B. S., 2006, "Time-Periodic Heating of Rayleigh-Benard Convection in a Vertical Magnetic Field," Phys. Scr., **73**(3), pp. 296–302.
[23] Chhuon, B., and Caltagirone, J. P., 1979, "Stability of a Horizontal Porous Layer With Timewise Periodic Boundary Conditions," ASME J. Heat Transfer, **101**, pp. 244–248.
[24] Rudraiah, N., and Malashetty, M. S., 1990, "Effect of Modulation on the Onset of Convection in a Sparsely Packed Porous Layer," ASME J. Heat Transfer, **112**, pp. 685–689.
[25] Malashetty, M. S., and Basavaraja, D., 2002, "Rayleigh-Benard Convection Subject to Time Dependent Wall Temperature/Gravity in a Fluid Saturated Anisotropic Porous Medium," Heat Mass Transfer, **38**, pp. 551–563.
[26] Bhadauria, B. S., 2007, "Thermal Modulation of Raleigh-Benard Convection in a Sparsely Packed Porous Medium," J. Porous Media, **10**(2), pp. 175–188.
[27] Bhadauria, B. S., 2007, "Fluid Convection in a Rotating Porous Layer Under Modulated Temperature on the Boundaries," Transp. Porous Media, **67**(2), pp. 297–315.
[28] Bhadauria, B. S., 2007, "Magnetofluidconvection in a Rotating Porous Layer Under Modulated Temperature on the Boundaries," ASME J. Heat Transfer, **129**, pp. 835–843.
[29] Vadasz, P., 1998, "Coriolis Effect on Gravity-Driven Convection in a Rotating Porous Layer Heated From Below," J. Fluid Mech., **376**, pp. 351–375.
[30] Givler, R. C., and Altobelli, S. A., 1994, "A Determination of the Effective Viscosity for the Brinkman-Forchheimer Flow Model," J. Fluid Mech., **258**, pp. 355–370.
[31] Nayfeh, A. H., 1981, *Introduction to Perturbation Techniques*, Wiley-Interscience, New York.
[32] Malkus, W. V. R., and Veronis, G., 1958, "Finite Amplitude Cellular Convection," J. Fluid Mech., **4**(3), pp. 225–232.
[33] Chandrasekhar, S., 1961, *Hydrodynamic and Hydromagnetic Stability*, Oxford University Press, London.
[34] Krishnamurti, R. E., 1967, Ph.D. thesis, University of California, Los Angeles.
[35] Veronis, G., 1963, "Penetrative Convection," Astrophys. J., **137**, pp. 641–663.

Temperature/Heat Analysis of Annular Fins of Hyperbolic Profile Relying on the Simple Theory for Straight Fins of Uniform Profile

Antonio Campo[1]
e-mail: acampo@uvm.edu

Jianhong Cui

Department of Mechanical Engineering,
The University of Vermont,
Burlington, VT 05405

This technical brief addresses an elementary analytic procedure for solving approximately the quasi-1D heat conduction equation (a generalized Airy equation) governing the annular fin of hyperbolic profile. The importance of this fin configuration stems from the fact that its geometrical shape and heat transfer performance are reminiscent of the annular fin of convex parabolic profile, the so-called optimal annular fin. To avoid the disturbing variable coefficient in the quasi-1D heat conduction equation, usage of the mean value theorem for integration is made. Thereafter, invoking a coordinate transformation, the product is a differential equation, which is equivalent to the quasi-1D heat conduction equation for the simple straight fin of uniform profile. The nearly exact analytic temperature distribution is conveniently written in terms of the two controlling parameters: the normalized radii ratio c and the dimensionless thermogeometric parameter M^2, also called the enlarged Biot number. For engineering analysis and design, the estimates of temperatures and heat transfer rates for annular fins of hyperbolic profile owing realistic combinations of c and M^2 give evidence of good quality. [DOI: 10.1115/1.2885162]

Keywords: annular fin, convex parabolic profile, mean value theorem

Introduction

In general, the augmentation of heat transfer from tubes carrying streams of hot fluids to surrounding cold gases is attainable by attaching arrays of annular fins to the outer surface of the tubes (Kraus et al. [1], Webb [2]). Typical industrial applications involving annular finned tubes are found in air-cooled internal combustion engines, in liquid-gas heat exchangers for refrigeration, in storage tanks of waste nuclear materials, etc.

From a historical perspective, Schmidt [3] was the first investigator who discovered that for a given volume of material, the annular fin of convex parabolic profile was able to reject maximum heat transfer from the hot surface of a tube to a neighboring cold fluid. Schneider [4] stated that, among the whole family of annular fins of tapered cross section, the annular fin of hyperbolic profile is the foremost fin shape for usage in tubes of high performance heat exchange devices. A major drawback posed by the optimal annular fin of convex parabolic profile relates to the incremental manufacturing cost. A minor drawback entails to the sharp tip, which may be viewed as a safety hazard for technical personnel working in plant environments. From an optimization standpoint, the heat removal from the annular fin of hyperbolic profile is very close to the heat removal from the annular fin of convex parabolic profile, the so-called optimal annular fin [4].

The temperature variation along an annular fin of hyperbolic profile obeys a quasi-1D heat equation. This equation, classified as a generalized Airy equation, admits an elegant analytical solution in terms of modified Bessel functions. Unfortunately, the analytical solution is so intricate that the numerical evaluations of temperatures and heat transfer rates are extremely complicated even with symbolic algebra codes, such as MAPLE, MATHEMATICA, and MATLAB.

Relying on the mean value theorem for integration, the present Technical Brief addresses an elementary analytic procedure for solving approximately the quasi-1D heat equation. Although not utilized before, the chosen procedure seems to be a rightful avenue for transforming the generalized Airy equation into an equivalent quasi-1D heat equation for a straight fin of uniform profile. Complete information about the straight fin of uniform profile is amply available in textbooks on heat transfer.

Three aspects of the solution scheme to be developed here are important to highlight: analytic structure, great simplicity, and reasonable accuracy. It is believed that the avenue of the mean value theorem for integration should be attractive to two communities: (1) to engineers engaged in the design of annular fins for heat exchange equipment, and (2) to instructors of heat transfer courses at undergraduate and postgraduate levels.

Formulation

An annular fin of hyperbolic profile is formed with the path of two symmetric hyperbolas $y(r)=\delta_1\ (r_1/r)$, as displayed in Fig. 1. The sizing of this fin depends on four dimensions: the inner radius r_1, the inner semithickness δ_1, the outer radius r_2, and the outer semithickness δ_2. According to Ref. [4], the cross section of the annular fin of hyperbolic profile is of remarkable significance because of its affinity to the cross section of the annular fin of convex parabolic profile capable of delivering maximum heat

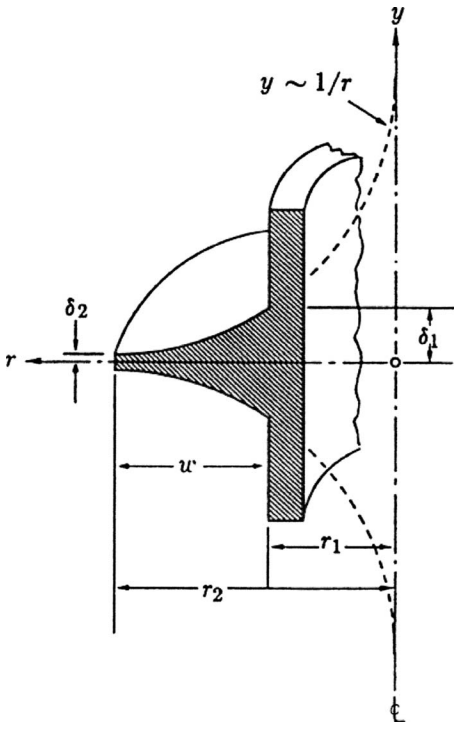

Fig. 1 Sketch of an annular fin of hyperbolic profile

[1]Corresponding author.

Contributed by the Heat Transfer Division for publication in the JOURNAL OF HEAT TRANSFER. Manuscript received November 2, 2006; final manuscript received December 1, 2007; published online April 8, 2008. Review conducted by Satish G. Kandlikar.

transfer for a given volume of material. In this sense, the latter fin has been aptly named the optimal annular fin in Ref. [4].

Adoption of the normalized dimensionless variables for the temperature T and the radial variable r,

$$\theta = \frac{T - T_\infty}{T_b - T_\infty}, \quad R = \frac{r}{r_2} \tag{1}$$

supplies the dimensionless quasi-1D fin equation [4],

$$\frac{d^2\theta}{dR^2} - M^2 R\theta = 0 \quad \text{in } c \leqslant R \leqslant 1 \tag{2}$$

This equation, having one variable coefficient R, is formally classified as a generalized Airy equation in Abramowitz and Stegun [5].

Due to Eq. (1), the dimensionless boundary conditions for prescribed temperature at the fin base and zero heat loss at the fin tip become

$$\theta = 1 \quad \text{at } R = c \quad \text{and} \quad \frac{d\theta}{dR} = 0 \text{ at } R = 1 \tag{3}$$

Furthermore, two parameters regulate the temperature change along the annular fin of hyperbolic profile $\theta(R)$: one is the dimensionless thermogeometric parameter or enlarged Biot number $M^2 = hr_2^3/(\delta_1 r_1 k)$ and the other is the normalized radii ratio $0 \leqslant c = r_1/r_2 \leqslant 1$.

The trademark of the class of quasi-1D fin equations descriptive of annular fins in cylindrical coordinates alludes to the curvature term $d\theta/dR$ [1–4]. Nonetheless, the absence of $d\theta/dR$ in the quasi-1D fin equation (2) for the annular fin of hyperbolic profile is striking.

The heat transfer rate Q from fins may be calculated indirectly through the fin efficiency concept

$$\eta = \frac{Q}{Q_{\text{ideal}}} \tag{4}$$

in two ways:

(a) differentiating $\theta(R)$ at the fin base

$$\eta_{\text{dif}} = \frac{-2 \left.\dfrac{d\theta}{dR}\right|_{R=c}}{M^2(1-c^2)} \tag{5a}$$

(b) integrating $\theta(R)$ over the fin length

$$\eta_{\text{int}} = \frac{2\int_c^1 \theta(R) R dR}{(1-c^2)} \tag{5b}$$

In the context of fin efficiency calculations, Arpaci [6] recommended that the integration approach should be preferred whenever the temperature distribution $\theta(R)$ is approximate.

Exact Analytic Method

The general solution of the generalized Airy equation (2) is

$$\theta(R) = C_1 \text{Ai}(M^{2/3}R) + C_2 \text{Bi}(M^{2/3}R) \tag{6a}$$

where Ai ($*$) and Bi ($*$) are the Airy functions [5]. For the special case $R > 0$, the alternate general solution is

$$\theta(R) = \frac{1}{3}\sqrt{R}\left[C_3 I_{-1/3}\left(\frac{2}{3}MR^{3/2}\right) - C_4 I_{1/3}\left(\frac{2}{3}MR^{3/2}\right)\right] \tag{6b}$$

where I_ν ($*$) denotes the modified Bessel functions of first kind of fractional order ν. Articulating Eq. (6*b*) with the boundary conditions in Eq. (3) furnishes the particular solution,

$$\theta(R) = \sqrt{\frac{R}{c}}\left[\frac{I_{1/3}\left(\frac{2}{3}MR^{3/2}\right) I_{2/3}\left(\frac{2}{3}M\right) - I_{-1/3}\left(\frac{2}{3}MR^{3/2}\right) I_{-2/3}\left(\frac{2}{3}M\right)}{I_{1/3}\left(\frac{2}{3}Mc^{3/2}\right) I_{2/3}\left(\frac{2}{3}M\right) - I_{-1/3}\left(\frac{2}{3}Mc^{3/2}\right) I_{-2/3}\left(\frac{2}{3}M\right)} \right] \tag{6c}$$

which is the exact dimensionless temperature distribution [4].

In passing, safety issues related to the safe-touch temperature of hot metallic objects have been discussed by Arthur and Anderson [7]. In this regard, the exact dimensionless tip temperature from Eq. (6*b*) reduces to

$$\theta(1) = \frac{1}{\sqrt{c}}\left[\frac{I_{1/3}\left(\frac{2}{3}M\right) I_{2/3}\left(\frac{2}{3}M\right) - I_{-1/3}\left(\frac{2}{3}M\right) I_{-2/3}\left(\frac{2}{3}M\right)}{I_{1/3}\left(\frac{2}{3}Mc^{3/2}\right) I_{2/3}\left(\frac{2}{3}M\right) - I_{-1/3}\left(\frac{2}{3}Mc^{3/2}\right) I_{-2/3}\left(\frac{2}{3}M\right)} \right] \tag{6d}$$

To determine the heat transfer rate Q, Eq. (4) is evaluated with Eq. (6*c*). This step delivers the exact fin efficiency,

$$\eta = \frac{\sqrt{2c(1-c)}}{\xi(1+c)}\left[\frac{I_{2/3}(u) I_{-2/3}(v) - I_{-2/3}(u) I_{2/3}(v)}{I_{-2/3}(u) I_{-1/3}(v) - I_{2/3}(u) I_{1/3}(v)} \right] \tag{7a}$$

containing two fin parameters u and v,

$$u = \frac{2}{3}\xi\sqrt{\frac{-2\ln c}{(1-c)^3}} \quad \text{and} \quad v = \frac{2}{3}\xi\sqrt{\frac{-2c^3\ln c}{(1-c)^3}} \tag{7b}$$

along with a third fin parameter ξ,

$$\xi = M\sqrt{\frac{(1-c)^3}{-2\ln c}} \tag{7c}$$

Let us go back momentarily to the generalized Airy equation (2). Owing that only one variable coefficient R shows up, the form of this equation can be considered simple. In contrast, the emerging exact temperature distribution $\theta(R)$ in Eq. (6*c*), together with the exact fin efficiency η in Eq. (7*a*), has convoluted forms with modified Bessel functions of first kind of fractional order I_ν ($*$). Correspondingly, the numerical evaluations of Eqs. (6*c*) and (7*a*) are laborious even with symbolic algebra codes, such as MAPLE, MATHEMATICA, and MATLAB.

Approximate Analytic Method: The Mean Value Theorem for Integration

Let us first isolate the troublesome dimensionless variable coefficient R in Eq. (2). Then, R can be conceived as a function outlining a straight line from the base $R = c$ to the tip $R = 1$ in the closed interval $[c, 1]$. Upon applying the mean value theorem for integration to the function R, the result is

$$\bar{R} = \frac{1}{1-c}\int_c^1 R dR = \frac{1+c}{2} \tag{8}$$

where $\bar{R}$ denotes the functional mean of R.[2]

The idea now is to replace R by $\bar{R}$ in Eq. (2), so that the dimensionless quasi-1D fin equation is converted to

$$\frac{d^2\theta}{dX^2} - M^2\bar{R}\theta = 0 \quad \text{in } c \leqslant R \leqslant 1 \tag{9}$$

As opposed to Eq. (2) that contains one variable coefficient, the product $M^2\,R$, now Eq. (9) possesses one constant coefficient, the product $M^2\,\bar{R}$.

For conciseness, let us name a new constant coefficient

$$W^2 = M^2\bar{R} \tag{10a}$$

and concurrently introduce the coordinate transformation

$$X = R - c \tag{10b}$$

Therefore, the quasi-1D fin equation (9) evolves into

$$\frac{d^2\theta}{dX^2} - W^2\theta = 0 \quad \text{in } 0 \leqslant X \leqslant 1-c \tag{11}$$

so that the two boundary conditions in Eq. (3) are

$$\theta(0) = 1 \text{ and } \frac{d\theta(1-c)}{dX} = 0 \tag{12}$$

At this juncture, it can be asserted that the new formulation given by Eqs. (11) and (12) is identical to the formulation for a straight fin of uniform profile of length $(1-c)$ [4,6]. Skipping the algebra, the solution of Eqs. (11) and (12) when rewritten in terms of R, renders the approximate temperature distribution of compact form

$$\theta(R) = \frac{e^{WR} + e^{W(2-R)}}{e^{Wc} + e^{W(2-c)}} \tag{13}$$

which embraces the two original parameters c and M, plus of course the new parameter $\bar{R}$.

Discussion of Results

Designating the fin efficiency by integration in Eq. (5*b*) by $\eta_{\text{int},1}$ and later inserting Eq. (13) into Eq. (5*b*) yield the approximate expression

$$\eta_{\text{int},1} = \frac{-4e^{W(1+c)} + 2(1-Wc)e^{2Wc} + 2(1+Wc)e^{2W}}{W^2(1-c^2)(e^{2Wc}+e^{2W})} \tag{14}$$

whose evaluation can be done with a calculator. In contrast, the evaluation of the exact fin efficiency in Eq. (7*a*) necessitates symbolic algebra codes, such as MAPLE, MATHEMATICA, or MATLAB.

Recalling that the mean value theorem for integration was the key step in the simplification of the quasi-1D fin equation (2), it may be logical to treat R in Eq. (5*b*) in the same manner. Accordingly, Eq. (5*b*) can be abridged to

$$\eta_{\text{int},2} = \frac{2\bar{R}\int_c^1 \theta(R)dR}{(1-c^2)} \tag{15}$$

Next, introducing the functional mean $\bar{R} = (1+c)/2$ from Eq. (8) in Eq. (15), it simplifies to

$$\eta_{\text{int},2} = \frac{\int_c^1 \theta(R)dR}{(1-c)} \tag{16}$$

The substitution of Eq. (13) in Eqs. (5*b*) and (16) provides an equality between the fin efficiency by differentiation η_{dif} and the fin efficiency by integration $\eta_{\text{int},2}$, the two coalescing into a single approximate relation

$$\eta_{\text{dif}} = \eta_{\text{int},2} = \frac{1}{W(1-c)}\left(\frac{e^{2W} - e^{2Wc}}{e^{2c} + e^{2Wc}}\right) \tag{17}$$

As far as the approximate dimensionless tip temperature $\theta(1)$ is concerned, it is obtained from Eq. (13) giving

$$\theta(1) = \frac{2e^W}{e^{Wc} + e^{W(2-c)}} \tag{18}$$

Table 1 (*a*) Dimensionless tip temperature θ (1) for a small normalized radii ratio $c=0.1$ and variable fin parameter ξ. (*b*) Fin efficiency η for a small normalized radii ratio $c=0.1$ and variable fin parameter ξ.

(*a*)	ξ	Approx. θ (1)	Exact θ (1)	% error		
	0.25	0.918	0.900	2.0		
	0.50	0.728	0.675	7.9		
	0.75	0.526	0.470	11.9		
(*b*)	ξ	Exact η	Approx. $\eta_{\text{int},1}$	% error	Approx. $\eta_{\text{dif}} = \eta_{\text{int},2}$	% error
	0.25	0.925	0.931	0.6	0.945	2.2
	0.50	0.750	0.780	4.0	0.817	8.9
	0.75	0.575	0.613	6.6	0.676	17.6

Inspection of the fin efficiency diagram for annular fins of hyperbolic profile reported in Ref. [4] reveals a family of three curves for the normalized radii ratios: $c = \frac{1}{4}, \frac{1}{2}$, and 1 (the straight fin of uniform profile) and the fin parameter ξ on the abscissa extends from 0.00 up to 3.00. In fact, it may be recognized that the limited graphical representation is deficient for engineering analysis and design because fin efficiencies for other combinations of c and ξ are needed.

Incidentally, it has been stated in Ref. [2] that real values for the fin efficiency η must lie above 50% for practical fin applications. With respect to the fin efficiency diagram in Ref. [4], this proper design space is located in the upper left part bounded by $\xi \leqslant 1.3$ and $c \geqslant 0.2$. In this work, we chose a design space that covers permutations of a small $c=0.1$ united to $\xi \leqslant 0.75$ and a large $c=0.7$ united to $\xi \leqslant 1.00$. The reason for not having $c > 0.7$ is because $c=1$ corresponds to the straight fin of rectangular profile.

The discussion of results is divided in two parts. First, from the items listed in Tables 1(a) and 1(b) concurrently for the pair of a small $c=0.1$ and $\xi \leqslant 0.50$, the relative error for $\theta(1)$ is $\leqslant 7.9\%$, the relative error for $\eta_{\text{int},1}$ is $\leqslant 4\%$, and the relative error for $\eta_{\text{dif}} = \eta_{\text{int},2}$ is $\leqslant 8.9\%$. Also, for the pair of a small $c=0.1$ and $\xi = 0.75$, the relative error for $\theta(1)$ is 11.9%, the relative error for $\eta_{\text{int},1}$ is 6.6%, and the relative error for $\eta_{\text{dif}} = \eta_{\text{int},2}$ is 17.6%. Second, from the items listed in Tables 2(a) and 2(b) concurrently for the pair of a large $c=0.7$ and $\xi \leqslant 0.75$, the relative error for $\theta(1)$ is $\leqslant 2.7.\%$, the relative error for $\eta_{\text{int},1}$ is $\leqslant 0.5\%$, and the relative error for $\eta_{\text{dif}} = \eta_{\text{int},2}$ is $\leqslant 1.9\%$. In synthesis, the above sets of numbers confirm that the fin efficiencies by integration $\eta_{\text{int},1}$ are more accurate than the fin efficiencies by differentiation η_{dif}. This statement indeed supports the recommendation made by Arpaci in Ref. [6], which has been cited before.

In view of the foregoing, the agreements between the approximate estimates and the exact predictions of the two quantities of interest, namely, the dimensionless tip temperature $\theta(1)$ (a local quantity) and the fin efficiency η (a global quantity) for the annular fin of hyperbolic profile are not only satisfactory; they simply exceeded our expectations.

[2]The same result is obtainable from the application of the arithmetic mean of the two extreme ordinates $R=c$ and $R=1$ in $[c, 1]$.

Table 2 (*a*) Dimensionless tip temperature $\theta(1)$ for a relatively large normalized radii ratio $c=0.7$ and variable fin parameter ξ. (*b*) Fin efficiency η for a relatively large normalized radii ratio $c=0.7$ and variable fin parameter ξ.

(*a*)	ξ	Exact $\theta(1)$	Approx. $\theta(1)$	% error
	0.25	0.940	0.940	0
	0.50	0.780	0.792	1.5
	0.75	0.600	0.616	2.7

(*b*)	ξ	Exact η	Approx. $\eta_{\text{int},1}$	% error	Approx. $\eta_{\text{dif}}=\eta_{\text{int},2}$	% error
	0.25	0.960	0.958	0.2	0.960	0.0
	0.50	0.850	0.854	0.4	0.860	1.2
	0.75	0.725	0.728	0.5	0.739	1.9

Conclusions

The main conclusion to be drawn in this Technical Brief is that when dealing with annular fins of hyperbolic profile, usage of modified Bessel functions for solving the quasi-1D heat conduction equation can be obviated. Application of the mean value theorem for integration furnishes an unexpected, facile route that permits the determination of approximate analytical temperature distributions and heat transfer rates for engineering applications. It turns out that both the temperature distribution and the fin efficiency are of simple algebraic form. Even more important, the algebraic forms correspond to their counterparts for the basal straight fin of uniform profile. Interestingly, the two expressions can be evaluated with a calculator for real values of the two controlling parameters, the normalized radii ratio c and the enlarged Biot number M^2. In numbers, for the pair of a small $c=0.1$ and $\xi \leqslant 0.75$, the relative error for $\eta_{\text{int},1}$ is $\leqslant 6.6\%$. Also, for the pair of a large $c=0.7$ and $\xi \leqslant 0.75$, the relative error for $\eta_{\text{int},1}$ is $\leqslant 0.5\%$

The computational methodology via the mean value theorem for integration implemented in this work may be extended to solve a large number of straight and/or annular fins owing tapered profiles [4,6]. Obviously, the most common annular fin, the annular fin of rectangular profile is included as a particular case.

Nomenclature

Ai (*) = Airy function
Bi (*) = Airy function
c = normalized radii ratio, r_1/r_2
h = convection heat transfer coefficient
H^2 = thermogeometric parameter, $h/(\delta_1 r_1 k)$
I_ν (*) = modified Bessel function of first kind and order ν
k = thermal conductivity
L = length, r_2-r_1
M^2 = dimensionless H^2 or enlarged Biot number, $H^2 r_2^3$
Q = heat transfer rate
Q_{ideal} = ideal heat transfer rate
r = radial coordinate
r_1 = inner radius
r_2 = outer radius
R = dimensionless r, r/r_2
$\bar{R}$ = mean value of the function R in $[c, 1]$
T = temperature
T_b = base temperature
T_∞ = fluid temperature
u, v = fin parameters, Eq. (7*b*)
W^2 = $M^2\,\bar{R}$, Eq. (10*a*)
X = coordinate transformation, Eq. (10*b*)

Greek Symbols

δ_1 = inner semithickness
δ_2 = outer semithickness
η = fin efficiency, Q/Q_{ideal}
θ = dimensionless T, $(T-T_\infty)/(T_b-T_\infty)$
ξ = fin parameter, Eq. (7*c*)

References

[1] Kraus, A. D., Aziz, A., and Welty, J. R., 2000, *Extended Surface Heat Transfer*, Wiley, New York.
[2] Webb, R., 1994, *Principles of Enhanced Heat Transfer*, Wiley, New York.
[3] Schmidt, E., 1926,"Die Wärmeübertragung durch Rippen," Zeitschrift des Vereines Deutscher Ingenieure, **70**, pp. 885–889, 947–951.
[4] Schneider, P. J., 1955, *Conduction Heat Transfer*, Addison-Wesley, Reading, MA.
[5] Abramowitz, M., and Stegun, A., 1964, *Handbook of Mathematical Functions*, U. S. Government Printing Office, Washington, DC, p. 446.
[6] Arpaci, V., 1966, *Conduction Heat Transfer*, Addison-Wesley, Reading, MA.
[7] Arthur, K., and Anderson, A. M., 2004, "Too hot to handle? An Investigation Into Safe-Touch Temperatures," *Proceedings of ASME/IMECE*, Anaheim, CA, Nov. 13–19.

Similarity Solution of Unaxisymmetric Heat Transfer in Stagnation-Point Flow on a Cylinder With Simultaneous Axial and Rotational Movements

Asghar B. Rahimi[1]
Professor
Faculty of Engineering,
Ferdowsi University of Mashhad,
P.O. Box 91775-1111,
Mashhad, Iran 91775
e-mail: rahimiab@yahoo.com

Reza Saleh
Assistant Professor
Azad University of Mashhad,
P.O. Box 91735-413,
Mashhad, Iran 91735

Similarity solution of unaxisymmetric heat transfer of an unsteady viscous flow in the vicinity of an axisymmetric stagnation point of an infinite circular cylinder with simultaneous axial and rotational movement along with transpiration U_o is investigated when the angular velocity, axial velocity, and wall temperature or wall heat flux vary arbitrarily with time. The impinging free stream is steady and with a strain rate of $\bar{k}$. The results presented are found by numerical integration. The local coefficient of heat transfer (Nusselt number) is found to be independent of time and place, though the cylinder wall temperature or wall heat flux are functions of both time and place. [DOI: 10.1115/1.2885173]

Keywords: stagnation flow, axial and rotational movement, unaxisymmetric heat transfer, transpiration, similarity solution

1 Introduction

Gorla [1–5], in a series of papers, studied the steady and unsteady flows and heat transfer over a circular cylinder in the vicinity of the stagnation point for the cases of constant axial movement and the special case of axial harmonic motion of a nonrotating cylinder. In more recent years, Cunning et al. [6] have considered the stagnation-flow problem on a rotating circular cylinder with constant angular velocity. They have also included the effects of suction and blowing in their study. The study considered by Saleh and Rahimi [7] and Rahimi and Saleh [8] presents the axisymmetric stagnation-point flow and heat transfer of a viscous fluid on axially moving cylinder and rotating cylinder with time-dependent velocity and uniform transpiration.

In the present analysis, similarity solution of unaxisymmetric heat transfer in axisymmetric stagnation-point flow of a viscous fluid on a cylinder with simultaneous axial and rotational movements along with transpiration is considered. The general self-similar solution of unsteady unaxisymmetric heat transfer is obtained in which unaxisymmetry is due to the sinusoidal variation of temperature with respect to surface position of rotating cylinder and unsteadiness is due to the sinusoidal variation of temperature of each point of the cylinder surface with respect to the time and also rotation of the cylinder. Particular cases of these results are compared with existing results of Gorla [2,4,5].

2 Problem Formulation

The flow configuration is as in Refs. [7,8] when the cylinder has a simultaneous time-dependent rotation and axial movements and the wall temperature or the wall heat flux is also a function of time. A radial external flow of strain rate $\bar{k}$ impinges on the cylinder of radius a, centered at $r=0$. The unsteady Navier–Stokes and energy equations in cylindrical polar coordinates governing the axisymmetric flow and unaxisymmetric heat transfer are as in Refs. [7,8] with the same notations.

The boundary conditions for the velocity field are as follows: $r=a$,

$$u = -U_o(t), \quad v = a\,.\,\omega(t), \quad w = V(t) \tag{1}$$

For $r\to\infty$

$$\frac{\partial u}{\partial r} = -\bar{k}, \quad \lim it_{r\to\infty} rv = 0, \quad w = 2\bar{k}z \tag{2}$$

Here, $\omega(t)$ is the angular velocity and $V(t)$ the axial velocity of the cylinder. For the temperature field, we have the following: For $r=a$,

$$T = T_w(\phi,t) \quad \text{for defined wall temperature}$$

$$\partial T/\partial r = -q_w(\phi,t)/k \quad \text{for defined wall heat flux}$$

For $r\to\infty$,

$$T \to T_\infty \tag{3}$$

and the two boundary conditions with respect to ϕ are

$$T(r,0,t) = T(r,2\pi,t), \quad \frac{\partial T}{\partial \phi}(r,0,t) = \frac{\partial T}{\partial \phi}(r,2\pi,t) \tag{4}$$

where k is the thermal conductivity of the fluid, T_∞ is a constant, and $T_w(\phi,t)$ and $q_w(\phi,t)$ are temperature and heat flux at the wall cylinder, respectively.

A reduction of the Navier–Stokes equations is obtained by applying the following transformations:

$$u = -\bar{k}\frac{a}{\sqrt{\eta}}f(\eta), \quad v = 2\bar{k}\frac{a}{\sqrt{\eta}}G(\eta,\tau),$$
$$w = 2\bar{k}f'(\eta)z + H(\eta,\tau), \quad P = \rho\bar{k}^2a^2p \tag{5}$$

where $\tau=2\bar{k}t$ and $\eta=(r/a)^2$ are the dimensionless time and radial variables and the prime denotes the differentiation with respect to η. Transformations (5) satisfy the mass equation automatically and their insertion into momentum and energy equations yields a coupled system of differential equations in terms of $f(\eta)$, $G(\eta,\tau)$, and $H(\eta,\tau)$ as in Refs. [7,8] with the boundary conditions as follows:

For $\eta=1$,

$$f = S(\tau), \quad f' = 0, \quad G = \Omega(\tau), \quad H = V(\tau)$$

For $\eta\to\infty$,

$$f' = 1, \quad G = 0, \quad H = 0 \tag{6}$$

in which $\Omega=\omega/2\bar{k}$ is dimensionless angular velocity of the cylinder.

To transform the energy equation into a nondimensional form for the case of defined wall temperature and defined wall heat flux, respectively, we introduce

[1]Corresponding author.

Contributed by the Heat Transfer Division for publication in the JOURNAL OF HEAT TRANSFER. Manuscript received November 22, 2006; final manuscript received June 19, 2007; published online April 8, 2008. Review conducted by Minking Chyu.

$$\Theta(\eta,\phi,\tau)=\frac{T(\eta,\phi,\tau)-T_\infty}{T_w(\phi,\tau)-T_\infty},\quad \Theta(\eta,\phi,\tau)=\frac{T(\eta,\phi,\tau)-T_\infty}{aq_w(\phi,\tau)/2k} \tag{7}$$

Making use of Eqs. (5) and (7), the energy equation and the boundary conditions may be written as

$$\eta\Theta''+\Theta'+\frac{1}{4\eta}\left(\frac{\partial^2\Theta}{\partial\phi^2}+2\frac{\partial T_w/\partial\phi}{(T_w-T_\infty)}\frac{\partial\Theta}{\partial\phi}+\frac{\partial^2T_w/\partial\phi^2}{(T_w-T_\infty)}\ \Theta\right.$$
$$+\mathrm{Re\,Pr}\left\{\left(f\Theta'-\frac{\partial\Theta}{\partial\tau}-\frac{\partial T_w/\partial\tau}{(T_w-T_\infty)}\Theta\right)\right.$$
$$\left.\left.-\frac{G}{\eta}\left(\frac{\partial\Theta}{\partial\phi}+\frac{\partial T_w/\partial\phi}{(T_w-T_\infty)}\Theta\right)\right\}\right=0 \tag{8}$$

$$\Theta(1,\phi,\tau)=1,\quad \Theta(\infty,\phi,\tau)=0 \tag{9}$$

$$\Theta(\eta,0,\tau)=\Theta(\eta,2\pi,\tau),\quad \frac{\partial\Theta}{\partial\phi}(\eta,0,\tau)=\frac{\partial\Theta}{\partial\phi}(\eta,2\pi,\tau) \tag{10}$$

where $\mathrm{Pr}=\nu/\alpha$ is Prandtl number. For the case of defined wall heat flux, the energy equation is the same if $(\partial T_w/\partial\phi)/(T_w-T_\infty)$ replaced by $(\partial q_w/\partial\phi)/q_w$. The boundary conditions in this case are

$$\Theta'(1,\phi,\tau)=-1,\quad \Theta(\infty,\phi,\tau)=0 \tag{11}$$

$$\Theta(\eta,0,\tau)=\Theta(\eta,2\pi,\tau),\quad \frac{\partial\Theta}{\partial\phi}(\eta,0,\tau)=\frac{\partial\Theta}{\partial\phi}(\eta,2\pi,\tau) \tag{12}$$

3 Self-Similar Solutions

Semi-similar momentum equations, like in Refs. [7,8], are reduced to exact differential equations with boundary conditions as follows. For $\eta=1$,

$$f=S,\quad f'=0,\quad g=1,\quad h=1$$

For $\eta\to\infty$,

$$f'=1,\quad g=0,\quad h=0 \tag{13}$$

To reduce energy equation to self-similar form, the following separation of variable is chosen:

$$\Theta(\eta,\phi,\tau)=\theta(\eta)Q(\phi,\tau) \tag{14}$$

For the boundary conditions (9)–(12) to admit this separation of variable, the following conditions must be satisfied:
For $\eta=1$,

$$\theta(1)=1\quad \text{for } \eta\to\infty,\quad \theta(\infty)=0\quad \text{for defined wall temperature} \tag{15}$$

For $\eta=1$,

$$\theta'(1)=-1\quad \text{for } \eta\to\infty,\quad \theta(\infty)=0\quad \text{for defined wall heat flux} \tag{16}$$

Substituting the separation of variable into energy, Eq. (8) give

$$\eta\theta''+(1.0+\mathrm{Re\,Pr}\,f)\theta'$$
$$+\left(\frac{1}{4\eta}\frac{\partial^2T_w}{\partial\phi}-\mathrm{Re\,Pr}\left(\Omega\frac{g}{\eta}\frac{\partial T_w}{\partial\phi}+\frac{\partial T_w}{\partial\tau}\right)\right)\frac{\theta}{(T_w-T_\infty)}$$
$$=0\quad \text{for defined wall temperature} \tag{17}$$

$$\eta\theta''+(1.0+\mathrm{Re\,Pr}\,f)\theta'+\left(\frac{1}{4\eta}\frac{\partial^2q_w}{\partial\phi^2}-\mathrm{Re\,Pr}\left(\Omega\frac{g}{\eta}\frac{\partial q_w}{\partial\phi}+\frac{\partial q_w}{\partial\tau}\right)\right)\frac{\theta}{q_w}$$
$$=0\quad \text{for defined wall heat flux} \tag{18}$$

In order for these to be self-similar, none of the terms should be a function of dimensionless time and the angle ϕ. Therefore, we must have the following:

(1) For the defined wall temperature case,

$$T_w(\phi,\tau)-T_\infty=C\exp\{\delta\tau+n(\Omega\tau+\phi)\} \tag{19}$$

which gives

$$(\partial T_w/\partial\phi)/(T_w-T_\infty)=in,\quad (\partial^2T_w/\partial\phi^2)/(T_w-T_\infty)=-n^2$$
$$(\partial T_w/\partial\tau)/(T_w-T_\infty)=i(\delta+n\Omega) \tag{20}$$

(2) For the defined wall heat flux case,

$$q_w(\phi,\tau)=C\exp\{\delta\tau+n(\Omega\tau+\phi)\} \tag{21}$$

which gives

$$(\partial q_w/\partial\phi)/q_w=in,\quad (\partial^2q_w/\partial\phi^2)/q_w=-n^2,$$
$$(\partial q_w/\partial\tau)/q_w=i(\delta+n\Omega) \tag{22}$$

For the quantities in Eqs. (17) and (18) to be constant, the angular velocity of the cylinder Ω must be constant. This means that the cylinder must rotate with a constant angular velocity. Taking the above relations into consideration, the temperature distribution function and heat flux of the cylinder wall have the following changes with respect to δ, n, Ω, and ϕ parameters:

(1) ϕ, temperature on the cylinder wall changes as a cosine function.
(2) Ω, the rotational speed of the cylinder is constant and thus the position of surface temperature alternates because of it.
(3) n shows the number of sinusoidal changes on the surface of the cylinder.
(4) δ shows the sinusoidal changes of temperature with respect to time on each point of the cylinder.

Finally, substituting the above relations into the energy equations, the following self-similar equation is obtained for the both cases of defined wall temperature and wall heat flux:

$$\eta\theta''+(1.0+\mathrm{Re\,Pr}\,f)\theta'-[(n^2)/4\eta+i\,\mathrm{Re\,Pr}\{n\Omega(g/\eta+1.0)+\delta\}]\theta$$
$$=0 \tag{23}$$

The boundary conditions for this equation are as follows:
For $\eta=1$,

$$\theta=1\quad \text{for } \eta\to\infty,\quad \theta=0\quad \text{for defined wall temperature} \tag{24}$$

For $\eta=1$,

$$\theta'=1\quad \text{for } \eta\to\infty,\quad \theta=0\quad \text{for defined wall heat flux} \tag{25}$$

Momentum equations along with the boundary conditions (13) can be solved by using the fourth-order Runge–Kutta method of numerical integration along with a shooting method.

To solve Eq. (23), the following two cases are considered.

3.1 Simple Case of Steady-State Unaxisymmetric Heat Transfer. Unsteadiness is due to the temperature boundary conditions (cylinder wall temperature and wall heat flux functions) being a function of time. To remove this unsteadiness, all the coefficients including δ and Ω must be zero. Based on this, Eq. (23) and the cylinder wall temperature and wall heat flux are simplified as follows:

$$\eta\theta''+(1.0+\mathrm{Re\,Pr}\,f)\theta'-(n^2/4\eta)\theta=0 \tag{26}$$

$$T_w(\phi)-T_\infty=C\exp(in\phi)=C[\cos(n\phi)+i\sin(n\phi)]=A\cos(n\phi) \tag{27}$$

$$q_w(\phi)=C\exp(in\phi)=C[\cos(n\phi)+i\sin(n\phi)]=A\cos(n\phi) \tag{28}$$

If $n=0$, the very simple cases of constant wall temperature and constant heat flux of cylinder are obtained, which were solved by Gorla [5]. The self-similar equation (26) along with the boundary conditions (24) and (25) and knowing the $f(\eta)$ function was solved using the fourth-order Runge–Kutta method of numerical integration along with a shooting method for different values of n, Reynolds number, and Prandtl number.

3.2 More General Case of Unsteady Unaxisymmetric Heat Transfer. The cylinder constant rotational speed Ω and coefficient δ presenting time-dependent variation of temperature of each point of the cylinder surface are the terms causing unsteadiness. In this case, Eq. (23) and boundary conditions (24) and (24) must be considered with no changes. Considering the dimensionless temperature as

$$\theta(\eta) = \theta_1(\eta) + i\theta_2(\eta) \tag{29}$$

gives

$$\eta\theta_1'' + (1.0 + \mathrm{Re\,Pr}\, f)\theta_1' - (n^2/4\eta)\theta_1 + \mathrm{Re\,Pr}[n\Omega(g/\eta + 1.0) + \delta]\theta_2 = 0$$

$$\eta\theta_2'' + (1.0 + \mathrm{Re\,Pr}\, f)\theta_2' - (n^2/4\eta) - \mathrm{Re\,Pr}[n\Omega(g/\eta + 1.0) + \delta]\theta_1 = 0 \tag{30}$$

The boundary conditions become as follows. For $\eta=1$,

$$\theta = 1 \rightarrow \theta_1 = 1, \quad \theta_2 = 0$$

For $\eta\rightarrow\infty$,

$$\theta = 0 \rightarrow \theta_1 = \theta_2 = 0 \quad \text{for defined wall temperature case} \tag{31}$$

For $\eta=1$,

$$\theta' = -1 \rightarrow \theta_1' = -1, \quad \theta_2' = 0$$

For $\eta\rightarrow\infty$,

$$\theta = 0 \rightarrow \theta_1 = \theta_2 = 0 \quad \text{for defined wall heat flux} \tag{32}$$

Considering relations (23) and (26), $n=0$, $\delta=0$, and $\Omega=0$ correspond to the very simple cases of cylinder with constant wall temperature and constant wall heat flux obtained by Gorla [5] for the first time. $n=0$, $\delta\neq 0$, and $\Omega\neq 0$ correspond to axial axisymmetric heat transfer discussed in Saleh and Rahimi [7] in which wall temperature or wall heat flux changes harmonically with the time. $n\neq 0$, $\delta=0$, and $\Omega=0$ correspond to the steady unaxisymmetric heat transfer case in which the temperature variation and heat flux variation on the cylinder wall is considered sinusoidal, like in Sec. 3.1. $n\neq 0$, $\delta\neq 0$, and $\Omega=0$ correspond to the case in which unaxisymmetry is due to the sinusoidal variation of the temperature with respect to the surface position of the rotating cylinder and the unsteadiness is due to the sinusoidal variation of temperature of each point of the cylinder surface with respect to time. $n\neq 0$, $\delta=0$, and $\Omega\neq 0$ correspond to the case in which unaxisymmetry is due to the sinusoidal variation of temperature with respect to surface position of rotating cylinder and its unsteadiness is due to the constant rotation of cylinder and the displacement of temperature of each point of cylinder surface with respect to time. $n\neq 0$, $\delta\neq 0$, and $\Omega\neq 0$ correspond to the most general case in which unaxisymmetry is due to the sinusoidal variation of temperature with respect to surface position of rotating cylinder and unsteadiness is due to the sinusoidal variation of temperature of each point of the cylinder surface with respect to time and also rotation of the cylinder.

The coupled system of Eq. (30) along with the boundary conditions (31) and (32) have been solved by using the fourth-order Runge–Kutta method of numerical integration along with a shooting method, Press et al. [9] for known values of $f(\eta)$ and $g(\eta)$ functions, and different values of n, δ, Ω, Reynolds number, and Prandtl number. The results are presented in later sections.

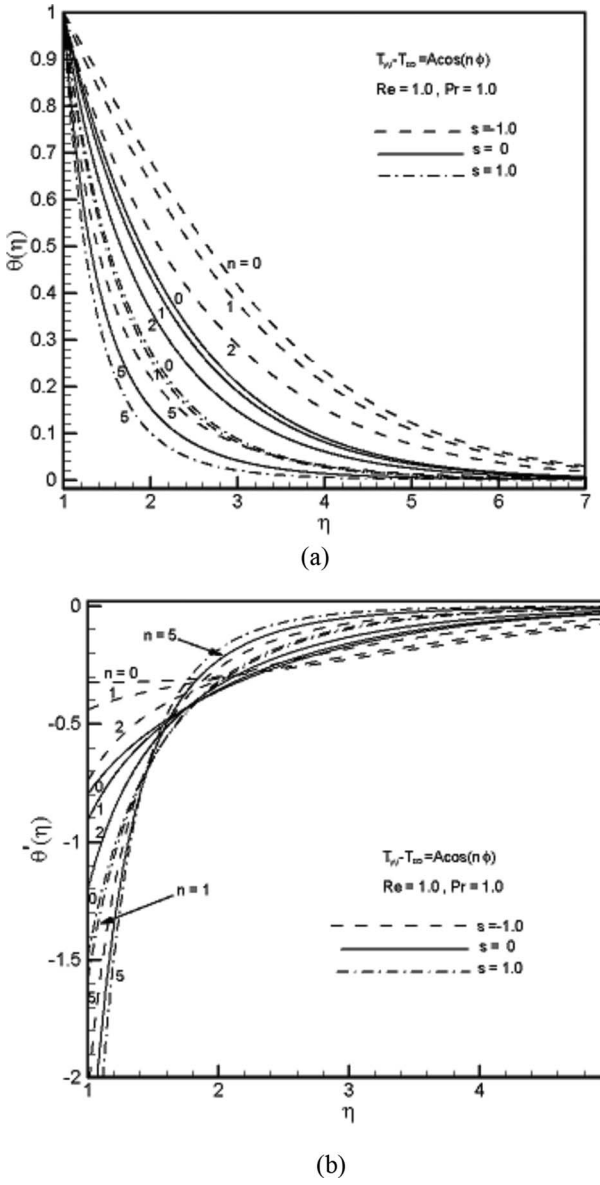

Fig. 1 Profiles of (a) $\theta(\eta)$, (b) $\theta'(\eta)$ for sinusoidal wall temperature function for $S=-1.0, 0.0, 1.0$, Pr=1, Re=1, and different values of n and for all ϕ

4 Heat Transfer Coefficient

The local heat transfer coefficient and the rate of heat transfer for defined wall temperature case are given by

$$h = q_w/(T_w - T_\infty) = -k(\partial T/\partial r)_{r=a}/(T_w - T_\infty) = -(2k/a)\Theta'(1,\phi,\tau)$$

for semi-similar case

$$h = h_r + ih_i = -(2k/a)[\theta_1'(1) + i\theta_2'(1)] \quad \text{for self-similar case} \tag{33}$$

or in terms of Nusselt number, $\mathrm{Nu}=ha/2k$ gives

$$\mathrm{Nu} = -\Theta'(1,\phi,\tau) \quad \text{for semi-similar case} \tag{34}$$

$$\mathrm{Nu} = \mathrm{Nu}_r + i\mathrm{Nu}_i = -[\theta_1'(1) + i\theta_2'(1)] \quad \text{for self-similar case} \tag{35}$$

and finally the heat flux through the cylinder wall is

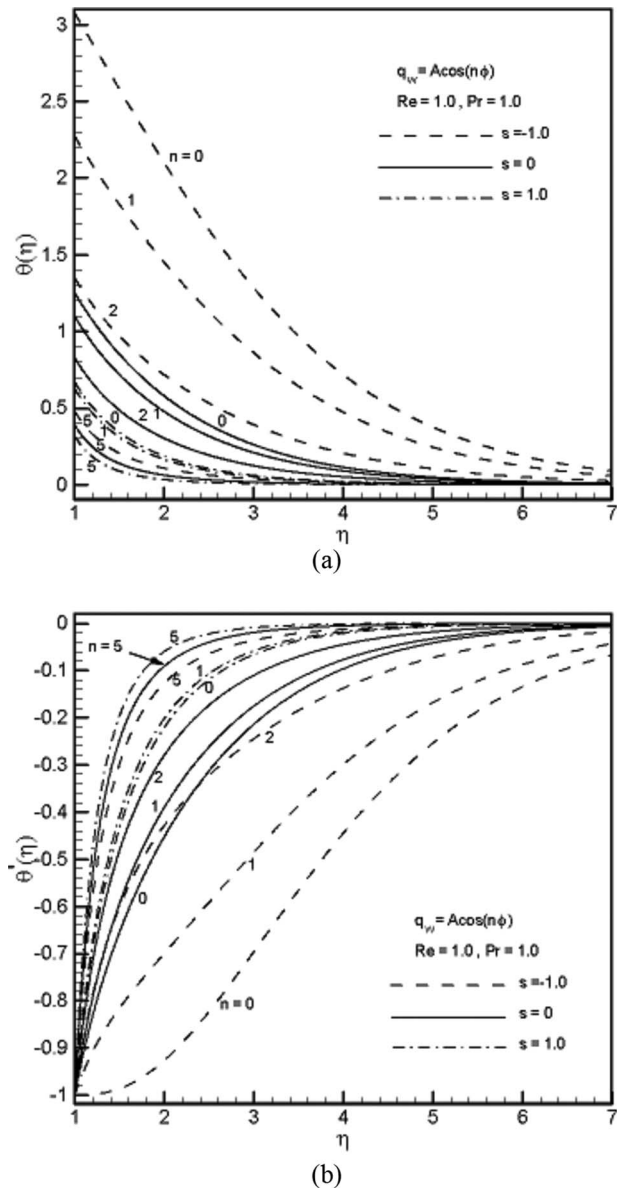

Fig. 2 Profiles of (a) $\theta(\eta)$, (b) $\theta'(\eta)$ for sinusoidal wall heat flux function for $S=-1.0, 0.0, 1.0$, Pr=1, Re=1, and different values of n and for all ϕ

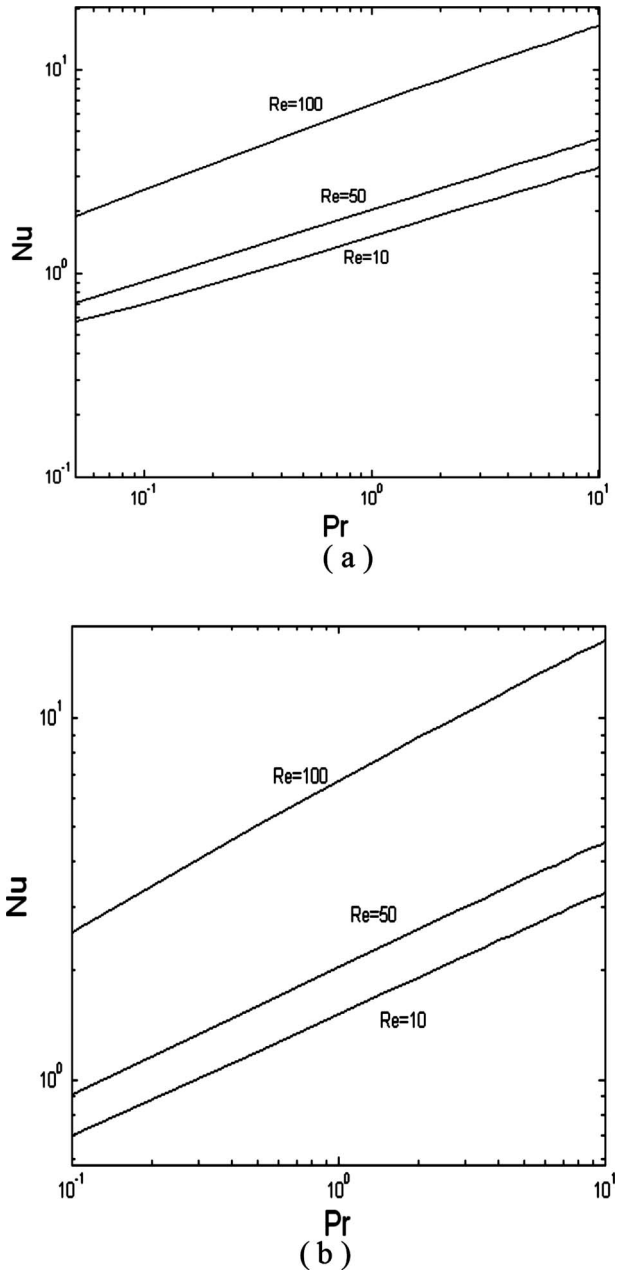

Fig. 3 Nusselt number in terms of Prandtl number for wall temperature function $T_w(\phi) - T_\infty = A\cos(n\phi)$ and selected values of Reynolds numbers for (a) $n=1$, $S=0$, and (b) $n=5$, $S=0$

$$q_w = (-2k/a)\Theta'(1,\phi,\tau)(T_w - T_\infty) \quad \text{for semi-similar case} \tag{36}$$

$$q_w = (-2k/a)C\exp[i\{\delta\tau + n(\Omega\tau + \phi)\}][\theta_1'(1) + i\theta_2'(1)] \quad \text{for self-similar case} \tag{37}$$

For the defined wall heat flux case,

$$h = q_w/(T_w - T_\infty) = (2k/a)/\Theta(1,\phi,\tau) \quad \text{for semi-similar case} \tag{38}$$

$$h = (2k/a)/(\theta_1(1) + i\theta_2(1)) = (2k/a)(\theta_1(1) - i\theta_2(1))/(\theta_1^2(1) + \theta_2^2(1)) \quad \text{for self-similar case} \tag{39}$$

and in terms of Nusselt number,

$$\mathrm{Nu} = 1/\Theta(1,\phi,\tau) \quad \text{for semi-similar case} \tag{40}$$

$$\mathrm{Nu} = ha/2k = 1/(\theta_1^2(1) + \theta_2^2(1)) = (\theta_1(1) - i\theta_2(1))/(\theta_1^2(1) + \theta_2^2(1)) \quad \text{for self-similar case} \tag{41}$$

and finally, the temperature distribution is

$$T_w - T_\infty = (a/2k)\Theta(1,\phi,\tau)q_w \quad \text{for semi-similar case} \tag{42}$$

$$T_w - T_\infty = (a/2k)c\exp[i\{\delta\tau + n(\Omega\tau + \phi)\}][\theta_1(1) + i\theta_2(1)] \quad \text{for self-similar case} \tag{43}$$

From Eqs. (35) and (40), it is clearly seen that for self-similar cases, the heat transfer coefficient (Nusselt number) is not a function of time or the place, contrary to the fact that cylinder wall temperature and wall heat flux are both functions of time and place.

5 Presentation of Results

Interesting results regarding the fluid flow in this problem have been discussed in detail in Refs. [7] and [8]. Here, merely the heat transfer results are discussed and presented.

Sample profiles of the nondimensional temperature $\theta(\eta)$ and temperature gradient $\theta'(\eta)$ in terms of η are presented in Fig. 1 for specified wall temperature function and for selected nondimensional transpiration rates, for all values of ϕ. As it is clear, these profiles are for $n=0.0, 1.0, 2.0, 5.0$, where n is the cycle number of the wall temperature cosine function and $n=0$ expresses the state of constant wall temperature. From Fig. 1(a), the increase of suction rate of fluid into the cylinder and the increase of n reduce the depth of diffusion of temperature into the fluid. From this figure, when $n \to \infty$, the thickness of thermal boundary layer tends toward zero. From Fig. 1(b), the increase of n and S causes the increase of absolute value of the profile of the initial temperature and therefore the coefficient of heat transfer increases and thus the thickness of thermal boundary layer decreases.

Sample profiles of the nondimensional temperature $\theta(\eta)$ and temperature gradient $\theta'(\eta)$ in terms of η are given in Fig. 2 for specified wall heat flux function and for selected nondimensional transpiration rate. Here, again the value of $n=0.0, 1.0, 2.0, 5.0$ has been used, where n is the cycle number of the cylinder wall heat flux and $n=0$ expresses a constant wall heat flux. From Fig. 2(a), again the increase of suction rate of fluid into the cylinder and increase of n reduce the cylinder wall temperature and naturally the depth of diffusion of temperature field of fluid adjacent to the cylinder wall decreases. Also, the distribution of nondimensional temperature in the fluid, which is in the form of cosine function, is going to tend to zero in a faster trend as n and S increase. Here, again as $n \to \infty$ the thickness of thermal boundary layer tends to zero. From Fig. 2(b), as n and S increase, the depth of diffusion of temperature field decreases and thus the thickness of thermal boundary layer decreases.

In Fig. 3, variations of Nusselt number in terms of Prandtl number for specified wall temperature function and selected values of Reynolds number for (a) $n=1$, $S=0$, and (b) $n=5$, $S=0$ are shown. It is interesting to note that the value of Nusselt number is a constant with respect to time and position, though the wall temperature or heat flux changes with both time and position.

6 Conclusions

In this paper, the unaxisymmetric heat transfer of cylinder for two types of functions as unaxisymmetric wall temperature and unaxisymmetric wall heat flux in axisymmetric radial stagnation-point flow on a cylinder with simultaneous rotational and axial movement along with transpiration has been studied. Here, a similarity solution has been obtained for energy equation for some specific functions of unaxisymmetric wall temperature distribution and unaxisymmetric wall heat flux. The effects of suction and blowing, Reynolds number, Prandtl number, and different forms of unaxisymmetric thermal functions on heat transfer rate have been discussed for selected cases in self-similar case. The results presented are found by numerical integration. It is interesting to note that in the case of self-similar solutions, the Nusselt number is a constant value with respect to time and position, though wall temperature or wall heat flux changes with respect to both time and position.

References

[1] Gorla, R. S. R., 1977, "Unsteady Laminar Axisymmetric Stagnation Flow Over a Circular Cylinder," Dev. Mech., **9**, pp. 286–288.

[2] Gorla, R. S. R., 1978, "Nonsimilar Axisymmetric Stagnation Flow on a Moving Cylinder," Int. J. Eng. Sci., **16**, pp. 397–400.

[3] Gorla, R. S. R., 1978, "Transient Response Behavior of an Axisymmetric: Stagnation Flow on a Circular Cylinder Due to Time Dependent Free Stream Velocity," Int. J. Eng. Sci., **16**, pp. 493–502.

[4] Gorla, R. S. R., 1979, "Unsteady Viscous Flow in the Vicinity of an Axisymmetric Stagnation-Point on a Cylinder," Int. J. Eng. Sci., **17**, pp. 87–93.

[5] Gorla, R. S. R., 1976, "Heat Transfer in an Axisymmetric Stagnation Flow on a Cylinder," Appl. Sci. Res., **32**, pp. 541–553.

[6] Cunning, G. M., Davis, A. M. J., and Weidman, P. D., 1998, "Radial Stagnation Flow on a Rotating Cylinder With Uniform Transpiration," J. Eng. Math., **33**, pp. 113–128.

[7] Saleh, R., and Rahimi, A. B., 2004, "Axisymmetric Stagnation-Point Flow and Heat Transfer of a Viscous Fluid on a Moving Cylinder With Time-Dependent Axial Velocity and Uniform Transpiration," ASME J. Fluids Eng., **126**, pp. 997–1005.

[8] Rahimi, A. B., and Saleh, R., 2007, "Axisymmetric Stagnation-Point Flow and Heat Transfer of a Viscous Fluid on a Rotating Cylinder With Time-Dependent Velocity and Uniform Transpiration," ASME J. Fluids Eng., **129**, pp. 106–115.

[9] Press, W. H., Flannery, B. P., Teukolsky, S. A., and Vetterling, W. T., 1997, *Numerical Recipes: The Art of Scientific Computing*, Cambridge University Press, Cambridge.

Transient Critical Heat Fluxes of Subcooled Water Flow Boiling in a Short Vertical Tube Caused by Exponentially Increasing Heat Inputs

Koichi Hata[1]
Mem. ASME
Institute of Advanced Energy,
Kyoto University,
Gokasho, Uji,
Kyoto 611-0011, Japan
e-mail: hata@iae.kyoto-u.ac.jp

Nobuaki Noda
National Institute for Fusion Science,
322-6 Oroshi-cho, Toki,
Gifu 509-5292, Japan

The transient critical heat fluxes (CHFs) of the subcooled water flow boiling for the flow velocities (u=4.0–13.3 m/s)*, the inlet subcoolings* ($\Delta T_{sub,in}$=68.08–161.12 K)*, the inlet pressures* (P_{in} =718.31–1314.62 kPa)*, the dissolved oxygen concentrations* (O_2=2.94 ppm *to the saturated one), and the exponentially increasing heat inputs* ($Q_0 \exp(t/\tau)$, τ=16.82 ms *to* 15.52 s*) are systematically measured with an experimental water loop comprised of a pressurizer. The SUS304 tubes of the inner diameters* (d=3 mm*,* 6 mm*,* 9 mm*, and* 12 mm*), heated lengths* (L =33.15–132.9 mm)*,* L/d=5.48–11.08*, and wall thickness* (δ =0.3 mm *and* 0.5 mm*) with the rough finished inner surface (surface roughness,* Ra=3.18 μm*) are used in this work. The transient CHF data* ($q_{cr,sub}$=6.91–60 MW/m^2) *are compared with the values calculated by the steady state CHF correlations against inlet and outlet subcoolings. The transient CHF correlations against inlet and outlet subcoolings are derived based on the experimental data. The dominant mechanisms of the subcooled flow boiling CHF for a high heating rate are discussed.*
[DOI: 10.1115/1.2887850]

Keywords: transient critical heat flux, subcooled water flow boiling, exponentially increasing heat input, short vertical tube

1 Introduction

A widely and precisely predictable correlation of transient critical heat fluxes (CHFs) for subcooled water flow boiling is necessary to investigate the reliability of a divertor in a nuclear fusion facility for a short pulse high heat flux test mode. Many researchers have experimentally studied the CHFs uniformly heated on the test tube by a steadily increasing current [1–7]. The transient CHF experiments on forced convective boiling were conducted to a platinum wire in water flowing upward by Kataoka et al. [8] and to a circular vertical tube using refrigerant-12 as the working fluid by Celata et al. [9–11]. We have already measured the steady state CHFs, $q_{cr,sub,st}$, (2229 points) for a wide range of experimental conditions to establish the database for designing the divertor of a helical-type fusion experimental device, which is a large helical device (LHD) located in the National Institute for Fusion Science, Japan [12–18]. We have given the steady state CHF correlations against inlet and outlet subcoolings based on the effects of test tube inner diameter (d), flow velocity (u), inlet and outlet subcoolings ($\Delta T_{sub,in}$ and $\Delta T_{sub,out}$), and ratio of heated length to inner diameter (L/d) on CHF,

$$\mathrm{Bo} = C_1 \left\{ \frac{d}{\sqrt{\sigma/g(\rho_l - \rho_g)}} \right\}^{-0.1} \mathrm{We}^{-0.3} \left(\frac{L}{d} \right)^{-0.1} e^{-(L/d)/(C_2 \mathrm{Re}^{0.4})} \mathrm{Sc}^{*C_3}$$

for inlet subcooling ($\Delta T_{sub,in} \geqslant 40$ K) (1)

$$\mathrm{Bo} = 0.082 \left\{ \frac{d}{\sqrt{\sigma/g(\rho_l - \rho_g)}} \right\}^{-0.1} \mathrm{We}^{-0.3} \left(\frac{L}{d} \right)^{-0.1} \mathrm{Sc}^{0.7}$$

for outlet subcooling ($\Delta T_{sub,out} \geqslant 30$ K) (2)

where C_1=0.082, C_2=0.53, and C_3=0.7 for $L/d \leqslant$ around 40 and C_1=0.092, C_2=0.85, and C_3=0.9 for $L/d >$ around 40. Bo, We, Sc*, and Sc are the boiling number ($=q_{cr,sub}/Gh_{fg}$), Weber number ($=G^2 d/\rho_l \sigma$), nondimensional inlet subcooling ($=c_{pl}\Delta T_{sub,in}/h_{fg}$), and nondimensional outlet subcooling ($=c_{pl}\Delta T_{sub,out}/h_{fg}$), respectively. Saturated thermophysical properties were evaluated at the outlet pressure. The correlations against inlet and outlet subcoolings can describe the authors' published steady state CHF data (2229 points) for the wide ranges of test tube inner diameters (d =2–12 mm), heated lengths (L=22–149.7 mm), L/d =4.08–74.85, outlet pressures (P_{out}=159 kPa to 1 MPa), flow velocities (u=4.0–13.3 m/s), dissolved oxygen concentrations (O_2 =8.63–0.0265 ppm), and surface roughness (R_a=3.18 μm, 0.26 μm, and 0.14 μm) within 15% difference for inlet subcoolings ($\Delta T_{sub,in}$=40–151 K) and outlet subcoolings ($\Delta T_{sub,out}$ =30–140 K) on test tubes with rough finished (RF), smooth finished (SF), and mirror finished (MF) inner surfaces, although the CHF data (32 points) with the MF inner surface (R_a=0.14 μm) are distributed within −30% to +7.6% difference of Eq. (2) for 71.4 K $\leqslant \Delta T_{sub,out} \leqslant$ 108.4 K.

The objectives of the present study are fourfold. First is to measure the transient CHFs for the wide ranges of test tube inner diameter, heated length, exponential period, and flow velocity. Second is to compare those with the values calculated by the steady state CHF correlations against inlet and outlet subcoolings. Third is to derive the transient CHF correlations against inlet and outlet subcoolings based on the experimental data for d ranging from 3 mm to 12 mm. Fourth is to discuss the mechanisms of the subcooled flow boiling CHF in a short vertical tube.

2 Experimental Apparatus and Method

2.1 Experimental Water Loop. The schematic diagram of the experimental water loop comprised of the pressurizer is shown in Fig. 1. The loop is made of SUS304 stainless steel and is capable of working up to 2 MPa. The loop has five test sections whose inner diameters are 2 mm, 3 mm, 6 mm, 9 mm, and 12 mm. Test sections were vertically oriented with water flowing upward. The four test sections of the inner diameters of 3 mm, 6 mm, 9 mm, and 12 mm were used in this work. The circulating water was distilled and de-ionized with about 5 MΩ cm specific resistivity. The circulating water through the loop was heated or cooled to keep a desired inlet temperature by a preheater or a cooler. The flow velocity was measured by a mass flow meter using a vibration tube (Nitto Seiko, CLEANFLOW 63FS25, flow range=100 kg/min and 750 kg/min). The flow velocity was controlled by regulating the frequency of the three-phase alternating power source to the canned-type circulation pump (Nikkiso Co., Ltd., Non-Seal Pump HT24B-B2, pump flow rate=75 m^3/h,

[1]Corresponding author.

Contributed by the Heat Transfer Division of ASME for publication in the JOURNAL OF HEAT TRANSFER. Manuscript received December 16, 2006; final manuscript received November 29, 2007; published online April 8, 2008. Review conducted by Chang Oh.

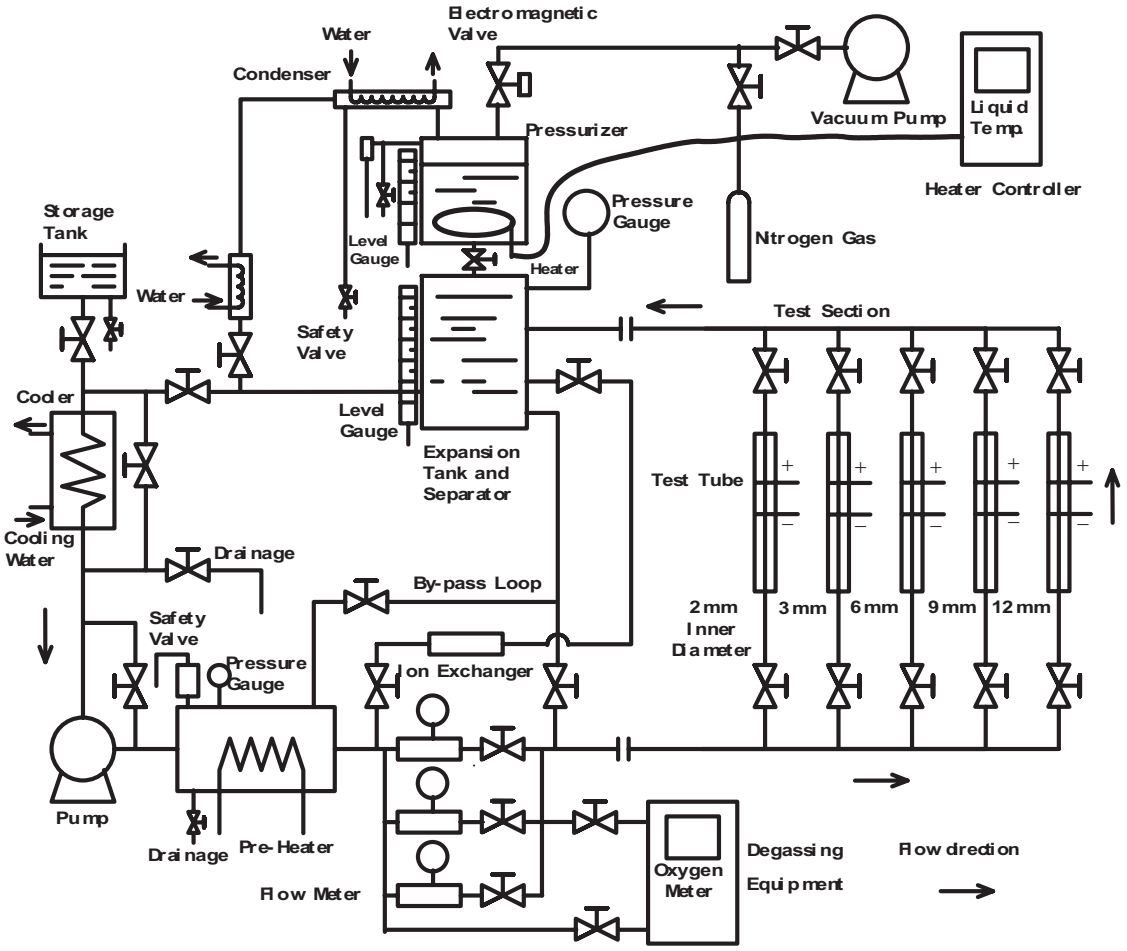

Fig. 1 Schematic diagram of experimental apparatus

pump head=18 m). The water was pressurized by saturated vapor in the pressurizer in this work. The pressure at the inlet of the test tube was controlled within ±1 kPa of a desired value by using a heater controller of the pressurizer.

2.2 Test Section. The cross-sectional view of 3 mm, 6 mm, 9 mm, and 12 mm inner diameter test sections used in this work is shown in Fig. 2. The test tubes with three different surface roughnesses have been generally used. The test tubes with RF and SF inner surfaces are commercially available. The RF inner surface was fabricated by annealing the test tubes first in the atmosphere of air and was then acidized, while the SF inner surface was fabricated by annealing the test tubes in the atmosphere of hydrogen gas. The SF inner surface test tube was polished up to around 25 μm deep by the electrolytic abrasive treatment to realize the MF one. The RF inner surface test tube was mainly used in this work. The wall thickness of the test tube δ was 0.3 mm and 0.5 mm. The inner surface condition of the test tube was observed by the SEM photograph, and the inner surface roughness was measured by Tokyo Seimitsu Co., Ltd.'s surface texture measuring instrument (SURFCOM 120A). Figure 3 shows the SEM photograph of the test tube with a RF inner surface. The inner surface roughness is measured to be 3.18 μm for R_a, 27.28 μm for $R_{\max}$, and 21.16 μm for R_z. The silver-coated 5 mm thickness copper-electrode plates to supply heating current were soldered to the surfaces of both ends of the test tube. Both ends of the test tube were electrically isolated from the loop by Bakelite plates of

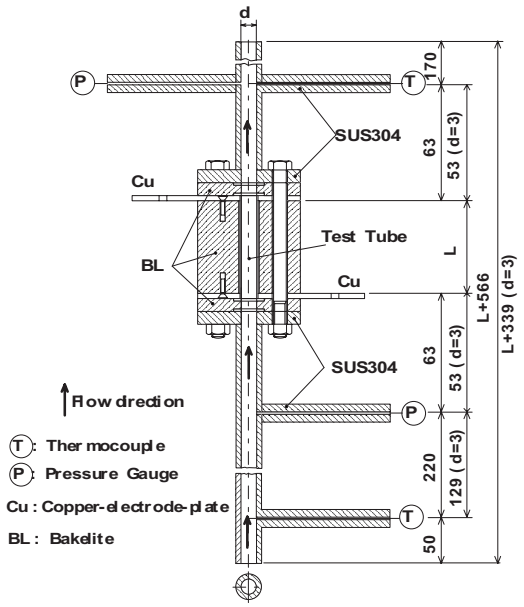

Fig. 2 Vertical cross-sectional view of 3 mm, 6 mm, 9 mm, and 12 mm inner diameter test sections

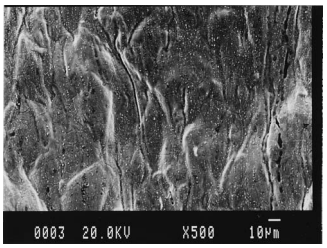

Fig. 3 SEM photograph of the rough finished inner surface

14 mm thickness. The test tube was also thermally insulated from atmosphere with a Bakelite block 120 mm wide, 80 mm deep, and L mm high.

2.3 Method of Heating Test Tube. The test tube was heated with an exponentially increasing heat input supplied from a direct current source (Takasago Ltd., NL035-500R, dc 35 V, 3000 A) through the two copper electrodes shown in Fig. 4. The common specifications of the direct current source are as follows. The constant-voltage (CV) mode regulation is 0.005% +3 mV of full scale, the CV mode ripple is 500 μV rms or better, and the CV mode transient response time is less than 200 μs (typical) against 5% to full range change of load. The transient CHFs, $q_{cr,sub}$, were realized by an exponentially increasing heat input to the test tube. At the CHF, the test tube average temperature rapidly increases. The current for the heat input to the test tube was automatically cut off when the measured average temperature increased up to the preset temperature, which was several tens of kelvin higher than corresponding CHF surface temperature. This procedure avoided the actual burnout of the test tube. Details of the preset temperature are shown in the Appendix.

2.4 Measurement of CHF, Temperature, and Pressure for the Test Tube. The transient average temperature of the test tube was measured with resistance thermometry, participating as a branch of a double bridge circuit for the temperature measurement. The output voltages from the bridge circuit, together with the voltage drop across the two electrodes and across a standard resistance, were amplified and were then sent via a digital-analog (D/A) converter to a digital computer. These voltages were simul-

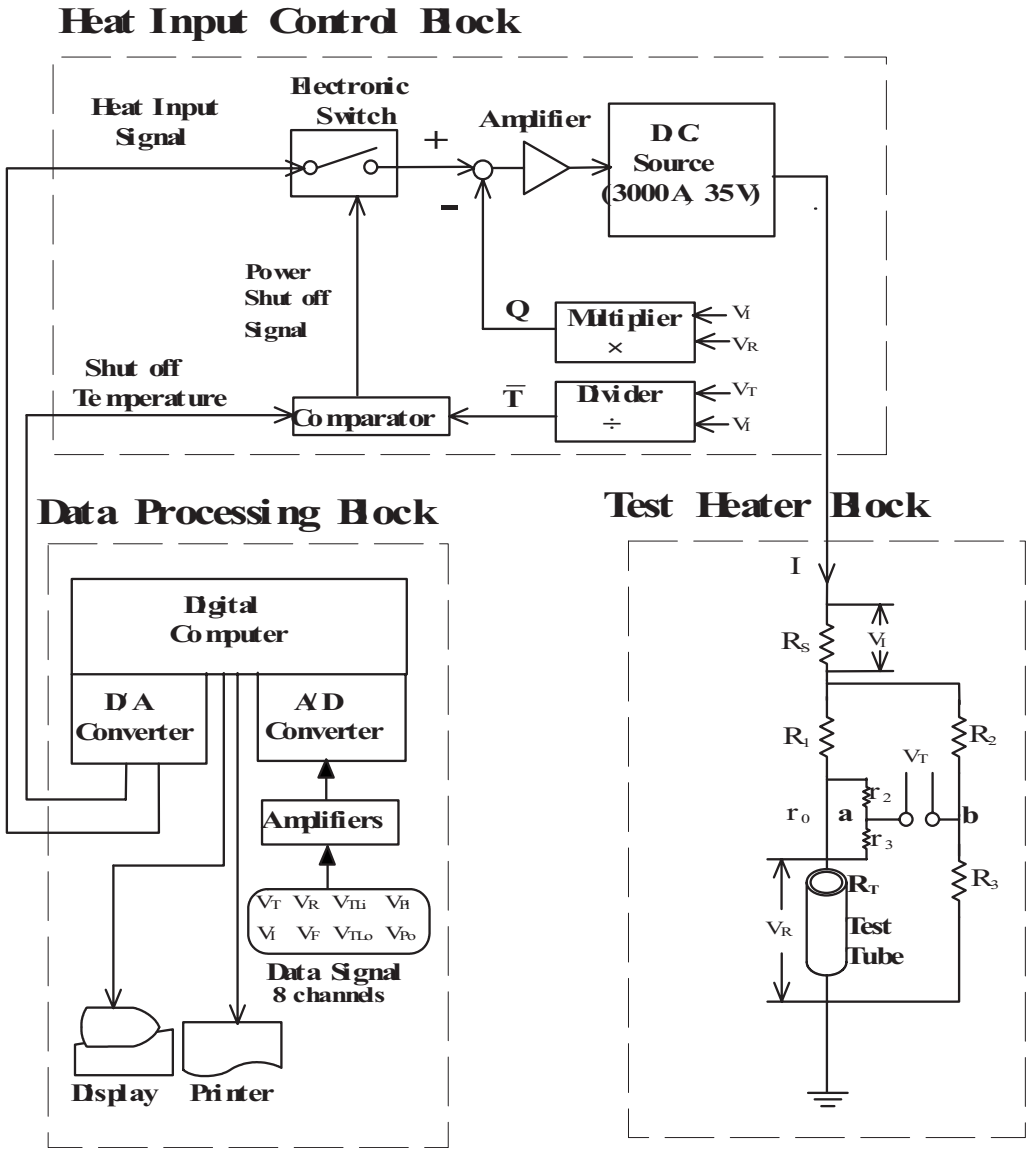

Fig. 4 Measurement and data processing systems

taneously sampled at a constant interval ranging from 60 μs to 200 ms. The average temperature of the test tube was calculated with the aid of a previously calibrated resistance-temperature relation. The heat generation rate in the test tube was calculated from the measured voltage difference between the potential taps of the test tube and the standard resistance. The surface heat flux is the difference between the heat generation rate per unit surface area and the rate of change of energy storage in the test tube obtained from the faired average temperature $\bar{\mathbf{T}}$ versus time t curve as follows:

$$q(t) = \frac{V}{S}\left(Q(t) - \rho c \frac{d\bar{T}}{dt} \right) \tag{3}$$

where ρ, c, V, and S are the density, the specific heat, the volume, and the inner surface area of the test tube, respectively. The inner surface temperature was also obtained by solving the heat conduction equation in the test tube under the conditions of measured average temperature and heat generation rate of the test tube.

In the case of the 3 mm, 6 mm, 9 mm, and 12 mm inner diameter test sections, before entering the test tube, the test water flows through the tube with the same inner diameter of the test tube to form the fully developed turbulent velocity profile. The entrance tube lengths L_e are given as 240 mm, 333 mm, 333 mm, and 333 mm (L_e/d=80, 55.5, 37, and 27.75), respectively. The values of L_e/d for d=3–12 mm in which the centerline velocity reaches 99% of the maximum value for the turbulent flow were obtained, ranging from 9.8 to 21.9 by the correlation of Brodkey and Hershey [19] as follows:

$$\frac{L_e}{d} = 0.693\mathrm{Re}^{1/4} \tag{4}$$

The inlet and outlet liquid temperatures were measured by 1 mm outside diameters, sheathed, *K*-type thermocouples (*Nimblox*, sheath material: SUS316, hot junction: ground, response time (63.2%): 46.5 ms), which are located at the centerline of the tube at the upper and lower stream points of 262 and 53 mm from the tube inlet and outlet points for the 3 mm inner diameter test section, and of 283 mm and 63 mm from those points for the 6 mm, 9 mm, and 12 mm inner diameter ones. The outlet liquid temperatures were performed corrections of time to account for the instrument lag. The values of the time lag for u=4.0–13.3 m/s were 13.25–3.98 ms for the d=3 mm test section, and 15.75–4.73 ms for d=6 mm, 9 mm, and 12 mm ones, respectively. The inlet and outlet pressures were measured by the strain gauge transducers (Kyowa Electronic Instruments Co., LTD., PHS-20A, natural frequency: approximately 30 kHz), which were located near the entrance of conduit at upper and lower stream points of 53 mm from the tube inlet and outlet points for the d=3 mm test section and of 63 mm from those points for d=6 mm, 9 mm, and 12 mm ones. The thermocouples and the transducers were installed in the conduits, as shown in Fig. 2. The inlet and outlet pressures were calculated from the pressures measured by inlet and outlet pressure transducers as follows:

$$P_{\mathrm{in}} = P_{\mathrm{ipt}} - \{(P_{\mathrm{ipt}})_{wnh} - (P_{\mathrm{opt}})_{wnh}\} \times \frac{L_{\mathrm{ipt}}}{L_{\mathrm{ipt}} + L + L_{\mathrm{opt}}} \tag{5}$$

$$P_{\mathrm{out}} = P_{\mathrm{in}} - (P_{\mathrm{in}} - P_{\mathrm{opt}}) \times \frac{L}{L + L_{\mathrm{opt}}} \tag{6}$$

where L_{ipt}=0.053 m and L_{opt}=0.053 m for the 3 mm inner diameter test section, and L_{ipt}=0.063 m and L_{opt}=0.063 m for the 6 mm, 9 mm, and 12 mm inner diameter ones.

Dissolved air concentration of the test water in the loop is controlled by the following procedure. Before each experiment, the room over the water level in the pressurizer is first evacuated with the vacuum pump. The water is degassed under the vacuum conditions at least for 30 min. The water temperature in the loop is around 298 K. Then, the water in the pressurizer is heated up to 373 K by the immersion heater installed into it while the water in the main loop is kept around 298 K. After that, dissolved air in the loop is removed by using a degassing membrane module (Dainippon Ink and Chemicals Inc., Separel KD0-15-5D). During this procedure, dissolved oxygen concentration is monitored by a low level dissolved oxygen meter (Toa DKK, Model DODI-1). Figure 5 shows the relations between saturated dissolved oxygen concentration (O_2), nitrogen one (N_2), and air one (air) versus water temperature at atmospheric pressure [20]. The ratio of saturated air concentration to the oxygen one is also shown in the figure. The value of air/O_2 ranges from 2.61 to 2.76 in the whole temperature range and almost 2.65 at the liquid temperature of around 298 K. The measured dissolved oxygen concentration can be directly related to the dissolved air concentration by using the ratio of 2.65.

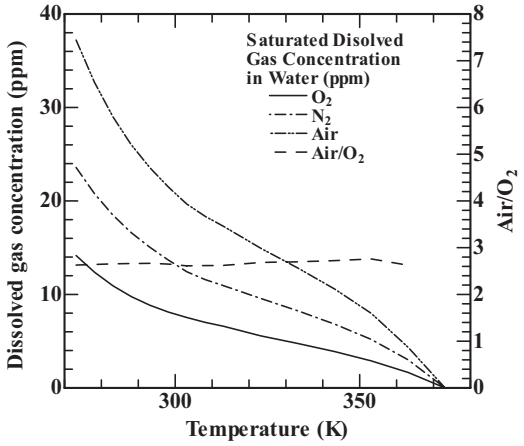

Fig. 5 The relations between saturated dissolved oxygen concentration (O_2), nitrogen one (N_2), air one (air) and air/O_2, and water temperature

Experimental errors are estimated to be ±1 K in inner tube surface temperature and ±2% in heat flux. Inlet flow velocity, inlet and outlet subcoolings, inlet and outlet pressures, dissolved oxygen concentration, and exponential period were measured within the accuracy ±2%, ±1 K, ±1 kPa, ±1% and ±2%, respectively.

3 Experimental Results and Discussion

3.1 Experimental Conditions. Transient heat transfer (HT) processes caused by exponentially increasing heat inputs, $Q_0 \exp(t/\tau)$, were measured for the test tubes. The exponential period τ of the heat input ranged from 16.82 ms to 15.52 s. The decrease of period means an increase in the rate of increasing heat input. The initial experimental conditions such as inlet flow velocity, inlet subcooling, outlet pressure, dissolved oxygen concentration, and exponential period for the flow boiling CHF experiments were independently determined before each experimental run.

The experimental conditions were as follows:

Heater material	304 stainless steel
Surface condition	rough finished inner surface
Surface roughness	3.18 μm for R_a, 27.28 μm for $R_{\max}$, and 21.16 μm for R_z
Inner diameter (d)	3 mm, 6 mm, 9 mm, and 12 mm
Heated length (L)	33.15 mm, 60 mm, 49.3 mm, and 132.9 mm
L/d	5.48–11.08
Wall thickness (δ)	0.3 mm and 0.5 mm

Dissolved oxygen concentration (O_2)	2.94 ppm to saturated one
Inlet flow velocity (u)	4.0 m/s, 6.9 m/s, 9.9 m/s, and 13.3 m/s
Inlet pressure (P_{in})	718.31–1314.62 kPa
Outlet pressure (P_{out})	771.32–1293.38 kPa
Inlet subcooling ($\Delta T_{sub,in}$)	68.08–161.12 K
Outlet subcooling ($\Delta T_{sub,out}$)	52.33–150.71 K
Inlet liquid temperature (T_{in})	296.10–375.49 K
Exponentially increasing heat input (Q_v)	$Q_0 \exp(t/\tau)$, τ=16.82 ms to 15.52 s

3.2 Critical Heat Flux. Figures 6–9 show the transient CHFs, $q_{cr,sub}$, for the test tube inner diameters (d=3 mm, 6 mm, 9 mm, and 12 mm), the heated lengths (L=33.15–132.9 mm), L/d=5.48–11.08, and wall thickness (δ=0.3 mm and 0.5 mm) obtained for the exponential periods τ ranging from 16.82 ms to 15.52 s at the inlet subcoolings $\Delta T_{sub,in}$ of around 70 K, 90 K, and 145 K. The exponential period represents the e-fold time of heat input. As shown in figures, the $q_{cr,sub}$ are almost constant for the exponential periods from 800 ms to 15.52 s, and they become higher with the decrease in exponential period from around 800 ms. The corresponding curves for the flow velocities obtained from the steady state CHF correlation against inlet subcooling (Eq. (1)), are also shown in the figure. The $q_{cr,sub,st}$ for higher flow velocities seem to be slightly lower than the predicted values although the data for lower flow velocities appear to be well expressed by Eq. (1) in the experimental range for the exponential period greater than 800 ms. The transient CHFs in the whole experimental range become higher with an increase in flow velocity at a fixed exponential period, as shown in Figs. 6–9. The changes of dissolved gas concentration from 2.94 ppm to a saturated one showed very little effect on the transient CHFs under the wide range of heating rate in this work.

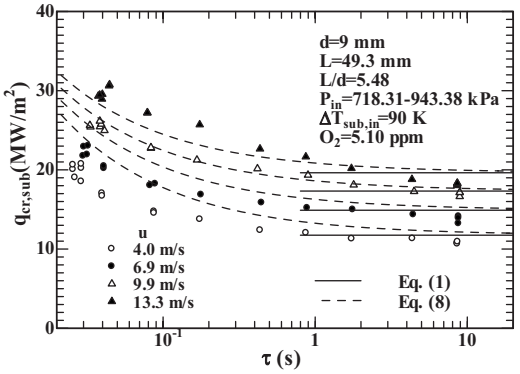

Fig. 8 The $q_{cr,sub}$ for d=9 mm and L=49.3 mm with the rough finished inner surface at $\Delta T_{sub,in}$=90 K for τ=25.61 ms to 8.91 s

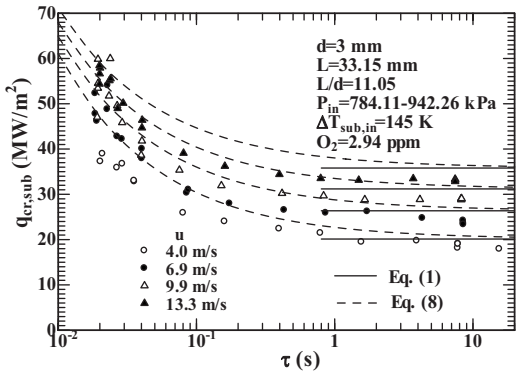

Fig. 6 The $q_{cr,sub}$ for d=3 mm and L=33.15 mm with the rough finished inner surface at $\Delta T_{sub,in}$=145 K for τ=16.82 ms to 15.52 s

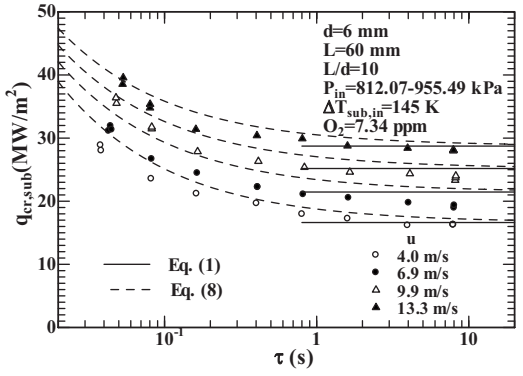

Fig. 7 The $q_{cr,sub}$ for d=6 mm and L=60 mm with the rough finished inner surface at $\Delta T_{sub,in}$=145 K for τ=38.07 ms to 8.22 s

3.2.1 Steady State CHF. Figures 10 and 11 show the ratios of the steady state CHF data obtained in this work (57 points) to the corresponding values calculated by Eqs. (1) and (2) versus $\Delta T_{sub,in}$ and $\Delta T_{sub,out}$, respectively. Most of the data for the tested range of $\Delta T_{sub,in}$ and $\Delta T_{sub,out}$ (68.08 K$\leq\Delta T_{sub,in}\leq$161.12 K and 61.35 K$\leq\Delta T_{sub,out}\leq$131.35 K) are within 15% difference of Eqs. (1) and (2), respectively.

3.2.2 Transient CHF. For power transient experiments, the rate of increasing heat input is very high. It takes time to form the fully developed temperature profile in the test tube because of some heat capacity. Then, the temperature profile in the thermal boundary layer on the test tube surface grows, and vaporization occurs. Furthermore, it takes time to occur the hydrodynamic instability on the vapor-liquid interface at the CHF. Namely, it is explained to be a result of the time lag of the formation of the transient CHF for the increasing rate of the heat input. The experi-

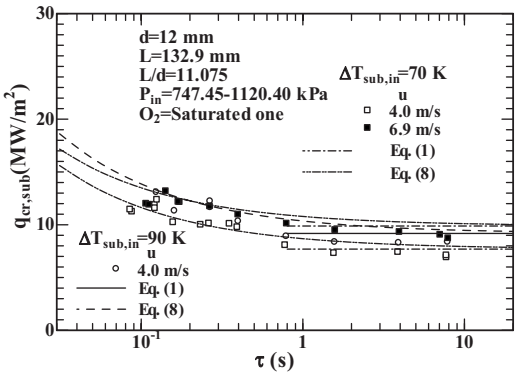

Fig. 9 The $q_{cr,sub}$ for d=12 mm and L=132.9 mm with the rough finished inner surface at $\Delta T_{sub,in}$=70 K and 90 K for τ=85.51 ms to 7.92 s

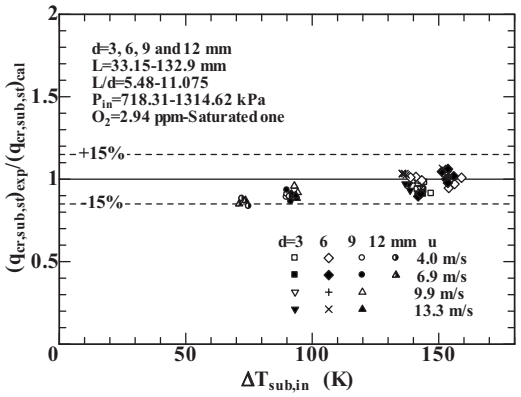

Fig. 10 Ratios of $q_{cr,sub,st}$ for d=3 mm, 6 mm, 9 mm, and 12 mm with the rough finished inner surface to the values derived from Eq. (1) versus $\Delta T_{sub,in}$ at P_{in}=718.31–1314.62 kPa

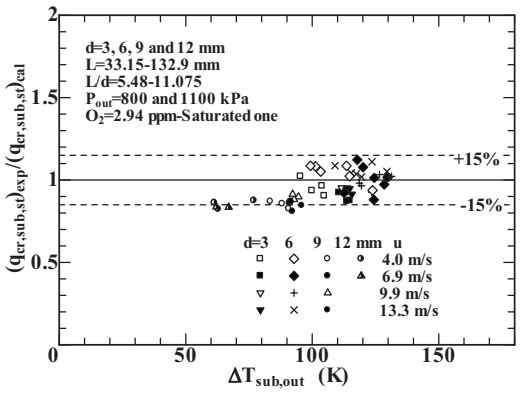

Fig. 11 Ratios of $q_{cr,sub,st}$ for d=3 mm, 6 mm, 9 mm, and 12 mm with the rough finished inner surface to the values derived from Eq. (2) versus $\Delta T_{sub,out}$ at P_{out}=800 kPa and 1100 kPa

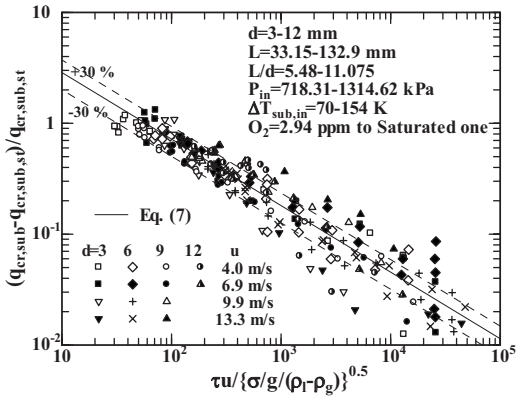

Fig. 12 $(q_{cr,sub}-q_{cr,sub,st})/q_{cr,sub,st}$ for d=3 mm, 6 mm, 9 mm, and 12 mm versus $\tau u/\{\sigma/g/(\rho_l-\rho_g)\}^{0.5}$ with u=4.0–13.3 m/s at P_{in}=718–1314 kPa

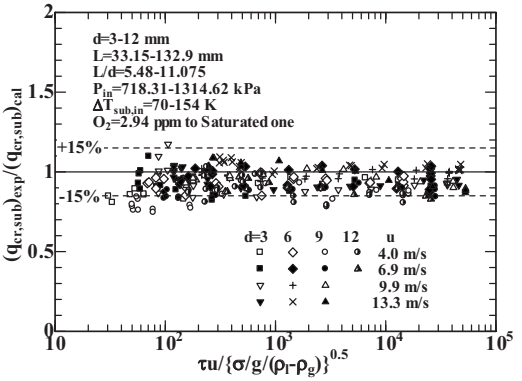

Fig. 13 Ratios of $q_{cr,sub}$ for d=3 mm, 6 mm, 9 mm, and 12 mm (286 points) to corresponding values calculated by Eq. (8) versus $\tau u/\{\sigma/g/\rho_l-\rho_g)\}^{0.5}$

mental results of the transient CHFs, $q_{cr,sub}$, for d=3 mm, 6 mm, 9 mm, and 12 mm are shown in Fig. 12 on the ratios of the difference between the transient CHF, $q_{cr,sub}$, and the steady state ones, $q_{cr,sub,st}$, to the $q_{cr,sub,st}$, $(q_{cr,sub}-q_{cr,sub,st})/q_{cr,sub,st}$, versus the nondimensional exponential period, $\tau u/\{\sigma/g/(\rho_l-\rho_g)\}^{0.5}$, graph with the flow velocity as a parameter. The ratios become linearly higher with the decrease in the $\tau u/\{\sigma/g/(\rho_l-\rho_g)\}^{0.5}$. The slope on the log-log graph is almost constant at about −0.6 for the flow velocities ranging from 4.0 m/s to 13.3 m/s. These data can also be expressed by the following empirical correlation [21–23]:

$$\frac{q_{cr,sub}-q_{cr,sub,st}}{q_{cr,sub,st}} = 11.4\left\{\frac{\tau u}{\sqrt{\sigma/g(\rho_l-\rho_g)}}\right\}^{-0.6} \tag{7}$$

where $L/\{\sigma/g/(\rho_l-\rho_g)\}^{0.5}$ is the dimensionless characteristic length associated with Taylor instability. The correlation can describe the CHF data (286 points) for the inner diameters of 3 mm, 6 mm, 9 mm, and 12 mm at the outlet pressure of around 800 kPa and 1100 kPa obtained in this work within 30% (256 out of 286) for 68.08 K$\leqslant\Delta T_{sub,in}\leqslant$161.12 K, as shown in Fig. 12.

3.3 Transient CHF Correlation Against Inlet Subcooling. The ratios of transient CHF data for the wide range of exponential periods (286 points) to the corresponding values calculated by the steady state CHF correlation against inlet subcooling (Eq. (1)), are almost constant for the $\tau u/\{\sigma/g/(\rho_l-\rho_g)\}^{0.5}$ greater than around 1500 and equivalent to unity, and it becomes higher with the decrease in nondimensional period from around 1500. Moreover the values of the transient CHF almost become two times as large as the steady state ones at the nondimensional exponential period of 57.8. The transient CHF correlation against inlet subcooling for a wide range of exponentially increasing heat inputs ($Q_0\exp(t/\tau)$, τ=16.82 ms to 15.52 s) is derived as follows based on the effect of the nondimensional exponential period clarified in this work:

$$\mathrm{Bo} = C_1\left\{\frac{d}{\sqrt{\sigma/g(\rho_l-\rho_g)}}\right\}^{-0.1}\mathrm{We}^{-0.3}\left(\frac{L}{d}\right)^{-0.1}e^{-(L/d)/(C_2\mathrm{Re}^{0.4})}\mathrm{Sc}^{*C_3} \times\left[1+11.4\left\{\frac{\tau u}{\sqrt{\sigma/g(\rho_l-\rho_g)}}\right\}^{-0.6}\right]$$

$$\text{for inlet subcooling } (\Delta T_{sub,in}\geqslant 40\text{ K}) \tag{8}$$

where C_1=0.082, C_2=0.53, and C_3=0.7 for $L/d\leqslant$ around 40 and C_1=0.092, C_2=0.85, and C_3=0.9 for $L/d>$ around 40. The corresponding curves for the flow velocities obtained from Eq. (8) are also shown in Figs. 6–9 for comparison. The $q_{cr,sub}$ appear to be well expressed by Eq. (8) in the wide range of the exponential periods tested here.

The ratios of transient CHF data (286 points) to the corresponding values calculated from the transient CHF correlation against inlet subcooling (Eq. (8)) are shown versus the nondimensional exponential period, $\tau u/\{\sigma/g/(\rho_l-\rho_g)\}^{0.5}$, for d=3 mm, 6 mm, 9 mm, and 12 mm in Fig. 13. Most of the data for increasing heat input ($Q_0\exp(t/\tau)$, τ=16.82 ms to 15.52 s) are within a range of 15% when compared with Eq. (8) for the wide ranges of the test

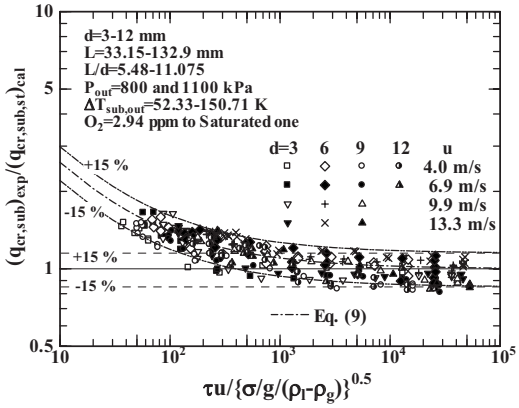

Fig. 14 Ratios of $q_{cr,sub}$ for the wide range of exponential periods (286 points) to corresponding values calculated by Eq. (2) versus $\tau u/\{\sigma/g/\rho_l-\rho_g)\}^{0.5}$

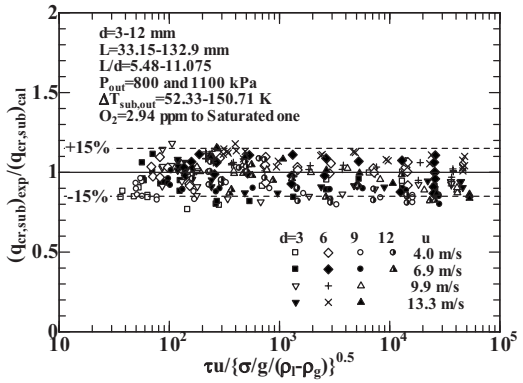

Fig. 15 Ratios of $q_{cr,sub}$ for d=3 mm, 6 mm, 9 mm, and 12 mm (286 points) to corresponding values calculated by Eq. (9) versus $\tau u/\{\sigma/g/\rho_l-\rho_g)\}^{0.5}$

tube inner diameters. It was confirmed that the equation can be applicable for the wider range of d and L/d tested in this work.

3.4 Transient CHF Correlation Against Outlet Subcooling. It can be considered that the transient CHFs are determined not by the inlet conditions but by the outlet ones. The ratios of transient CHF data for the wide range of exponential periods (286 points) to the corresponding values calculated by the steady state CHF correlation against outlet subcooling (Eq. (2)) are shown versus the nondimensional exponential period, $\tau u/\{\sigma/g/(\rho_l-\rho_g)\}^{0.5}$, in Fig. 14. The ratios are almost constant for the nondimensional exponential period, $\tau u/\{\sigma/g/(\rho_l-\rho_g)\}^{0.5}$, higher than 500 and equivalent to unity, and they become higher with the decrease in the nondimensional exponential period from around 500. Moreover, the values of the transient CHFs become two times as large as the steady state ones at the nondimensional exponential period of 21.7. The transient CHF correlation against outlet subcooling for the wide range of exponentially increasing heat inputs ($Q_0 \exp(t/\tau)$, τ=16.82 ms to 15.52 s) is derived as follows based on the effect of the nondimensional exponential period clarified in this work:

$$\mathrm{Bo} = 0.082\left\{\frac{d}{\sqrt{\sigma/g(\rho_l-\rho_g)}}\right\}^{-0.1}\mathrm{We}^{-0.3}\left(\frac{L}{d}\right)^{-0.1}\mathrm{Sc}^{0.7} \times\left[1+6.34\left\{\frac{\tau u}{\sqrt{\sigma/g(\rho_l-\rho_g)}}\right\}^{-0.6}\right] \quad \text{for outlet subcooling } (\Delta T_{sub,out} \geqslant 30\ \mathrm{K}) \tag{9}$$

The ratios of transient CHF data for the wide range of exponential periods (286 points) to the corresponding values calculated from the transient CHF correlation against outlet subcooling [Eq. (9)] are shown versus the nondimensional exponential period, $\tau u/\{\sigma/g/(\rho_l-\rho_g)\}^{0.5}$, for d=3 mm, 6 mm, 9 mm, and 12 mm in Fig. 15. Most of the data for increasing heat inputs ($Q_0 \exp(t/\tau)$, τ=16.82 ms to 15.52 s) are within the range of 15% when compared with Eq. (9).

Even in the steady state CHF experiments, the test tube is sometimes heated by increasing a current step by step. The step increase of the heat input induces instantaneously a very high heating rate in the test tube. We have assumed that surface roughness, dissolved gas concentration, and heating rate will affect the incipient boiling superheat and the nucleate boiling HT up to the CHF. Incipient boiling superheat may shift to a high value at a low dissolved gas concentration and a high heating rate, and direct transition to film boiling already observed in a pool of liquid nitrogen and water [24] may occur in such a case. This may be the cause of very few published data [3,6,7] that were about half or fewer than those given by our CHF correlations [12,13,16]. However, changes of surface roughness from rough to mirror within the commercially obtainable pipes showed very little effect on incipient boiling superheat, nucleate boiling HT, and transient CHFs under the wide range of dissolved gas content and heating rate [14,15,21–23]. The $q_{cr,sub}$ at a fixed flow velocity are also constant for the exponential period longer than 800 ms, and they become monotonously higher with the decrease in the exponential period from the value. Further, no direct transition to film boiling and no trend of a decrease in CHF with a decrease in the exponential period in a smaller exponential period range was observed for the inner diameters (d=3 mm, 6 mm, 9 mm, and 12 mm) with the RF surface (R_a=3.18 μm) used here even at the highest heating rate ($Q_0 \exp(t/\tau)$, τ=16.82 ms) and the lowest dissolved oxygen concentration (O_2=2.94 ppm), as shown in Figs. 6–9.

4 Conclusions

The CHFs of subcooled water flow boiling for the inner diameters (d=3 mm, 6 mm, 9 mm, and 12 mm), the heated lengths (L=33.15–132.9 mm), and L/d=5.48–11.075 with the inner surface of RF are systematically measured for the wide ranges of the dissolved oxygen concentrations (O_2=2.94 ppm to a saturated one), the flow velocities (u=4.0–13.3 m/s), the inlet subcoolings ($\Delta T_{sub,in}$=68.08–161.12 K), the outlet subcoolings ($\Delta T_{sub,out}$=52.33–150.71 K), the inlet pressures (P_{in}=718.31–1314.62 kPa), the outlet pressures (P_{out}=771.32–1293.38 kPa), and the exponentially increasing heat inputs ($Q_0 \exp(t/\tau)$, τ=16.82 ms to 15.52 s). Experimental results lead to the following conclusions.

(1) The transient CHFs, $q_{cr,sub}$, for d=3 mm, 6 mm, 9 mm, and 12 mm are almost constant for the exponential periods greater than 800 ms, and they become higher with the decrease in the exponential period from around 800 ms. The transient CHFs become higher with an increase in flow velocity at a fixed exponential period.

(2) Most of the steady state CHF data (57 points) with the RF inner surface for $\Delta T_{sub,in}$ and $\Delta T_{sub,out}$ are within 15% difference of Eqs. (1) and (2) in the steady state experimental range.

(3) The ratios of the difference between the transient CHF, $q_{cr,sub}$, and the steady state ones, $q_{cr,sub,st}$, to the $q_{cr,sub,st}$ become linearly higher with the decrease in the nondimensional exponential period, $\tau u/\{\sigma/g/(\rho_l-\rho_g)\}^{0.5}$. The slope on the log-log graph is almost constant at about −0.6, with the flow velocity ranging from 4.0 m/s to 13.3 m/s.

(4) The correlation expressed by $(q_{cr,sub}-q_{cr,sub,st})/q_{cr,sub,st}$, Eq.

(7), can describe the CHF data (256 points) for the inner diameters of 3 mm, 6 mm, 9 mm, and 12 mm at the outlet pressures of around 800 kPa and 1100 kPa obtained in this work within a 30% difference.

(5) The transient CHF correlations against inlet and outlet subcoolings, Eqs. (8) and (9), for the wide range of the exponentially increasing heat inputs ($Q_0 \exp(t/\tau)$, τ =16.82 ms to 15.52 s) are derived based on the effect of the nondimensional exponential period clarified for d ranging from 3 mm to 12 mm in this work. Most of the data (286 points) for the increasing heat inputs ($Q_0 \exp(t/\tau)$, τ =16.82 ms to 15.52 s) are within the range of 15% when compared with Eqs. (8) and (9), respectively.

(6) The ratios of transient CHF data (286 points) for the wide ranges of the exponential periods ($Q_0 \exp(t/\tau)$, τ =16.82 ms to 15.52 s) and the inner diameters (d=3 mm, 6 mm, 9 mm, and 12 mm) to the corresponding values calculated from the steady state CHF correlations against inlet and outlet subcoolings (Eqs. (1) and (2)), are constant for the $\tau u/\{\sigma/g/(\rho_l-\rho_g)\}^{0.5}$ greater than 1500 and 500, and equivalent to unity, and they become higher with the decrease in nondimensional exponential period from the values up to two times of the steady state ones at the nondimensional exponential periods of 57.8 and 21.7, respectively.

(7) Neither a direct transition to film boiling nor a trend of a decrease in CHF with a decrease in the exponential period in a smaller exponential period range was observed on the RF surface (R_a=3.18 μm) used here even at the highest heating rate ($Q_0 \exp(t/\tau)$, τ=16.82 ms) and the lowest dissolved oxygen concentration (O_2=2.94 ppm).

Acknowledgment

This research was performed as a LHD joint research project of the NIFS (National Institute for Fusion Science), Japan, NIFS05KFRF015, 2005.

Nomenclature

a, b, c = fitted constant in Eqs. (A4) and (A5)
Bo = $q_{cr,sub}/Gh_{fg}$, boiling number
C_1, C_2, C_3 = constant in Eqs. (1) and (8)
c = specific heat, J/kg K
c_p = specific heat at constant pressure, J/kg K
d = test tube inner diameter, m
G = $\rho_l u$, mass flux, kg/m^2 s
g = acceleration of gravity, m/s^2
h_{fg} = latent heat of vaporization, J/kg
I = current flowing through standard resistance, A
L = heated length or characteristic length, m
L_e = entrance length, m
L_{ipt} = distance between inlet pressure transducer and inlet of the heated section, m
L_{opt} = distance between outlet pressure transducer and outlet of the heated section, m
$L\{\sigma/g/(\rho_l-\rho_g)\}^{0.5}$ = dimensionless characteristic length associated with Taylor instability
O_2 = dissolved oxygen concentration, ppm
P = pressure, kPa
P_{in} = pressure at inlet of heated section, kPa
P_{ipt} = pressure measured by inlet pressure transducer, kPa
P_{out} = pressure at outlet of heated section, kPa
P_{opt} = pressure measured by outlet pressure transducer, kPa
Q = heat input, W
Q_v = heat input per unit volume, W/m^3
Q_0 = initial exponential heat input, W/m^3
q = heat flux, W/m^2
$q_{cr,sub}$ = transient CHF for subcooled condition, W/m^2
$q_{cr,sub,st}$ = steady state CHF for subcooled condition, W/m^2
R_1 to R_3 = resistance in a double bridge circuit, Ω
R_a = average roughness, μm
Re = $=Gd/\mu_l$, Reynolds number
R_{max} = maximum roughness depth, μm
R_z = mean roughness depth, μm
r = resistance in a double bridge circuit, Ω
r_{trip} = trip resistance, Ω
S = surface area, m^2
Sc = $c_{pl}(\Delta T_{sub,out})_{cal}/h_{fg}$, $=c_{pl}\Delta T_{sub,out}/h_{fg}$, nondimensional outlet subcooling
Sc* = $c_{pl}\Delta T_{sub,in}/h_{fg}$, nondimensional inlet subcooling
T = temperature of the test tube, K
$\bar{T}$, T_{av} = average temperature of the test tube, K
T_{in} = inlet liquid temperature, K
T_{out} = outlet liquid temperature, K
T_{sat} = saturation temperature, K
T_{trip} = trip temperature, K
t = time, s
$\Delta T_{sub,in}$ = $(T_{sat}-T_{in})$, inlet liquid subcooling, K
$\Delta T_{sub,out}$ = $(T_{sat}-T_{out})$, outlet liquid subcooling, K
u = flow velocity, m/s
V = volume, m^3
V_T = unbalance voltage in a double bridge circuit, V
$(V_T)_{trip}$ = trip voltage, V
We = $G^2 d/\rho_l \sigma$, Weber number
α = step temperature, K
δ = wall thickness, mm
λ = thermal conductivity, W/mK
ρ = density, kg/m^3
σ = surface tension, N/m
τ = exponential period, s

Subscripts

cr = CHF
g = vapor
in = inlet
out = outlet
l = liquid
sat = saturated conditions
sub = subcooled conditions
wnh = with no heating

Appendix: Method of Calculation of Preset Temperature

The subcooled flow boiling HT and transient CHF for the wide ranges of the flow velocity, the inlet subcooling, the inlet pressure, and the exponentially increasing heat input ($Q_0 \exp(t/\tau)$) are systematically measured. We have given the steady state CHF correlations against inlet and outlet subcoolings based on the effects of test tube inner diameter (d), flow velocity (u), inlet and outlet subcoolings ($\Delta T_{sub,in}$ and $\Delta T_{sub,out}$), and ratio of heated length to inner diameter (L/d) on CHF. The relation between the steady state CHF, $q_{cr,sub,st}$, and the average temperature of the test tube at CHF, $(T_{av})_{cr}$, for a given experimental condition could be roughly estimated by using boiling curve database and CHF correlation. The power trip temperature (preset temperature) is given as follows:

$$T_{\text{trip}} = (T_{\text{av}})_{\text{cr}} + \alpha \tag{A1}$$

where α is increased step by step from 0 to some hundred kelvins until the measured test tube surface temperature rapidly jumps from the nucleate boiling HT regime to the film boiling one. The maximum value of the heat flux, q, which is larger than the $q_{\text{cr,sub,st}}$ is given, and that of the heat input per unit volume, Q_v, for the test tube is calculated as follows:

$$q = q_{\text{cr,sub,st}} + \Delta q \tag{A2}$$

$$Q_v = q\frac{\pi dL}{\pi\{(d+2\delta)^2 - d^2\}L/4} \tag{A3}$$

The electrical resistance of the test tube is measured at various temperatures before each experiment, and the relationship between the electrical resistance and temperature is calibrated by the following approximate form:

$$r = a(1 + bT + cT^2) \tag{A4}$$

where a, b, and c are fitted values based on the measured data. The electrical resistance of the power trip for the test tube, r_{trip}, is obtained by substituting the power trip temperature, T_{trip}, into Eq. (A4),

$$r_{\text{trip}} = a(1 + bT_{\text{trip}} + cT_{\text{trip}}^2) \tag{A5}$$

The schematic of a double bridge circuit is shown in Fig. 4. The current I through the standard resistance R_s can be regarded as that through the test tube. Therefore, the heat generation of the test tube, Q, is expressed by the following form. The current at the power trip temperature is calculated,

$$Q = I^2 r_{\text{trip}} = Q_v\frac{\pi\{(d+2\delta)^2 - d^2\}L}{4} \tag{A6}$$

$$I = \sqrt{Q_v\frac{\pi\{(d+2\delta)^2 - d^2\}L}{4r_{\text{trip}}}} \tag{A7}$$

The double bridge circuit is balanced for a small current at a liquid temperature. When the direct current is supplied to the test tube, the electrical resistance of the test tube increases. As a result, the unbalance voltage V_T is expressed by means of Ohm's low. The power trip voltage $(V_T)_{\text{trip}}$ at the power trip temperature is calculated as the following form:

$$(V_T)_{\text{trip}} = \frac{I(r_{\text{trip}} \times R2 - R1 \times R3)}{R2 + R3} \tag{A8}$$

The value of $(V_T)_{\text{trip}}$ is given the comparator in Fig. 4 as the preset temperature to avoid test tube damage. This procedure avoided actual burnout of the test tube.

References

[1] Bergles, A. E., 1963, "Subcooled Burnout in Tubes of Small Diameter," ASME Paper No. 63-WA-182, pp. 1–9.

[2] Nariai, H., Inasaka, F., and Shimura, T., 1987, "Critical Heat Flux of Subcooled Flow Boiling in Narrow Tube," *Proceedings of the 1987 ASME-JSME Thermal Engineering Joint Conference*, Vol. 5, Hemisphere, New York, pp. 455–462.

[3] Celata, G. P., Cumo, M., and Mariani, A., 1992, "Subcooled Water Flow Boiling CHF With Very High Heat Fluxes," Rev. Gen. Therm., **362**, pp. 29–37.

[4] Celata, G. P., Cumo, M., and Mariani, A., 1994, "Enhancement of CHF Water Subcooled Flow Boiling in Tubes Using Helically Coiled Wires," Int. J. Heat Mass Transfer, **37**(1), pp. 53–67.

[5] Celata, G. P., 1998, "Critical Heat Flux in Subcooled Flow Boiling," *Heat Transfer 1998, Proceedings of the 11th International Heat Transfer Conference*, Vol. 1, pp. 261–277.

[6] Vandervort, C. L., Bergles, A. E., and Jensen, M. K., 1994, "An Experiment Study of Critical Heat Flux in Very High Heat Flux Subcooled Boiling," Int. J. Heat Mass Transfer, **37**, pp. 161–173.

[7] Mudawar, I., and Bowers, M. B., 1999, "Ultra-High Critical Heat Flux (CHF) for Subcooled Water Flow Boiling-I: CHF Data and Parametric Effects for Small Diameter Tubes," Int. J. Heat Mass Transfer, **42**, pp. 1405–1428.

[8] Kataoka, I., Serizawa, A., and Sakurai, A., 1983, "Transient Boiling Heat Transfer Under Forced Convection," Int. J. Heat Mass Transfer, **26**, pp. 583–595.

[9] Celata, G. P., Cumo, M., D'Annibale, F., Farello, G. E., and Said, S. A., 1988, "Critical Heat Flux Phenomena During Power Transients," Heat Technol., **6**(1–2), pp. 38–69.

[10] Celata, G. P., Cumo, M., D'Annibale, F., and Farello, G. E., 1989, "Critical Heat Flux in Transient Flow Boiling During Simultaneous Variations in Flow Rate and Thermal Power," Exp. Therm. Fluid Sci., **2**(2), pp. 134–145.

[11] Celata, G. P., Cumo, M., and D'Annibale, F., 1992, "A Data Set of Critical Heat Flux of Boiling R-12 in Uniformly Heated Vertical Tubes Under Transient Conditions," Exp. Therm. Fluid Sci., **5**(1), pp. 78–107.

[12] Hata, K., Shiotsu, M., and Noda, N., 2004, "Critical Heat Fluxes of Subcooled Water Flow Boiling Against Outlet Subcooling in Short Vertical Tube," Trans. ASME, Ser. C: J. Heat Transfer, **126**, pp. 312–320.

[13] Hata, K., Komori, H., Shiotsu, M., and Noda, N., 2004, "Critical Heat Fluxes of Subcooled Water Flow Boiling Against Inlet Subcooling in Short Vertical Tube," JSME Int. J., Ser. B, **47**(2), pp. 306–315.

[14] Hata, K., Komori, H., Shiotsu, M., and Noda, N., 2004, "Influence of Dissolved Gas Concentration on Subcooled Flow Boiling Critical Heat Flux in Short Vertical Tube," ASME Paper No. ICONE12–49194.

[15] Hata, K., Shiotsu, M., and Noda, N., 2004, "Subcooled Flow Boiling Critical Heat Flux in Short Vertical Tube (Influence of Inner Surface Roughness)," ASME Paper No. IMECE2004-61453.

[16] Hata, K., Shiotsu, M., and Noda, N., 2006, "Critical Heat Flux of Subcooled Water Flow Boiling for High L/d Region," Nucl. Sci. Eng., **154**(1), pp. 94–109.

[17] Hata, K., Shiotsu, M., and Noda, N., 2007, "Influence of Test Tube Material on Subcooled Flow Boiling Critical Heat Flux in Short Vertical Tube," JSME, J. Power Energy Syst., **1**(1), pp. 49–63.

[18] Hata, K., Shiotsu, M., and Noda, N., 2007, "Turbulent Heat Transfer for Heating of Water in a Short Vertical Tube," ASME Paper No. ICONE15–10035.

[19] Brodkey, R. S., and Hershey, H. C., 1988, *Transport Phenomena*, McGraw-Hill, New York, pp. 568.

[20] Mizushori Kanribinran Henshuiinkai (Editorial Committee of Water Treatment), 1998, Mizushori Kanribinran, *Handbook of Water Treatment Control*, Maruzen K. K., Tokyo (in Japanese).

[21] Hata, K., and Noda, N., 2005, "Subcooled Flow Boiling Heat Transfer and Critical Heat Flux in Short Vertical Tube With Mirror Finished Inner Surface," *Proceedings of the 11th International Topical Meeting on Nuclear Reactor Thermal Hydraulics*, Paper No. NURETH11–281.

[22] Hata, K., Shiotsu, M., and Noda, N., 2006, "Influence of Heating Rate on Subcooled Flow Boiling Critical Heat Flux in a Short Vertical Tube," JSME Int. J., Ser. B, **49**(2), pp. 309–317.

[23] Hata, K., Shiotsu, M., and Noda, N., 2006, "Transient Critical Heat Fluxes of Subcooled Water Flow Boiling in a Short Vertical Tube Caused by Exponentially Increasing Heat Inputs," *Proceedings of the 13th International Heat Transfer Conference*, Sydney, Australia, Paper No. IHTC13-BOI-07.

[24] Sakurai, A., Shiotsu, M., Hata, K., and Fukuda, K., 2000, "Photographic Study on Transitions from Non-Boiling and Nucleate Boiling Regime to Film Boiling Due to Increasing Heat Inputs in Liquid Nitrogen and Water," Nucl. Eng. Des., **200**, pp. 39–54.

Boiling Heat Transfer Rates for Small Precisely Placed Water Droplets on a Heated Horizontal Plate

Sally M. Sellers
General Dynamics Land Systems,
Tallahassee, FL 32303
e-mail: sellersm@gdls.com

W. Z. Black
George W. Woodruff School of Mechanical Engineering,
Georgia Institute of Technology,
Atlanta, GA 30332-0405
e-mail: william.black@me.gatech.edu

Two small horizontal surfaces, heated to temperatures up to 220°C, were cooled by small (50–300 mm diameter) room-temperature droplets at 1 atmosphere pressure. One surface was a 10×10 mm thin-film nichrome heater that was used to measure heat fluxes below 100 W/cm^2. The other surface, used for fluxes in excess of 100 W/cm^2, was a solid copper heater with an 8×8 mm exposed surface. A continuous jet droplet generator coupled with two mutually perpendicular deflection plates was used to manipulate the path of constant diameter water droplets so that the impact of the drops could be precisely located on the heated surfaces. The droplet generator and the deflection plates were employed so that the effect of the impact frequency, droplet diameter, droplet velocity and spacing on the resulting heat transfer rates could be studied under controlled conditions. Optimal droplet spacing between 0.75 and 1.5 times the droplet diameter increased the critical heat flux approximately 30 percent above the value that was achieved when the drops were deposited in one location. For area-averaged mass flow rates less than about 0.08 g/(cm^{2}s), there was no trend in the critical heat flux with the Weber number. However, for larger mass flux rates, the critical heat flux increased with an increasing Weber number. The measured critical heat flux values were roughly twice the heat flux of traditional pool boiling for identical superheat temperatures. Two droplet cooling dimensionless critical heat flux correlations are proposed as a function of Weber and Strouhal numbers; one for a single stream of drops and the other for drops that are spaced across the heated surface. The correlation for the spaced droplets is a function of a dimensionless droplet spacing on the heater.
[DOI: 10.1115/1.2884183]

Keywords: two phase heat transfer, evaporative cooling, spray cooling, droplet evaporation

Introduction

Nucleate boiling of a liquid on a heated surface is known to be a very effective technique for dissipating a large amount of heat at moderate temperature differences while maintaining small fluctuations in the temperature of the heated surface. In general, droplet impact cooling has been shown to exhibit the same type of heat transfer characteristics as traditional pool boiling [1,2], and it has the capability to exceed the heat transfer rates that are experienced under normal pool boiling conditions [3–6]. If the impacting droplets are regulated properly and judiciously deposited on the surface in a precise pattern, a stable, uniformly thin film can be created and relatively high heat transfer rates can be accomplished.

This study differs in a number of fundamental ways from previous work in the area of spray or droplet cooling. Most previous work in the area of spray cooling involves droplets with a range of diameters, and they are often propelled to the surface at high velocities with the aid of a secondary fluid [7–9]. In the current study, the drops simply fall toward the surface under the influence of gravity and therefore the heat flux values reported here can be expected to fall short of other heat flux values reported for air-assisted droplet experiments. Critical heat flux values for air-assisted sprays have been reported as high as 1180 W/cm^2 or almost four times greater than values measured in this investigation. However, the water flow rates for the air-assisted spray studies were nearly twice that required to achieve the measured heat transfer rate, resulting in a significant amount of liquid leaving the heated surface without experiencing a phase change.

Nearly all spray cooling studies involve the impact of the drops on the surface in which the size of drops cannot be precisely regulated or their trajectory cannot be accurately predicted. Also, many droplet cooling studies have concentrated on the heat transfer rates that result when drops impact only a single location on the surface [10,11]. In contrast, this study considers only a uniform droplet size and all drops are deposited on the heated surface at a low velocity. Furthermore, the method of producing the drops and directing their precise path lend itself to control of the drop size, frequency, and impact spot on the heated surface.

Experimental Apparatus

The method of generating monodispersed sprays for this study was based on the controlled breakup of liquid jets first proposed by Rayleigh in the late 1800s [12–15]. The continuous stream of room temperature distilled and de-ionized water that was formed at the single hole in the orifice plate was decomposed into uniform, small diameter drops as the nozzle was vibrated by a piezoelectric driver mounted within the droplet generator. Generating frequencies ranged between 2.5 kHz and 38 kHz produced droplet diameters between 97 μm and 392 μm. The drops were charged as they passed between the two electrodes, and they were subsequently deflected by two sets of charged orthogonal plates. The deflection process controlled the path of the droplets and therefore the flight of the droplets could be directed in two dimensions to completely cover the heater surface in a predetermined pattern. Two different types of heated surfaces were utilized in the tests, a nichrome thin-film heater and a higher heat flux copper block heater. For a complete description of the heaters, refer to Ref. [16].

Images of the droplet patterns and boiling process were recorded with a video system and single images were used to determine the droplet diameter, velocity, frequency, and patterns as the droplets impacted the surface.

Test Protocol

The driver frequency was selected to provide a stable, uniform droplet production that did not contain satellite drops. The droplet mass flow rate, velocity, and frequency were used to select the voltage wave forms that were applied to the charging electrodes and the horizontal deflection plates, thereby producing the desired droplet pattern and spacing. Temperature and heat flux data were continually recorded as the heater temperature increased and data were collected as the heat flux exceeded the critical value.

A detailed error analysis was carried out to determine the experimental errors that could be expected when both the nichrome and copper heaters were used. Measurements on the nichrome heater resulted in uncertainty errors in the heat flux of less than 4% and uncertainty in average surface temperatures of less than

Contributed by the Heat Transfer Division for publication in the JOURNAL OF HEAT TRANSFER. Manuscript received April 3, 2006; final manuscript received November 26, 2007; published online April 10, 2008. Review conducted by Chang Oh.

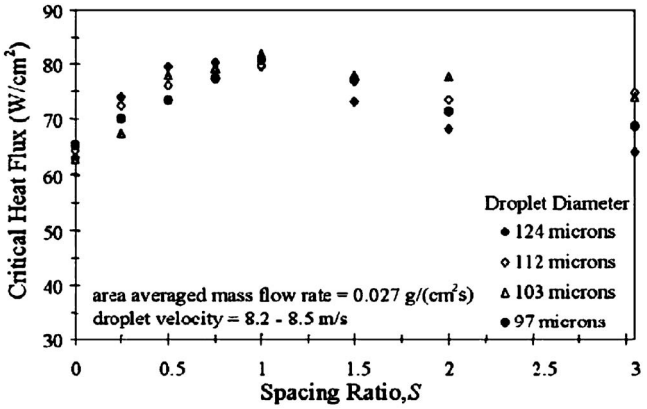

Fig. 1 Critical heat flux as a function of spacing ratio

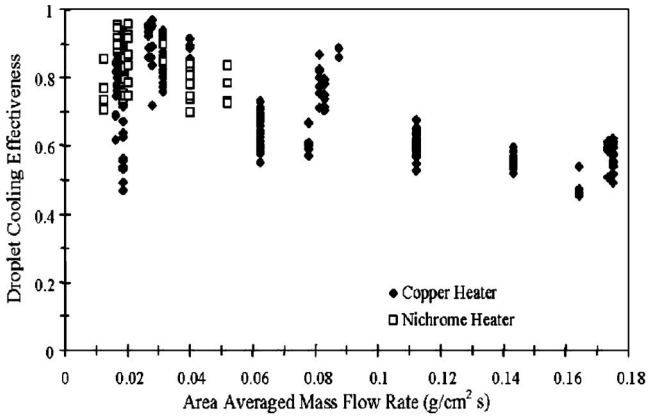

Fig. 2 Cooling effectiveness as a function of mass flow rates

0.32 °C. When the copper heater was used, the uncertainty in the heat flux values was less than 9% and the uncertainty in the average surface temperature was less than 1 °C.

Results

The heat transfer results can be expressed as a function of the droplet spacing ratio ($S=s/D$), which is defined as the ratio of the centerline distance between adjacent drops on the surface to the wetted diameter of the drop after it comes to rest on the heater surface.The value of droplet wetted diameter was calculated from a correlation originally developed by Kurabayashi et al. [17] and later modified by Yang [18].

A total of 407 critical heat flux tests were performed, and of those, 52 utilized the nichrome heater. To assure the consistency of the test data, approximately 10% of the tests were randomly repeated for the same droplet conditions. These tests confirmed that for a given heater, the heat flux values were repeatable within 6.5% and the surface temperatures at the critical heat flux were repeatable within 4 °C. Additionally, to justify a comparison of the data regardless of heater design, the CHF was measured for common droplet parameters and various impact spacings on both heaters. The measured CHF data for both heaters compared favorably with the largest difference of 9.9%.

Critical heat flux measurements for four droplet sizes and a fixed area-averaged mass flow rate are shown in Fig. 1 as a function of the droplet spacing ratio. The results in Fig. 1 show the moderate optimum that exists in the critical heat flux regardless of drop diameter. The optimum spacing ratio occurs when the drops are placed so that they just touch one another ($S=1$) and form a uniform, thin film once they spread on the surface.

The droplet velocity could be varied by changing the pressure in the water supply tank. For all of the tests conducted, the droplet velocities varied from a minimum value of 2.5 m/s to a maximum value of 9.1 m/s. If all other parameters are held constant while the drop velocity is varied over its maximum range, the critical heat flux values remained nearly constant with variations of up to only a few percent. Changes in the critical heat flux value were shown to be far more influenced by the droplet size, mass flow rate, and spacing than on the droplet velocity.

A quantity defined as the cooling effectiveness ε was used to quantify the efficiency of the droplets that cooled the surface. As with other researchers [19], this parameter is defined as the ratio of the critical heat flux to the theoretical maximum heat removal rate or

$$\varepsilon = \frac{q''_{\mathrm{CHF}}}{\dot{m}''_i[c_p(T_{\mathrm{sat}} - T_\infty) + h_{\mathrm{fg}}]} \tag{1}$$

The cooling effectiveness values measured with both heater designs are shown in Fig. 2 for various droplet mass flow rates. The spread in data shown in Fig. 2 can be expected. A fixed value of area-averaged mass flow rate can be achieved by many combinations of droplet properties. Identical flow rates can be produced by many small closely spaced drops, deposited at a high refresh frequency or by a few large, widely spaced drops, propelled at a low refresh rate. Therefore, the results in Fig. 2 disguise the influence of droplet size, spacing, and refresh rate and show the trend in effectiveness only as a function of a single variable. In general, however, the droplet cooling effectiveness decreases with an increase in the water mass flow rate. Therefore, as the mass flow increases, a smaller percentage of the liquid is vaporized on the surface and more of the water does not remain on the heater and change phase. The limit for very high mass flow rates would be the conditions that would exist for submerged pool boiling.

Critical heat flux correlations were determined in terms of the Weber and Strouhal numbers, which have traditionally been used in boiling correlations that involve periodic phenomena [10,19,20]. Two correlations are proposed, one for a single point of droplet impact ($S=0$) and another for spaced points of impact ($S>0$). The Weber number in the following correlations is defined as

$$\mathrm{We} = \frac{\rho v^2 d}{\sigma} \tag{2}$$

and the Strouhal number is defined as

$$\mathrm{St} = \frac{fd}{v} \tag{3}$$

This form of the Strouhal number is based on the refresh frequency, which is defined as the frequency that a droplet impacts a fixed location on the heater. The refresh frequency is more indicative of the heat transfer from the surface and is used instead of the droplet generation frequency, because drops that leave the orifice do not necessarily reach the surface at the generation frequency.

The dimensionless critical heat flux that is used in the following correlations is defined as

$$q''_* = \frac{q''_{\mathrm{CHF}}}{\dot{m}''_i h_{\mathrm{fg}}} \tag{4}$$

For a droplet stream impacting a single location ($S=0$), the correlation for the dimensionless critical heat flux was determined to be

$$q''^{m}_* = 1.1145\ \mathrm{We}^{-0.1202}\ \mathrm{St}^{-0.1431} \quad \text{for } S=0 \tag{5}$$

where the correlation is limited by

$$23.0 < \mathrm{We} < 202$$

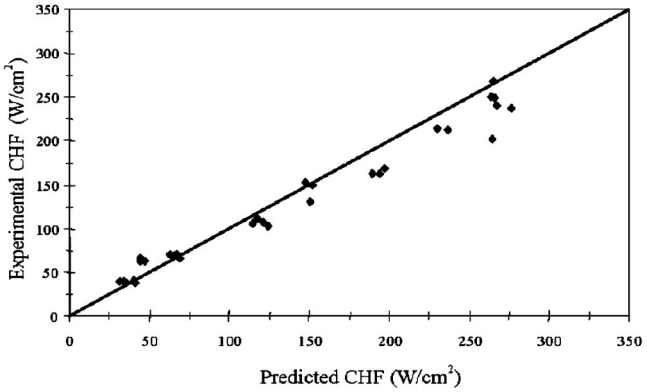

Fig. 3 Comparison of experimental and predicted (Eq. (5)) critical heat fluxes for droplets that impact at one location ($S=0$)

$$0.047 < \mathrm{St} < 0.58$$

When the droplets impact at different locations ($S>0$), the correlation is expressed in terms of an additional dimensionless group, which is the droplet spacing divided by the length of the heated surface (s/L) or

$$q''_* = 0.8382\ \mathrm{We}^{-0.0826}\ \mathrm{St}^{-0.1654}\left(\frac{s}{L}\right)^{0.2391} \quad \text{for } S>0 \qquad (6)$$

where

$$21.6 < \mathrm{We} < 202$$

$$2.6\times10^{-5} < \mathrm{St} < 0.30$$

$$8.5\times10^{-3} < \frac{s}{L} < 0.47$$

A comparison of the correlation for critical heat flux for a single impact location, Eq. (5), and the experimental results for $S=0$ is shown in Fig. 3. The standard deviation between the experimental and predicted critical heat flux is less than 10% for 82% of the data, and the coefficient of determination is 0.307. For the critical heat flux data obtained with deflected droplet sprays ($S>0$), a comparison of the experimental and predicted data (Eq. (6)) is shown in Fig. 4. The standard deviation between the experimental and predicted critical heat flux was less than 10% for 83% of the data, and the coefficient of determination was 0.388.

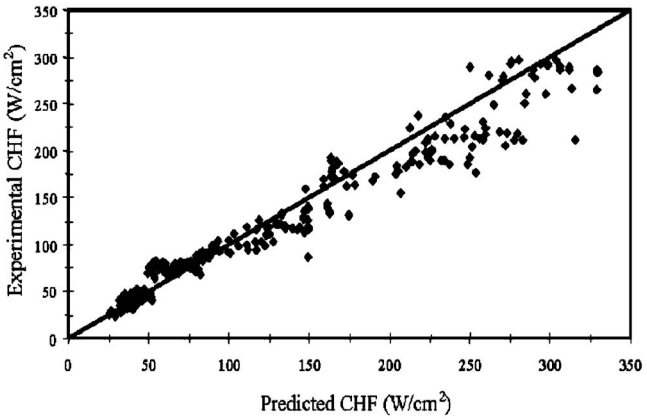

Fig. 4 Comparison of experimental and predicted (Eq. (6)) critical heat fluxes for spaced droplets ($S>0$)

Conclusions

The critical heat flux measured for the limited range of mass flow rates that were generated by the experimental apparatus was 24–297 W/cm^2 for surface temperatures between 117°C, and 130°C. The droplet cooling effectiveness, defined as the ratio of the critical heat flux to the theoretical maximum heat removal rate, ranged from 0.45 to 0.96. For a similar mass flow rate, an optimal spacing ratio between droplet impacts was found to exist between 0.75 and 1.5. By spacing the droplets at the optimal spacing, the critical heat flux can be increased by approximately 30%. A correlation for the critical heat flux as a function of the Weber number, the modified Strouhal number defined on the basis of refresh rate frequency, and a nondimensional spacing was determined. Regardless of the droplet parameters, droplet cooling was capable of achieving approximately twice the heat flux of traditional pool boiling at similar conditions.

Nomenclature

c_p = specific heat at constant pressure
d = diameter of drop prior to impact
D = wetted diameter of impacted drop
f = frequency that a drop hits a fixed location
h_{fg} = latent heat of vaporization
L = length of heated surface
m''_i = area-averaged mass flow rate
q'' = heat flux
q''_* = dimensionless CHF defined in Eq. (4)
Re = Reynolds number
s = spacing between drops on surface
S = drop spacing ratio defined as s/D
St = Strouhal number defined by Eq. (3)
T = temperature
We = Weber number defined by Eq. (2)

Greek Symbols

β = drop spreading ratio
ε = cooling effectiveness
μ = dynamic viscosity
ν = kinematic viscosity
ρ = density
σ = surface tension

Subscripts

CHF = critical heat flux
L = value for the bulk liquid phase
s = property of heated surface
S = value at surface conditions
sat = property of saturated liquid
∞ = property of ambient fluid

References

[1] Toda, S., 1972, "A Study of Mist Cooling (1st Report: Investigation of Mist Cooling)," Heat Transfer-Jpn. Res., **1**(3), pp. 39–50.
[2] Toda, S., 1974, "A Study of Mist Cooling (2nd Report: Theory of Mist Cooling and Its Fundamental Experiments)," Heat Transfer-Jpn. Res., **3**(1), pp. 1–44.
[3] Bonacina, C., Del Giudice, S., and Comini, G., 1979, "Dropwise Evaporation," ASME J. Heat Transfer, **101**, pp. 441–446.
[4] Yang, J., Pais, M. R., and Chow, L. C., 1992, "High Heat-Flux Spray Cooling," Proc. SPIE, **1739**, pp. 29–40.
[5] Kurokawa, M., and Toda S., 1991, "Heat Transfer of an Impacted Single Droplets on the Wall," *ASME/JSME Thermal Engineering Proceedings*, Vol. 2, pp. 141–146.
[6] Xiong, T. Y., and Yuen, M. C., 1991, "Evaporation of a Liquid Droplet on a Hot Plate," Int. J. Heat Mass Transfer, **34**(7), pp. 1881–1894.
[7] Tilton, D. E., Chow, L. C., and Mahefkey, E. T., 1987, "High Power Density Evaporative Cooling," AIAA 22nd Thermophysics Conference, Honolulu, HI, June 8–10, Paper No. AIAA-87-1536.
[8] Pais, M., Tilton, D., Chow, L., and Mahefkey, E., 1989, "High Heat Flux, Low Superheat Evaporative Spray Cooling," 27th Aerospace Sciences Meeting, Reno, NV, Jan. 9–12, Paper No. AIAA 89-0241.
[9] Yao, S. C., and Choi, K. J., 1987, "Heat Transfer Experiments of Mono-Dispersed Vertically Impacting Sprays," Int. J. Multiphase Flow, **13**(5), pp.

639–648.
[10] Sheffield, R. J., 1994, "High Heat Flux Spray Cooling," Ph.D. thesis, George W. Woodruff School of Mechanical Engineering, Georgia Institute of Technology, Atlanta, GA, June.
[11] Halvorson, P. J., Carson, R. J., Jeter, S. M., and Abdel-Khalik, S. I., 1994, "Critical Heat Flux Limits for a Heated Surface Impacted by a Stream of Liquid Droplets," ASME J. Heat Transfer, **116**, pp. 679–685.
[12] Rayleigh, F. R. S., 1878, "On the Instability of Jets," Proc. London Math. Soc., **10**, pp. 4–13.
[13] Dabora, E. K., 1967, "Production of Monodisperse Sprays," Rev. Sci. Instrum., **38**(4), pp. 502–506.
[14] Schneider, J. M., and Hendricks, C. D., 1964, "Source of Uniform-Sized Liquid Droplets," Rev. Sci. Instrum., **35**(10), pp. 1349–1350.
[15] J. Dressler, 1993, "Two Dimensional, High Flow, Precisely Controlled Monodisperse Drop Source," Aero Propulsion and Power Directorate, Wright Laboratory, Wright-Patterson Air Force Base, Technical Report No. WL-TR-93-2049.
[16] Sellers, S. M., 2000, "Heat Transfer Resulting from the Evaporation of Liquid Droplets on a Horizontal Heated Surface," Ph.D. thesis, School of Mechanical Engineering, Georgia Institute of Technology.
[17] Kurabayashi, T., Karasawa, T., and Iida, K., 1967, "Impact of Liquid Droplets on a Solid Surface," JSME, pp. 153–156.
[18] Yang, W. J., 1975, "Theory on Vaporization and Combustion of Liquid Drops of Pure Substances and Binary Mixtures on Heated Surfaces," Institute of Space and Aeronautical Sciences, University of Tokyo, Technical Report No. 535.
[19] Sawyer, M. L., Jeter, S. M., and Abdel-Khalik, S. I., 1997, "A Critical Heat Flux Correlation for Droplet Impact Cooling," Int. J. Heat Mass Transfer, **40**(9), pp. 2123–2131.
[20] Healy, W. M., Halvorson, P. J., Hartley, J. G., and Abdel-Khalik, S. I., 1998, "A Critical Heat Flux Correlation for Droplet Impact Cooling at Low Weber Numbers and Various Ambient Pressures," Int. J. Heat Mass Transfer, **41**(6–7), pp. 975–978.